Minnesota Department of Transportation

RESEARCH SERVICES & LIBRARY

Office of Transportation System Management

Quantifying Moisture Effects in DCP and LWD Tests Using Unsaturated Mechanics

Kimberly Hill, Principal Investigator
Department of Civil Engineering
University of Minnesota

February 2014

Research Project
Final Report 2014-13

LRRB
LOCAL ROAD RESEARCH BOARD

To request this document in an alternative format call 651-366-4718 or 1-800-657-3774 (Greater Minnesota) or email your request to ADArequest.dot@state.mn.us. Please request at least one week in advance.

Technical Report Documentation Page

1. Report No.	2.	3. Recipients Accession No.	
MN/RC 2014-13			
4. Title and Subtitle Quantifying Moisture Effects in DCP and LWD Tests Using Unsaturated Mechanics		5. Report Date February 2014 6.	
7. Author(s) Danielle Tan, Kimberly Hill, Lev Khazanovich		8. Performing Organization Report No. CTS Project #2011026	
9. Performing Organization Name and Address Department of Civil Engineering University of Minnesota 500 Pillsbury Drive S.E. Minneapolis, MN 55455-0220		10. Project/Task/Work Unit No. 11. Contract (C) or Grant (G) No. (C) 89261 (WO) 190	
12. Sponsoring Organization Name and Address Minnesota Department of Transportation Research Services & Library 395 John Ireland Boulevard, MS 330 St. Paul, MN 55155		13. Type of Report and Period Covered Final Report 14. Sponsoring Agency Code	
15. Supplementary Notes http://www.lrrb.org/PDF/201413.pdf			

16. Abstract (Limit: 250 words)

Minnesota counties and the Minnesota Department of Transportation (MnDOT) use the Dynamic Cone Penetrometer (DCP) and the Lightweight Deflectometer (LWD) for *in situ* evaluation of stiffness and strength of soil and aggregate bases. The *in situ* test of choice (DCP or LWD) varies somewhat by county and region, depending partly on the local soil conditions and partly on historical preferences. The LWD is considered a measure of modulus while the DCP is considered a measure of shear strength. Recent field and laboratory tests have provided calibration for these tests for several specific granular samples. However, the results are likely less reliable for a broader range of potential granular materials used for granular bases.

The objective of this research is to build on a mechanistic model developed for dry aggregate bases under LRRB INV 850 to increase its applicability to more materials and tests used in Minnesota. There were three primary thrusts to these new additions: (1) A model for the LWD test has been added so that computational predictions for DCP tests could be compared with those from LWD tests; (2) Particle-scale models for moisture and fine particle content have been included for the user to input these among the other existing material input parameters, and (3) Analogous algorithms have been developed for the DCP and LWD tests to be used with PFC3D, a commercial code maintained by Itasca Consulting Group.

17. Document Analysis/Descriptors	18. Availability Statement		
Discrete element method, Dynamic cone penetrometer, Light weight deflectometer, Granular materials, Aggregates	No restrictions. Document available from: National Technical Information Services, Alexandria, VA 22312		
19. Security Class (this report) Unclassified	20. Security Class (this page) Unclassified	21. No. of Pages 188	22. Price

Quantifying Moisture Effects in DCP and LWD Tests Using Unsaturated Mechanics

Final Report

Prepared by:

Danielle Tan
Lev Khazanovich
Kimberly Hill

Department of Civil Engineering
Univeresity of Minnesota

February 2014

Published by:

Minnesota Department of Transportation
Research Services & Library
395 John Ireland Boulevard, MS 330
St. Paul, MN 55155

Acknowledgments

The authors express appreciation to the Local Road Research Board and the Materials and Research Laboratory of the Minnesota Department of Transportation for their support of this research. The authors are indebted to Technical Liaison John Siekmeier of the Minnesota Department of Transportation for his constructive comments, suggestions and leadership throughout the project. Indeed, the authors would like to express gratitude to all of the members of the Technical Advisory Panel for their input throughout the project and helpful critiques of this report. In addition to John Siekmeier, this list includes: Lee Amundson, Tim Andersen, Terry Beaudry, Shontao Dai, Derrick Dasenbrock, Rebecca Embacher, Bernard Izevbekhai, Maureen Jensen, Ruth Roberson, and Bruce Tanquist. The authors also express their gratitude to Administrative Liaison Nelson Cruz for his guidance during the project and also to Dr. David Potyondy of Itasca Consulting group for his instruction and help in developing the PFC3D macros for this project and for his documentation of the translation from DEMP3D formulation to PFC3D macros documented in Appendix D of this document. Finally, the authors are also grateful to Itasca Consulting Group, for donating a temporary license of PFC3D to the authors for their use of the software over the duration of this project.

Table of Contents

List of Figures

List of Tables

Executive Summary

The strength and stability of unbound granular bases and subbases play a key role in the performance of the pavement system. There is no standard constitutive model for the bulk behavior of granular bases, so the pavement community relies on careful systematic testing for predicting the response of granular materials to stress and subsequently developing best practices for their use. Two of the most common performance-based *in situ* tests are the Dynamic Cone Penetrometer (DCP) test and the Lightweight Deflectometer (LWD) test because of their effectiveness and relative ease in use. The specific device used varies depending on the local soil type and regional practices. Field tests and experimental results have shown that the mechanical response of granular materials is particularly sensitive to the particle size distribution and moisture content of the material.

The DCP and LWD devices are invaluable, and, for certain commonly-used materials, they have enabled the development of established relationships between certain measures of the particle size distribution, moisture content, and measures of the bulk modulus necessary for pavement design. However, because of practical restrictions, the data acquired for developing best practices for reaching preferred pavement behavior is limited. Two extensive sets of data and analysis help illustrate the simultaneous benefits and limitations to these physical results: (1) DCP field tests compiled by Oman (2004) with corresponding analysis and (2) LWD and DCP laboratory tests compiled and analyzed in the context of field data by Davich et al. (2006) and Siekmeier et al. (2009). The results illustrate the need to go beyond physical sample testing for quality assurance / quality control, so they are briefly summarized below.

In the first case, Oman (2004) compiled documented DCP results for granular bases comprised of a wide range of materials under a variety of conditions in Minnesota. He noted that up to 19% of aggregate bases meeting earlier DCP requirements were inadequate in that they either had relative densities below 95% or were inadequate in the opinion of a grading and base inspector. While the DCP had otherwise been given good reviews, one criticism was that the specifications did not include consideration of particle size distribution or moisture content. In this context, Oman used compiled data to produce an empirical formula for recommended DCP target values that included moisture content and a new representative grain size number, the "grading number," the sum of the percentages passing the seven most common sieves divided by one hundred. The use of Oman's new formulation helped to greatly reduce the percentage of poorly compacted bases being accepted. However, for each set of material parameters – representative grain size distribution and moisture content – he found a wide range of DCP results, indicating additional details may need to be considered for best practices in the field, particularly when considering use of new and recycled materials for which there are no established data.

In the second case, to validate Oman's 2004 results and to provide some test data needed to draft a similar specification for LWD devices, MnDOT's Office of Materials and Road Research carried out a series of DCP and LWD tests on controlled laboratory specimens during the summer of 2005 (Davich et al., 2006). The specimens were prepared using three granular borrow samples at varying moisture contents and densities. Portable testing devices, which included a DCP, an LWD, a Percometer, and a Trident moisture meter, were used upon the specimens to produce independent strength, stiffness, and moisture measurements. As an added benefit, it was possible to evaluate the performance of each of these in-situ test devices in a controlled setting so that a specification for their use could be created. As part of the conclusions, Davich and co-workers provided empirically derived recommendations for use of the DCP and LWD tests. However, the samples

used to provide the calibration were limited. It would be preferable to perform tests over a wider range of particle size distributions reflective of bases used throughout Minnesota, but the tests are both labor and time intensive. Furthermore, there is not the extensive data set available from field results for the LWD as there was for the DCP results analyzed by Oman (2004).

The pavement community faces two problems that this current report addresses. First, there is the realization of a need for more data to improve LWD and DCP specifications. Second, there is an increasing cost to the labor and time required to perform the physical tests needed to acquire this data. To obtain a greater range of data, we consider the possibility of using the computer as a potential virtual laboratory to perform numerical experiments on related systems with the goal of improving the understanding of parameter dependence of the strength and resilience of these systems. With an accurate model to perform computational tests paired with increasing power of digital image analysis and field image acquisition, such a computational tool has the potential to revolutionize the construction standards for using moist unbound pavement materials.

In this project, we focused on the development of a computational framework that could be used to accurately model the variability of DCP and LWD test results with different amounts of moisture and fine particles. We use the discrete element method (DEM) to model the effects of particle properties, particle size distribution, and moisture of a granular mixture responding to applied stresses. The DEM model we use incorporates details such as the properties and size distribution of the coarse particles directly. Over the course of the project, we investigated three models to represent the effect of moisture and fine particles on the results at a particle-scale level:

(1) The first model is based on established liquid bridge theory. This model accounts for moisture in a fully mechanistic way and fines in a significantly more empirical way through a surface tension parameter.
(2) The second model is based on experimental work by Gupta and colleagues. From their experiments, they developed an empirical relationship which related moisture content in a soil to the mixture composition and measured suction (negative pore pressure). We adapted this relationship for moisture and fines content into our DEM model as a more direct way of including fines and moisture content.
(3) The third model is a 'hybrid' that essentially combines the first two models with a consideration of a frictional coefficient. One component of the hybrid framework involves details of the explicit composition model implemented with a similar mathematical form to the liquid bridge model to represent the moisture content in the granular materials. The second component involves a change in interparticle friction coefficient to represent the fine particle content in a relatively coarse granular base, where increasing fines results in increasing lubrication (or decreasing interparticle friction) within the model.

The model tests for each framework were performed using DEM simulations with particle size distributions similar to the coarse fraction of MnDOT Class 5 aggregate base material and calibrated and compared with experimental target values. The moisture contents in the model LWD tests were similar to those used for the experimental target values (7% to 11%). The friction coefficients in the model LWD tests described here represented grading numbers from approximately 3 to 4.5, compared with the experimental target values that reached 6.

As detailed in the report, the results from the first two model frameworks reproduced some details of the experimental test results reasonably, but certain other details were lacking. Based on a comparison between the results obtained from the first two models and estimated target data, it appears that both model frameworks missed some fundamental detail of the inter-particle interactions. Both the adaptations of the liquid bridge and explicit composition models into DEMP-3D involved the use of an attractive force between particle pairs but no change in lubrication or friction between particles typically seen when fine particles are present. The third model incorporated an additional component that involved a change of the interparticle friction coefficient. This model had the ability to represent the full range of behavior measured by the DCP and LWD tests. As detailed in the report, the model results acquired using this third model are in qualitative agreement with experimental data and associated target values reported by Siekmeier and colleagues (2006 and 2009).

In its current form utilizing "moisture model (3)" our DEM model can be used to predict behavior for a relatively narrow range of base materials. With some modest improvements, specifically the manner in which the fine particles and moisture parameters are represented by the friction and suction coefficients within the force model, this framework can be extended to a wide range of granular bases. To enable MnDOT engineers to do this, as part of the project, we developed macros for commercial DEM software PFC 3D developed by Itasca Consulting Group, with the help of Itasca expert of Dr. David Potyondy. This can be paired with other DEM modeling techniques accessible within PFC 3D macros such as clumping to represent angularity and particle shape to investigate a wide range of effects related to both short-term and long-term responses of granular bases to applied stresses. In addition, future application includes the simulation of granular bases containing recycled pavement materials. Both the larger recycled aggregate and the bitumen between the particles could be included once the effects of how interstitial fluid properties such as surface tension are modified by the inclusion of these materials are better understood and quantified.

Combined with tremendous advances in portable high resolution digital cameras and associated digital analysis applications, this model framework shows exciting promise for vastly improving quality assessment / quality control in the field. The DEM simulations could aid in developing more effective guidelines for granular bases that includes consideration of more specific details of the materials comprising the base, including particle shape. We expect these numerical tools will become more efficient in their ability both to evaluate many details of material properties and more effective than physical tests in developing target values for the use of new and recycled materials. Analysis of images taken in the field can be paired with DEM simulations to create recommendations associated with specific field conditions. As computer speeds increase, this framework may be able to represent scales closer to that in the field, expanding the range of applicability and usefulness in the design of more efficient pavement systems. Ultimately, we can envision MnDOT pavement inspectors will be able to take a picture of granular material in the field with high resolution cameras on smart phones, analyze the pictures for size and shape distributions with applications ("apps") developed for the phone and use databases created from the DEM software described in this report to choose the most appropriate DCP and LWD target values on a case-by-case basis.

Chapter 1 Introduction

Many flexible and rigid pavement systems incorporate unbound granular bases and subbases. Strength and stability of the unbound layers play a key role in the strength, stability, and lifetime of the pavement itself. There is no standard constitutive model for the bulk behavior of granular bases, so the pavement community relies on careful systematic testing for predicting the response of granular materials to stress and subsequently developing best practices for their use. Two of the most common *in situ* tests are the Dynamic Cone Penetrometer (DCP) test and the Lightweight Deflectometer (LWD) test because of their effectiveness and relative ease in use. The specific test used varies depending on the local soil type, or regional practices.

Field tests and other experimental results have shown that the mechanical response of granular materials is particularly sensitive to the particle size distribution and moisture content (e.g., Refs. [1, 2, 3, 4, 5, 6]), among other physical properties like particle shape and density [1, 2]. For example, the dependence of the bulk material strength and stiffness of some granular materials on certain measures of the particle size distribution and moisture content have been measured experimentally (e.g., Refs. [3, 4, 5]). However, there is as yet no complete mechanistic understanding of these relationships. As such, the reliability of predictions made using these results for granular mixtures comprised of new (e.g., recycled) materials is limited. Further, the prospect of performing similar tests for all possible current and future granular bases is prohibitively expensive and time consuming. We therefore adapt the philosophy of Cundall and Hart [7] in considering the computer as a potential virtual laboratory to perform numerical experiments with the goal to improve our understanding of parameter dependence of the strength and resilience of these materials for use in pavement systems. The focus of this project is in the development of a model framework, informed by experimental results, that may be used to predict the variability of DCP and LWD test results with different amounts of moisture and fine particles.

For this project we use the discrete element method (DEM) to model the effects of particle properties, particle size distribution and moisture on the response of a granular mixture to applied stresses. This is not a new idea; models based on the DEM have been applied in various fields of soil and rock mechanics, granular flow, and powder mechanics (e.g., [8, 9, 10, 11, 12, 13, 14, 15, 16, 17, 18, 19, 20, 21, 22, 23, 24, 25, 26]). This method is particularly useful for representing the influence of the discrete and heterogeneous nature of granular materials on the bulk properties, as the method can track each particle separately and model the inter-particle interaction based on physical properties of the particles and details of the surrounding medium such as moisture. The DEM is a versatile tool and can be adapted to simulate very complicated applications, even capturing details such as the angularity in particle shapes and adhesive forces between particles (e.g.,[17]). Using this method the microscopic properties can be directly linked to the macroscopic properties of the granular materials as measured by laboratory and field tests.

To date, DEM has been used to model several tests of unbound granular materials [8, 10, 11, 12, 13, 15, 16, 19, 22], as reviewed in some detail in Refs. [24, 25, 26]. For example, a number of researchers (detailed in, for example, Refs. [12, 14, 18, 20, 23, 25, 26]) have used DEM to model the resilient modulus test and the dependence of the results on the deviator stress and confining pressure. They found that the numerical simulation results compared favorably with trends seen in physical experiments and field observations (e.g., [1, 2, 27]). The DEM model has also been used to model penetration tests (e.g., [9, 13, 14, 21, 26]). These DEM studies reproduced certain qualitative and quantitative details of physical experiments, such as the dependence of the depth of

penetration after different numbers of DCP blows in Ref. [24]. The agreement between DEM simulation results and physical observations and experiments suggests that DEM is a promising tool for modelling such tests of granular materials.

Adding a small amount of moisture into a granular material can change its response to applied stresses dramatically. In their 1948 Highway Research Board report, Hveem and Carmany summarized some of what has been qualitatively understood about the problem for decades: “Resistance of soils or granular materials is due to friction between the solid particles and the cohesion or tensile strength furnished by films of moisture. Liquid films also cause lubrication and this reduction in particle friction is often responsible for an overall reduction in resistance value." [28]. Ganesan et al. [29] presented a review on experiments on bulk powders and solids, observing that the bulk density decreased and compressibility increased with increasing moisture content. Pierrat et al. [30] theorised that moisture introduced an isotropic compressive stress, resulting in the bulk yield locus translating by the magnitude of that stress. According to Lekarp et al. [1], as moisture content increases to near saturation, the resilient (elastic) modulus decreases. This is supported by the studies of Yang et al. [31] where they found that soil suction decreased with increasing moisture content. Experimental work by Gupta and Larson [32] and Gupta et al. [33] showed a similar trend.

To capture the effect of moisture within our DEM model, we consider physical experiments which focused solely on how the moisture force manifests at the particle scale. Mason and Clark [34] and Shimada et al. [35] measured an apparent attractive force between pairs of identical particles in the presence of moisture. Further, their results indicate that the attractive forces due to moisture increase with moisture content. This behaviour can be modelled quantitatively using what is known of the manner in which droplets of liquid modify interparticle forces between neighbouring particles via *liquid bridges* formed between the particles (e.g., Refs. [36, 37, 38, 39]). This has the benefit of providing a direct mechanistically-based model for the manner in which moisture modifies the particle-particle interactions. DEM models that represent moisture effects in granular materials using the liquid bridge theory have successfully reproduced experimental behaviour, e.g. the collapse of an unsaturated granular mixture upon addition of liquid in Ref. [40]. We describe the liquid bridge model and our use of this framework in the modeling sections that follow shortly.

In this project, we developed three different frameworks to capture the effects of moisture and the presence of fine particles on the bulk behavior of tests of unbound materials used for pavement systems. First we focused on the adaptation of a basic “liquid bridge” model for moisture content into our DEM model for tests of granular bases, DEMP-3D. Next we applied this new version of DEMP-3D to model LWD tests and DCP tests. We then investigated the effectiveness of modifications to the basic bridge model inspired in part by experimental measurements by Gupta and colleagues [32, 33] that included explicit considerations of fine particles and moisture. These modelling efforts results are in qualitative agreement with estimated targer values reported by Siekmeier et al. [4] (i.e., Figs. 5, 6 and 7). Based on these results, we developed a set of empirical relationships between model parameters and experimental parameters so that the new DEMP-3D model may be used as a better predictive tool for test results of coarse granular bases.

This report is organized as follows. We first describe results from physical experiments we use to test, validate and further refine our models. We then present the DEM model briefly and include more details in Appendix A. We then present the three moisture / fines models we tested for effectiveness over the duration of this project, followed by our results in some detail. We discuss

these results as well as the pros and cons of each in the sections that follow. Additional test results relevant to investigation of the boundary conditions may be found in Appendix B.

Finally, we describe parallel model development we performed for commercial DEM software PFC 3D developed by Itasca Consulting Group, with the help of Itasca expert of Dr. David Potyondy. We present a comparison between DEMP-3D and PFC3D implementation of the model. Appendix C contains a user's guide to the PFC3D macros we developed. Appendix D contain details of the translation between the DEMP-3D moisture model and that adapted to the PFC3D macro format. We conclude with a summary of the project results and an outlook for future possibilities for the models developed for this project.

Chapter 2 Field Tests and Estimated Target Values

Recently Siekmeier et al. [4] reported estimated target values derived from lightweight deflectometer (LWD) and dynamic cone penetrometer (DCP) tests conducted in the laboratory and field on typical Minnesota soils, for a limited range of moisture contents and particle size distributions. We use these target values to validate and further refine our model, so we describe them in some detail here. We first describe the physical properties of these tests.

2.1 Lightweight Deflectometer (LWD) Test

Figure 1 shows a sketch of a typical lightweight deflectometer (LWD) with some physical parameters labeled. Figure 2 shows a lightweight deflectometer in use in the field (from Siekmeier et al. [4]). The test procedure is as follows: First the plate of the LWD is placed firmly on the ground; A weight is released from a predetermined height, and the deflection of the plate is measured as a function of time during the test; The weight is dropped three times without recording the deflection to ensure that the LWD is seated firmly on the surface; Then, the weight is dropped three more times, and the resulting peak deflections are recorded. The average of these recorded peak deflections is used to calculate an effective modulus.

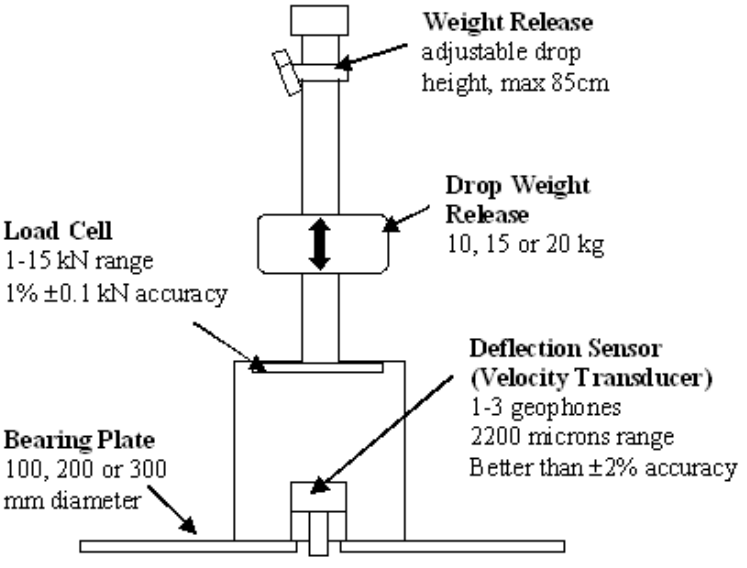

Figure 1: Sketch of typical light weight deflectometer (LWD).

Significant parameters for the LWD test are the applied load (resulting from the dropped weight of 10, 15 or 20 kg), drop height (25, 50 or 75-cm) and plate diameter (10, 20 or 30-cm diameter). The experimental target values we use for comparison were obtained using a 20-cm diameter plate and a weight and drop-height combination such that the peak stress exerted was 0.2 MPa. A detailed description of the LWD and the standardized testing procedure can be found in Refs. [3, 4].

Figure 2: Photograph of the Light weight deflectometer (LWD) in the field (Seikmeier et al. [4]).

2.2 Dynamic Cone Penetrometer (DCP) Test

Figures 3 and 4 illustrate salient details of the field Dynamic Cone Penetrometer (DCP) Test. Figure 3 shows a sketch of a typical dynamic cone penetrometer. Figure 4 shows pictures of a dynamic cone penetrometer in use in the field (Siekmeier et al. [4]).

The procedure for using the DCP in Minnesota (e.g., see Ref. [4]) is as follows: first the user places the DCP so that the cone penetrates the ground slightly with the rod oriented vertically (normal to the ground surface). The user then measures and records the initial height of the bottom of the anvil. Next, the user raises the hammer (8 kg) off of the anvil up to the handle and then releases the hammer. The subsequent impact between the hammer and the anvil causes the DCP cone to penetrate into the ground by some distance. The user measures and records the new height of the bottom of the anvil. The user then raises the hammer to the handle of the DCP again, releases it onto the anvil and records the new height of the anvil resulting from the additional penetration of the DCP cone into the granular material. The user repeats these drops several times, and records the subsequent additional distances of ground penetration.

Typically, the user drops the hammer a total of twelve times. The results from the first two drops are recorded but are considered only for ‘seating’ the DCP, not for calculating the strength or

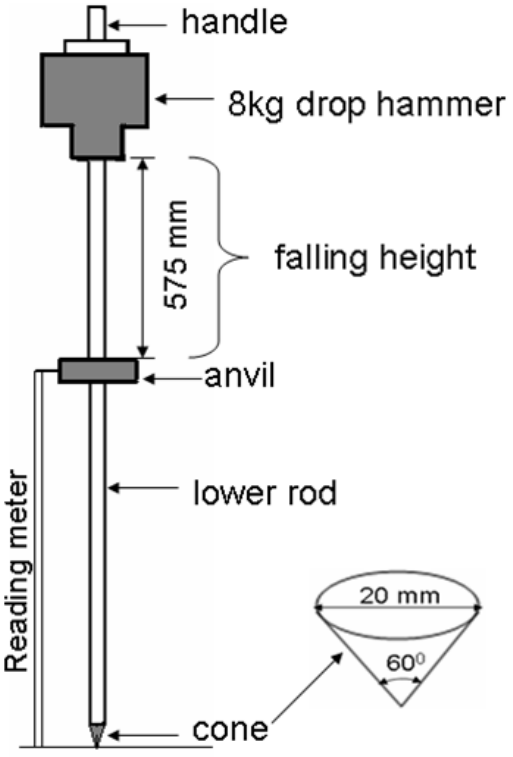

Figure 3: Sketch of typical dynamic cone penetrometer (DCP) (Yohannes et al. [24]).

modulus of the granular materials, because the top portion of the granular material is usually disturbed and non-representative of the bulk material. The average penetration from 3rd-7th drops and another average penetration from the 8th-12th drops are typically used to represent two values of the DCP penetration index (DPI). A detailed description of the DCP and the standardized testing procedure can be found in [4].

Significant parameters for the DCP test are the hammer mass (8kg) and the drop height of 575mm. MnDOT recommends using the 8 kg hammer as the granular material in the aggregate base is typically highly-compacted. We compare our simulation results to estimated target values based on experimental and field measurements where a 8kg hammer is used.

2.3 Experimental Results: Estimated Target Values

The DCP and LWD have recently been used to establish relationships between certain measures of the particle size distribution, moisture content, and measures of the bulk modulus necessary for pavement design. Two extensive sets of data and analysis have provided information for this purpose: (1) DCP field tests compiled by Oman [41] with corresponding analysis and (2) LWD and DCP laboratory tests compiled and analyzed in the context of field data by Davich et al. [3] and Siekmeier et al. [4]. Both are relatively new in considering the simultaneous influence of particle size distribution and moisture content.

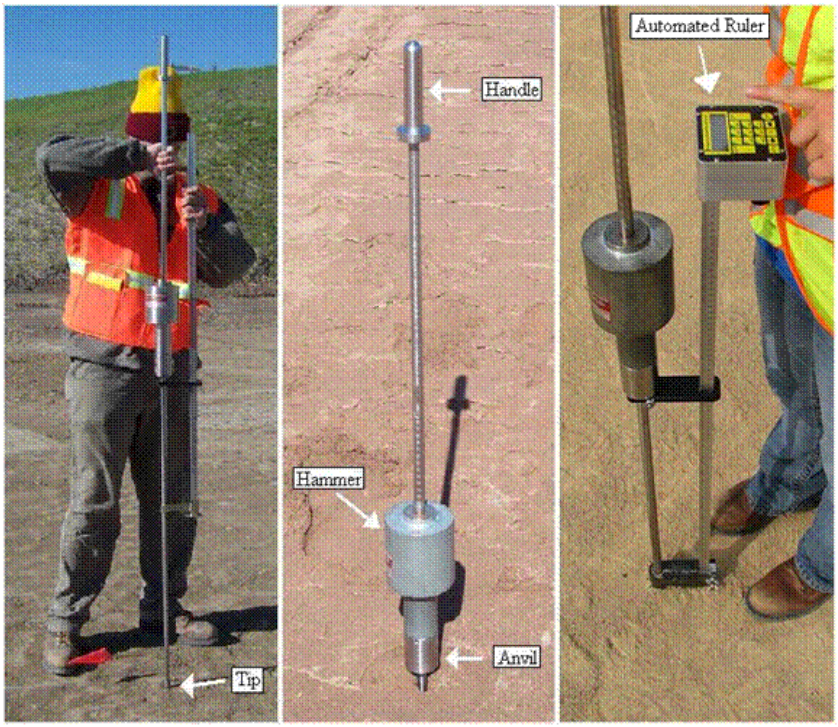

Figure 4: Pictures of a dynamic cone penetrometer (DCP) in the field (Siekmeier et al. [4]).

To date there is no standardized single parameter used to describe a mixture's particle size distribution. In this project we use a parameter defined by Oman [41]: a 'grading number' (*GN*), which is defined as the sum of the percent passing values from the seven most common sieves divided by 100:

$$GN = \frac{(\%\leq 25mm)+(\%\leq 19mm)+(\%\leq 9.5mm)+(\%\leq 4.75mm)}{100\%} + \frac{(\%\leq 2.0mm)+(\%\leq 425\mu m)+(\%\leq 75\mu m)}{100\%} . \quad (1)$$

In Equation 1, the notation %≤*x mm* refers to the percentage of particles in the mixture (by weight) that pass through a sieve with *x* mm openings. While the *GN* is a non-unique measure of the size distribution, generally a higher value indicates a mixture with a higher proportion of smaller particles.

The moisture content is expressed in terms of the *gravimetric moisture content* ω_g, i.e., the mass of water m_w per unit mass of dry granular material m_s:

$$\omega_g = m_w/m_s \quad (2)$$

Typically, there is some non-zero moisture in a granular base, but not much higher than 10%. We consider data from granular materials ranging from 4% to 12%.

Figure 5 presents the experimentally-based estimated target values from LWD tests reported in Ref. [4] in terms of the maximum deflection Δ and effective modulus of elasticity E_{LWD} each plotted as a function of gravimetric moisture content ω_g. The maximum deflection of the LWD test is related to an effective modulus of elasticity according to Davich et al. [3]:

$$E_{LWD}=2r_p\sigma\left(1-\nu_s^2\right)\frac{10^6 D}{\Delta}, \tag{3}$$

where E_{LWD} is in MPa, and the peak deflection during loading, Δ, is in μm. For our results, $r_p = 0.1m$ is the LWD plate radius, σ=0.2 MPa is the peak stress applied to the LWD plate, ν_s= 0.35 is the Poisson's ratio of the bulk granular material, and *D*=0.79 is the LWD plate rigidity. We note that in Siekmeier et al. [4] ω_g was provided over a range of values; we used the central values for plotting the data Figure 5. Also, in Ref. [4] the estimated target values were presented in terms of E_{LWD} and no values for the peak deflections in LWD tests were given. Therefore, for the results plotted in Figure 5 we back-calculated the values for Δ from the values given for E_{LWD} using Equation 3.

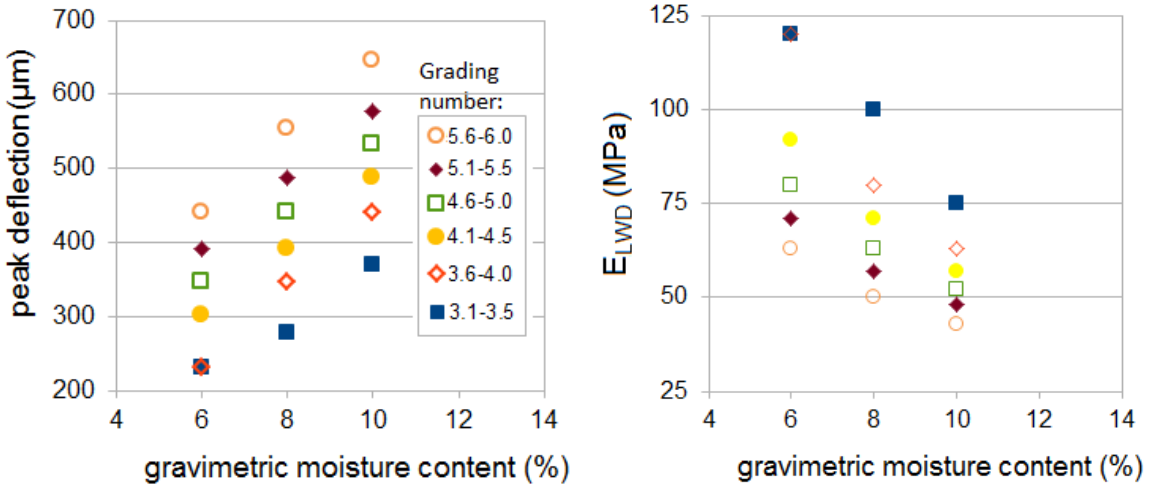

Figure 5: Experimentally-based estimated target values from Siekmeier et al. [4] showing trend in peak deflection (left) during the LWD tests as a function of gravimetric moisture content, and the corresponding effective bulk modulus (right), for mixtures with different values of grading number.

The data in Figure 5 indicates that for any particular particle size distribution (or *GN*), the maximum deflection increases with increasing moisture content, and the effective modulus E_{LWD} decreases. Also, for any particular moisture content, the maximum deflection increases with increasing *GN* (or increasing fines content), and the effective modulus, E_{LWD} decreases with increasing *GN*. The latter is even more clear in Figure 6 where the maximum deflection Δ and effective modulus of elasticity E_{LWD} are each plotted as a function of gravimetric moisture content. Since the *GN* was provided in Ref. [4] in terms of a range of values, we used the central values of each range for the plots in Figure 5.

Figure 7 presents the experimentally-based target values from DCP tests reported in Ref. [4] plotted as a function of gravimetric moisture content ω_g and also as a function of grading number *GN*. These results show that the average penetration increased with both increasing moisture

content and increasing fines content. Similar to the LWD target, this typically corresponds to a decreasing effective bulk modulus with increasing moisture content and increasing fines content.

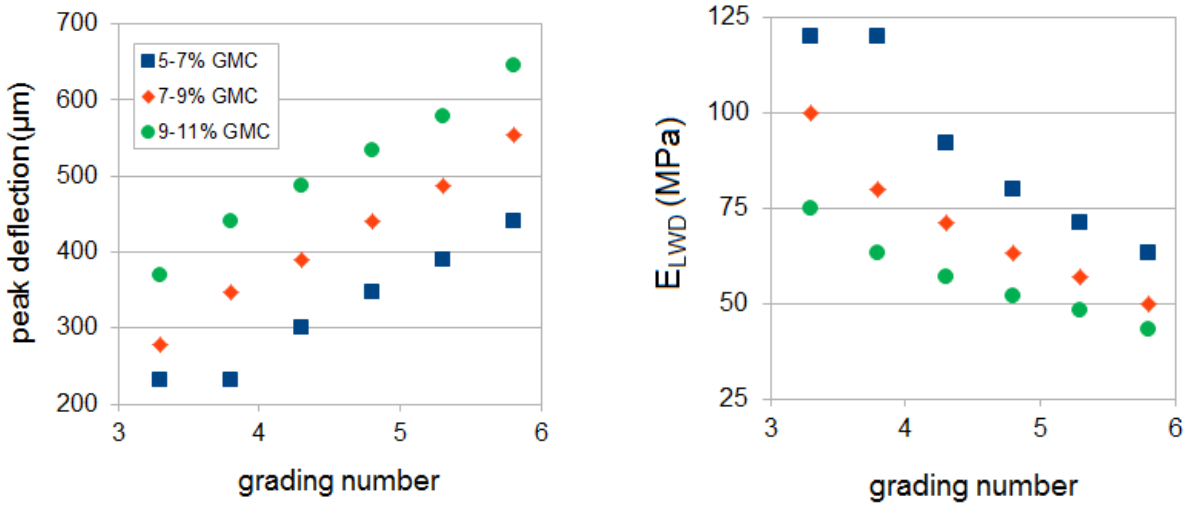

Figure 6: Experimetnally-based estimated target values from Siekmeier et al. [4] showing trend in peak deflection (left) during the LWD tests as a function of grading number, and the corresponding effective bulk modulus (right), for mixtures with different moisture contents.

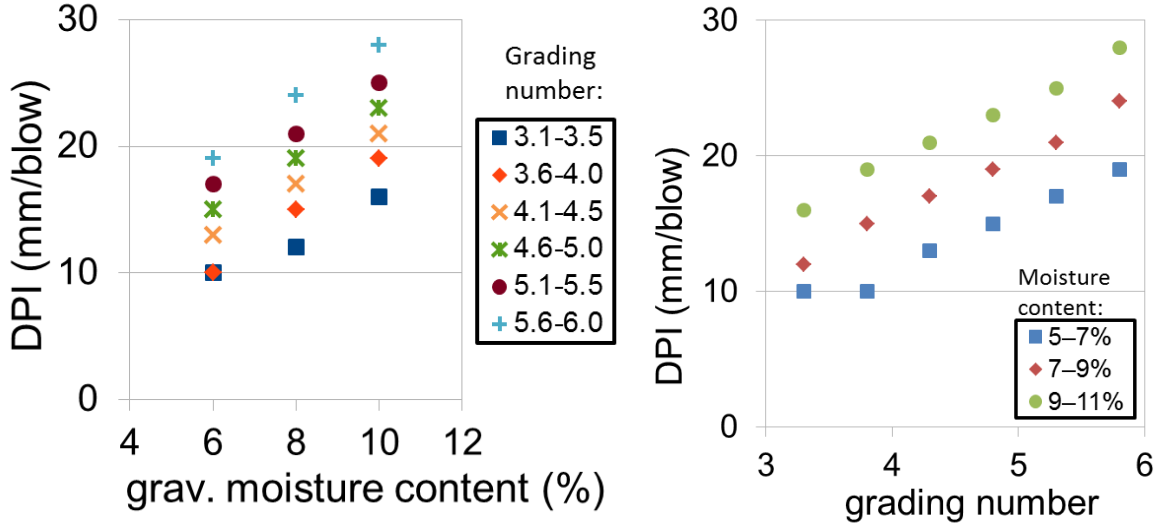

Figure 7: Experimentally-based estimated target values from Siekmeier et al. [4] showing trend in average penetration per blow as a function of gravimetric moisture content (left), and as a function of grading number (right) during DCP tests.

We now describe our efforts to develop a computational simulation that has the capability to reproduce these results both qualitatively and quantitatively.

Chapter 3 Model Particle Size Distribution and Moisture Parameters

The particle size distribution of aggregate bases and moisture content may vary significantly from one site to the next. Both the particle size distribution and the moisture content may affect the behavior of the aggregate base.

Ideally, we would perform simulations using a model of a real granular material. However it is computationally infeasible to do so in a DEM. For this project we only model the coarse particles explicitly, and use indirect means to model the fine particles. This is following in the spirit of Oman [41]'s suggestion of decomposing the grading number into two components: a *coarse* grading number *CGN* and a *fine* grading number *FGN*. In this sense the coarse portion of the granular mixture is considered essentially independently from the fine portion.

In this project we use four different coarse particle size distributions. The majority of the simulation results presented here were obtained using either a unimodal (10±1mm diameter spheres) or a trimodal (22±2.2mm, 13±1.3mm and 7±0.7mm diameter spheres) mixture. The latter reflects a class of materials known in Minnesota as 'Class 5' (details below). We also perform a limited set of simulations using one of two bimodal particle size distributions for some focused studies as detailed in Section 1.

3.1 Model Details for the Class 5 Aggregate Base

The Minnesota Department of Transportation specifies a handful of grain size distributions as appropriate for aggregate bases for pavement systems. For most of our simulations for our coarse particle size distribution, we focused on one of these, known as Class 5, on which we based our modeled granular material. The specified grading for Class 5 aggregate bases is given in Table 1. As noted, the particle sizes range from medium gravel-sized particles (a maximum of 25.0 mm) down to silt and clay particles (less than 75 μm).

Table 1: Class 5 aggregate base grading as specified by Minnesota Department of Transportation

% finer	particle size
100	25.0 mm
90 *to* 100	19.0 mm
50 *to* 90	9.5 mm
35 *to* 80	4.75 mm
20 *to* 65	2.0 mm
10 *to* 35	425 μm
3 *to* 10	75 μm

The modeling approach we use – our adaptation of the Discrete Element Method (DEM) – represents the movement of each *coarse* particle explicitly and independently from one another.

The computational demands increase rather dramatically with number of particles N (the computational time increases with N as $N\ln N$). Thus it is not feasible for us to model explicitly the finer particles in a typical base such as Class 5. We model the finer particles – those smaller than 4.0 mm – implicitly within the force model as described shortly.

The mixture particle size distribution we use in our model for the results described here is detailed in Table 2. Essentially, the coarses particles are divided among three average particle sizes defined by sieve sizes, with some range of distributed sizes (approximately 10% variance) around each mean. Compare contents of first two columns in Table 2 with data in Table 1 for Class 5 aggregate bases. The sizes noted in the last column of the first three rows in Table 2 indicate a random particle size assignment within that range. Particles less than 4.0 mm noted in the last column are not represented explicitly, but rather represented implicitly as a 'fines factor' in the force model described in Chapter 3 in this report.

Table 2: Mixture composition of spherical particles used in DEM model.

% finer	particle size	% in range	particle size
100	25.0 mm	10	19.8 *to* 24.9 mm
90	19.0 mm	30	11.7 *to* 14.3 mm
60	9.5 mm	25	6.3 *to* 7.7 mm
35	4.75 mm	35	$\leq$ 4.0 mm

To summarize, we conducted the majority of our simulations using this single trimodal mixture to represent the coarser particles explicitly and model the effects of fine particles implicitly. Then we investigated the effectiveness of three moisture models for representing the fine particles and moisture content. In the next subsection we summarize the models briefly, and describe them in more detail in later sections.

3.2 Three Implicit Models for Moisture and Fine Particle Content

The first model for moisture and fines content was based on established liquid bridge theory. We implemented this model into both the LWD and DCP model tests on unimodal particle systems, and the results are reported in detail in Sections 5.3 and 5.4 . We investigated a range of 5-14% gravimetric moisture content, and surface tension values of $0.1\gamma^*$ to $100\gamma^*$, which is an implicit representation of fines content (details in Section 5.2).

The second model for moisture and fines is based on experimental work by Gupta et al. [32] and Gupta and Larson [33]. From their experiments, they developed an empirical relationship which predicted moisture content in a soil based on the mixture composition and measured suction (negative pore pressure). We adapted this model for moisture and fines content into DEMP-3D as a more direct way of including both fines and moisture content. A range of 10-20% gravimetric moisture content and 10-30% fines content was considered, which gave rise to seven 'suction' values (see details in Section 6.2).

As we will describe below, the first two models represented some details of the experimental test results reasonably, but some details were lacking. Based on the results obtained from the first two models, we hypothesized that both model frameworks missed some fundamental piece of the interparticle interactions as they were modified by both moisture and fines content. Both our adaptations of the liquid bridge and explicit composition models into DEMP-3D involved the use of an attractive force between particle pairs but no change in lubrication or friction between particles typically seen when fine particles are present. In this third model we introduced an additional component to the interparticle model that involved change of the interparticle friction coefficient.

The third and last model we investigated for its effectiveness in representing moisture and fines content in our DEMP-3D model is a 'hybrid' that essentially combines the first two models with a consideration of a frictional coefficient. Essentially the model has two primary components. The first component involves details of the explicit composition model implemented with a similar mathematical form to the liquid bridge model to represent the moisture content in the granular materials. The second component involves a change in friction coefficient to represent the fines content in a relatively coarse granular base, where increasing fines results in increasing lubrication (or decreasing interparticle friction) within the model. Here we used five of the 'suction' values from the previous moisture model (derived from a range of 10-20% gravimetric moisture content and 10-20% fines content) and friction values of 0.2-0.4 (see Section 7.1 for details).

In the next section we summarize the basic DEM set-up. Then we follow with sections on the three different moisture / fines model and the associated test results described in detail.

Chapter 4 Simulation Set-up

4.1 Introduction to the Discrete Element Method

In this section we include a brief overview of the Discrete Element Method (DEM) and our 3d model in which we implement the DEM to model unbound materials, (DEMP-3D). More details of the model are in Appendix A.

The discrete element method (DEM) treats individual components in a system - in this case, the individual particles in a granular mixture and boundaries such as walls - as separate objects, each with their own masses and forces acting upon them. This is different from a continuum approach, where the granular mixture would be viewed as a continuous system and constitutive rules would be imposed relating its material properties to its response to loading. This makes it very appropriate for investigating how changes that occur on a particle scale such as moisture and fines content as well as changes in local grain size distribution (e.g., due to segregation) affect the bulk properties of a granular material.

In a discrete element model, the rotational and translational positions (and velocities and accelerations) are tracked throughout the simulation. The net forces and moments associated with the particle masses and all contacting particles are calculated at each time step. Next, the equations of motion for all particles in the whole system for each time step is calculated. Then, numerical integration is performed to calculate subsequent particle velocities and displacements. This gives a new set of particle positions and velocities, and the process is repeated.

The properties of the particles are inputs into the DEM contact model - how the effective particle deformations relate to interparticle forces. The model we used for Phase 1 [24], and here for dry systems, uses Hertz-Mindlin contact theory with a damping component specified by Tsuji et al. [42] and Coulomb sliding friction:

$$F_n = \begin{cases} -k_n\delta_n^{3/2} - \eta_n\delta_n^{1/4}\dot{\delta}_n & ;\delta_n > 0 \\ 0 & ;\delta_n < 0 \end{cases} \tag{4}$$

$$F_t = \begin{cases} min\left\{-k_t\delta_n^{1/2}\delta_t - \eta_t\delta_n^{1/4}\dot{\delta}_t ; \mu F_n\right\} & ;\delta_n > 0 \\ 0 & ;\delta_n < 0 \end{cases} \tag{5}$$

Here, F_n and F_t are the contact forces in the directions normal and tangential directions to the contact plane between two contacting particles and δ_n and δ_t are the corresponding deformations. To help illustrate the model framework, Figure 8 shows a sketch of a pair of particles in contact. The relationships between the stiffness and damping coefficients (k_n, k_t, η_n, and η_t) and the particle properties are described in detail in Appendix A.

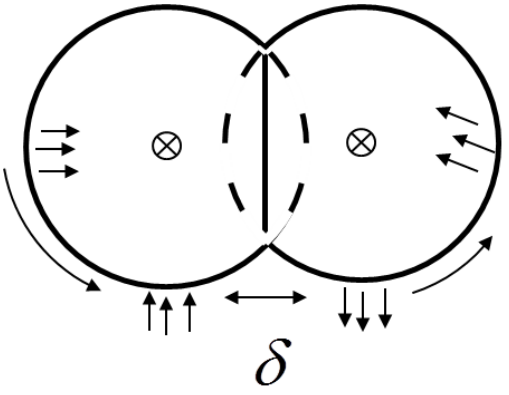

Figure 8: Sketch of a pair of overlapping particles, with the deformation δ labelled.

In this project, we investigated the dynamics using primarily one of two mixtures: (1) a unimodal mixture (10±1 mm diameter) and (2) a trimodal mixture, based on the Class 5 particle system described in Section 3.1, composed of particles with 22±2.2 mm, 13±1.3 mm and 7±0.7 mm diameter. All the particles have properties characteristic of granite (elastic modulus 29 GPa, density 2650 kg/m^3 and Poisson's ratio 0.15) and, unless stated otherwise, interparticle coefficient of friction 0.4. The LWD/DCP components are steel (elastic modulus 210 GPa, density 7850 kg/m^3 and Poisson's ratio 0.3). We use a coefficient of friction of 0.3 for interactions between the particles and the cylinder walls or LWD/DCP components. Sample stiffness and damping coefficients for contacts involving granite particles of 7 and 22 mm diameter, calculated based on Equations A.3 to A.10 in Appendix A, are presented in Table 3. The fine particles (as well as the moisture content) are modeled implicitly through modifications to this framework as described shortly.

Table 3: Stiffness and damping coefficients for 7 mm and 22 mm particles in contact, with granite material properties (elastic modulus 29GPa, density 2650 kg/m^3 and Poisson's ratio 0.15).

Particle Pair	k_n (N/m$^{3/2}$)	k_t (N/m$^{3/2}$)	η_n (Ns/m$^{5/4}$)	η_t (Ns/m$^{5/4}$)
7mm & 7mm	8.27e8	1.14e9	31.1	36.5
7mm & 22mm	1.02e9	1.40e9	48.0	56.3
22mm & 22mm	1.47e9	2.02e9	230.0	271.0

4.2 LWD Test Simulation Procedure

For this project we follow specifications from a MnDOT study [3], using a 20 cm diameter plate and a combination of mass and drop height of the weight resulting in a peak applied stress of 0.2 MPa. It is not possible to model an entire half-space of granular material, so instead we use a cylindrical container (26 cm diameter) filled with spherical particles. We made sure the container

size was sufficiently large so that boundary conditions did not play a role in the results through some systematic simulations described in Appendix

The specific steps taken in the DEM simulations (to be detailed in the following subsections) are:

1. Sample is prepared to specified solid fraction or maximum possible solid fraction, whichever results in a higher packing fraction.
   (a) Dry particles are dropped into the cylindrical container.
   (b) Moisture is introduced.
   (c) A disc is dropped repeatedly to compact the system.
2. LWD test is run on prepared sample.
   (a) The LWD plate is placed on top of the particles.
   (b) LWD loading is applied multiple times, until the peak deflection is relatively unchanging from one application to the next.
   (c) The effective modulus is calculated.

4.2.1 LWD Particle Initiation

The first step in the simulations is to create a random array of particles for our simulated LWD experiment. For this, particles are first released with random velocities into a cylinder of 260mm inner diameter, sketched in Figure 70.

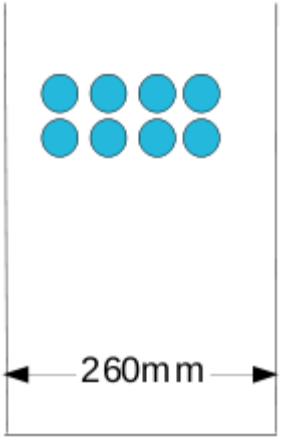

Figure 9: Sketch of the DEM simulation procedure of the initialization stage of the LWD test: A suspended arrangement of spheres is dropped into a cylinder of 260 mm diameter. This initialization method results in an non-segregated mixture.

To reduce computational time, no moisture forces are included in this stage. To determine the approach of the system to a steady settled state, the average vertical position and velocity of the

bulk particles are tracked over time. Due to limits in the numerical precision of the simulations, the change in average vertical position and velocity will never be zero, so we consider the system to be sufficiently settled when the system changes less than 1 mm in vertical position per second, and less than 1 mm/s in velocity per second

4.2.2 LWD Compaction

After the particles have settled, moisture is added. Then, a steel disc of mass 15 kg and with the same diameter as the cylinder (see sketch in Figure 72) is dropped onto the particles from a small height a few times to compact the system.

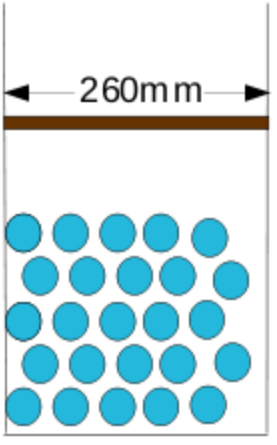

Figure 10: Sketch of the DEM simulation procedure of the compaction stage of the LWD test: The cylinder (260 mm diameter) filled with spheres representing the macroscopic particles, and the 'lid' used to compact the system. The 'lid' is dropped from a short height repeatedly until the solid fraction of the system does not change more than 0.1% between impacts.

To determine the manner in which the compaction evolves (and when the system reaches a steady state), the average vertical position of the bulk particles is tracked, as well as the position of the disc and the solid fraction. The solid fraction is calculated by summing up the volumes of particles below the disc, and dividing by the volume of the cylinder below the disc.

For the results described here, we found that four impacts were sufficient to reach near steady state - for the third and forth impacts the increase in solid fraction was less than 0.001 - so we stopped compacting after four cycles. However, the user can specify the number of impacts or another criteria for stopping the compression process.

After this active compaction process, we remove the disc entirely, and allow the system to settle once again. We found relatively little change in the system during this time. We generally obtain solid fractions of 0.61-0.66 which is, as expected, less than typical solid fractions of 0.66-0.78 (equivalent solid fractions for granular material with maximum densities 109-128 lb/ft^3), because we do not explicitly include small particles in our DEM simulations.

4.2.3 LWD Plate Placement

Before the LWD test is applied, the LWD plate (essentially a solid disc of 200 mm diameter with 2 mm diameter particles glued around the edge) is released from rest onto the top of the particles

(Figure 11). Due to the weight of the LWD plate, the system generally compacts a bit more during this stage. It is important to allow the system to settle before applying the LWD load to avoid instabilities that otherwise may arise. When the change in plate position and the average vertical position of the bulk particles are both less than 1 mm/s, we consider the system to be settled and ready for loading.

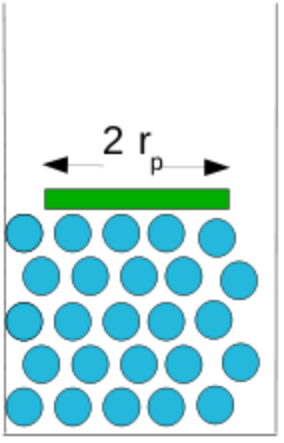

Figure 11: Sketch of the DEM simulation procedure of the position of the plate in the LWD test: The cylinder (260 mm diameter) filled with spheres representing the macroscopic particles, and the 'plate' representing the LWD plate of 200 mm diameter. The 'plate' is allowed to sit on top of the compacted system for a short time before applying the load.

4.2.4 LWD Loading

In the physical implementation of the LWD test, the LWD load is applied by dropping a known load from a fixed height (see sketch in Figure 12). In the DEM model of the LWD test, we follow the results in Fleming et al. [43] to save computation time, and we replace the falling load with an equivalent time-varying load $F_{load}(t)$ applied to the plate. $F_{load}(t)$ increases linearly from zero to a peak force of 6.28 kN (0.2 MPa on the 200 mm diameter plate) over 20 ms, decreases linearly back to zero over the next 20 ms, and then remains zero.

During this process we track the vertical position of the plate. The first few impacts are seating drops, during which the LWD plate becomes more firmly positioned on the surface of the granular material. The effective modulus is calculated using the later results, when there is no significant change in the deflection from loading round to the next. Δ, the average peak deflection during the last three impacts - the difference between the plate's original position and the lowest vertical position the plate reaches during each cycle - is used to calculate an effective modulus of the bulk material E_{LWD} according to Davich et al. [3] as:

$$E_{LWD}=2r_p\sigma\left(1-\nu_s^2\right)\frac{10^6 D}{\Delta}, \tag{6}$$

where E_{LWD} is in MPa if Δ is the peak deflection during loading in μm. For our results, r_p = 0.1 m is the LWD plate radius, σ=0.2 MPa is the peak stress applied to the LWD plate, ν_s=0.35 is the Poisson's ratio of the bulk granular material, and *D*=0.79 is the LWD plate rigidity.

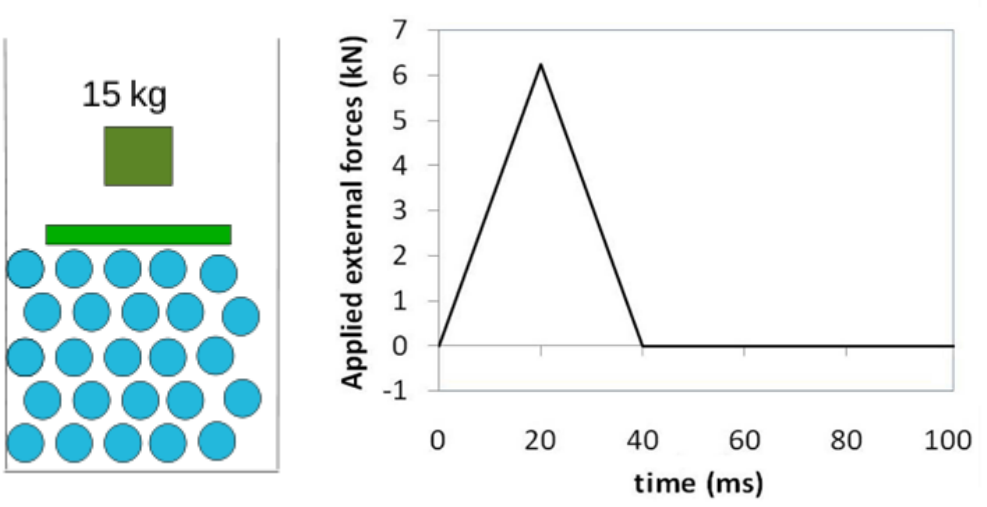

Figure 12: (Left) Sketch of the DEM simulation procedure of the loading phase of the LWD test: The cylinder (260 mm diameter) filled with spheres representing the macroscopic particles, and the 15 kg load dropped onto the LWD 'plate'. The maximum deflection of the 'plate' due to the falling load is used to calculate an effective bulk modulus. (Right) Loading history applied during simulation procedure, to represent falling load. The force increases linearly over 20 ms to 6.28 kN, decreases linearly back to zero over the next 20 ms, and then remains at zero.

4.3 DCP Test Simulation Procedure

In our DEM simulation of the DCP field tests, we model an 8 kg load falling onto a cone-rod assembly of 20 mm diameter submerged in a cylindrical container (150 mm diameter) filled with spherical particles.

The specific steps taken in the DEM simulations (to be detailed in the following subsections) are:

1. The sample is prepared to specified solid fraction or maximum possible solid fraction, whichever results in a higher packing fraction.
   (a) Dry particles are dropped into the cylindrical container.
   (b) Moisture is introduced.
   (c) A surcharge load (disc) is dropped repeatedly to compact the system.
2. The DCP test is run on the prepared sample.
   (a) The DCP cone-rod assembly is placed on top of the particles.
   (b) The DCP loading is applied five times.
   (c) The DPI is calculated.

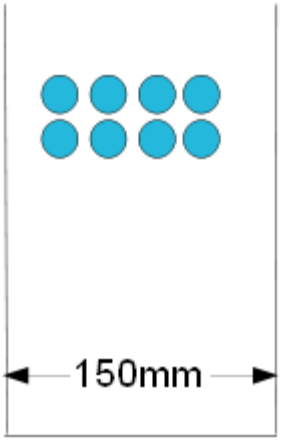

Figure 13: Sketch of the DEM simulation procedure of the initialization stage of the model DCP test: A suspended arrangement of spheres is dropped into a cylinder of 150 mm diameter. This initialization method results in an non-segregated mixture.

4.3.1 DCP Particle Initiation

The first step in the simulations is to create a random array of particles for our simulated DCP experiment. For this, particles are first released with random velocities into a cylinder of 150 mm inner diameter, sketched in Figure 77. To reduce computation time, no moisture forces are included in this stage. To determine the approach of the system to a steady settled state, the average vertical position and velocity of the bulk particles are tracked over time. Due to limits in the numerical precision of the simulations, the change in average vertical position and velocity will never be zero, so we consider the system to be sufficiently settled when the system changes less than 1 mm/s in vertical position, and less than 1 mm/s^2 in velocity.

4.3.2 DCP Compaction

After the particles have settled, moisture is added. Then, a granite disc of thickness t_s and with the same diameter as the cylinder (see sketch in Figure 79) is dropped onto the particles from a small height a few times to compact the system.

The 'lid' or disc represents the surcharge load of loose particles above the compacted material, and has a mass of 16.9 kg, equivalent to a 600 mm-thick disk of granite material with 0.6 solid fraction and material density 2650 kg/m^3. The surcharge is dropped from a short height repeatedly until the solid fraction of the material below it does not change more than significantly between impacts. The surcharge remains on top of the compacted material in the rest of the simulation. We leave this surcharge on top of the particles after compaction as this saves the computational expense of modeling the loose top layer of granular material, and also reduces the need to perform seating drops as is usually done in the field.

To determine the manner in which the compaction evolves (and when the system reaches a steady state), the average vertical position of the bulk particles is tracked, as well as the position of the disc and the solid fraction. The solid fraction is calculated by summing up the volumes of particles below the disc, and dividing by the volume of the cylinder below the disc.

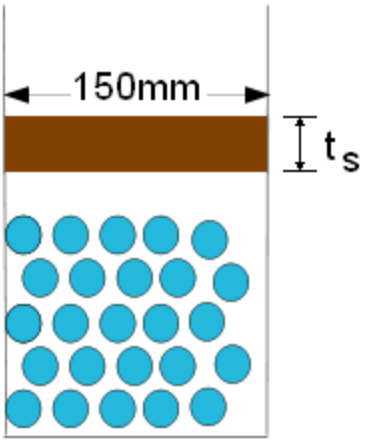

Figure 14: Sketch of the DEM simulation procedure of the compaction phase of the DCP test: The cylinder (150 mm diameter) filled with spheres representing the macroscopic particles, and the 'lid' used to compact the system.

For the results described here, we found that six impacts were sufficient to reach near steady state - for the fifth and sixth impacts the increase in solid fraction was less than 0.001 - so we stopped compacting after six cycles. However, the user can specify the number of impacts or another criteria for stopping the compression process.

4.3.3 DCP Cone Placement

Before the DCP test is applied, the cone-rod assembly is released from rest at the interface between the disc (surcharge load) and the particles (see sketch in Figure 15). There is no interaction between the cone-rod assembly and the disc (surcharge), as the DCP is assumed to have already penetrated through that layer during the seating drops and thus will only interact with the particles below the disc (surcharge).

Due to its weight, the cone-rod assembly penetrates the system of particles a short distance. It is important to allow the system to settle before applying the DCP load to avoid instabilities that may otherwise arise. When the change in cone-tip position and the average vertical position of the bulk particles are both less than 1 mm/s, we consider the system to be settled and ready for loading.

4.3.4 DCP Loading

In the physical implementation of the DCP test, an 8 kg hammer is dropped from a height of 575 mm onto the anvil connected to the top of the rod (see sketch in Figure 16). In the DEM simulations, to save computation time, we replace the load applied by the falling hammer with an equivalent time-varying load $F_{load}(t)$ applied to the cone-rod assembly. $F_{load}(t)$ increases linearly from zero to a peak force of 105 kN over 0.05 ms, decreases linearly back to zero over the next 0.05 ms, and then remains zero as shown in Figure 16.

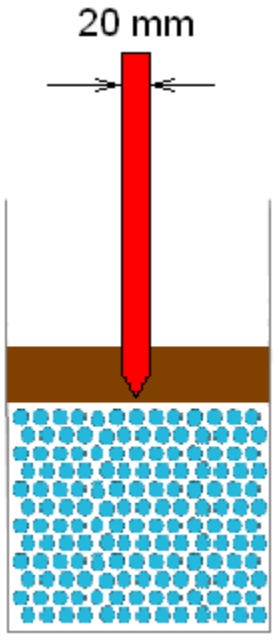

Figure 15: Sketch of the DEM simulation procedure of the cone placement in the model DCP test.

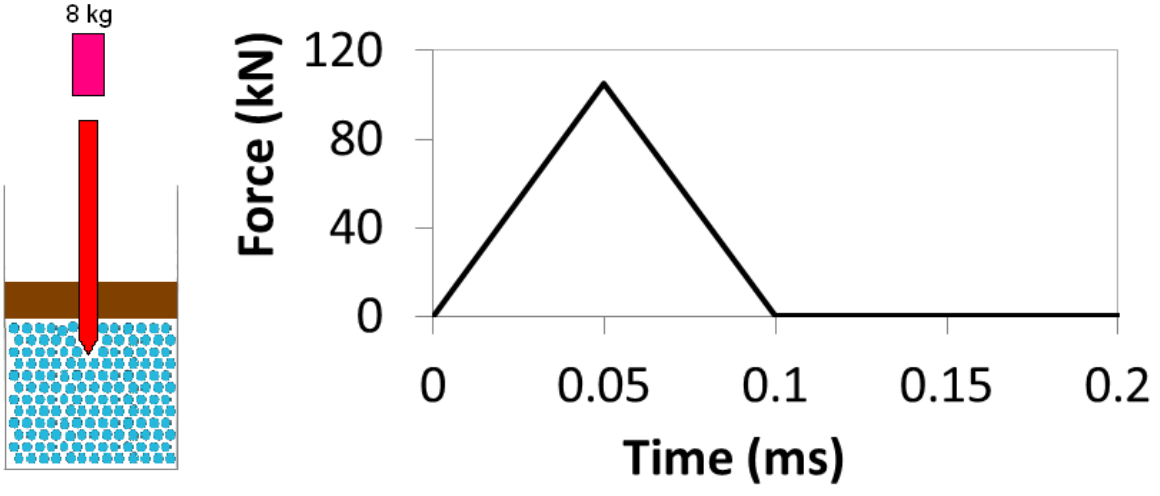

Figure 16: (Left) Sketch of the DEM simulation procedure of the hammer drop phase of the DCP test: (Right) Loading history of othe model DCP test, representing the falling hammer.

During the loading process we track the vertical position of the cone tip, from which we obtain the penetration during each hammer drop. The DPI is then calculated by averaging the penetration of five consecutive impacts or, equivalently, the total penetration after five drops divided by five.

Chapter 5 Moisture Model I: Liquid Bridge Model

5.1 Liquid Bridge Theory

In the liquid bridge theory, the moisture present in an unsaturated system is modeled as 'liquid bridges' between pairs of particles (see Figure 17). These liquid bridges attract the particles towards each other with a force that depends on the amount of liquid comprising the bridge and also the distance between the particles.

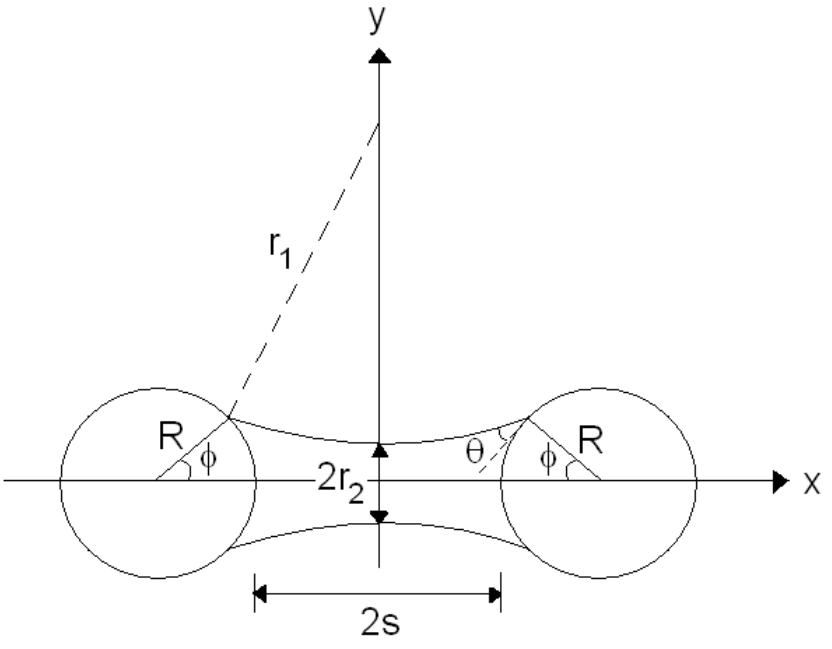

Figure 17: Liquid bridge between a pair of particles with radius R

This attractive force is included in the contact as $F_{m(f)}$, a component in the normal direction, so that the original force model for dry particles expressed in Equations 4 and 5 is modified to:

$$F_n = \begin{cases} -k_n\delta_n^{3/2} - \eta_n\delta_n^{1/4}\delta_n + F_{m(f)}; \delta_n > 0 \\ F_{m(f)} \qquad\qquad\qquad\qquad ; \delta_n \le 0 \end{cases} \tag{7}$$

$$F_t = \begin{cases} min\left\{-k_t\delta_n^{1/2}\delta_t - \eta_t\delta_n^{1/4}\delta_t ;: \mu F_n\right\}; \delta_n > 0 \\ 0 \qquad\qquad\qquad\qquad\qquad\qquad ; \delta_n \le 0 \end{cases} \tag{8}$$

Here $F_{m(f)}$ is the magnitude of the force associated with moisture between two particles. We calculate this using the approximation of Lian et al. [38] where the attractive forces between a pair of particles with radius *R* is modeled by a liquid bridge, the profile of which is approximated as a

toroidal shell. The principal radii of the torus, r_1 and r_2, are included in Figure 17 showing a sketch of the liquid bridge between a pair of particles. The moisture force is given as

$$F_{m\,(f)}=\pi\gamma\,\frac{r_2\left(r_1+r_2\right)}{r_1}. \tag{9}$$

Both r_1 and r_2 are functions of the moisture level, contact angle (of the liquid/particle interface) and distance between particle centers. They may be expressed geometrically in terms of the particle size, contact angle, half-filling angle and half-separation distance *s*:

$$r_1=R\left[\frac{s/R+1-\cos\varphi}{\cos\left(\varphi+\Theta\right)}\right], \tag{10}$$

$$r_2=R\left[\sin\varphi-\frac{\left(1-\sin\left(\varphi+\Theta\right)\right)\left(s/R+1-\cos\varphi\right)}{\cos\left(\varphi+\Theta\right)}\right]. \tag{11}$$

To solve for r_1 and r_2 for all interparticle moisture droplets, we need to find the half-filling angle φ as a function of particle separation distance *s* for each near particle contact. To do so, we follow Muguruma et al. [39] in noting that φ is related to the volume of a liquid bridge V_{br} according to:

$$V_{br}=2\pi R\left\{r_1^2\left[\left(1+\frac{s}{R}\right)-\frac{r_1+r_2}{R}\left(\frac{\pi}{2}-\varphi\right)\right]-\frac{s^2\left(s/R+3\right)}{3}\right\}, \tag{12}$$

for $s\leq S_{cr}$, whereS_{cr} is the critical half-separation distance at which the liquid bridge ruptures.

To find V_{br} and also S_{cr} we make the approximation that the liquid is ideally dispersed so that all droplets are approximately the same size, a simplification that has been shown to approximate other behaviors in moist granular materials. Additionally, we use the result demonstrated by Lian et al. [38] that $V_{br}\approx(2S_{cr})^3$ for systems of small contact angles (such as in our case, for water and quartz, Θ≈0). We can use these two approximations together to solve for V_{br} and S_{cr} together iteratively given two pieces of information: (1) the particular volume of moisture in the system (fixed, according to the gravimetric moisture content) and (2) the separation distances among all of the particles in the system. We can then use Equation 12 to solve for φ numerically as a function of separation distance *s*. Then we can use this in Equations 10 and 11 to solve for r_1 and r_2 as functions of separation distance *s*.

5.2 Surface Tension and Scaling the Liquid Bridge Model

Throughout this project, we use particles in our DEM simulations that are somewhat larger than smaller particles in a typical pavement system. We need to do this with care, because surface tension forces are more significant for these smaller particles. To address this, we scale the surface tension forces in the DEM model to ensure that it remains dynamically similar to a prototype system with small particles, i.e. the relative magnitudes of inertial forces to surface tension forces are the same in both systems. The resulting scaling is:

$$\gamma_{DEM} = \left(\frac{R_{DEM}}{R_{prototype}} \right)^2 \gamma_{prototype}. \tag{13}$$

For water at room temperature, the surface tension $\gamma_{prototype}$=0.0756 N/m. Taking 1 mm to be a typical average particle diameter for the prototype experiments, the scaled surface tension for the DEM model with 10 mm volume-averaged diameter particles is then 7.56 N/m.

Additionally, we use this scaling principle to simulate the effect of changing the quantity of fine particles by decreasing the average prototype particle size, and scaling the surface tension accordingly. We use the base value of surface tension $\gamma^* \equiv 7.56$ N/m.

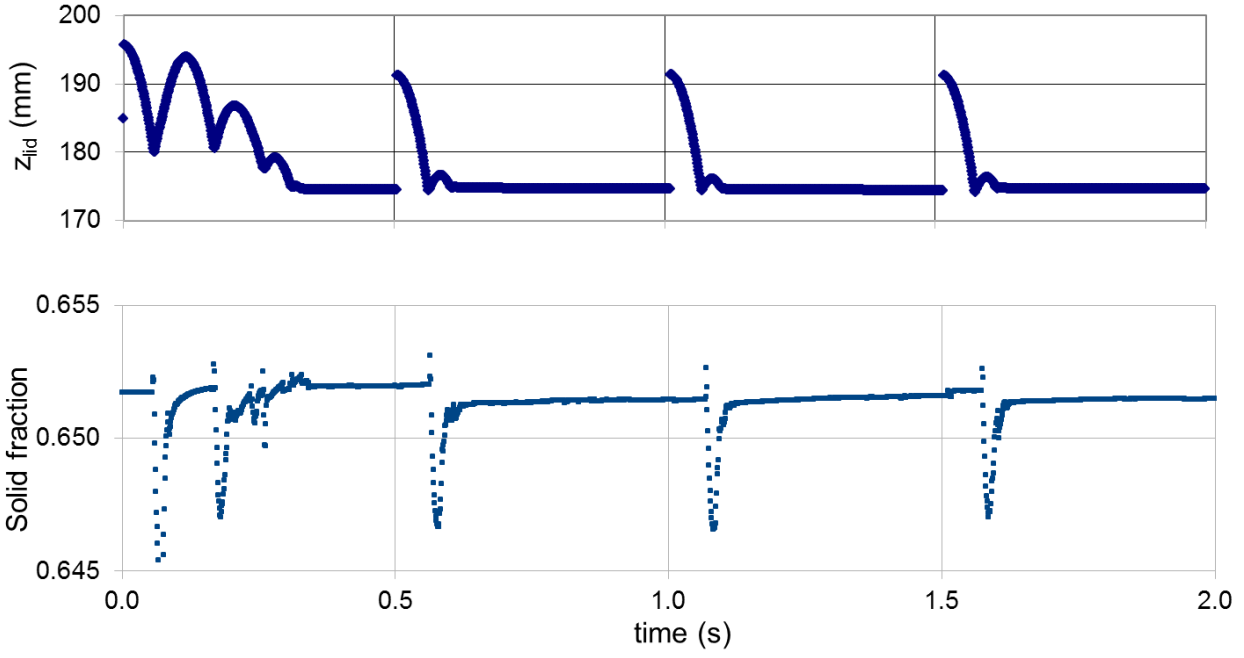

Figure 18: Data from compaction using Moisture Model I and the DEM mixture representing the Class 5 mixture described in Section 3.1. Lid position and solid fraction are plotted as functions of time during compaction for a system with 5% gravimetric moisture content and surface tension $0.1\gamma^*$.

5.3 LWD Model Test Results Using Moisture Model I

5.3.1 LWD Preparation Results Using Moisture Model I

As detailed in Section 4.2, the particles are initially dropped into a cylinder, without moisture. The resulting system state after this initialization stage is used as the starting point for all the LWD simulations involving the same particle size distribution, and hence we focus more on the subsequent stages.

Figure 18 shows the vertical position of the 'lid' (see Section 4.2.2) during the compaction process, and the resulting solid fraction, for a mixture with 5% gravimetric moisture content and a surface tension of 0.1 γ^*. Typically, four impacts were found to be sufficient for attaining sufficient compaction, and the 'lid' was removed at this point.

The LWD 'plate' (see Section 4.2.3) was placed onto the granular mixture after compaction, and allowed to settle. Figure 19 shows the plate's vertical position and the solid fraction of the mixture below it. There is a very small increase in solid fraction due to the additional compaction and some particle rearrangement.

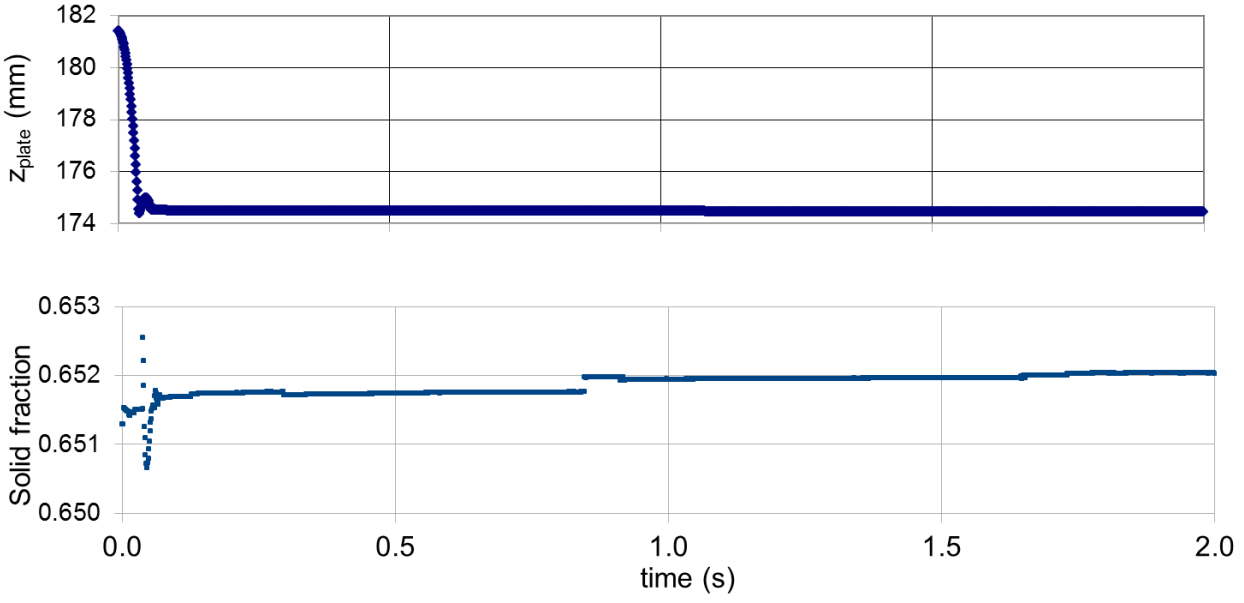

Figure 19: Data from initial placement of the LWD plate using Moisture Model I and the DEM mixture representing the Class 5 mixture described in Section 3.1. Plots shows the LWD plate position and solid fraction plotted as functions of time for a system with 5% gravimetric moisture content and surface tension 0.1 γ^*..

The triangular impact force representing the falling weight (see Section B.3) is applied to the system in a series of consecutive impacts, and the corresponding deflection of the plate is shown in Figure 20. Averaging the final three impacts gives a peak deflection which is used to calculate the effective bulk modulus for this mixture.

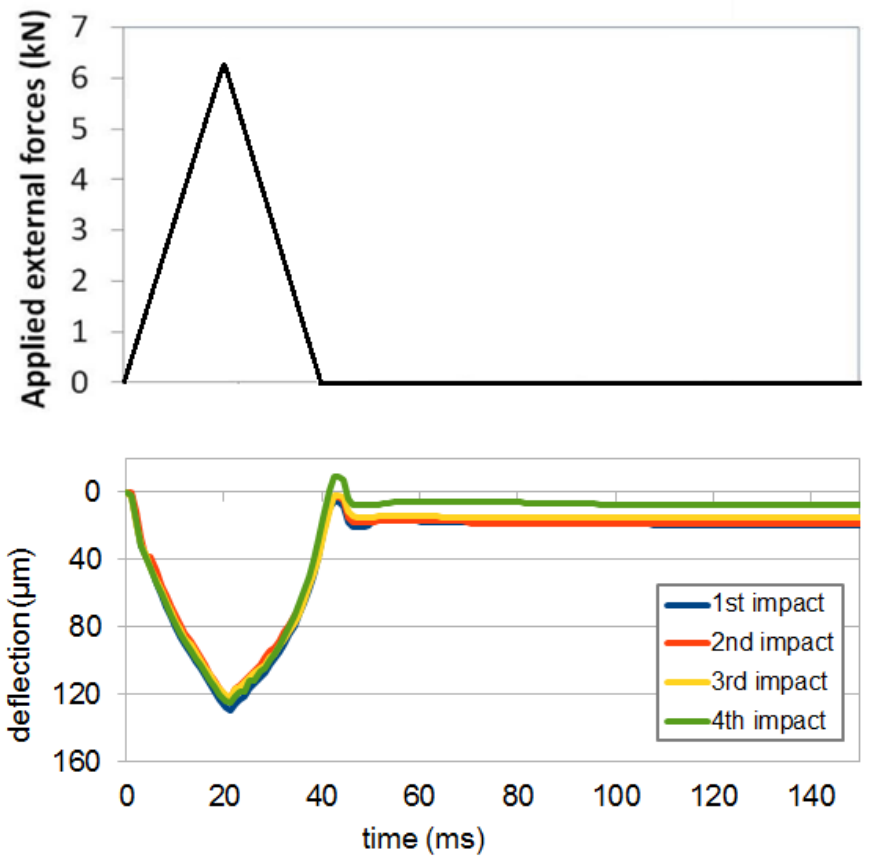

Figure 20: Data from LWD test using Moisture Model I and the DEM mixture representing the Class 5 mixture described in Section 3.1. LWD loading and plate deflection are plotted as functions of time during a series of consecutive impacts for a system with 5% gravimetric moisture content and surface tension 0.1 γ^*.

5.3.2 LWD Model Results Using Moisture Model I: Unimodal Mixture

We performed the steps in the LWD preparation and test for several moisture levels and surface tensions for a 1mm prototype system. Figure 21 shows the solid fraction achieved after the LWD plate placement fraction as a function of gravimetric moisture content (left) and surface tension (right).

We consider these data in light of the physical phenomenology the variations of moisture level and surface tension are intended to represent within the structure of the "liquid bridge" model for moisture content. While the moisture content has a rather straightforward interpretation within the model, there is no direct representation of fines content. Therefore, as mentioned, we loosely model the effects of increasing amounts of fine particles by scaling the surface tension value γ^*.

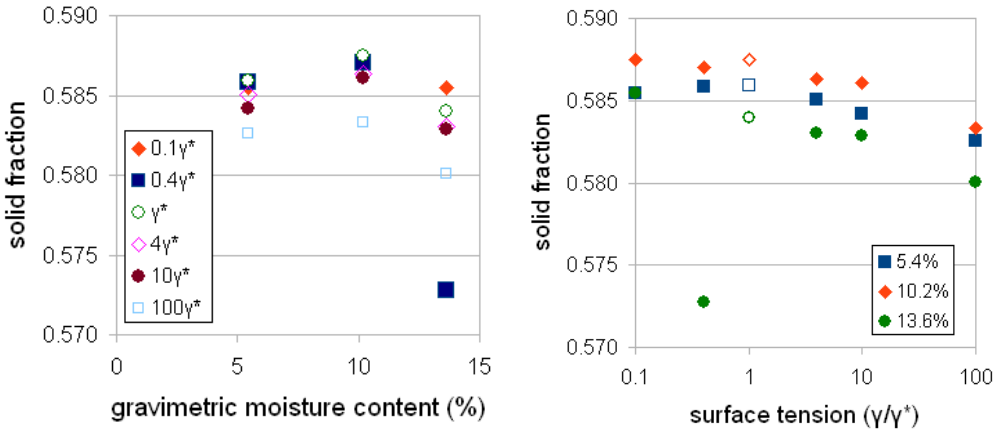

Figure 21: Data from the LWD model test using Moisture Model I and a unimodal mixture. Plots show the solid fraction plotted as a function of gravimetric moisture content (left) and surface tension (right) after careful preparation.

In the context of the modeling framework of liquid bridges within the DEM model, the solid fraction seems much less sensitive to gravimetric moisture content than surface tension (i.e., qualitatively related to fines content). This is consistent with the observation that interparticle forces are orders of magnitude more sensitive to surface tension than moisture content. Most notably, as surface tension increases (a likely effect in systems of a higher fines content), the solid fraction decreases.

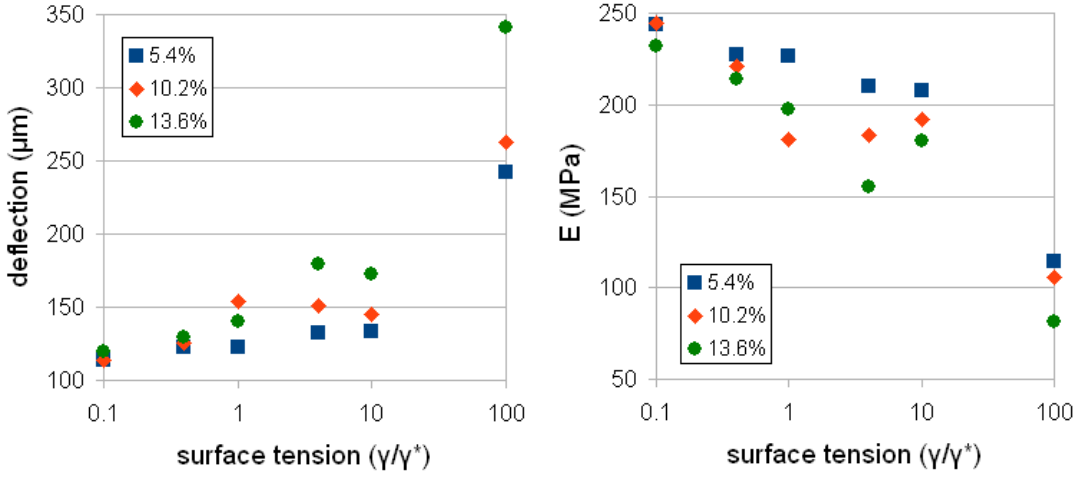

Figure 22: Data from the LWD model test using Moisture Model I and a unimodal mixture. Plots show the peak deflection (left) and effective modulus (right) plotted as functions of surface tension, on a logarithmic scale for gravimetric moisture contents 5.4%, 10.2% and 13.6%.

Figure 22 (left) shows the average peak deflection for three different moisture contents plotted as a function of surface tension (in this moisture model, qualitatively representing the effective fines

content). As surface tension (effective fines content) increases, the peak deflection also increases, that is, the resistance to deformation decreases. The effective modulus E_{LWD} is calculated based on these averaged values, and Figure 22 (left) shows the corresponding values of E_{LWD} plotted as a function of surface tension at three different moisture contents.

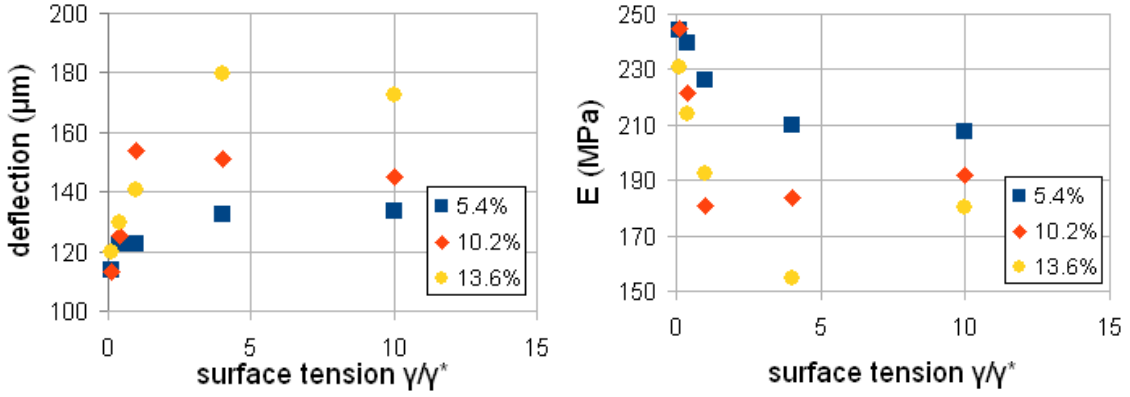

Figure 23: Data from the LWD model test using Moisture Model I and a unimodal mixture. Plots show the peak deflection (left) and effective modulus (right) plotted as functions of surface tension, on a linear scale, for gravimetric moisture contents 5.4%, 10.2% and 13.6%.

Figure 24 shows the analogous results plotted as a function of gravimetric moisture content. The average deflection plotted as a function of gravimetric moisture content (Figure 24 (left)) shows a modest increase in peak deflection with increasing moisture content, resulting in a decrease in effective modulus with increasing moisture content (Figure 24 (right)).

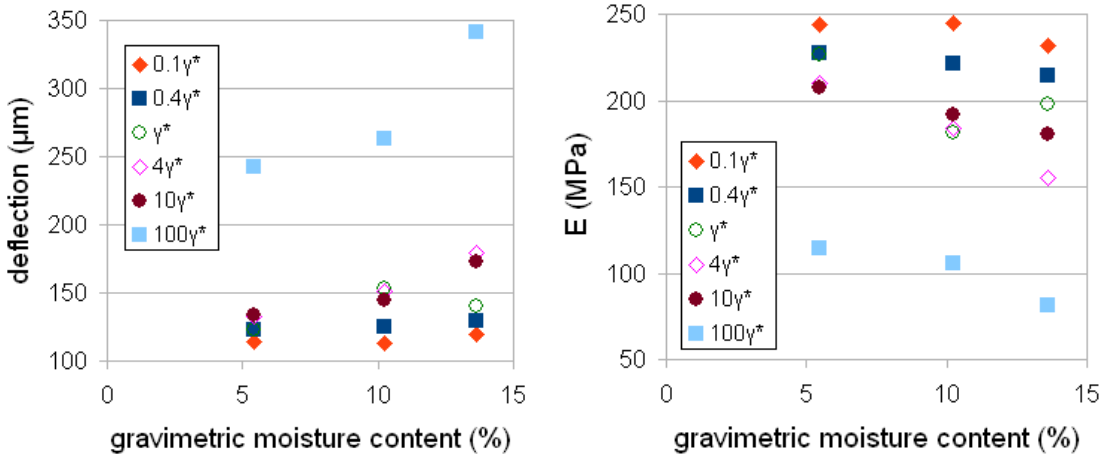

Figure 24. Data from the LWD model test using Moisture Model I and a unimodal mixture. Plots show the peak deflection (left) and effective modulus (right) plotted as a function of gravimetric moisture content, for four different surface tensions (γ*=7.56N/m).

To summarize: with either increasing moisture content *or* increasing surface tension (which we use in this model to represent increasing amounts of fine material), the peak deflection increases and effective modulus decreases. These results for a unimodal mixture are in qualitative agreement with estimated 'target values' provided in the report by Siekmeier et al. [4], plotted in Figs. 5 and 6.

5.3.3 LWD Model Results Using Moisture Model I: Trimodal Mixture

We ran simulations for three moisture contents and four surface tension values on our 'Class 5' trimodal mixture, the results of which are shown in Figs. Figure 25 and 26.

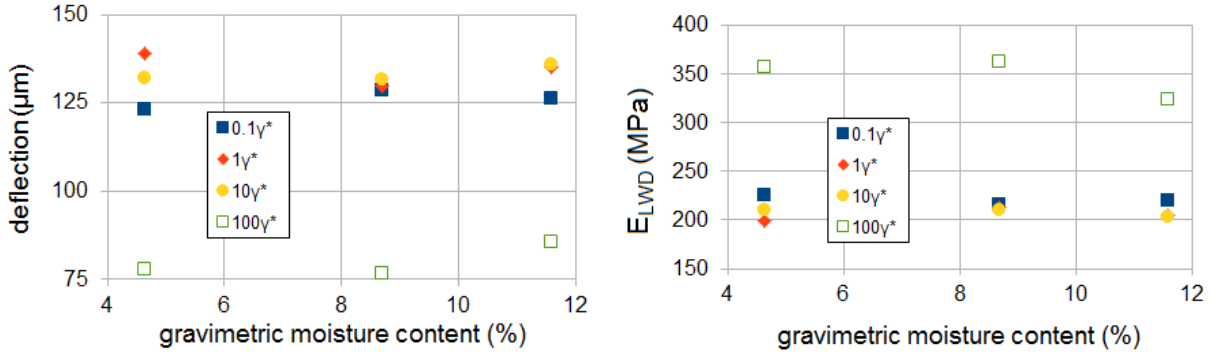

Figure 25: Data from the LWD model test using Moisture Model I and the DEM mixture representing the Class 5 mixture described in Section 3.1. Plots show the average peak deflection (left) plotted as a function of gravimetric moisture content for four values of surface tension, and the corresponding effective bulk modulus (right).

In Figure 25 the peak deflection and corresponding bulk modulus are plotted as functions for gravimetric moisture content for different surface tension values. There is a slight increase in peak deflection with moisture content, which agrees qualitatively with the trend in 'target values' plotted in Figures 5 and 6[4].

However in Figure 26, where the peak deflection and corresponding bulk modulus are plotted as functions of surface tension for different moisture contents, the trend is clearly non-monotonic. For small values of surface tension, the peak deflection increases and the bulk modulus decreases with increasing surface tension (presumably increasing fines content). For larger values of surface tension, the peak deflection decreases and the bulk modulus increases with increasing surface tension (presumably increasing fines content). This is different from the 'target values' in Figure 7 where deflection increased (and bulk modulus decreased) with increasing grading number *GN* (increasing fines content), which is represented in this model as increasing surface tension value. In other words, the results from the trimodal mixtures indicate that the liquid bridge model does not capture the effect of fines and moisture on the results from the LWD test.

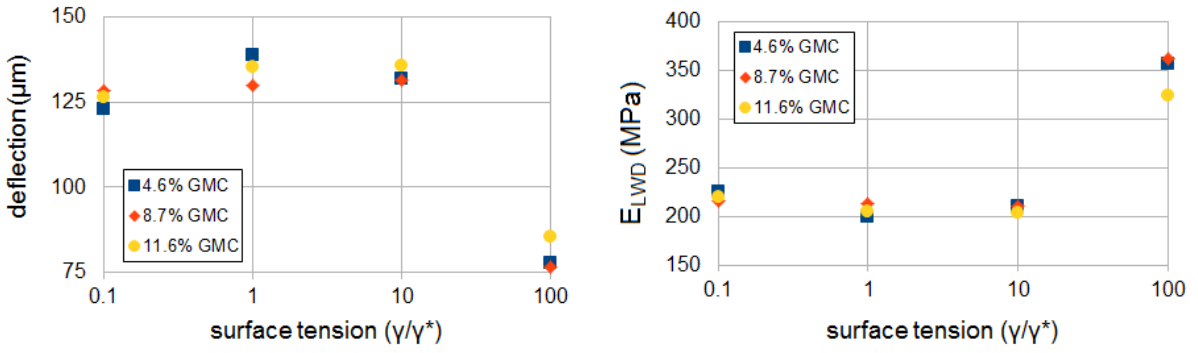

Figure 26: Data from mode LWD tests using Moisture Model I and the DEM mixture representing the Class 5 mixture described in Section 3.1. Average peak deflection (left) is plotted as a function of surface tension parameter γ^* for three gravimetric moisture contents. The corresponding effective bulk modulus is also plotted as a function of surface tension parameter (right).

5.4 DCP Model Test Results Using Moisture Model I

5.4.1 DCP Preparation Results Using Moisture Model I

As detailed in Section 4.3.1, to initialize the DCP model test, the particles are initially dropped into a cylinder, without moisture. The resulting system state after this initialization stage is used as the starting point for all the DCP simulations involving the same particle size distribution, and hence we focus more on the subsequent stages where moisture has been added.

Figure 27 shows the vertical position of the base of the disc representing the surcharge load (see Section 4.3.2) during compaction, and the resulting solid fraction, of a mixture with 6% gravimetric moisture content and surface tension value 0.1 γ^*. We found that generally six impacts were sufficient for good results, so the compaction was stopped after six impacts.

After allowing the bulk particles and surcharge to settle, the cone-rod assembly (see Section 4.3.3) was added with the cone-tip positioned at the vertical height of the base of the surcharge. The cone-rod assembly was then allowed to penetrate the granular mixture under its own weight. The vertical position of the cone-tip is shown in Figure 28, for a mixture with 6% gravimetric moisture content and surface tension of γ^*.

Once the cone-rod assembly has reached a steady state, a series of loading impacts (see Section 4.3.4) corresponding to the falling hammer is applied. The vertical position of the cone-tip is tracked through these impacts, as shown in Figure 29. The DPI is calculated as the average penetration of the five consecutive hammer blows.

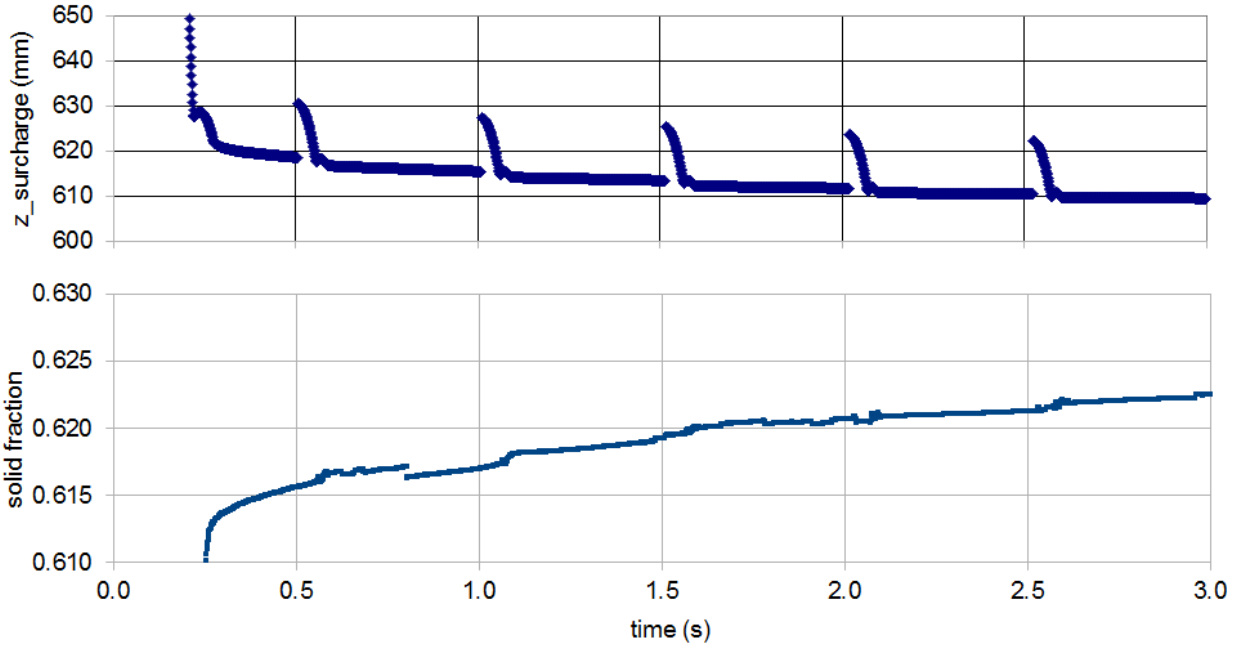

Figure 27: Data from compaction for a DCP model test using Moisture Model I and the DEM mixture representing the Class 5 mixture described in Chapter 3. Surcharge position and solid fraction are plotted as functions of time during compaction for a system with 6% gravimetric moisture content and surface tension 0.1 γ^*.

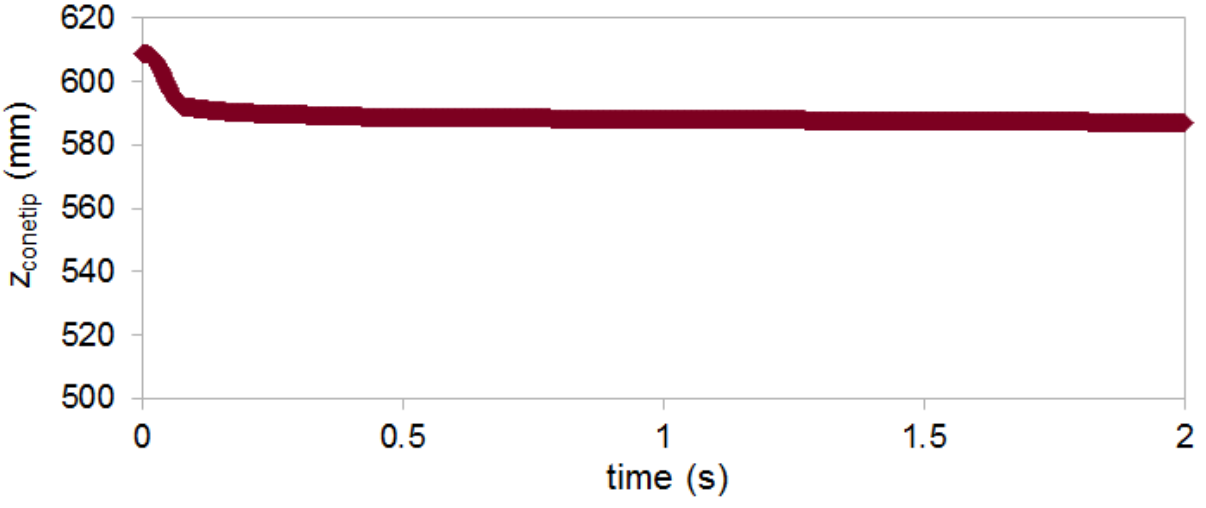

Figure 28: Data from initial placement of the DCP rod/cone assembly using Moisture Model I and the DEM mixture representing the Class 5 mixture described in Chapter 3. Position of cone-tip (base of cone-rod assembly) is plotted as a function of time during initial placement for a system with 6% gravimetric moisture content and surface tension γ^*.

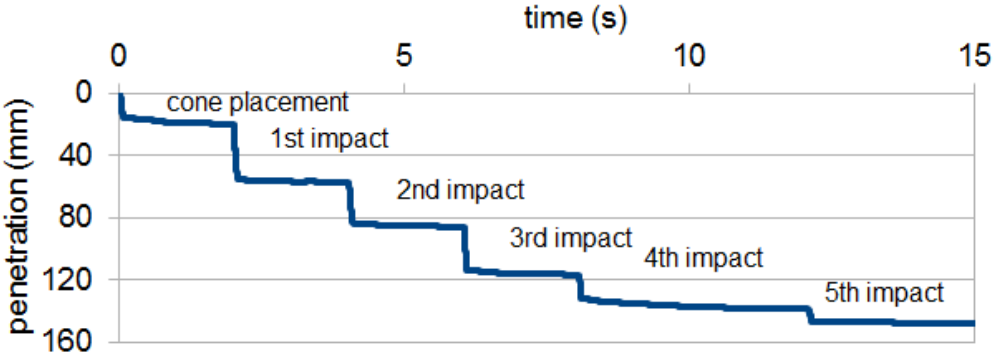

Figure 29: Data from model DCP test using Moisture Model I and the DEM mixture representing the Class 5 mixture described in Chapter 3. DCP penetration is plotted as a function of time during including initial placement and consecutive hammer blows for a system with 6% gravimetric moisture content and surface tension γ^*.

5.4.2 DCP Model Results Using Moisture Model I: Unimodal Mixture

For the first generation of results obtained from using nearly monosized systems, we first report on results obtained by systematically varying the moisture content keeping the surface tension the same, γ^*. Figures 30 and 31 (left) show the measured penetration from the time the cone was first placed on top of the particles, to the end of the first hammer drop for a range of moisture contents at surface tension γ^*. The penetration during the hammer drop is plotted as a function of moisture content in Figure 31 (right). Apart from the system with 5.1% gravimetric moisture content, penetration generally increases with moisture content. This agrees qualitatively with the trend in target DPI values provided by Siekmeier et al. [4] (see Figure 7).

Following this, we varied the surface tension for a smaller range of moisture contents to determine the degree to which increasing surface tension could reflect the effect of increasing fines content. Figure 32 shows the penetration of the DCP cone as a function of time for each moisture content at surface tensions $0.1\gamma^*$ and $10\gamma^*$. The penetration measured after the first hammer drop for each case in Figs. 31 and 32 is plotted in Figure 33, as a function of moisture content (left) and as a function of surface tension (right).

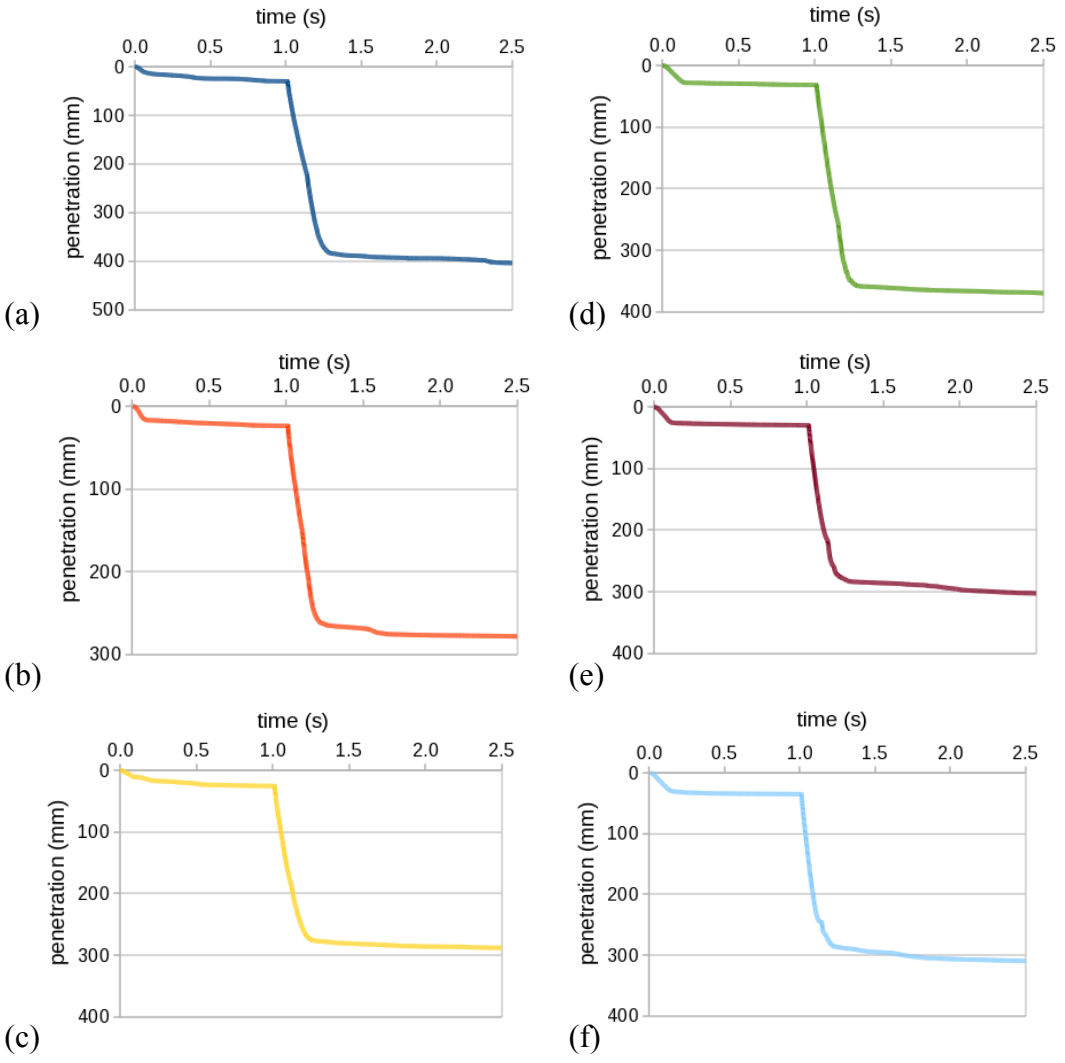

Figure 30: Data from model DCP test using Moisture Model I and unimodal mixture. Plots show the penetration during cone-placement and first hammer impact for gravimetric moisture contents a) 0%, b) 1.3%, c) 3.2%, d) 5.1%, e) 9.6% and f) 12.9%, all at surface tension $\gamma = \gamma^*$.

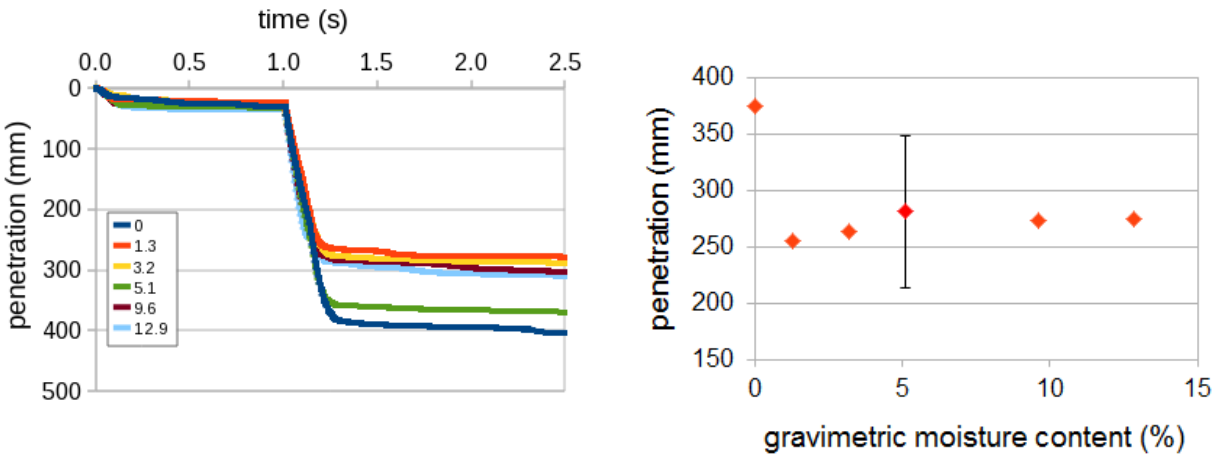

Figure 31: Results from Figure 30 compiled into a single plot. Left: Penetration during cone-placement and first hammer impact for mono-sized systems with different gravimetric moisture contents and a single surface tension $\gamma = \gamma^*$; right: penetration during first impact plotted as a function of gravimetric moisture content. The data point with error bars (at 5.1% moisture content) was obtained by calculating the average and standard deviation of the penetration obtained during the first hammer impact for five different cone positions (center, and 1 mm displacement in four directions; see Figure 34) in an identical system.

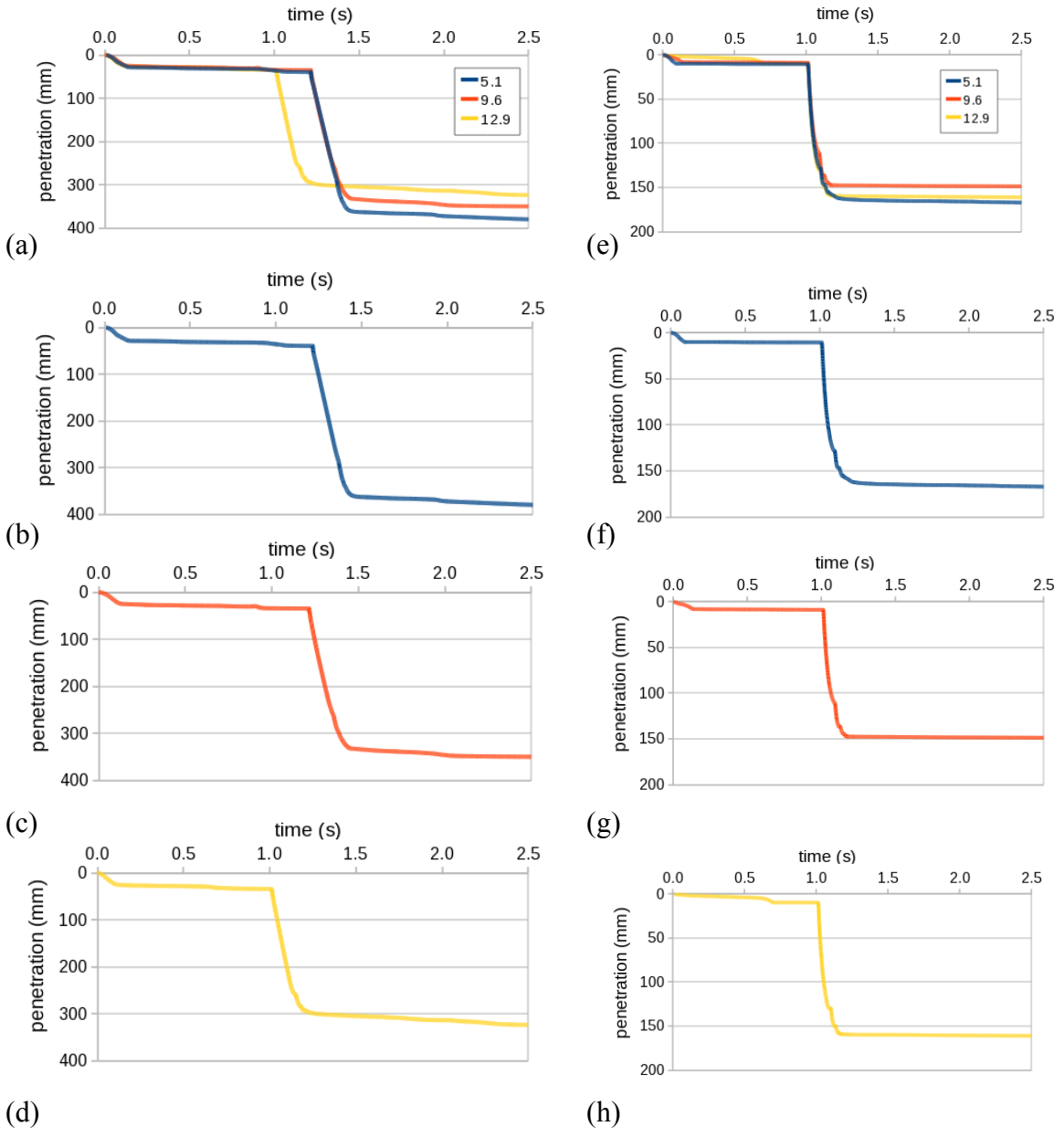

Figure 32: Data from model DCP test using Moisture Model I and unimodal mixture. Plots show the penetration during cone-placement and first hammer impact for gravimetric moisture contents 5.1% (b,f), 9.6% (c,g) and 12.9% (d,h), at surface tensions 0.1 γ* (a-d) and 10 γ* (e-h).

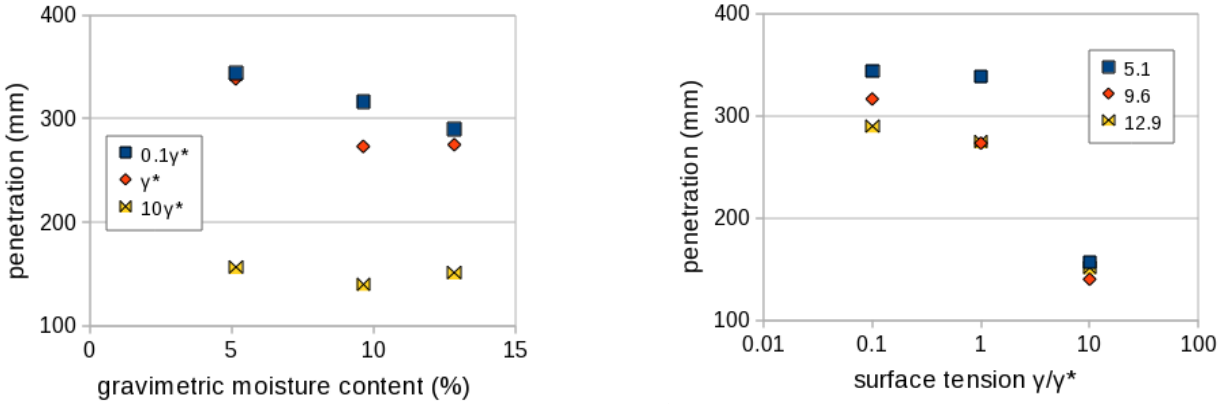

Figure 33: Data from Figs. 31 and 32. Penetration during 1st hammer impact plotted as a function of (left) gravimetric moisture content for surface tensions 0.1 γ*, γ* and 100 γ*; and (right) as a function of surface tension, for gravimetric moisture contents 5.1%, 9.6% and 12.9%.

As can be seen from Figure 33, while there is no clear trend with moisture content, the penetration generally decreases with surface tension, a representative for fines content in our model. When we compare these results with the estimated target data from Siekmeier et al. (2009) [4] (Figure 7), we find the trends obtained from the model results are generally inconsistent. We hypothesize that the inconsistencies could be due to a combination of several effects. First, we were only able to perform measurements for a single drop in each case because of the large penetration per blow compared to the size of our container. If the system is sensitive to initial conditions, such as the placement of the DCP cone, this sensitivity could be affecting our results. Second, the modeling of the DCP blows could be unrealistic, as suggested by the large penetration per blow compared with that observed experimentally. Third, the modeling of a wide particle size distribution used experimentally with a relatively monosized system as we did for the results in this section may be unrealistic. Fourth, our method of approximating an increasing fines content by changing the value of surface tension, likely does not fully reproduce all the relevant physics. For example, it is possible that increasing fines content results in more 'lubrication' between particles, and this 'lubrication' effect has a more dominant effect in the mechanics as compared to the increased 'stickiness' between fine particles.

To determine the sensitivity of the results to the initial position of the cone, we ran one test for the same initial conditions (at 5.1% moisture content and $\gamma=\gamma^*$) for five different initial cone positions. These five initial positions are obtained using the same position as for the other tests along with four points obtained by shifting the initial position by 1mm in four different directions and are illustrated in Figure 34.

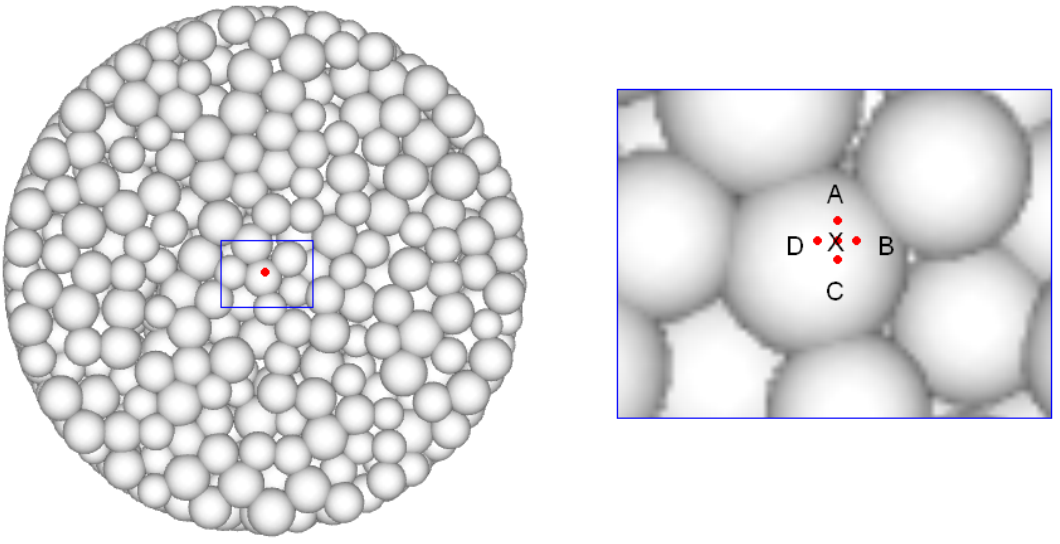

Figure 34: Top view of the mono-sized system with 5.1% gravimetric moisture content and surface tension γ*. Initial positions of the cone for several test runs whose results are shown in Figure 35 are marked. Points A-D are each 1mm away from the center position X.

The resulting penetration histories are plotted in Figure 35. The point is also reported in Figure 31 with error bars around it. The data point in Figure 31 is calculated using the average penetration for the five different initial cone positions, while the error bars represent the standard deviation of the displacements from these initial positions.

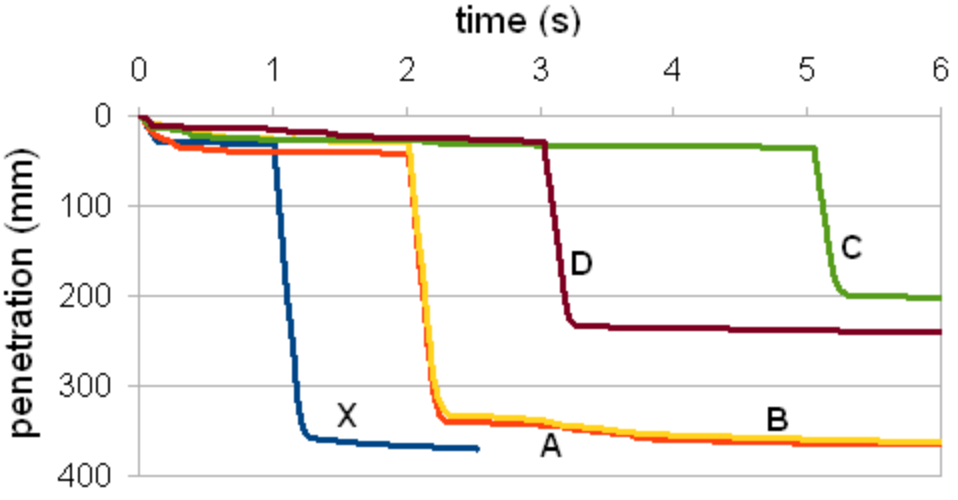

Figure 35: Data from model DCP test using Moisture Model I and unimodal mixture. Plots show the penetration over time during cone-placement and a single hammer impact, for mono-sized system with 5.1% gravimetric moisture content and surface tension γ*, for different initial cone positions.

The variation of the penetration from a single blow with minor variation in initial cone position demonstrates two things. First, there can be rather significant uncertainty in the result reported from a single hammer blow in the DCP test procedure. Second, the reporting of an average penetration for several blows is critical to determine a number representative of the average strength and/or modulus of the bulk granular materials (rather than simply a reflection of initial positioning of the DCP cone.

To address these issues, in Appendix B (Section B.3), we develop an alternative model for the DCP loading history based on published experimental results [44]. The new model gives rise to significantly lower penetration of the cone per blow and therefore allows for multiple blows per experiment. We test the effectiveness of this new force model using a mixture of different sized particles – specifically, our model Class 5 system – and report the results below.

5.4.3 DCP Model Results Using Moisture Model I: Trimodal Mixture

Figure 36 shows the average penetration per blow for three different moisture contents and four different surface tension values, plotted as a function of gravimetric moisture content (left) and as a function of the surface tension parameter (right). There is no consistent trend with increasing moisture content - for high surface tension values the penetration increased slightly with moisture content, but generally decreased for low surface tension values.

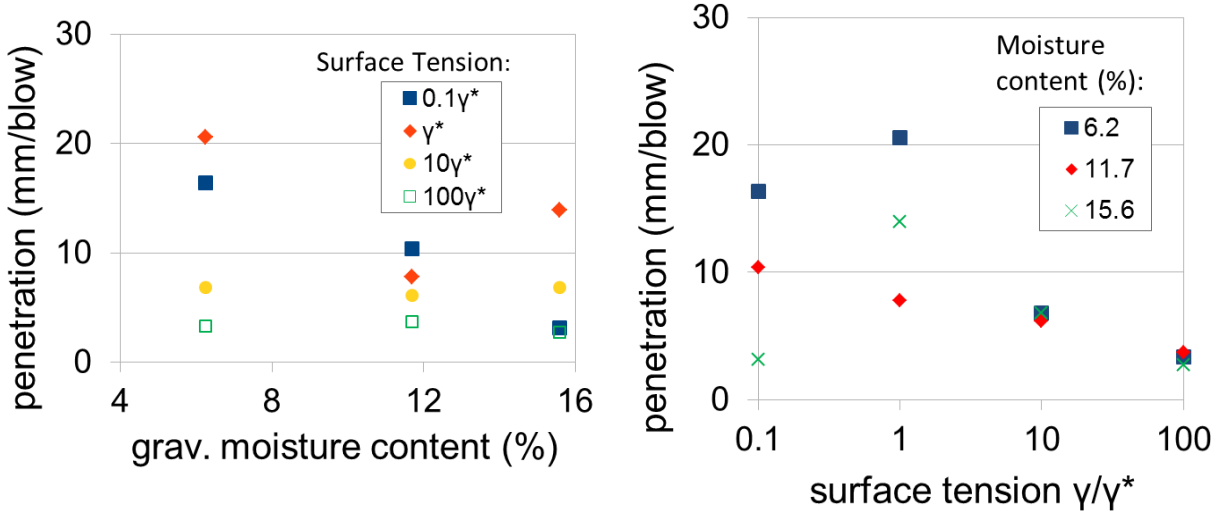

Figure 36: Data from multiple DCP tests using Moisture Model I and the DEM mixture representing the Class 5 mixture described in Section 3.1. DPI (average penetration per blow) is plotted as a function of gravimetric moisture content (left) and surface tension parameter (right) for a trimodal mixture undergoing the DCP test.

When the surface tension value was varied, for high surface tension (representing high fines content) the average penetration decreased with increasing surface tension. This is inconsistent with the trend in Siekmeier et al. [4]'s 'target values' (see Figure 7), which shows an increase in penetration with increasing grading number *GN* (represents an increasing fines content).

5.5 Discussion: Results from Moisture Model I

As mentioned, the trends in our model test results were not typically qualitatively consistent with trends in the experimentally-based estimated target values. In the LWD test simulations we observed a slight increase in peak deflection with moisture content, but a non-monotonic trend with increasing surface tension (fines content). In the DCP test simulations, there was no consistent trend with moisture content, and the average penetration generally decreased with increasing surface tension (fines content). While the trends with moisture content are tentatively agreeing qualitatively with trends of the estimated target values, the results with varying surface tension does not agree with these estimated target value trends at all. This is an indication that modelling the effects of fine particles by varying the surface tension value, rather than explicitly including them in the DEM simulation, is not fully accounting for all the resulting physics.

However the liquid bridge model provides a starting framework for other moisture models - namely that the attractive moisture force is at a maximum when the particle pair is in contact, and decreases as the particles separate.

Chapter 6 Moisture Model II: Explicit Composition Model

6.1 Introduction: Two Explicit Composition Models

For a model that more explicitly considered the effect of different amounts of fines and moisture on the bulk behavior of a granular material, we considered experimental work by Gupta et al. [32] and Gupta and Larson [33]. In these papers, Gupta and colleagues propose empirical relationships that relate suction (negative pore pressure) of an unsaturated granular mixture to its volumetric moisture content, mixture composition (including fine particle content), and bulk density.

6.1.1 Coarse Mixture Model

The model proposed by Gupta et al. in Ref. [32] is expressed in terms of the amount of sand and moisture in an unsaturated granular material containing also of mixture of coarse particles. Since our DEM simulation explicitly models coarse particles only, we first considered this to be an appropriate model for our DEM simulation. This model can be expressed relatively succinctly as:

$$\Theta_p = a + b \times (sand\%) + c \times (bulkdensity) \tag{14}$$

where Θ_p is the predicted volumetric moisture content (cm^3/cm^3) in a mixture made up of sand and particles coarser than sand. The bulk density is in g/cm^3. The coefficients *a*, *b*, and *c* are empirical coefficients that vary with suction (Figure 37).

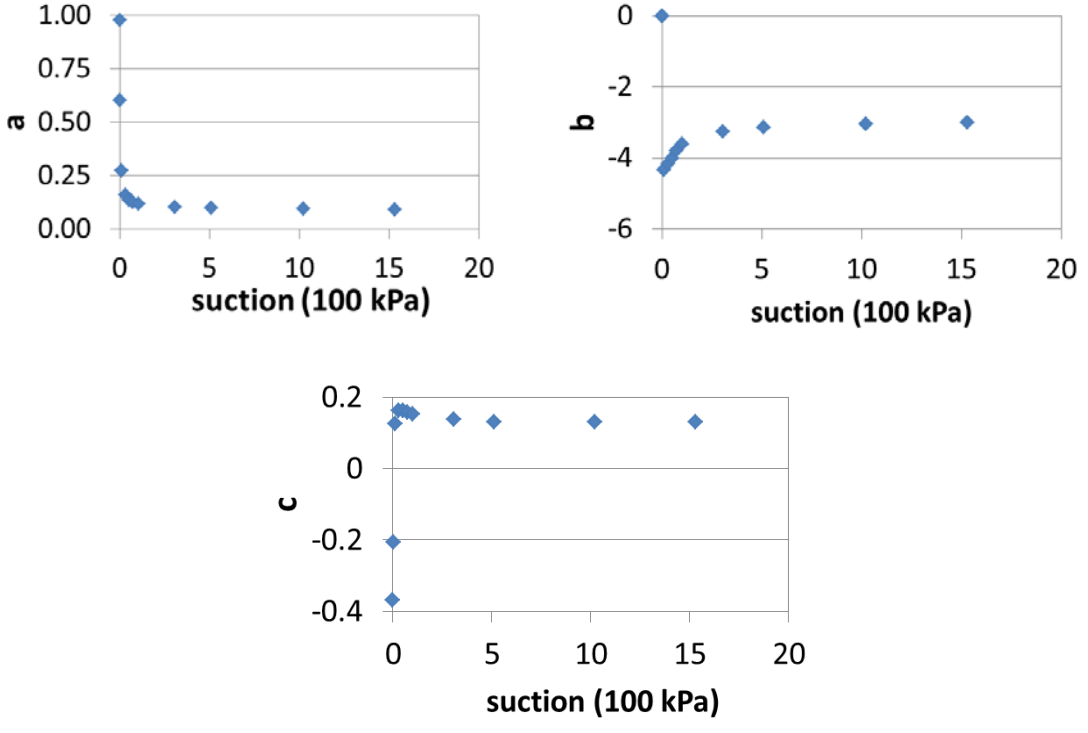

Figure 37: Empirical fit coefficients *a*, *b* and *c* from Gupta et al. [32], as in Equation 14.

There is no analytical form available for these coefficients; instead, Gupta and colleagues presented values determined for them numerically for several discrete experimental conditions. The empirical coefficients are plotted as functions of suction for the discrete values given by Gupta and colleagues [32] in Figure 37. Since the coefficients *a*, *b*, and *c* all vary with suction, Equation 14 is essentially an implicit relationship between volumetric moisture content, fines (sand), and suction (negative pore pressure) in a coarse granular mixture. Figure 38 shows a surface plot relating moisture content and sand content to suction as calculated from this empirical expression.

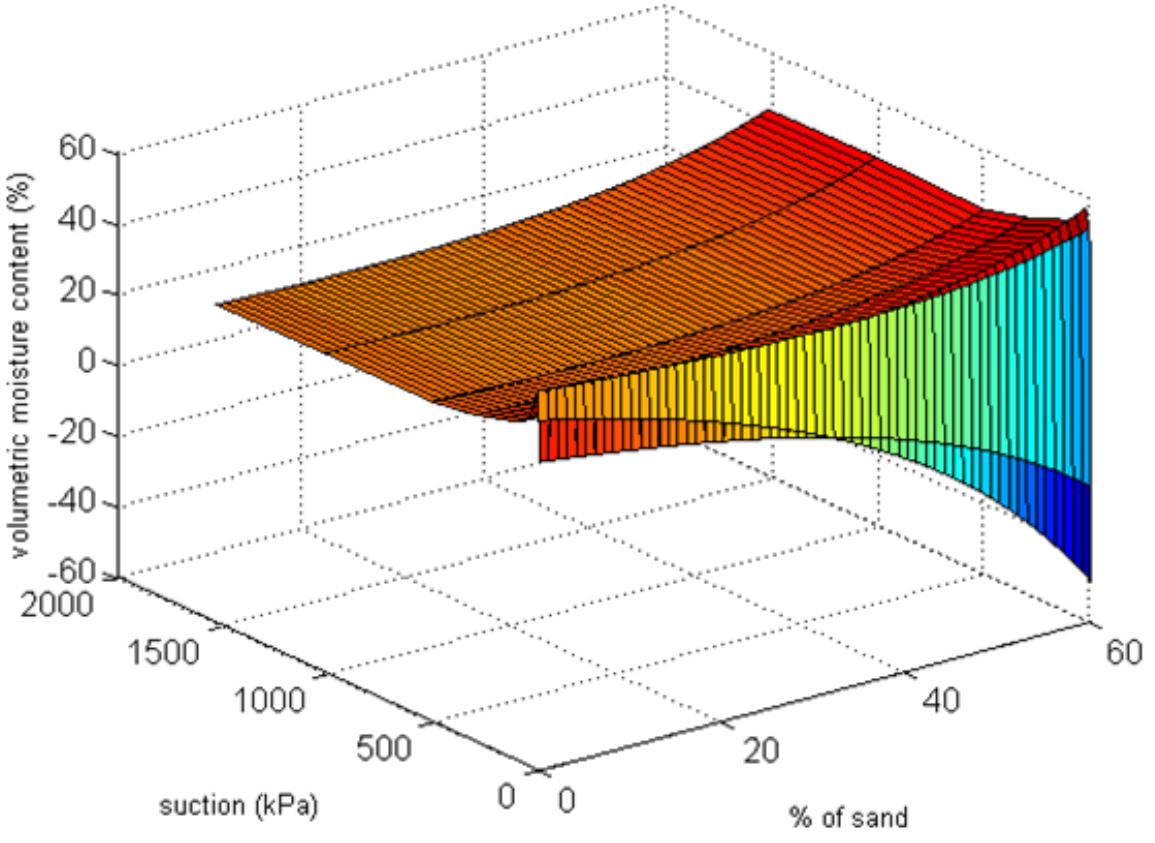

Figure 38: Volumetric moisture content as a function of suction (negative pore pressure) and fines percentage (percentage of sand), based on Equation 14 reproduced from Ref. [32].

Figure 39 shows the same data from the 3D plot in Figure 38, but with curves representing several discrete values for the fines content. The discrete points represent the discrete points from Figure 37 for the coefficients *a*, *b*, and *c*. The data plotted in Figure 39 shows two trends. At the lowest suction values, corresponding to the lowest values for the moisture content, the suction increases with increasing moisture content. For most of the data plotted, the suction decreases with increasing moisture content. To determine what is appropriate for our DEMP-3D model, we consider suction correlates with resistance of a granular material to deformation and compare these results to estimated target values plotted in Figs. 5, 6, and 7.

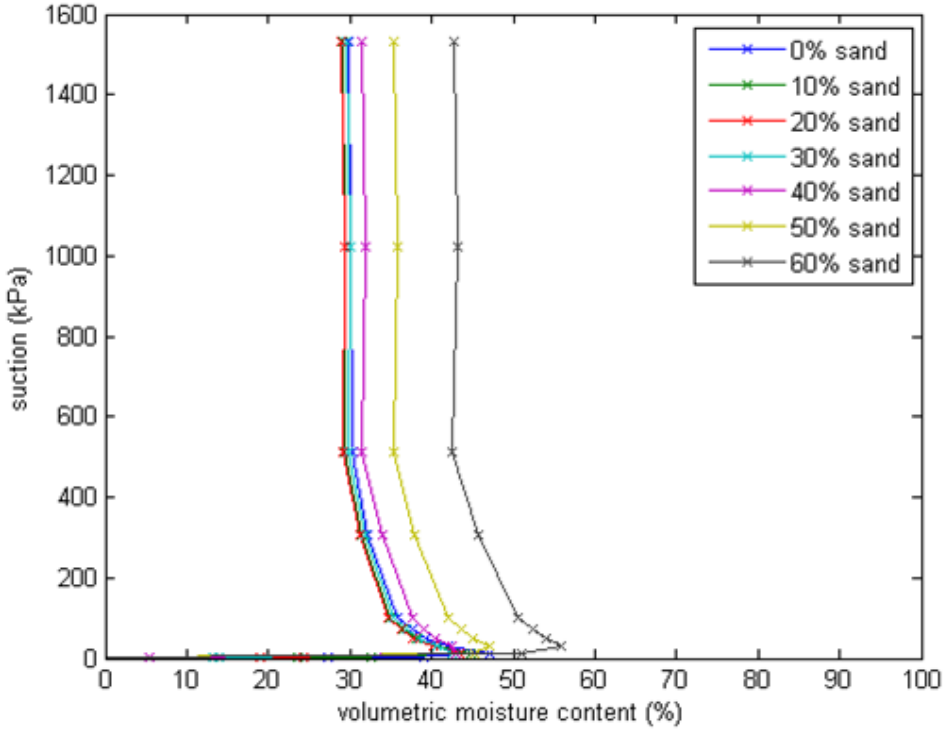

Figure 39: Suction (negative pore pressure) as a function of moisture content, based on Equation 14 reproduced from Ref. [32], for different fines percentages (% sand).

Estimated target values plotted in Figs. 5 and 7 indicate that resistance to deformation decreases with increasing moisture. This correlates best with the predictions for the range of higher moisture content from the Gupta model. On the other hand for the data which correlate well qualitatively with physical observations, the moisture contents ranges from 30% to 50%, much higher than in a typical unsaturated granular base in a pavement system. Therefore, we determined this model was not appropriate for this project. Hence we consider a similar work by Gupta and Larson [33] which, as we describe below, has more focus on moisture levels closer to those in typical pavement systems.

6.1.2 Fine Mixture Model

Gupta and Larson [33] studied mixtures of mostly fine particles (sand, silt and clay), proposing an empirical relationship between volumetric moisture content and the percentages of each of these components. While the results are more promising, we note that there is a length scale difference between our DEM simulation particles and the mixtures in Gupta and Larson's work. We address this with dynamic similarity calculations similar to those we used for the liquid bridge model, which will be detailed later in this report.

From Gupta and Larson [33],

$$\Theta_p = a\times(sand\%) + b\times(silt\%) + c\times(clay\%) + d\times(organicmatter\%) + e\times(bulkdensity) \quad (15)$$

where Θ_p is the predicted volumetric moisture content (cm^3/cm^3), *a*, *b*, *c*, *d* and *e* are empirical coefficients, and the bulk density is in g/cm^3. The mixture is made up entirely of sand, silt and clay, i.e. (sand %) + (silt %) + (clay %) = 100%. Plots of the empirical coefficients as functions of suction are shown in Figure 40.

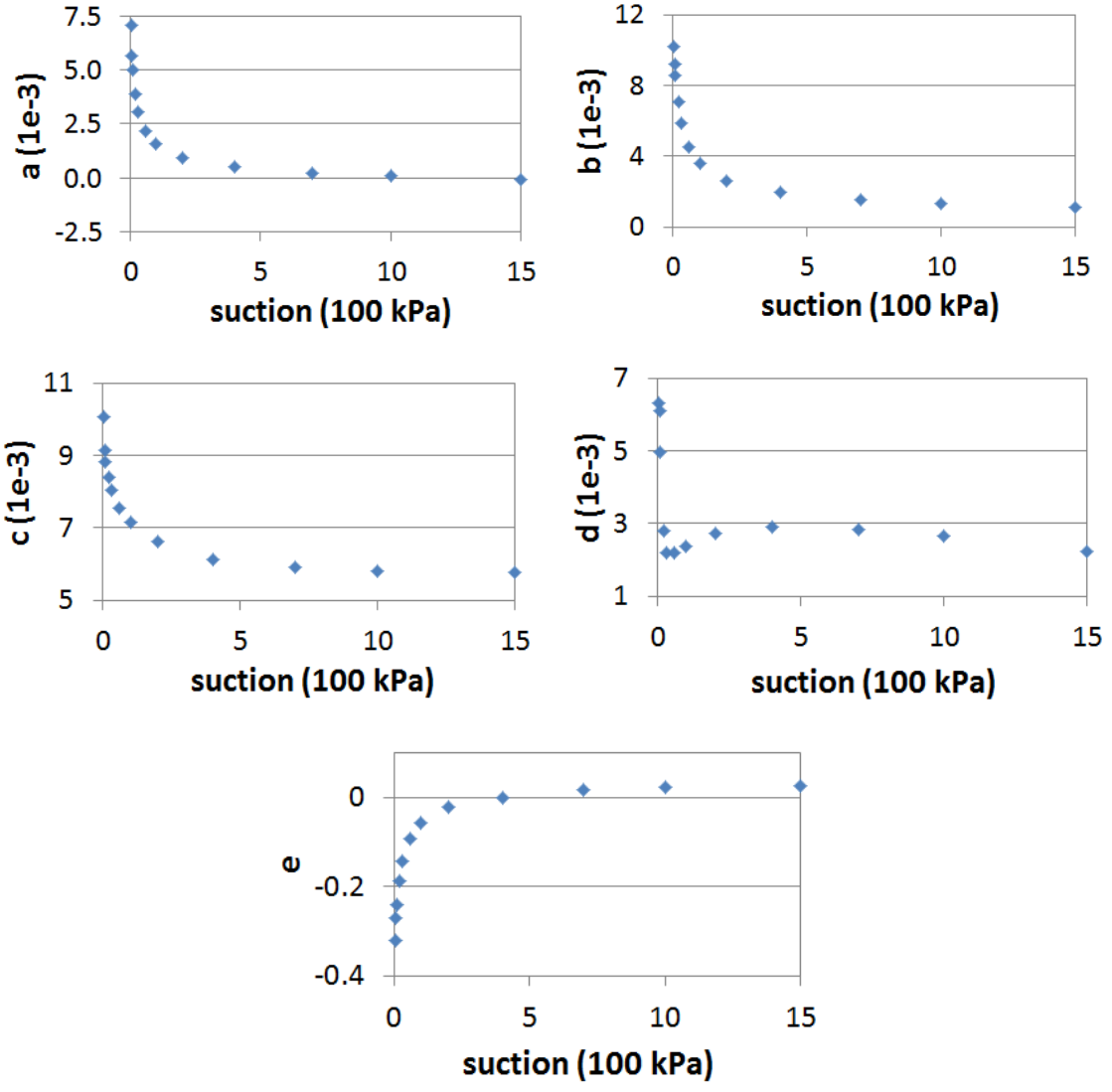

Figure 40: Empirical fit coefficients *a*, *b*, *c*, *d* and *e* for Equation 15 described in detail by Gupta and Larson [33].

The fit coefficients *a*, *b*, *c*, *d* and *e* all vary with suction, so Equation 15 is essentially an implicit relationship between volumetric moisture content and suction (negative pore pressure) in a granular mixture. Given the composition of the mixture, this relationship can be determined. For example in a mixture composed of only sand and silt, a three-dimensional plot of moisture content

as a function of suction and fines percentage (volume percentage of silt in the sand-silt mixture) is obtained as shown in Figs. 41-43.

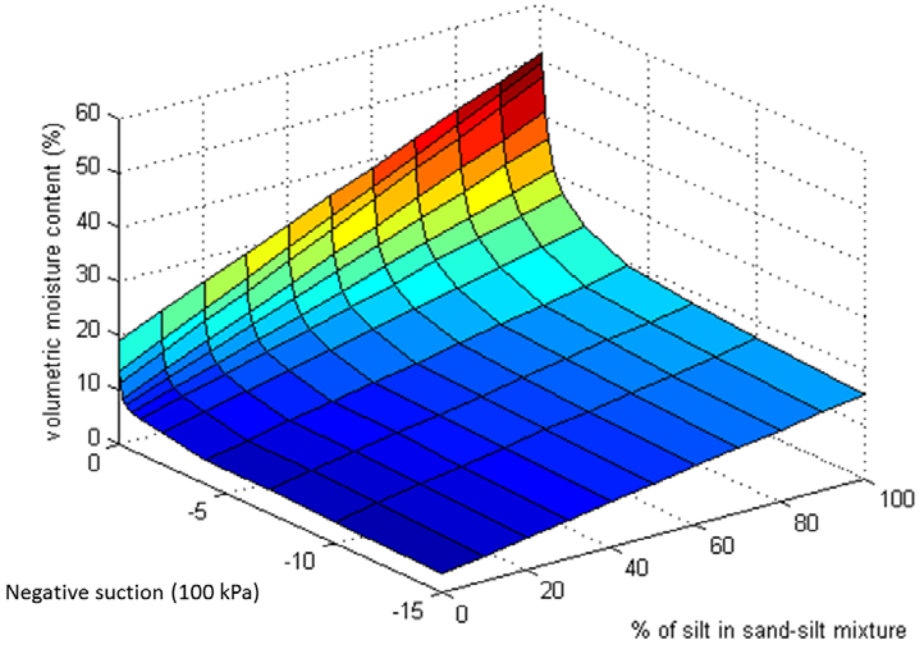

Figure 41: Volumetric moisture content as a function of suction (negative pore pressure) and fines percentage (percentage of silt in a sand-silt mixture), based on Equation 15 as detailed in Ref. [33].

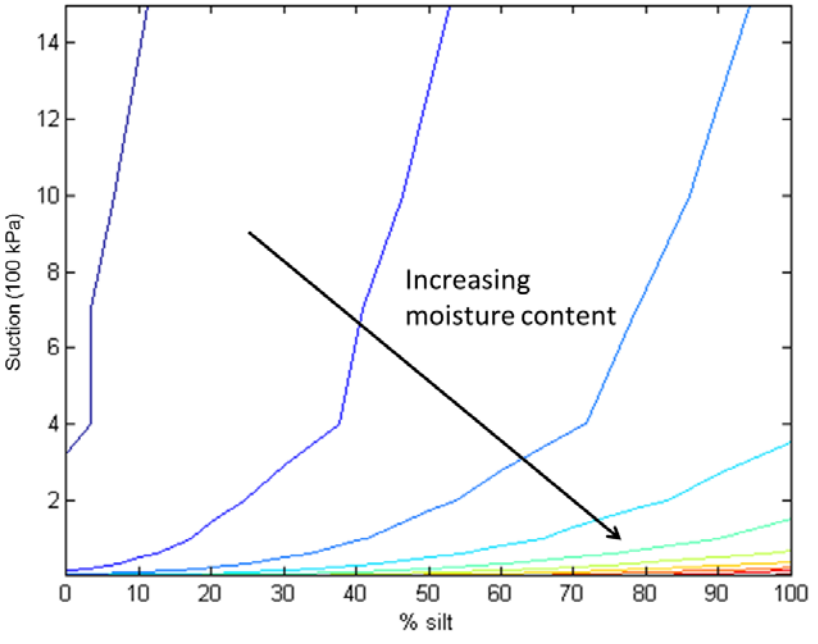

Figure 42: Suction (negative pore pressure) as a function of fines percentage (% silt in a sand-silt mixture), based on Equation 15 as detailed in Ref. [33], for different moisture contents.

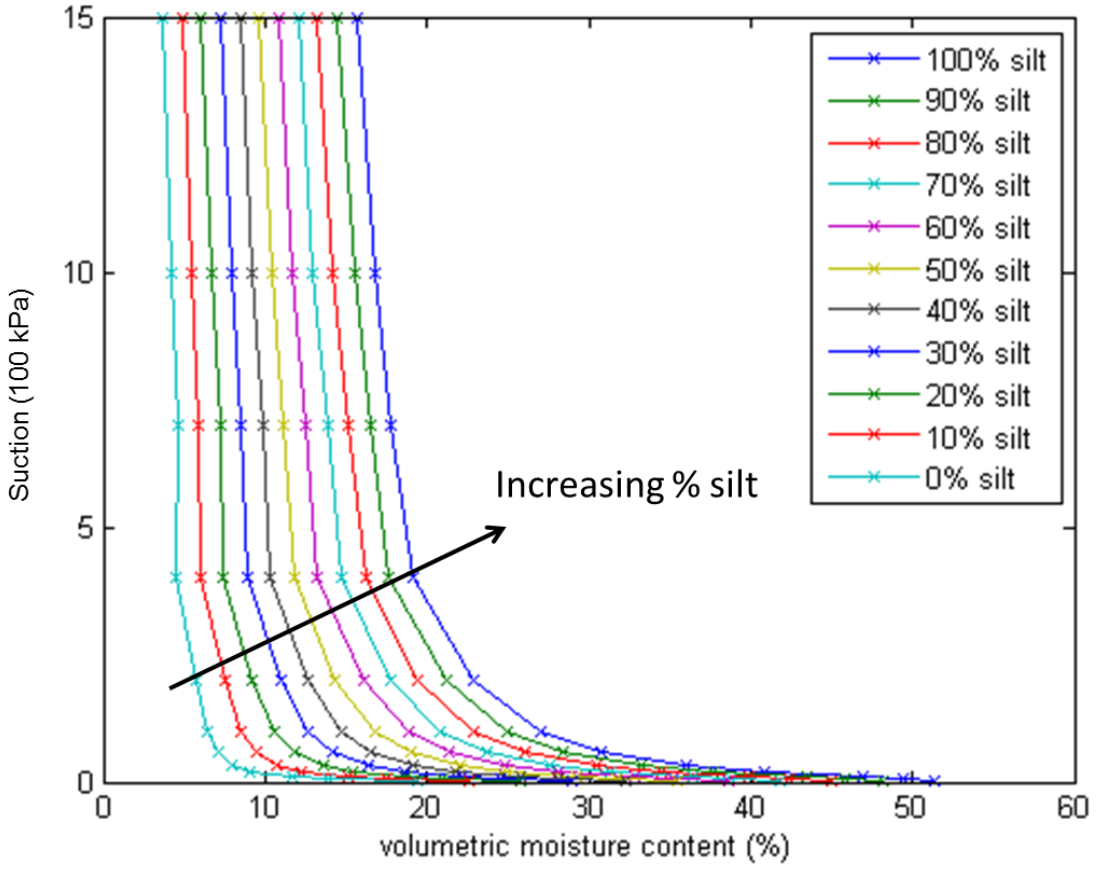

Figure 43: Suction (negative pore pressure) as a function of moisture content, based on Equation 15 as detailed in Ref. [33], for different fines percentages (% silt in a sand-silt mixture).

From Figure 42, for a fixed moisture content, suction (negative pore pressure) increases with increasing amounts of fine material. Conversely in Figure 43, for a fixed fines content, suction decreases with increasing amounts of moisture. We also note that this model involves lower amounts of moisture than the previous, closer to the values of interest for this project. Therefore we will proceed using this model to determine a suction corresponding to a given moisture and fines content.

6.2 Implementation of Moisture Model II into the DEM

Similar to the liquid bridge model, we incorporate the effect of moisture by introducing an attractive force, $F_{m\,(f)}$ in the normal direction:

$$F_n = \begin{cases} -k_n \delta_n^{3/2} - \eta_n \delta_n^{1/4} \dot{\delta}_n + F_{m\,(f)}; \delta_n > 0 \\ F_{m\,(f)} \qquad\qquad\qquad\qquad ; \delta_n \leq 0 \end{cases} \tag{16}$$

$$F_t = \begin{cases} min\left\{ -k_t \delta_n^{1/2} \delta_t - \eta_t \delta_n^{1/4} \dot{\delta}_t ; : \mu F_n \right\}; \delta_n > 0 \\ 0 \qquad\qquad\qquad\qquad\qquad\qquad ; \delta_n \leq 0 \end{cases} \tag{17}$$

For Equation 16, we need to obtain an expression for the fines-dependent moisture force $F_{m\,(f)}$. We start by calculating a suction value corresponding to a given moisture content and mixture

composition (i.e., fines content). The suction is determined from the Gupta model using number such as those shown in Figure 43.

We then translate this into an equivalent suction for each particle-particle contact in our DEM model. As mentioned earlier, there is a length-scale difference between the DEM simulation particles and the mixture particles studied by Gupta and Larson. We address this difference by applying dynamic similarity between the prototype system and the DEM system, i.e. the ratio of the moisture and inertial forces in both systems remain constant. This results in a scaling of the equivalent DEM suction:

$$\tau_{DEM,eq}=\tau_{prototype,eq}\left(\frac{R_{DEM}}{R_{prototype}}\right). \tag{18}$$

In Gupta and Larson's work, their largest particles are sand (≈2 mm) while in our simulations the particles have a average diameter (averaged by weight) of ≈10 mm. Assuming that the equivalent suction in the prototype system is the same as the suction determined from the empirical expression, this scaling results in an equivalent DEM suction with magnitude five times that of the prototype suction.

We use the stress $\tau_{DEM,eq}$ calculated in Equation 18 to calculate a moisture / fines component force $F_{m(f)}$ by performing two steps. First, we assume that the magnitude of $F_{m(f)}$ decreases with separation distance of the two contacting particles 2*s*, similar to the liquid bridge model. We calculate the maximum value of $F_{m(f)}$ by first assuming that the maximum attractive force due to moisture between a pair of particles is equivalent to a projected cross-sectional area multiplied by the suction:

$$F_{m(f),max} = \tau_{DEM,eq}\pi {R_o}^2 \tag{19}$$

where R_0 is the average radius of the pair of particles in contact.

Finally, we approximate the spatial dependence of the fines-mediated moisture force as an exponential whose decay length is R_o is the average radius of the pair of particles in contact. We express this moisture / fines force as:

$$F_{m(f)} = F_{m(f),max}e^{-s/R_o} = \left(\tau_{DEM,eq}\pi {R_o}^2\right)e^{-s/R_o} \tag{20}$$

To investigate the effectiveness of this model, we perform several simulations. The parameters involve 3 different values for the moisture content (volumetric moisture content ω_v=10%, 15%, 20%) and 3 different fines contents (f_{silt}=10%, 20%, 30% in a sand-silt mixture). For the values we used, this resulted in seven values for the model suction. These are given in Table 4.

Table 4: Empirical suction values used for LWD test simulations of the explicit composition model, obtained using Eqn. 15 for a sand-silt mixture, and the corresponding equivalent model suction.

ω_v (%)	f_{silt} (%)	empirical suction (kPa)	$\tau_{DEM,eq}$(kPa)
10	10	50.0	250
15	30	50.0	250
15	20	22.8	114
15	10	10.6	530
20	30	16.1	80.5
20	20	8.3	41.5
20	10	5.5	27.5

6.3 LWD Model Test Results Using Moisture Model II

6.3.1 LWD Preparation Results Using Moisture Model II

The simulation procedure for the LWD model test is the same as that followed for the liquid bridge model described inChapter 4. Again, for all cases, the particles are initialized by releasing them dry into a cylinder. The steady state reached after this point is the same for all the LWD simulations involving the same particle size distribution, at which point moisture is added. For this report we focus on the parts of the simulation the depend on the moisture / fines model: the compaction and subsequent application of the LWD test.

Figure 44 shows the vertical position of the 'lid' (see Section 4.2.2) during compaction and the resulting solid fraction, for a mixture with an equivalent model suction of 41.5 kPa, which corresponds to the calculated prototype suction for a granular mixture with 20% volumetric moisture content and 20% silt in a sand-silt mixture. We apply at least four impacts with the 'lid' to ensure the system is sufficiently compacted. Figure 45 shows the vertical position of the LWD 'plate' (see Section 4.2.2) and the system's solid fraction after the compaction stage.

A series of loading impacts (see Section 4.2.2) are applied to the LWD plate and the corresponding deflection is tracked (Figure 46). There is no significant qualitative difference between the system's behavior when this model is applied as compared to the previous liquid bridge model, which is perhaps expected as the overall application of the model via the moisture force is similar.

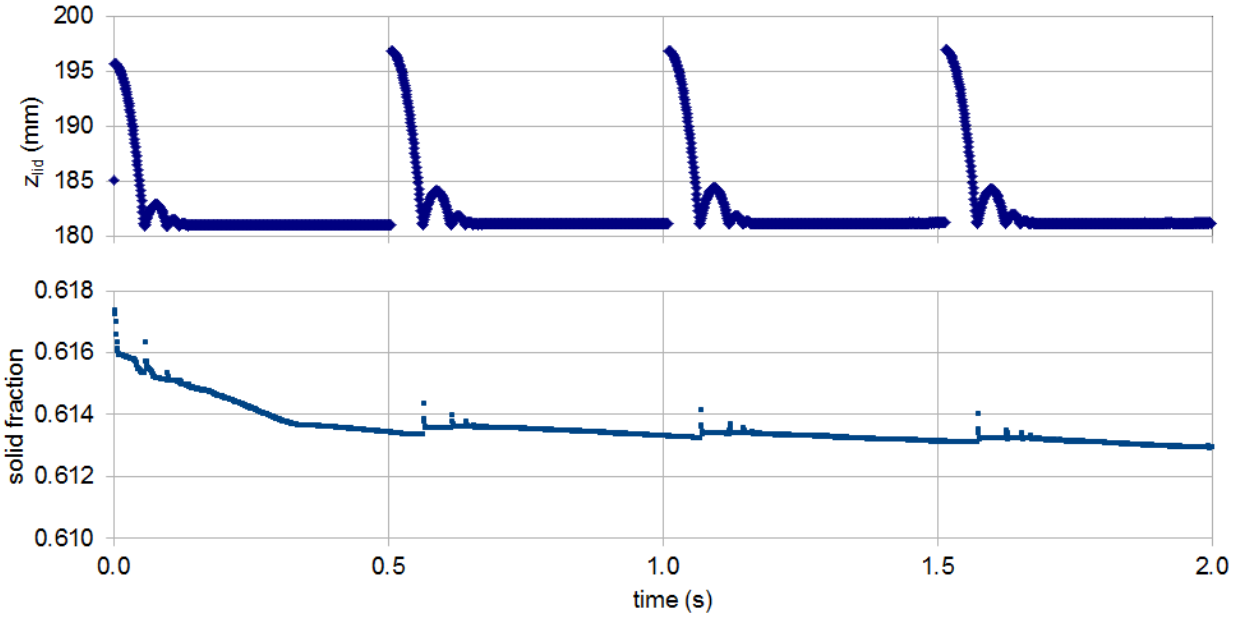

Figure 44: Data from compaction for LWD model test using Moisture Model II and the DEM mixture representing the Class 5 mixture described in Section 3.1. Lid position and solid fraction during compaction for a system with equivalent model suction of 41.5 kPa.

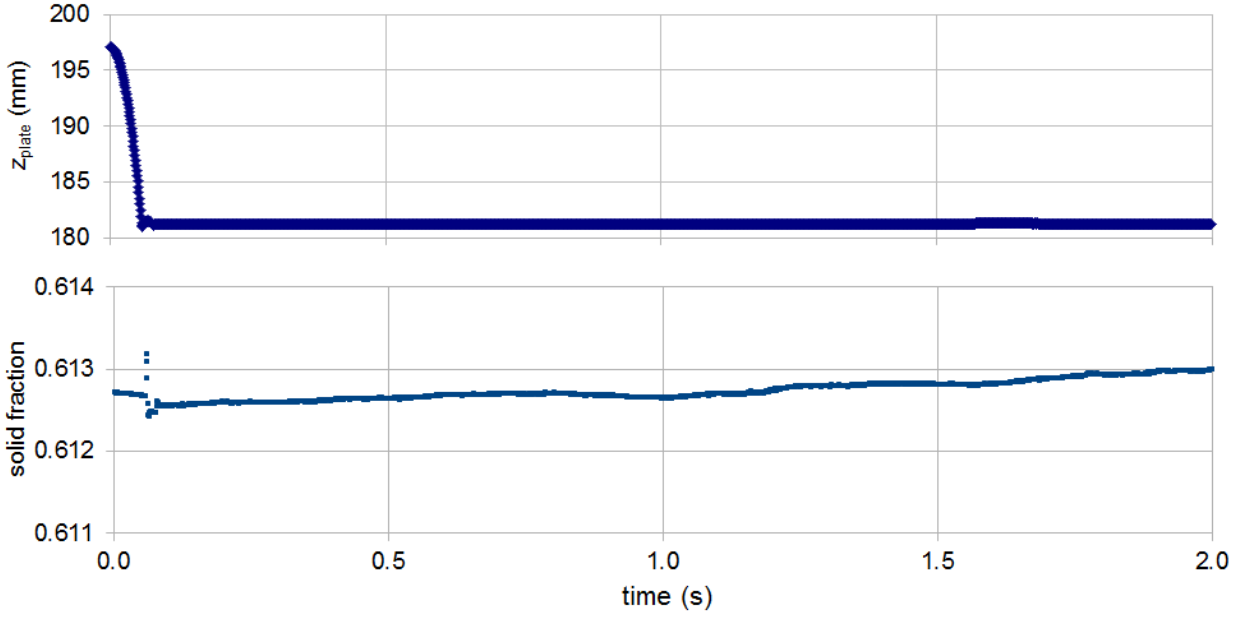

Figure 45: Data from placement of LWD plate using Moisture Model II and the DEM mixture representing the Class 5 mixture described in Section 3.1. Plots show the temporal dependence of the LWD plate and solid fraction for a system with equivalent model suction of 41.5 kPa.

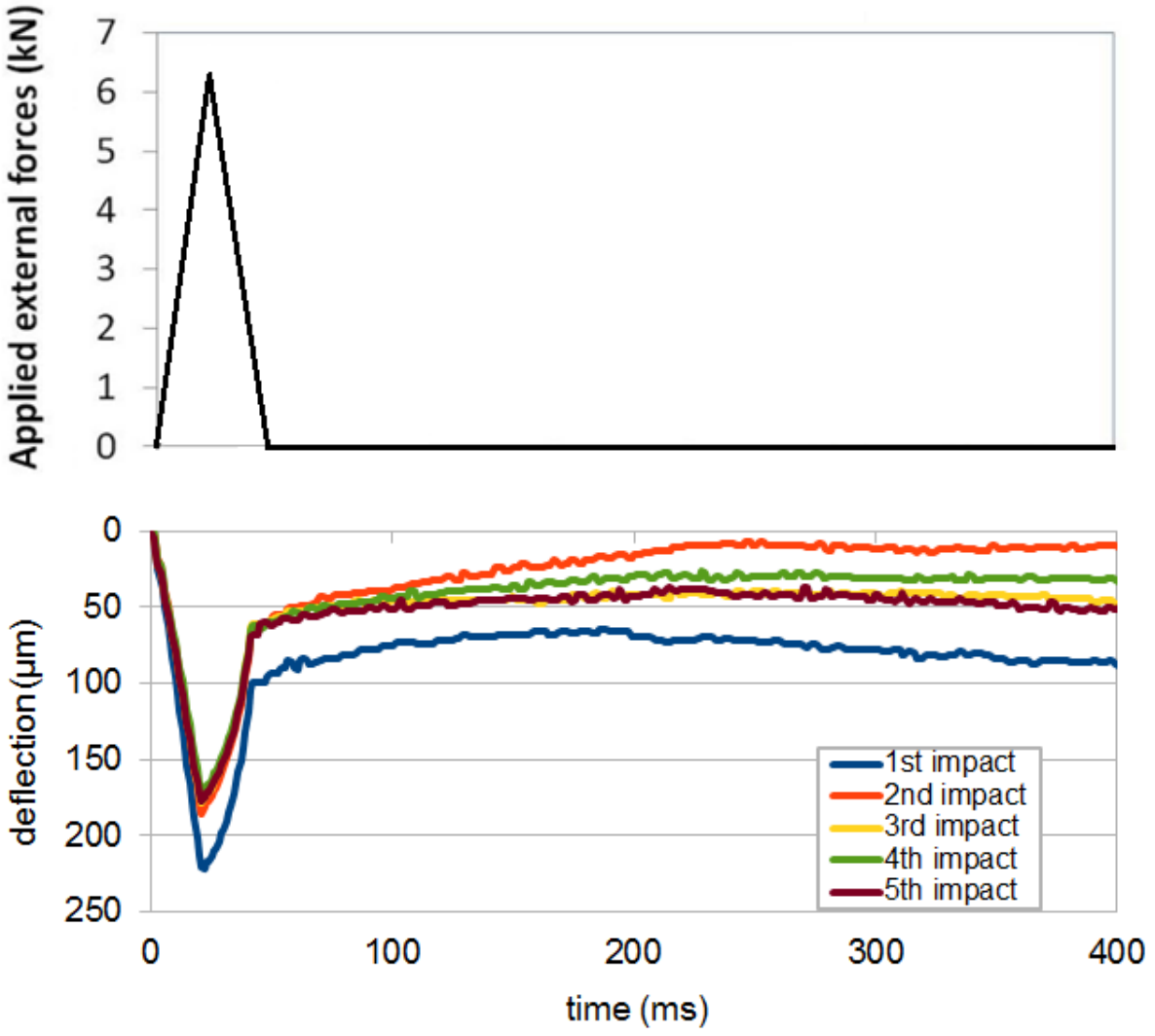

Figure 46: Data from an LWD model test using Moisture Model II and the DEM mixture representing the Class 5 mixture described in Section 3.1. The plots show the temporal dependence of the loading and plate deflection during a series of consecutive impacts for a system with equivalent model suction of 41.5 kPa.

6.3.2 LWD Model Test Results Using Moisture Model II: Trimodal Mixture

In Figure 47, we plot the peak deflections and corresponding effective bulk moduli as a function of model suction obtained for seven combinations of moisture and fines content (see Table 4). Except for at very low suction values, average peak deflection decreases (and correspondingly effective bulk modulus increases) with increasing equivalent model suction in a monotonic fashion. This corresponds to increasing moisture and decreasing fines.

Figs. 48 and 49 show the peak deflections and corresponding effective bulk moduli obtained for seven combinations of moisture and fines content, plotted as functions of moisture content and

fines content respectively. From Figure 48, the peak deflection increases (and effective modulus decreases) with increasing moisture content, which is in qualitative agreement with the 'target values' [4] plotted in Figure 5. However the opposite is seen with increasing fines content (Figure 49), which directly contradicts the trend seen in 'target values' in Figure 6.

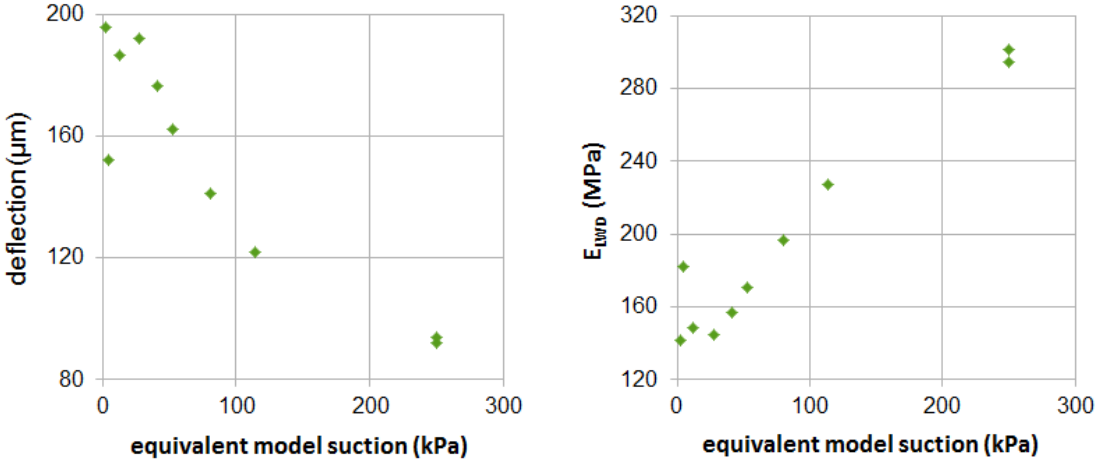

Figure 47: Data from LWD tests using Moisture Model II and the DEM mixture representing the Class 5 mixture described in Section 3.1. Average peak deflection (left) as a function of equivalent model suction, and the corresponding effective bulk modulus (right).

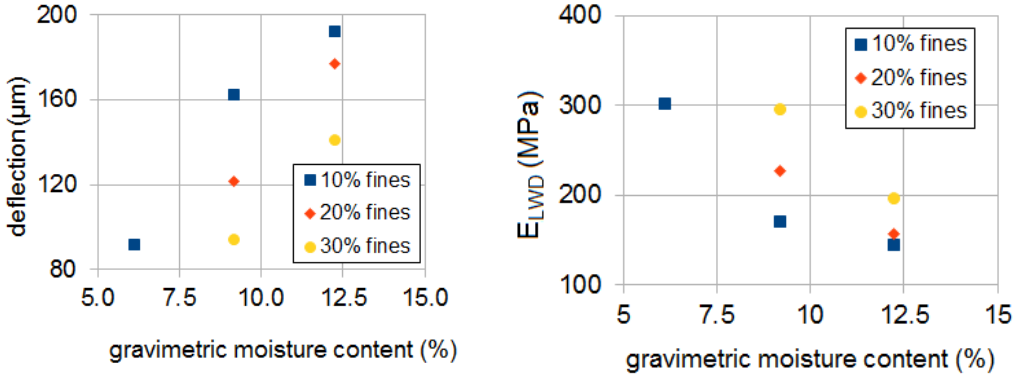

Figure 48: Data from LWD tests using Moisture Model II and the DEM mixture representing the Class 5 mixture described in Section 3.1. Average peak deflection (left) plotted as a function of gravimetric moisture content for three values of fines content (percentage silt in a sand-silt mixture), and the corresponding effective bulk modulus (right).

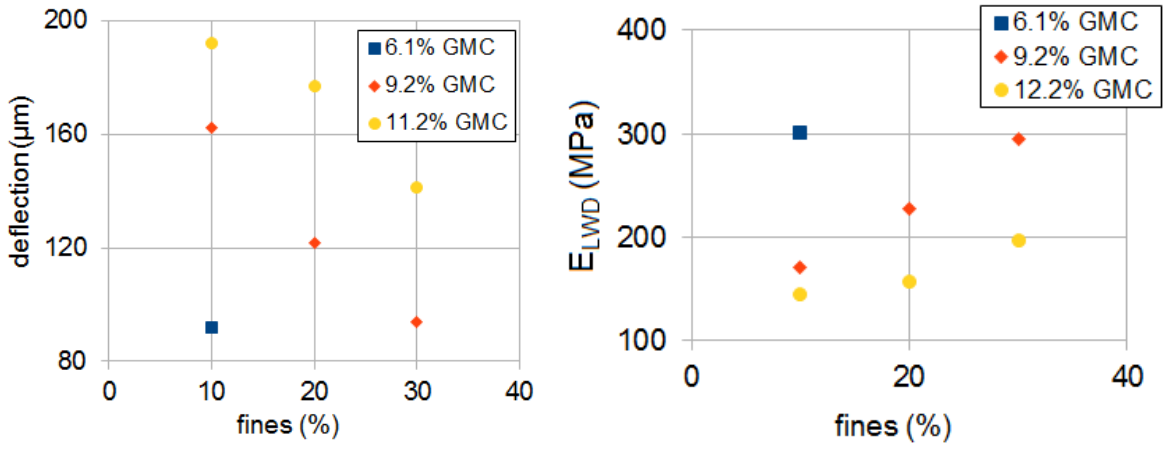

Figure 49: Data from LWD model tests using Moisture Model II and the DEM mixture representing the Class 5 mixture described in Section 3.1. Average peak deflection (left) as a function of fines content (percentage silt in a sand-silt mixture) for three gravimetric moisture contents, and the corresponding effective bulk modulus (right).

From Equation 15, it is possible to obtain the same suction value for different combinations of moisture and fines content (e.g. the first two combinations in Table 4), and also different mixture compositions (for which the definition of 'fines' would then be different). Hence while it helps with physical understanding to break the results of Figure 47 up into plots as functions of grading number or moisture content (Figs. 48 and 49), considering them as a function of model suction is more encompassing.

6.4 DCP Model Test Results Using Moisture Model II

6.4.1 DCP Preparation Results Using Moisture Model II

As detailed in Section 4.3.1, the particles are initially dropped into a cylinder, without moisture. The resulting system state after this initialization stage is used as the starting point for all the DCP simulations involving the same particle size distribution, and hence we focus on the subsequent stages where moisture has been added.

Figure 50 shows the vertical position of the base of the disc representing the surcharge load (see Section 4.3.2) during compaction, and the resulting solid fraction, of a mixture with equivalent model suction of 114 kPa. We found that generally six impacts provided sufficient compaction for good results, so the compaction was stopped after that.

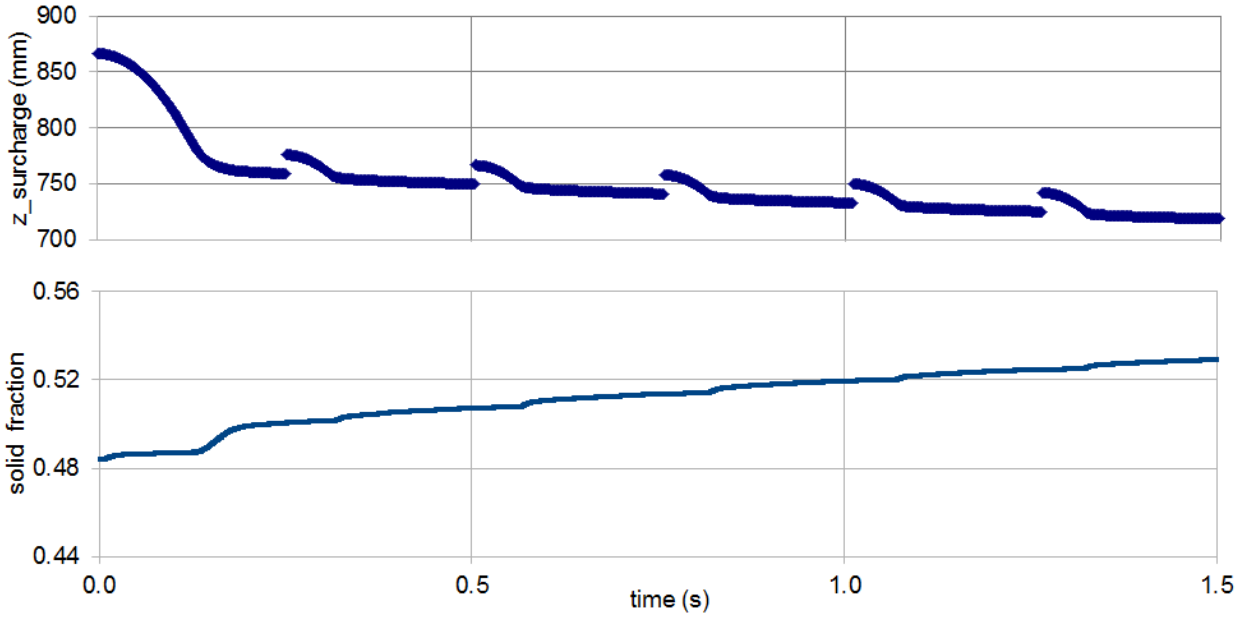

Figure 50: Data from compaction for a DCP model test using Moisture Model II and the DEM mixture representing the Class 5 mixture described in Section 3.1. The temporal dependence of the surcharge position and solid fraction are plotted during compaction for a system with equivalent model suction of 114 kPa.

After allowing the system and surcharge to settle, the cone-rod assembly (see Section 4.3.3) was added with the cone-tip positioned at the vertical height of the base of the surcharge. The cone-rod assembly was then allowed to penetrate the granular mixture under its own weight. The vertical position of the cone-tip is shown in Figure 51, for the same mixture as in Figure 50.

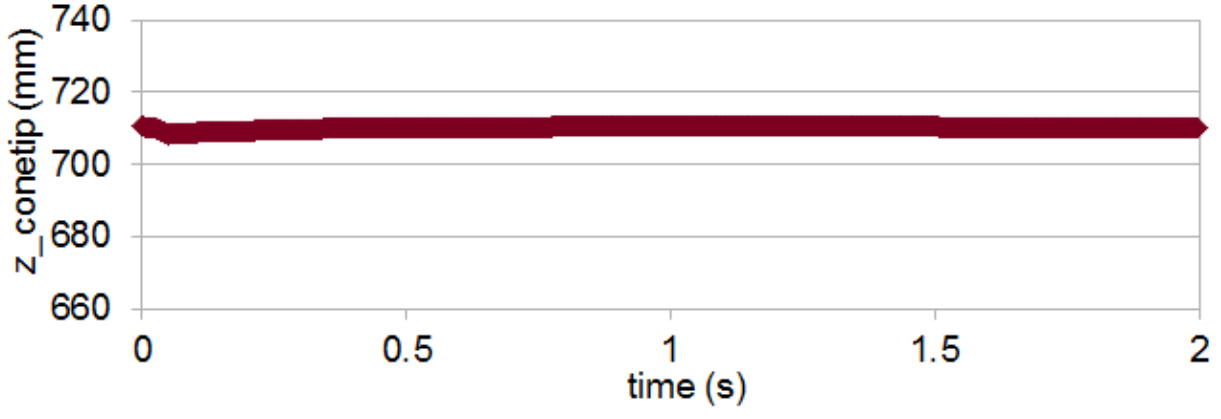

Figure 51: Data from initial placement of cone for a DCP model test using Moisture Model II and the DEM mixture representing the Class 5 mixture described in Section 3.1. Position of cone-tip (base of cone-rod assembly) during initial placement for a system with equivalent model suction of 114 kPa.

Once the cone-rod assembly has reached a steady state, a series of loading impacts (see Section 4.3.4) corresponding to the falling hammer is applied. The vertical position of the cone-tip is tracked through these impacts, as shown in Figure 52. The DPI is calculated as the average penetration of the five consecutive hammer blows.

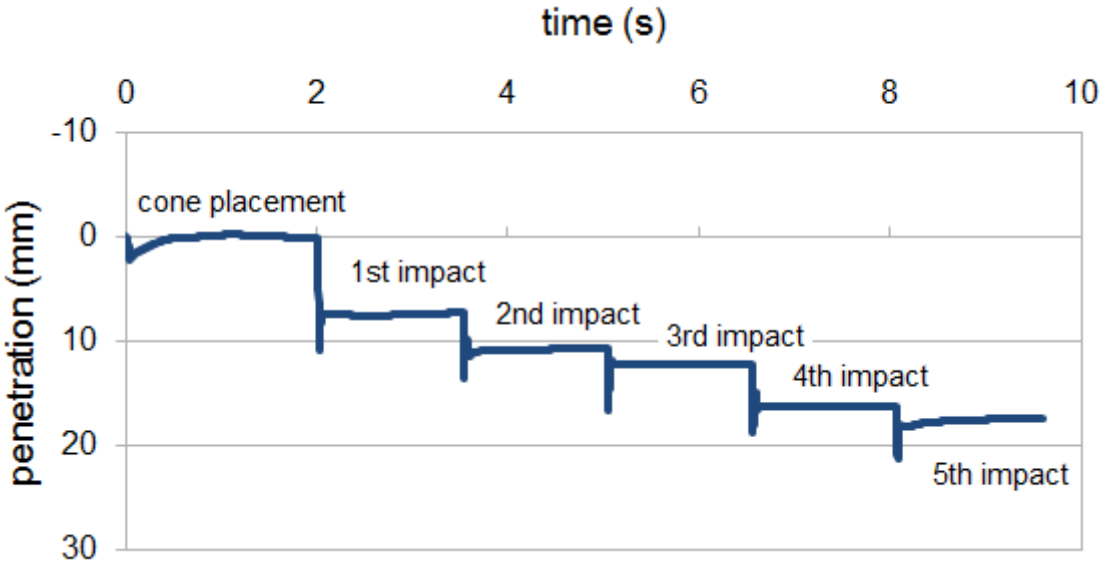

Figure 52: Data from a DCP model test using Moisture Model II and the DEM mixture representing the Class 5 mixture described in Section 3.1. Temporal dependence of the cone penetration during including initial placement and consecutive hammer blows for a system with equivalent model suction of 114 kPa.

6.4.2 DCP Model Test Results Using Moisture Model II: Trimodal Mixture

Figure 53 shows the results of the DCP test performed on a trimodal mixture, using a few model suction values to cover the range explored with the LWD test. We observe that as model suction increases, the average penetration generally decreases. This consistent with the LWD simulation test results, where the average peak deflection decreases with increasing model suction.

In considering these results, we recall that the model suction increases with decreasing amounts of moisture - this implies that the average penetration decreases with decreasing amounts of moisture, which is consistent with trends in the estimated target values. Conversely, the model suction increases with increasing amounts of fines which implies that the average penetration decreases with increasing amounts of fines (reflected as a higher grading number). This is exactly opposite the trend observed from physical tests.

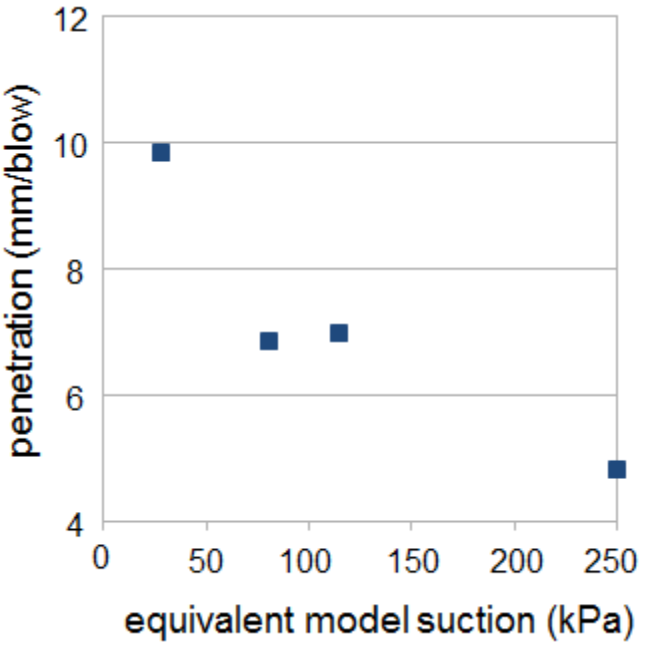

Figure 53: Data from DCP model tests using Moisture Model II and the DEM mixture representing the Class 5 mixture described in Section 3.1. Average penetration per blow as a function of model suction.

6.5 Discussion: Results from Moisture Model II

To summarize the results from our "Model II" simulations, we consider three points: (1) LWD and DCP model results show that the average peak deflection/ average penetration decreases monotonically with model suction. (2) Model suction increases with increasing fines or decreasing moisture content. (3) These first two points considered together imply that model deflections / penetrations increase with increasing moisture content and decrease with increasing fines content. From the data reported by Siekmeier et al. [4] and plotted in Figs. 5, 6 and 7, peak deflection and average penetration increase - and equivalently, the effective bulk modulus decreases - with both increasing fines and increasing moisture content in a granular material. In other words, our model results are in qualitative agreement with the dependence of the estimated target value on moisture content s but inconsistent with the dependence of the estimated target value on fines content. These results indicate that, while Gupta's framework may represent the dependence of suction on deformation well, it is not sufficient to contain all of the physics of resistance of a granular material to deformation. In particular, this model framework does not have the capacity to account for a change in the effective friction between coarse particles that occurs in the presence of greater fractions of fines. Thus, we hypothesize the addition of this extra "physics" in the model may more accurately reflect measured resistance of a granular material to deformation.

Chapter 7 Moisture Model III: Hybrid Moisture / Fines Model

7.1 Introduction: Considerations for Moisture Model III

Our results from Moisture Models I and II (Sections 5 and 6) indicate that modeling the effect of fines and moisture by only changing the form of the normal force F_n alone does not fully reproduce the trends seen in estimated target data [4]. In particular, while the dependence of the estimated target value on moisture content was captured by the models, the dependence of the estimated target value on fines was not.

To improve the model, we consider some qualitative phenomena that accompany the addition of fines. Often the addition of fines can make relative contacts between particles more slippery, that is, the addition can lower the effective interparticle coefficient of friction. For example, fine particles may occupy spaces between roughness elements on surfaces of coarse particles; subsequently, an increasing amount of fine materials would result in 'smoother' coarse particles and hence decreased friction between them. Based on this, we hypothesize that we could model the effects of fine contents by varying the friction coefficient between coarse model DEM particles. Our third "moisture model", uses this to build on Models I and II. Specifically, instead of viewing the friction coefficient μ as a constant material property, we allow it to vary as a measure of the fines content, i.e. $\mu=\mu_{m(f)}$. Then, to represent the moisture, we simply adapt the form of $F_{m(f)}$ from Model II. That is, each granular material is assigned a value for effective stress $\tau_{DEM,eq}$. Then, for each pair of particles whose separation distance 2*s* is less than the average of the two particle radii, R_0, $F_{m(f)} = F_{m(f),max}e^{-s/R_0} = \left(\tau_{DEM,eq}\pi {R_0}^2\right)e^{-s/R_0}$. For simplicity, we interpret $F_{m(f)}$ as solely representing moisture content. In other words, we associate a unique value of $\tau_{DEM,eq}$ with each moisture level.

The contact model then takes the following form:

$$F_n = \begin{cases} -k_n\delta_n^{3/2} - \eta_n\delta_n^{1/4}\dot{\delta}_n + F_{m(f)}; & \delta_n > 0 \\ F_{m(f)}; & \delta_n \le 0 \end{cases} \tag{21}$$

$$F_t = \begin{cases} min\left\{-k_t\delta_n^{1/2}\delta_t - \eta_t\delta_n^{1/4}\dot{\delta}_t; : \mu_{m(f)}F_n\right\}; & \delta_n > 0 \\ 0; & \delta_n \le 0 \end{cases} \tag{22}$$

We perform simulations using four of the suction values from Section 6.3 (the same values as in Figure 53), and three values of inter-particle friction coefficient to represent increasing amounts of fine particles. We don't use the lowest suction values which correspond to high moisture contents and are thus not of interest in this project. These conditions are summarized in Table 5.

Table 5: Friction coefficients $\mu_{m(f)}$ and values of the model suction $\tau_{DEM,eq}$ used in simulations performed using Moisture Model III.

$\tau_{DEM,eq}$ (kPa)	27.5	80.5	114	250
μ=0.2	×	×	×	×
μ=0.3	×	×	×	×
μ=0.4	×	×	×	×

7.2 LWD Test Results Using Moisture Model III

Here we describe results from our model LWD tests using Moisture Model III

7.2.1 LWD Preparation Results Using Moisture Model III

As detailed in Section 4.2.1, the particles are initially dropped into a cylinder, without moisture. The resulting system state after this initialization stage is used as the starting point for all the LWD simulations involving the same particle size distribution, and hence we focus more on the subsequent stages.

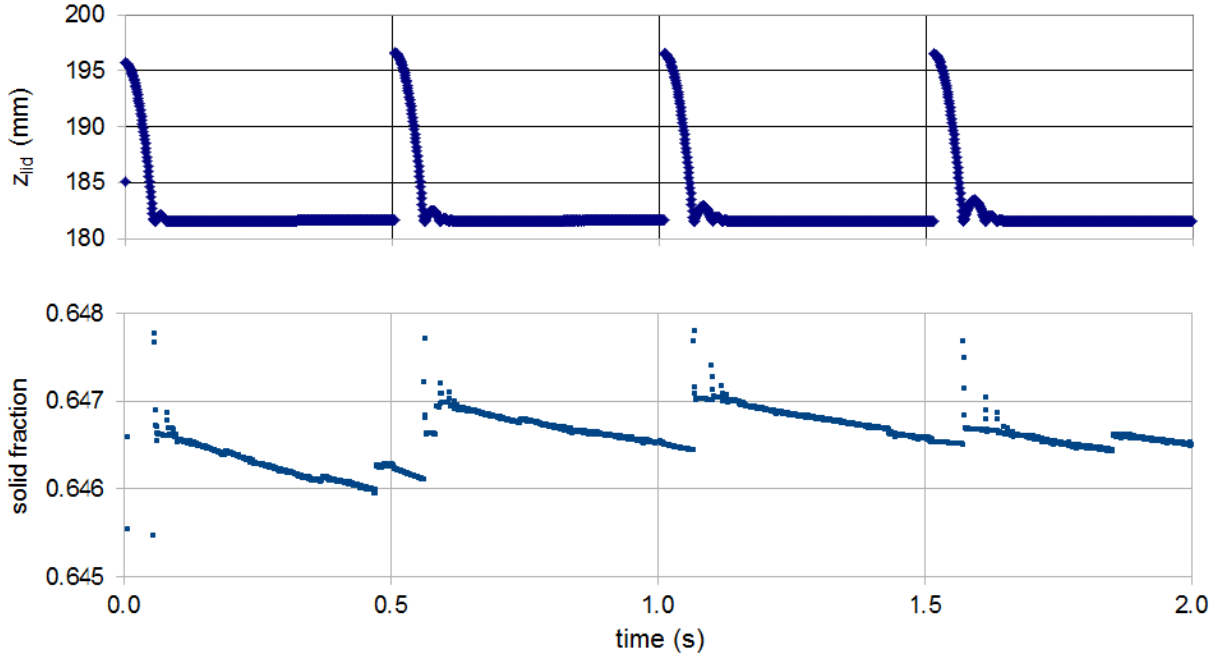

Figure 54: Data from compaction for LWD model tests using Moisture Model III and the DEM mixture representing the Class 5 mixture described in Section 3.1. Lid position and solid fraction during compaction for a system with equivalent model suction of 114 kPa, and an interparticle friction coefficient of 0.2.

Figure 54 shows the vertical position of the ‘lid’ and the resulting solid fraction during the compaction stage. After at least four impacts, the ‘lid’ is removed and replaced with the LWD ‘plate’ (see Section 4.2.3) which is allowed to settle before loading. The vertical position of the LWD plate and system solid fraction are shown in Figure 55.

A series of loading impacts (see Section 4.2.4) are applied to the LWD plate, and the resulting deflection tracked (see Figure 56). The average peak deflection of the final three impacts are used to calculate an effective bulk modulus.

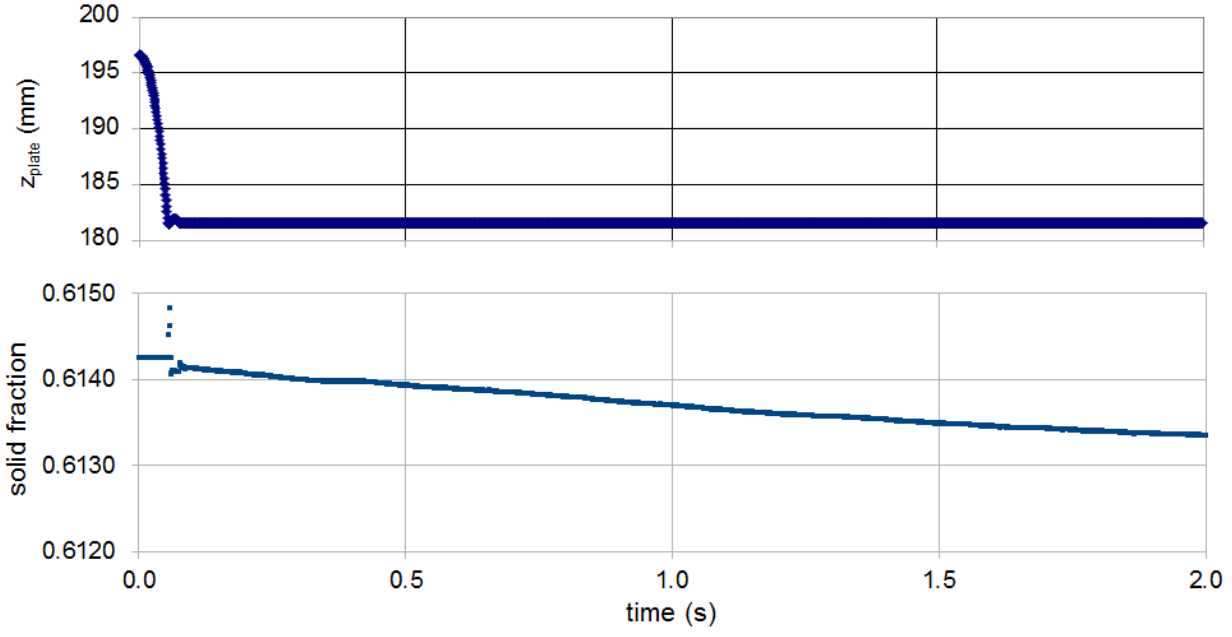

Figure 55: Data from initial placement of model LWD plate using Moisture Model III and the DEM mixture representing the Class 5 mixture described in Section 3.1. The initial placement of LWD plate and solid fraction are plotted as functions of time for a system with equivalent model suction of 114 kPa, and an interparticle friction coefficient of 0.2.

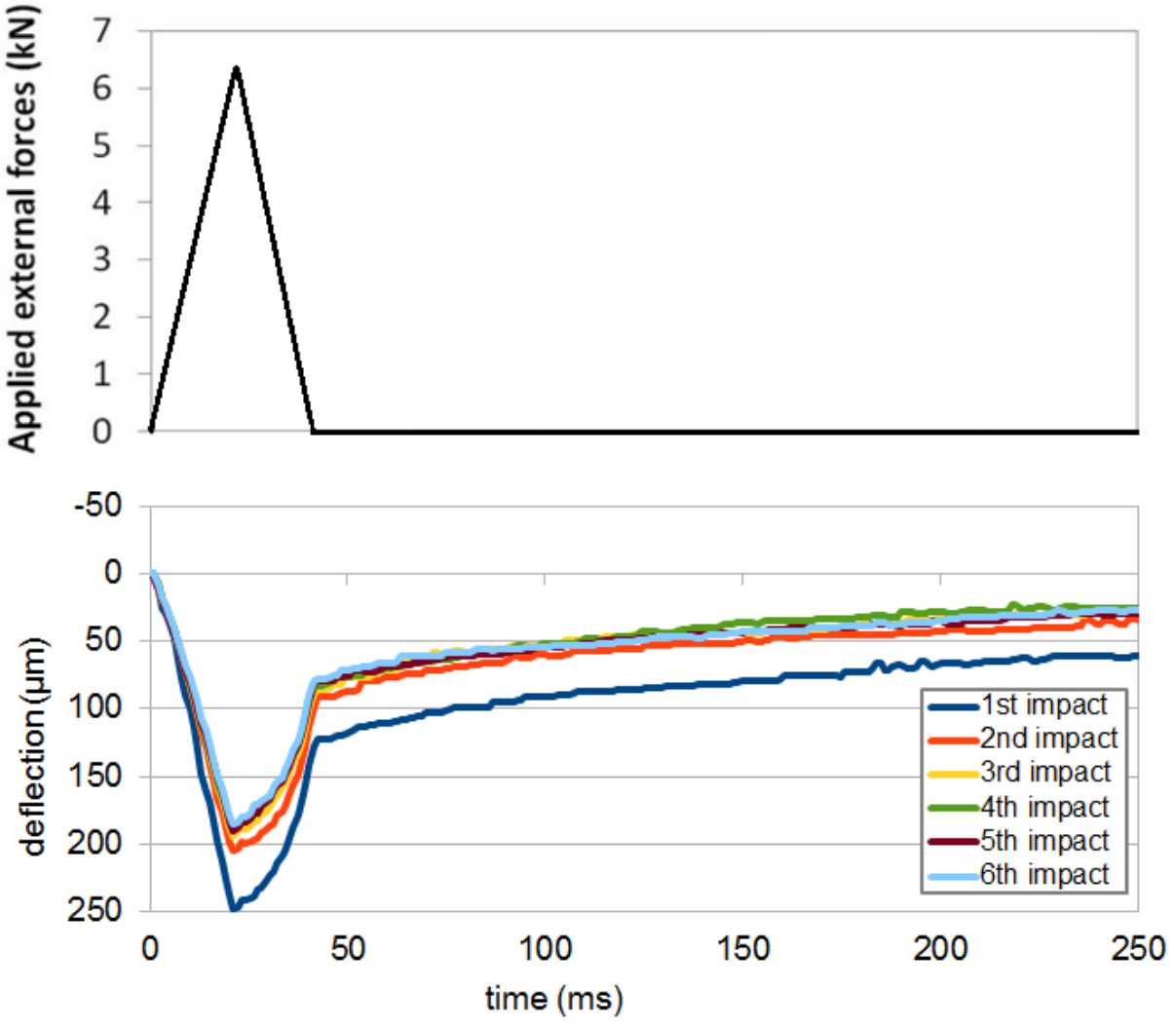

Figure 56: Data from an LWD model test using Moisture Model III and the DEM mixture representing the Class 5 mixture described in Section 3.1. The temporal dependence of the LWD loading history and the plate deflection are shown during a series of consecutive impacts for a system with equivalent model suction of 114 kPa, and an interparticle friction coefficient of 0.2.

7.2.2 LWD Model Test Results Using Moisture Model III: Trimodal Mixture

Figure 57 shows that, independent of the friction coefficient, peak LWD deflection increases with decreasing equivalent model suction. According to Moisture Model II which employs only the explicit composition model by Gupta and colleagues [33], this corresponds to an increase in peak deflection with increasing moisture content. In other words, the bulk (and correspondingly effective bulk modulus decreases) with increasing moisture content with this model, consistent, qualitatively, with the results of the explicit composition moisture model (Chapter 6) and the target value trends in Ref. [4].

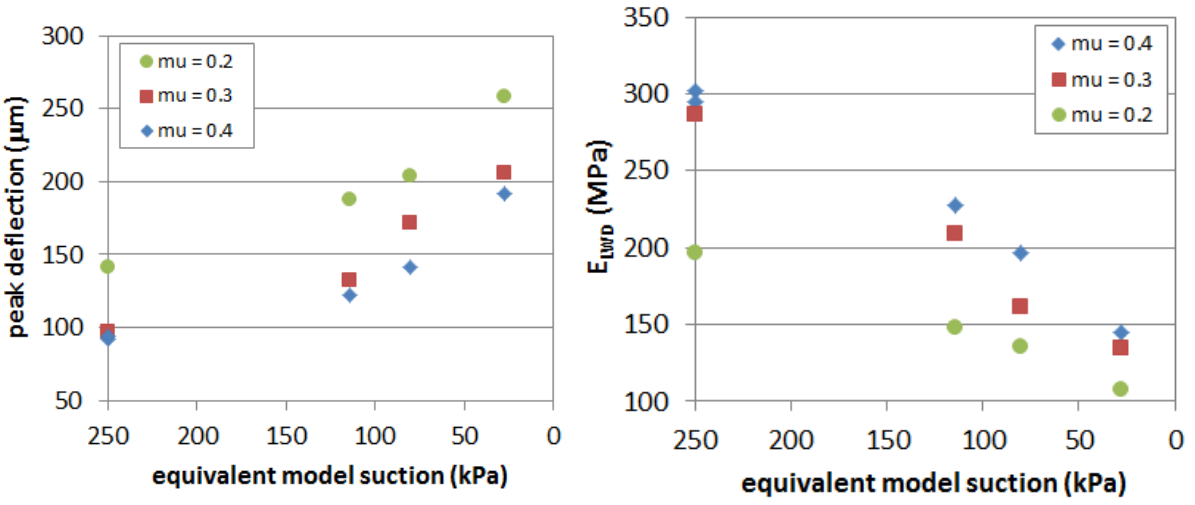

Figure 57: Results from simulations using Moisture Model III and the DEM mixture representing the Class 5 mixture described in Section 3.1 undergoing the LWD test. These plots show the dependence of the LWD results plotted as a function of equivalent model suction, which we correlate inversely with increasing moisture content. (left) Average peak deflection plotted as a function of equivalent model suction. (right) Effective bulk modulus calculated from data shown in the plot to the left. Equivalent model suction is plotted increasing from right to left, to reflect increasing moisture content from left to right.

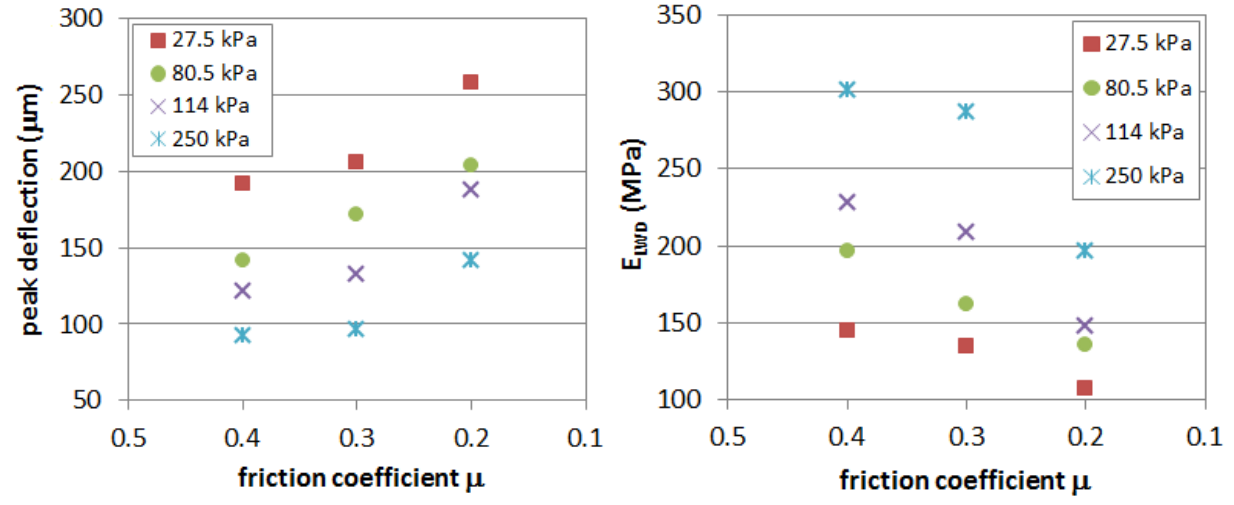

Figure 58: Data from LWD tests using Moisture Model III and the DEM mixture representing the Class 5 mixture described in Section 3.1. Average peak deflection (left) as a function of friction coefficient, and the corresponding effective bulk modulus (right). Friction coefficient is plotted increasing from right to left, to reflect increasing fines content from left to right.

Figure 58 shows the same data as in Figure 57, but plotted as a function of friction coefficient. As mentioned, we hypothesize that the friction coefficient should decrease with increasing fines content. Therefore, in the plots, the friction coefficient is plotted decreasing from left to right to

reflect increasing fines content from left to right. Deflection increases (and correspondingly effective bulk modulus decreases) with decreasing friction coefficient - implicitly, increasing fines content - for all five values of equivalent model suction. These results are consistent with physical observations that indicate deflection increases with increasing fines content, independent of moisture content plotted in Figure 6 from Ref. [4].

These results from Model III are very promising but need a more direct link between model parameters "friction" and "effective bulk modulus" and the corresponding physical parameters *GN* and moisture content. We will describe this after discussing the DCP results.

7.3 DCP Model Test Results Using Moisture Model III

7.3.1 DCP Preparation Results Using Moisture Model III

As with the previous two moisture models, the initialization stage where dry particles are dropped (details in Section 4.3.1) into a cylinder is used as the base for all simulations with the same particle size distribution. We are more concerned with the stages in the simulation that have moisture added.

Figure 59 shows the vertical position of the base of the disc representing the surcharge load (see Section 4.3.2) during compaction, and the resulting solid fraction, of a mixture with equivalent model suction of 114 kPa and interparticle friction coefficient 0.2. We found that generally six impacts provided sufficient compaction for good results, so the compaction process was stopped after six impacts.

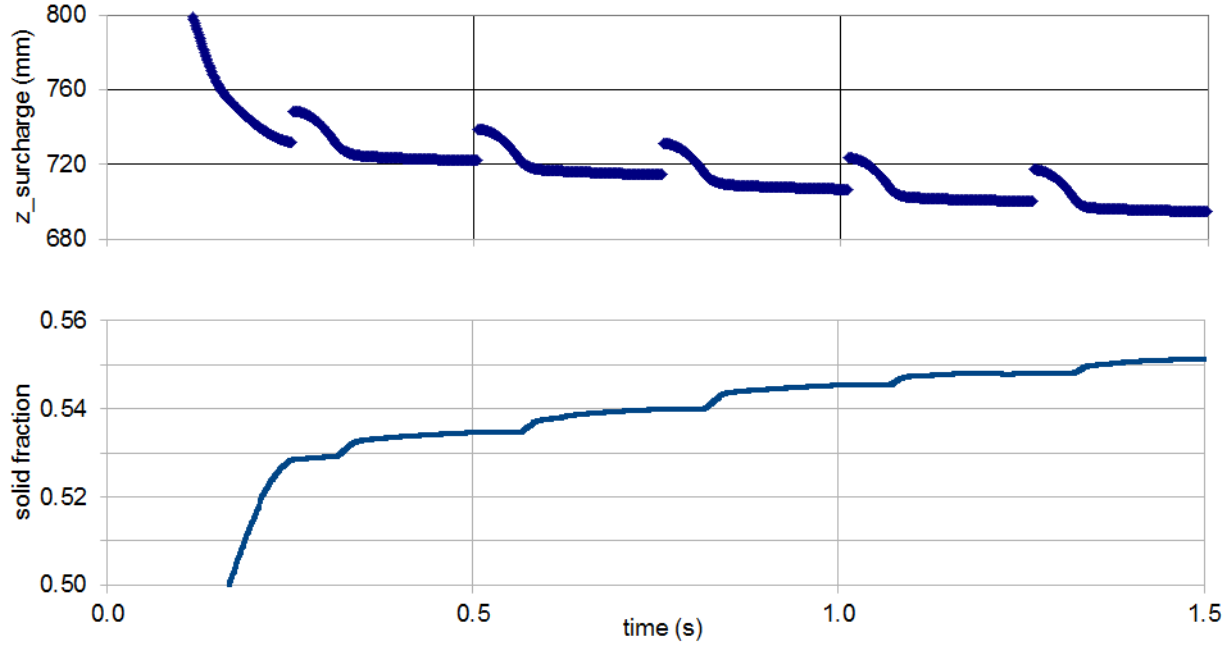

Figure 59: Data from compaction for a DCP model test using Moisture Model III and the DEM mixture representing the Class 5 mixture described in Section 3.1. Surcharge position and solid fraction during compaction for a system with equivalent model suction of 114 kPa, and an interparticle friction coefficient of 0.2.

After allowing the system and surcharge to settle, the cone-rod assembly (see Section 4.3.3) was added with the cone-tip positioned at the vertical height of the base of the surcharge. The cone-rod assembly was then allowed to penetrate the granular mixture under its own weight. The vertical position of the cone-tip is shown in Figure 60, for the same mixture as in Figure 59.

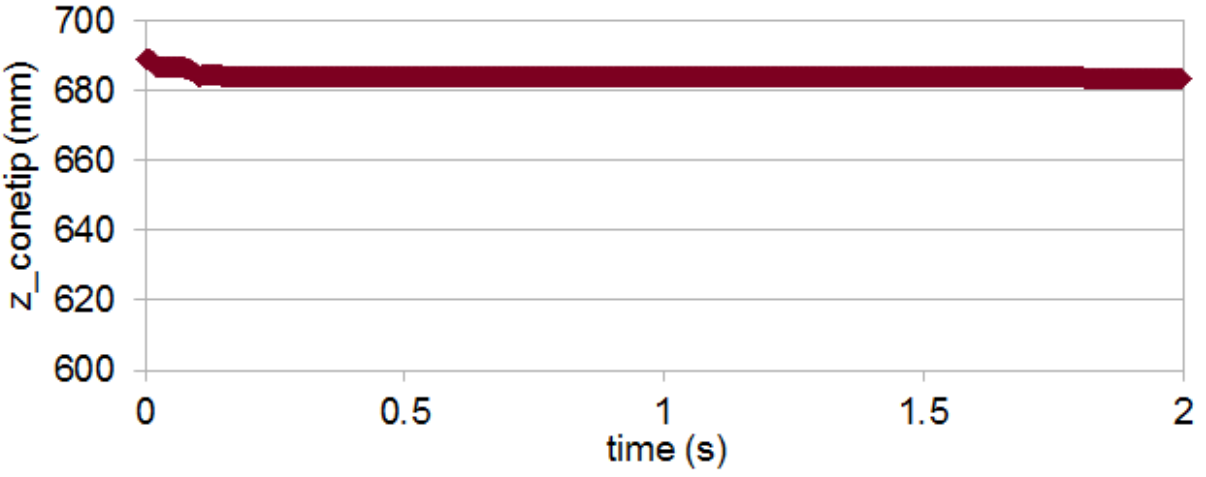

Figure 60: Data from model DCP test preparation using Moisture Model III and the DEM mixture representing the Class 5 mixture described in Section 3.1. Position of cone-tip (base of cone-rod assembly) is plotted as a function of time during initial placement for a system with equivalent model suction of 114 kPa, and an interparticle friction coefficient of 0.2.

Once the cone-rod assembly has reached a steady state, a series of loading impacts (see Section 4.3.4) corresponding to the falling hammer in the DCP test is applied. The vertical position of the cone-tip is tracked through these impacts, as shown in Figure 61. The DPI is calculated as the average penetration of the five consecutive hammer blows.

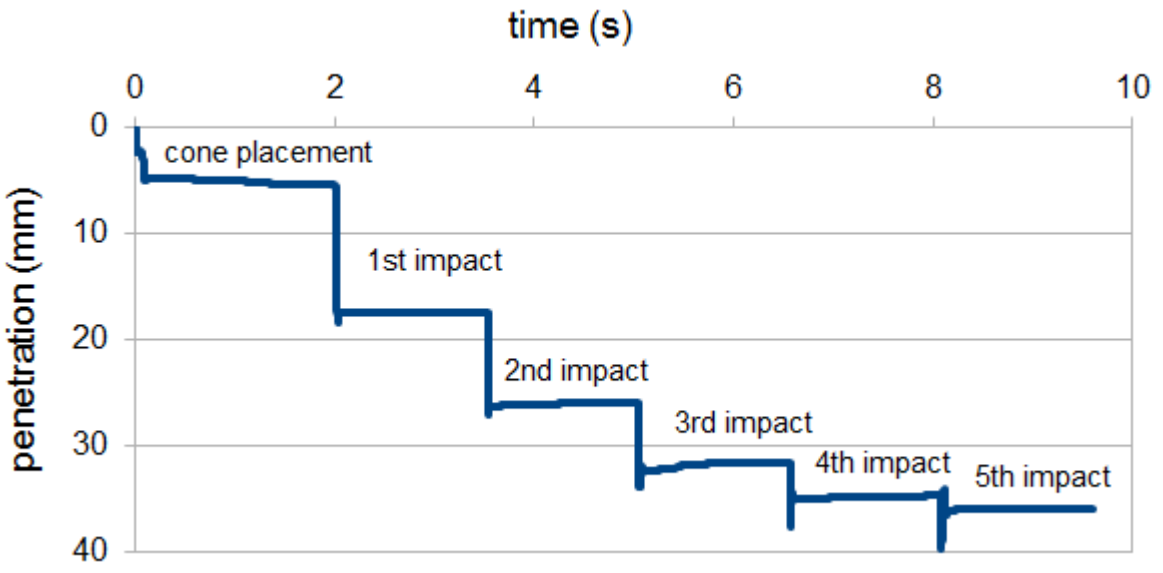

Figure 61: Data from a DCP model test using Moisture Model III and the DEM mixture representing the Class 5 mixture described in Section 3.1. DCP penetration during including initial placement and consecutive hammer blows for a system with equivalent model suction of 114 kPa, and an interparticle friction coefficient of 0.2.

7.3.2 DCP Model Test Results Using Moisture Model III: Trimodal Mixture

Figure 62 (left) shows that, independent of the friction coefficient, the average penetration per blow increases with decreasing equivalent model suction. We recall that according to Moisture Model II which employs only the explicit composition model by Gupta and colleagues [33], this corresponds to an increase in the average penetration per blow with increasing moisture content. In other words, the deflection increases (and correspondingly strength decreases) with increasing moisture content with this model, consistent, qualitatively, with the results of the explicit composition moisture model (Chapter 6) and the trends of the estimated target value in Ref. [4].

Figure 62 (right) shows the same data as in Figure 62 (left), but plotted as a function of friction coefficient. As mentioned, we hypothesize that the friction coefficient should decrease with increasing fines content. Therefore, in the plots, the friction coefficient is plotted decreasing from left to right to reflect increasing fines content from left to right. The average penetration per blow increases (and correspondingly strength decreases) with decreasing friction coefficient - implicitly, increasing fines content - for all five values of equivalent model suction. These results are consistent with trends of the estimated target valuethat indicate the average penetration per blow increases with increasing fines content, independent of moisture content plotted in Figure 6 from Ref. [4].

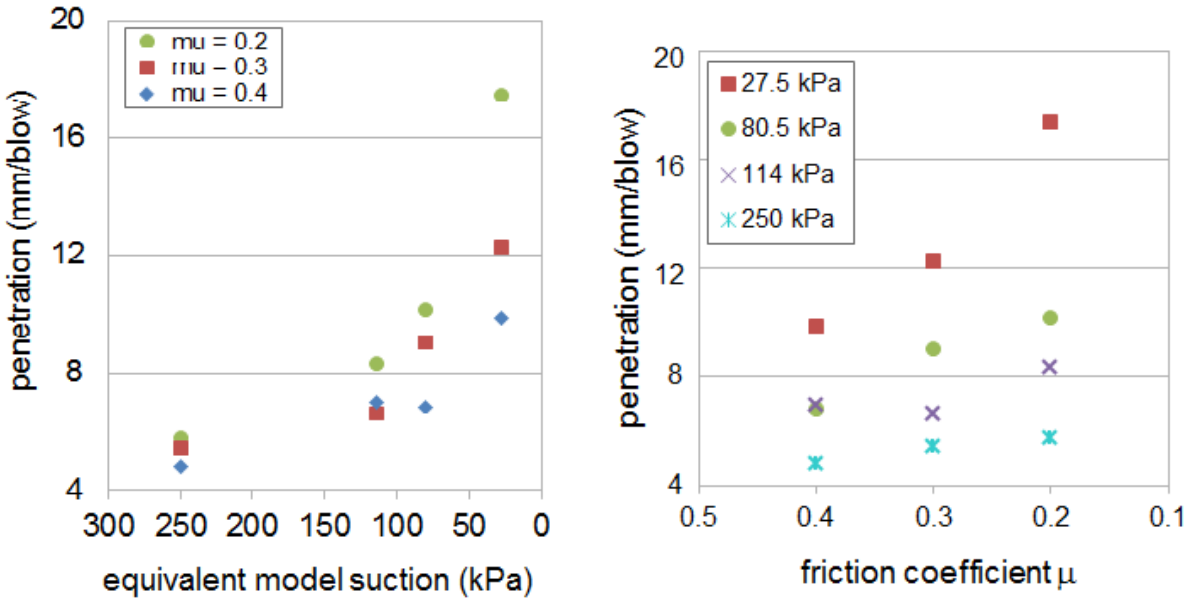

Figure 62: Data from DCP model tests using Moisture Model III and the DEM mixture representing the Class 5 mixture described in Section 3.1. Average penetration per blow is plotted as a function of equivalent model suction (left). Equivalent model suction is plotted increasing from right to left to reflect increasing moisture content. Average penetration per blow is plotted as a function of friction coefficient (right). Friction coefficient is plotted increasing from right to left, to reflect increasing fines content from left to right.

7.4 Discussion: Results from Moisture Model III

Modeling moisture content through attractive force $F_{m(f)}$ and fines content through friction coefficient $\mu_{m(f)}$ in conjunction achieves similar trends with increasing moisture and fines content as that shown in the estimated target values. This indicates Model III may be effectively used to model the response of a granular material to different types of applied stresses for these systems as the response varies with fines and moisture content. However as of now there is no explicit relationship between friction coefficient and fines content. Also the current translation between suction obtained from the explicit composition model and the equivalent model suction is not necessarily entirely appropriate. In the next sections, we describe the derivation of relationships between our DEM results and the results of Siekmeier et al. [4] as well as fitted relationship between model parameters (friction coefficient and model suction) and physical parameters (fines content and moisture content).

Chapter 8 Translation between Simulation Results & Target Values

In this section, we describe how we derive a translation between the experiment-based target values of Siekmeier et al. [4] and our simulation results using the moisture model III. To do so, we follow three steps: (1) We first obtain general expressions for the deflection (for the LWD test) or penetration (for the DCP test) in terms of the two independent input parameters (moisture content and grading number for the physical results; model suction and friction coefficient for the simulation results); (2) Then after defining the region in which the two sets of results overlap, we compare the expressions for the physical and computational results, and from this (3) We determine a) the transformation needed for the simulation results to be comparable to the physical results and b) translations between each set of independent parameters.

8.1 Translation Steps Taken with the LWD Model Test Data

Figure 63 shows the target deflection values for the LWD test for different gravimetric moisture contents ($5 \leq \omega_g \leq 11\%$) and a range of grading numbers ($3 \leq GN \leq 6$). We applied least-squares best fit lines have been applied to the data, and include the equations (with the coefficient of determination R^2 denoting goodness of fit) a in the plot. The deflection appears to vary linearly in terms of both moisture content and grading number, and so a general expression for deflection would be a linear combination of these two parameters, i.e. of the form $a_1 + b_1(GN) + c_2(\omega_g)$.

By minimizing the square of the error between the actual data and the fit prediction, this general expression for the target deflection Δ_{expt} is:

$$\Delta_{expt} = 122 + 100\,(GN - 3) + 46.3\,(\omega_g - 5). \tag{23}$$

The corresponding LWD simulation results are shown in Figs. 57 and 58. Again we consider the deflections, and we note straightaway that it is not a simple linear function of either of the two parameters (model suction $\tau_{DEM,eq}$ and friction coefficient μ). Some trial and error reveals that within this small amount of data, the deflection appears to vary linearly with $ln(1/\tau_{DEM,eq})$ and $1/\mu^2$, as shown in Figure 64. We can then expect a general expression of the form $a_2 + b_2(1/\mu^2) + c_2 ln(1/\tau_{DEM,eq})$.

Using a least-squares fit again, the general expression for the deflection obtained from the simulations, Δ_{DEM}, is:

$$\Delta_{DEM} = 340 + 3.25(1/\mu^2) + 49.8 ln(1/\tau_{DEM,eq}) \tag{24}$$

We use these relationships to determine relationships between the simulation parameters and associated results and the corresponding estimated target value. Since the model parameters corresponding to moisture and fine particles are not quantitatively mechanistically linked to their physical counterparts, the measured results in the model (i.e., LWD deflection and DCP penetration) should not necessarily be equal to the estimated target values.

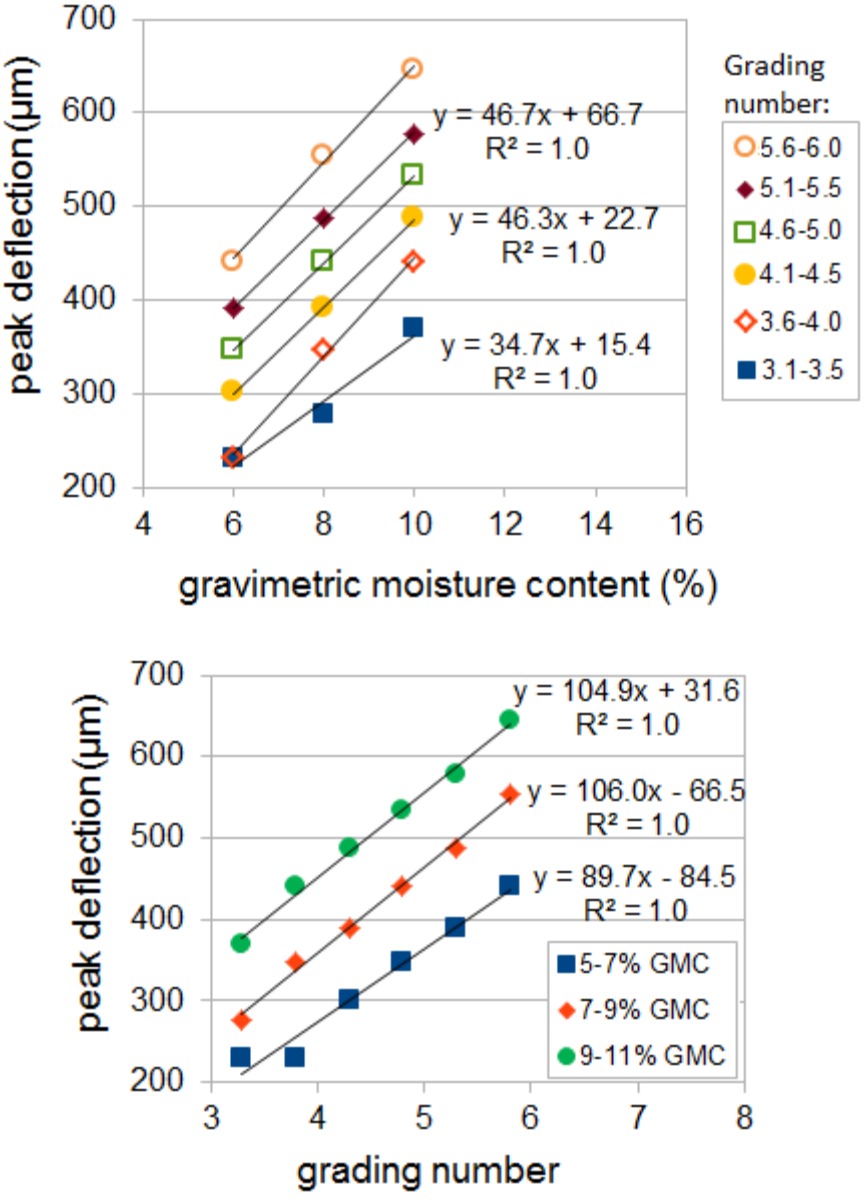

Figure 63: Target deflection values for LWD test plotted as a function of gravimetric moisture content (top), and grading number (bottom). These values were back-calculated from the bulk modulus values given in Siekmeier et al.[4] using Eq. 3. Some trendline equations are shown to provide an idea of the variation and goodness of the fits.

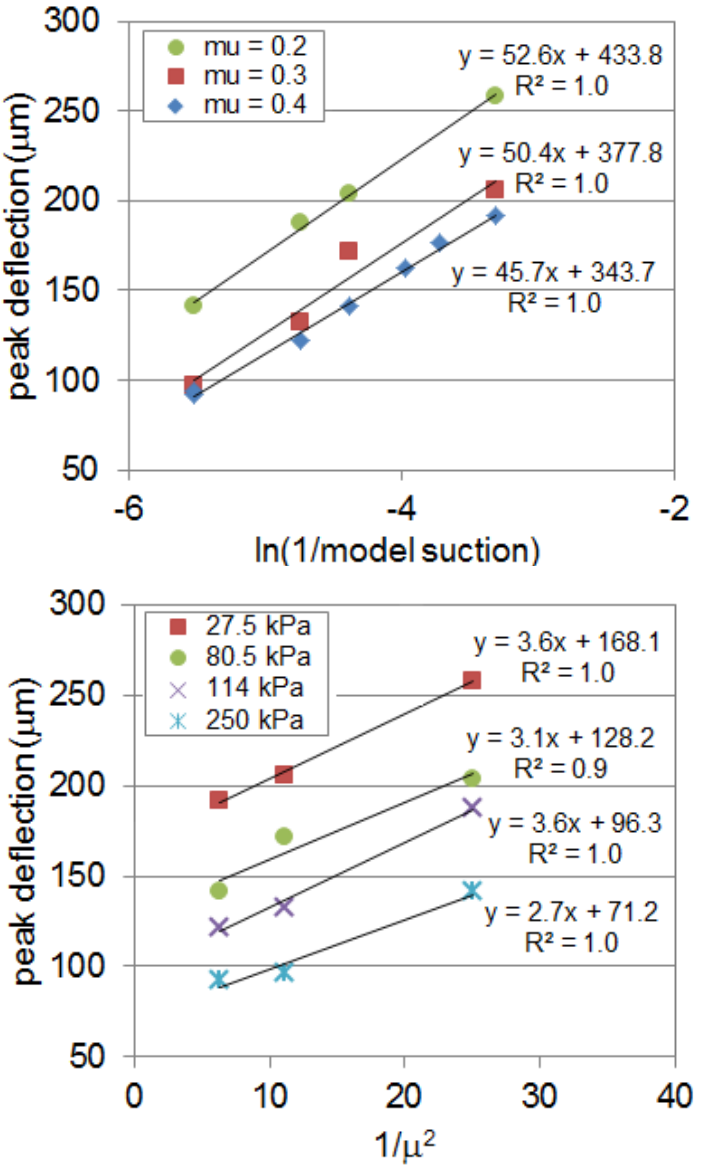

Figure 64: Linear fits for deflection results obtained from LWD simulation tests, in terms of functions of the DEM model suction (top) and interparticle friction coefficient (bottom). We base the calculations on a few approximations detailed in the text.

Considering this choice of overlap region, the lowest model deflection obtained for $\tau_{DEM,eq}$ = 250 kPa and μ = 0.4 would then correspond to the physical value for ω_g=6% and *GN*=3.3, and the largest simulation deflection obtained for $\tau_{DEM,eq}$ = 27.5 kPa and μ = 0.2 would then correspond to the physical value for ω_g=10% and *GN*=4.3. This then leads to the transformation between physical LWD deflection Δ_{expt} and simulation LWD deflection Δ_{DEM}:

$$\Delta_{expt} \approx \Delta^{*}_{DEM} = 2.1\Delta_{DEM}. \quad (25)$$

Then, we perform an iterative process to derive the relationship between the two sets of parameters: (1) "model moisture" in the LWD test (model stress) and physical moisture and (2) "model *GN*" in the LWD model test (model friction coefficient) and physical *GN*.

1. We start by substituting initial "guesses" for corresponding values of ω_g and $\tau_{DEM,eq}$ into Eqs. 23, 24 and 25. Somewhat arbitrarily, we choose $\omega_g = 6\%$ and $\tau_{DEM,eq} = 250$ kPa. We solve the resulting equation to obtain an approximate relationship between *GN* and μ.
2. We substitute μ=0.2 into this expression for *GN* as a function of μ to obtain a trial value for *GN*.
3. We substitute this pair of μ and *GN* values into Eqs. 23, 24 and 25 to obtain an approximate relationship between ω_g and $\tau_{DEM,eq}$.
4. We substitute $\tau_{DEM,eq} = 250\ kg$ into this expression to obtain a new value for the corresponding value of ω_g. If the new value of ω_g is close enough to that from step 1, we consider our work to be done. The relationship between μ and *GN* from step 1 is final and the relationship for ω_g and $\tau_{DEM,eq}$ from step 3 is final.
5. If the new value of ω_g is not close enough to that from step 1, we use this pair of $\tau_{DEM,eq}$ and ω_g values to repeat steps 1-4. We keep repeating until convergence is obtained.

When we followed this procedure for the LWD model results described in Section 7.2 we found the relationship that emerged between *GN* and μ is:

$$GN \approx 2.67 + \frac{0.0683}{\mu^2}, \quad (26)$$

or equivalently,

$$\mu \approx \sqrt{\frac{0.0683}{GN - 2.67}}. \quad (27)$$

We found the relationship that emerged between gravimetric moisture content (%) and model suction (kPa) is:

$$\omega_g \approx 18.5 + 2.26ln\left(1/\tau_{DEM,eq}\right) \quad (28)$$

or

$$\tau_{DEM,eq} \approx exp\left(\frac{18.5 - \omega_g}{2.26}\right). \quad (29)$$

where the gravimetric moisture content ω_g is a percentage value and the model suction $\tau_{DEM,eq}$ has units of kPa.

We used these equations to calculate the effective values of *GN* and ω_g corresponding to the parameters we chose for the LWD simulations we performed. These are presented in Tables 6 and 7.

Table 6: Values of grading number *GN* corresponding to friction coefficient μ, according to Eq. 26, for the LWD simulation test.

μ	0.2	0.3	0.4
GN	4.38	3.43	3.10

Table 7: Values of gravimetric moisture content ω_g corresponding to model suction $\tau_{DEM,eq}$, according to Eq. 28, for the LWD simulation test.

$\tau_{DEM,eq}$ (kPa)	27.5	80.5	114	250
ω_g (%)	11.0	8.58	7.80	6.02

The model LWD test results are presented in terms of all translated values in Figure 65. When we compare these results to those for the lower *GN*'s from estimated target values from Ref. [4] presented in Figs. 5 and 6, we find the translated model results are comparable.

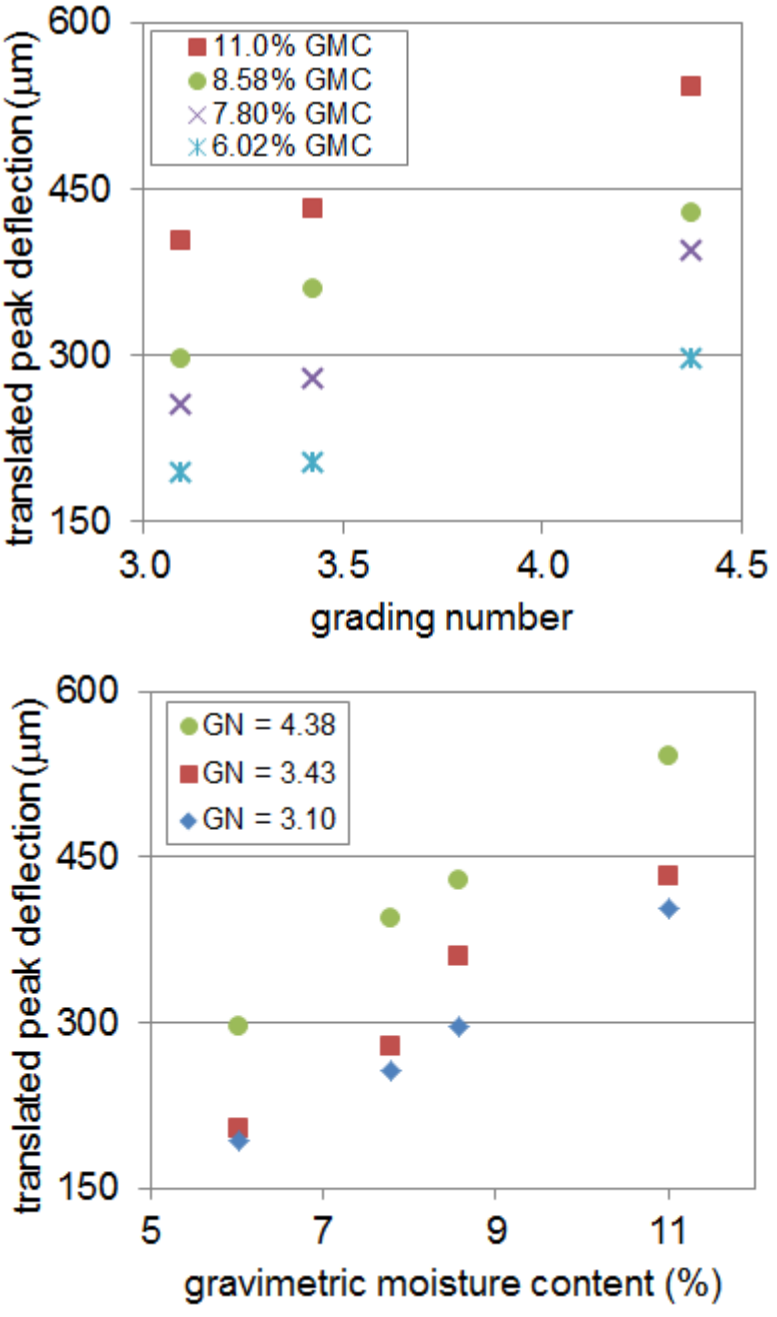

Figure 65: LWD model test results in terms of all translated parameters according to Equations 25, 26, and 29.

8.2 Translation Steps Taken with the LWD Model Test Data

Figure 66 shows the target penetration values for the DCP test for different gravimetric moisture contents ($5 \leq \omega_g \leq 11\%$) and a range of grading numbers ($3 \leq GN \leq 6$). Least-squares best fit lines have been applied to the data, and equations (with the coefficient of determination R^2 denoting goodness of fit) are also plotted. The penetration appears to vary linearly in terms of both moisture

content and grading number, and so a general expression would be a linear combination of these two parameters, i.e. of the form $a_3+b_3\ (GN)+c_3\ (\omega_g)$.

By minimizing the square of the error between the actual data and the fit prediction, this general expression for the target penetration (DPI_{expt}) is:

$$DPI_{expt}=5.22+4.34\ (GN-3)+2.02\ (\omega_g-5). \tag{30}$$

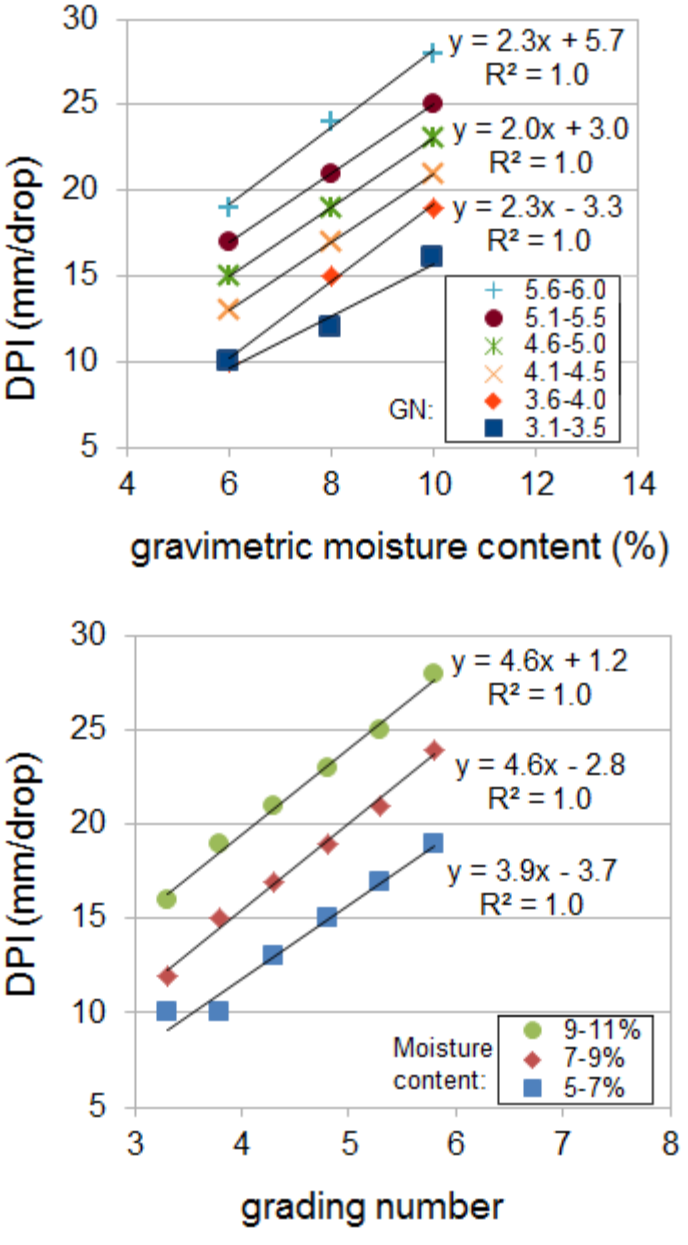

Figure 66: Target DPI values for DCP test as a function of gravimetric moisture content (top), and grading number (bottom), given in Siekmeier et al. [4]. Some trendlines' equations are shown to provide an idea of the variation and goodness of the fits.

The corresponding DCP simulation results were shown earlier in Figure Figure 62. We note immediately that the average penetration per blow is not a simple linear function of either of the two parameters (model suction $\tau_{DEM,eq}$ and friction coefficient μ). Figure 67 shows the data plotted as functions of $1/\mu^2$ and $\ln(1/\tau_{DEM,eq})$ and the corresponding best-fit linear expressions, similar to what was done with the LWD simulation results in Figure 64.

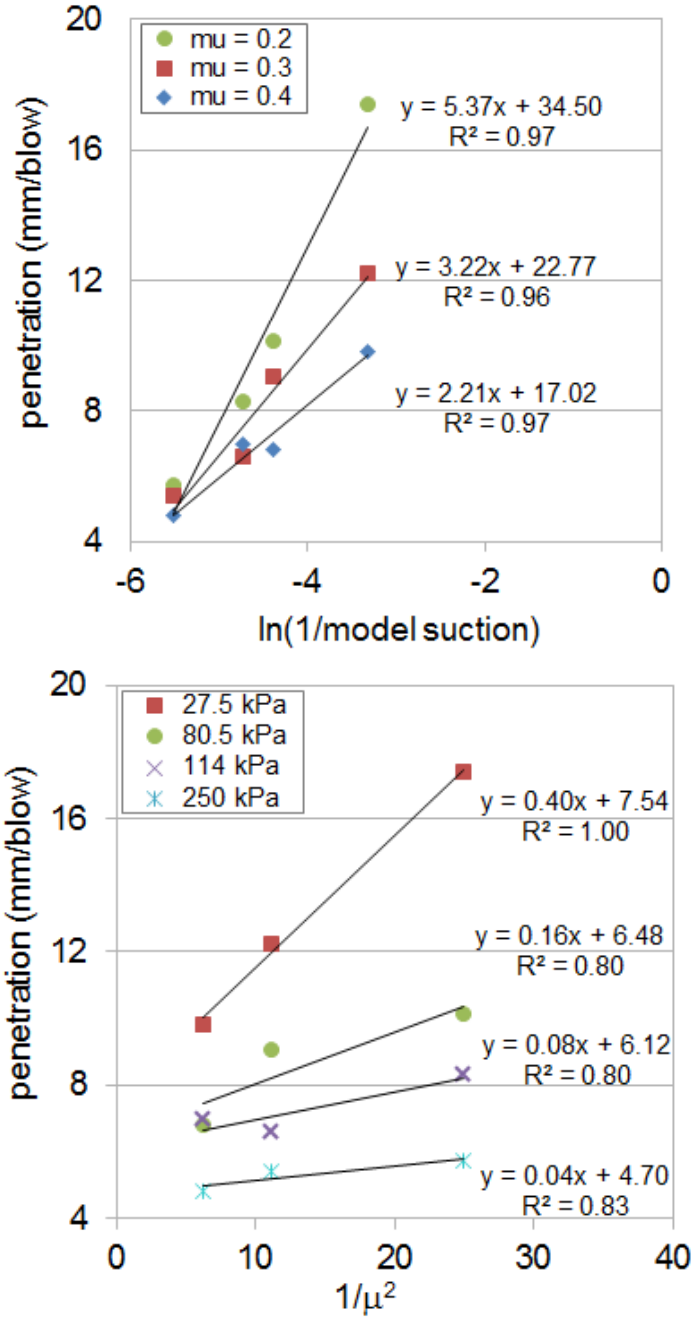

Figure 67: Linear fit for average penetration per blow obtained from DCP simulation tests, in terms of functions of the DEM model suction (top) and interparticle friction coefficient (bottom).

However unlike with the LWD results, the best-fit lines do not have similar slopes. Thus a linear combination for the DCP results of the form $a_4 + b_4(1/\mu^2) + c_4 ln(1/\tau_{DEM,eq})$ will not match all the data very well if the coefficients a_4, b_4 and c_4 are all constants.

Instead if we allow b_4 to vary with model suction, this could account for the varying slopes in Figure 67. In fact, the data is well-fit by the expression:

$$DPI_{DEM} = 12.4 + (10.6/\tau_{DEM,eq})(1/\mu^2) + 1.36 ln(1/\tau_{DEM,eq}) \quad (31)$$

plotted in Figure 68 as dashed lines. The values of the coefficients were found by minimising the square of the difference between the simulation results and the corresponding fit value from Eqn. 31.

Now that we have similar forms fitting both the estimated DPI target values and the average penetration per blow from the numerical simulations, and assuming that the simulation results correspond to the physical data obtained from the lower three grading number ranges (the same overlap region as defined for the LWD computational-physical results translation), we can relate the two sets of results using:

$$DPI_{expt} \approx DPI_{DEM} = DPI_{DEM} + 5 \quad (32)$$

Next, assuming that the friction coefficient varies only as a function of grading number, and that model suction varies only as a function of moisture content, we can obtain relationships between the independent parameters in the experiments and simulations. Using the same logic as for the LWD results we perform a similar iterative process:

1. We start by substituting initial "guesses" for corresponding values of ω_g and $\tau_{DEM,eq}$ kPa into Eqs. 30, 31 and 32. Somewhat arbitrarily, we chose ω_g=6% and $\tau_{DEM,eq}$=250 kPa. We solve the resulting equation to obtain an approximate relationship between *GN* and μ.
2. We substitute μ=0.2 into this expression to obtain a trial value for *GN*.
3. We substitute this pair of μ and *GN* values into Eqs. 30, 31 and 32 to obtain a relationship between ω_g and $\tau_{DEM,eq}$.
4. We substitute $\tau_{DEM,eq}$=250 into this expression to obtain a new value for the corresponding value of ω_g. If the new value of ω_g is close enough to that from step 1, we consider our work to be done. The relationship between μ and *GN* from step 1 is final and the relationship for ω_g and $\tau_{DEM,eq}$ from step 3 is final.
5. If the new value of ω_g is not close enough to that from step 1, we use this pair of $\tau_{DEM,eq}$ and ω_g values to repeat steps 1-4. We keep repeating until convergence is obtained.

When we followed this procedure for the LWD model results, we found the relationship that emerged between *GN* and μ is:

$$GN \approx 3.61 + \frac{0.00977}{\mu^2}, \tag{33}$$

or equivalently,

$$\mu \approx \sqrt{\frac{0.00977}{GN - 3.61}}. \tag{34}$$

For the other pair of parameters, we obtain the relationship (implicit in terms of model suction):

$$\omega_g = 9.20 + \left(131/\tau_{DEM,eq}\right) + 0.673ln\left(1/\tau_{DEM,eq}\right) \tag{35}$$

where the gravimetric moisture content ω_g is a percentage value and the model suction $\tau_{DEM,eq}$ has units of kPa.

We used these equations to calculate the effective values of *GN* and ω_g corresponding to the parameters we chose for the LWD simulations we performed. These are presented in Tables 8 and 9.

Table 8: Values of grading number *GN* corresponding to friction coefficient μ, according to Eq. 33, for the DcP simulation test.

μ	0.2	0.3	0.4
GN	3.85	3.72	3.67

Table 9: Values of gravimetric moisture content ω_g corresponding to model suction $\tau_{DEM,eq}$, according to Eq. 35, for the DCP simulation test.

$\tau_{DEM,eq}$ (kPa)	27.5	80.5	114	250
ω_g (%)	11.7	7.87	7.16	6.01

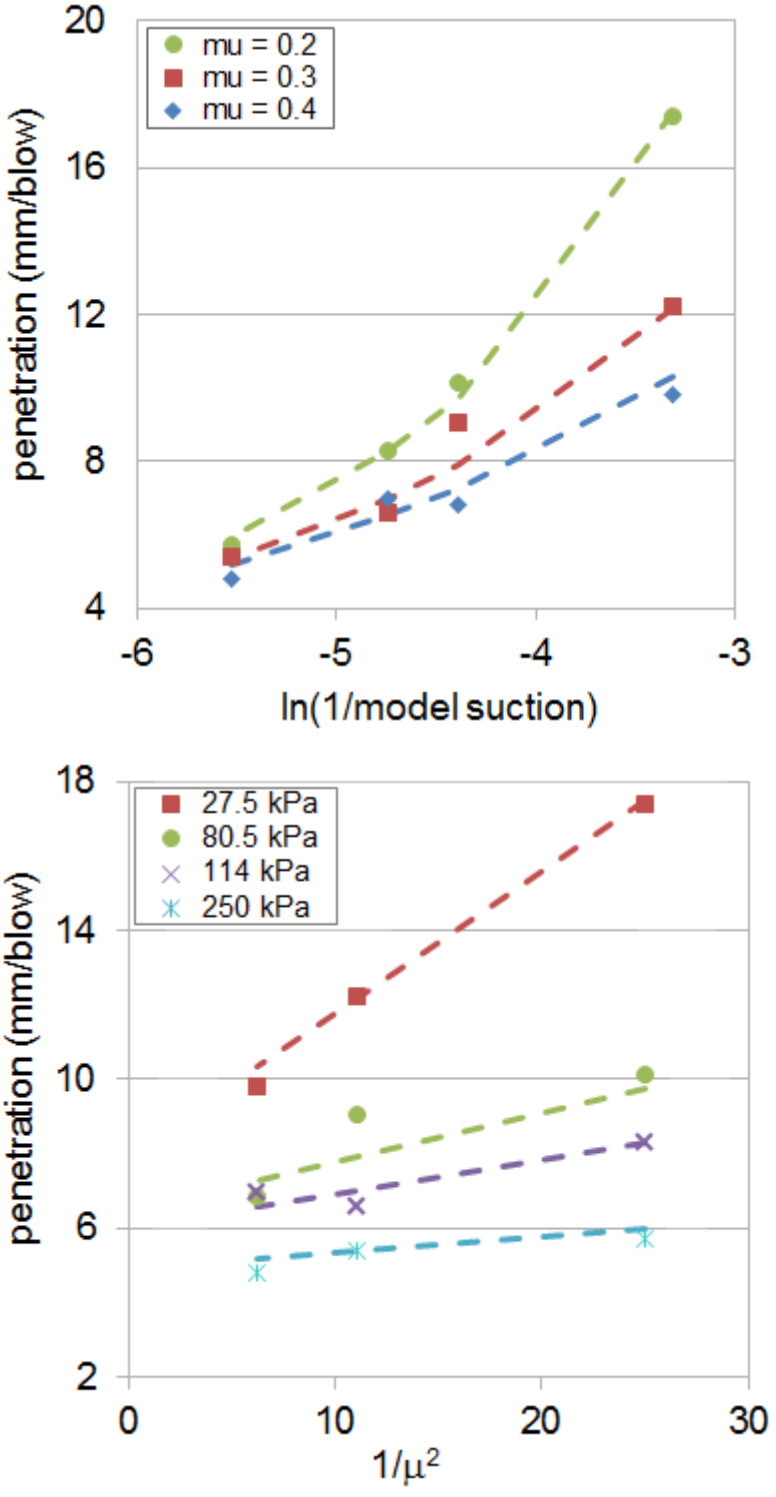

Figure 68: Average penetration per blow obtained from DCP simulation tests (symbols), and the least-squares best-fit (dashed lines) from Eq. 31 in terms of functions of the DEM model suction (top) and interparticle friction coefficient (bottom).

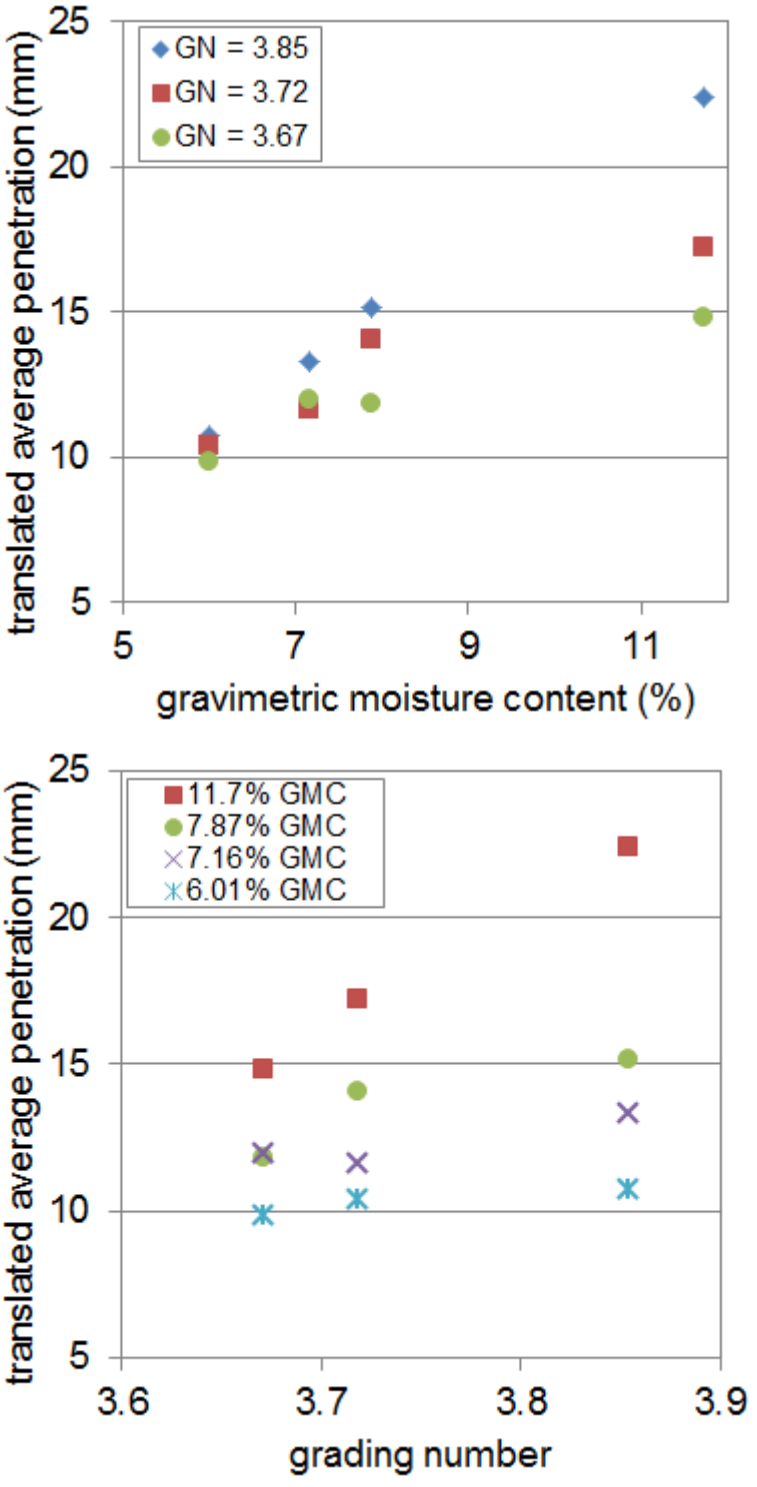

Figure 69: DCP model test results in terms of all translated parameters according to Equations 32, 33, and 35.

8.3 Discussion of Translation: Some Strengths and Limitations of the First-Order Model

We were able to fit the estimated target value data and DEM simulation results for both the LWD and DCP tests with a linear combination of functions of the parameters relating to fines and moisture content. For the estimated target value data, expressions for the deflection and penetration were of the form $a+b\ (GN)+c\ (\omega_g)$. For the numerical simulations, the expressions had the general form $a+b\ (1/\mu^2)+c\ \ln(1/\tau_{DEM,eq})$. The coefficients were determined using a least-squares method, such that the sum of the squared-differences between the estimated target value data and fit expressions were minimized.

For both the estimated target value data and the LWD simulation results, the coefficients were all constants. However for the DCP simulation results, the second coefficient *b* was allowed to vary as a function of model suction $\tau_{DEM,eq}$. Intuitively we expect that the expressions for both the LWD and DCP simulation results would be similar; but ultimately both tests involve different characteristics of the bulk material and so their results could have some correlation but are not likely to be identical.

In order to establish a relationship between the estimated target value and simulation fits, we first assumed that the simulation results corresponded to the full range of moisture content involved in the estimated target values (5-11%), but only the lower grading numbers (3-4.5). This is not unreasonable as the DEM simulations only modeled coarse particles explicitly, and relatively large values of the friction coefficient μ (loosely used to model fines content) were used, which would likely correspond to small amounts of fine particles.

Another major assumption used to obtain direct relationships between the respective fines and moisture content parameters, was that the simulation parameters (friction coefficient μ and model suction $\tau_{DEM,eq}$) are functions of only one physical parameter each (grading number *GN* and moisture content ω_g respectively), instead of depending on both parameters. Intuitively we know that a dependence on both fines and moisture content is physically more correct, but explicit knowledge of this relationship is not available. Although investigation in this direction would be very interesting, it is however outside the scope of this project.

Chapter 9 PFC3D Macro Development and Simulations

For a commercially supported and maintained version of the models developed in this report, we translated the DEMP-3D code as closely as possible into PFC3D, a commercial DEM software produced by Itasca Consulting Group. Specifically, we wrote a pair of macros for both the LWD and DCP tests, which a user can readily run in PFC3D. The codes have the capability of incorporating any of the three models we described earlier in the report moisture and fines content.

In this last section before the summary of this report, we describe the work done toward developing these macros. We first outline the integral parts of the DEMP-3D test simulations that were implemented into PFC3D and highlight required input parameters specific to the moisture model. Next we describe the general procedure of each of the simulated tests. Finally we compare the results from the DEMP-3D and PFC3D versions of the tests. A user's guide for each of the tests, as well as technical documentation from PFC3D specifically regarding the adaptation of the DEMP-3D contact model into PFC3D, is included in the appendices.

9.1 Validation Test Conditions

To compare the results from the LWD and DCP test simulations performed using the original DEMP-3D model run in fortran and the version translated into the macros of PFC3D, the trimodal mixture described in Section 3.1 was used. Table 2 outlines the particle size distribution of this trimodal mixture, which was chosen based on the size distribution of Class 5 aggregate soils specified by the Minnesota Department of Transportation as appropriate for aggregate bases in pavement systems (see Table 1).

As for the DEMP-3D model results, in the PFC3D simulations described in this report the coarse particles are represented by spheres and assigned the material properties of granite; components making up the LWD/DCP are assigned the material properties of steel. These material properties are listed in Table 10.

Table 10: Material properties of granite and steel: elastic modulus E, Poisson's ratio ν, and density ρ. The friction of coefficient μ for granite-granite interactions is 0.4, and 0.3 for granite-steel interactions.

material	E (GPa)	ν	ρ (kg/m^3)
granite	29	0.15	2650
steel	210	0.3	7850

Finally, Tables 11 and 12 list the different test conditions for the LWD and DCP simulations that were used to provide a comparison between DEMP-3D and PFC3D simulations. To summarize: the same initial configurations (size distribution and arrangement of particles, and cylinder size) were used for both DEMP-3D and PFC3D, each with three different moisture contents applied.

The moisture contents were chosen arbitrarily within the range of moisture levels typically found in Minnesota bases.

Table 11: LWD simulation test conditions for comparison between DEMP-3D and PFC3D used in this report.

Test No.	#particles	cylinder dia.	plate dia.	grav. moisture content
1	14662	260 mm	200 mm	0 %
2	14662	260 mm	200 mm	5 %
3	14662	260 mm	200 mm	8 %

Table 12: DCP simulation test conditions for comparison between DEMP-3D and PFC3D used in this report.

Test No.	#particles	cylinder dia.	surcharge	grav. moisture content
1	17476	150 mm	600 mm	0 %
2	17476	150 mm	600 mm	6 %
3	17476	150 mm	600 mm	12 %

9.2 Adaptations for PFC3D macros

PFC3D, as a commerical discrete element method software, has many of the required functions. Thus essentially only two items need to be translated from the DEMP-3D code into PFC3D: the contact model which governs the relationship between the particles' positions and velocities into the forces they experience, and the boundary conditions specific to the LWD and DCP tests.

The contact model in DEMP-3D is based on Hertz-Mindlin contact theory, with the normal and tangential forces between a pair of particles in contact defined in Chapter 4 of this document.

PFC3D does have an existing similar Hertz-Mindlin contact model. However, the user typically must simply specify the values of the coefficents. In DEMP-3D, instead of having specified constant values, the stiffness and damping coefficients used to calculate the contact forces depend on the material properties of the contacting particles. These relationships are detailed in Appendix A of this document. For this project, the relationship between the particle contact model and particle properties such as the interparticle friction coefficient, the values of Young's modulus, Poisson's ratio, density and friction for both the particles and cylinders, discs etc. had be specified within the new macros for PFC3D.

In addition to the relationships between material properties and model stiffness and damping coefficients, the DEMP-3D contact model also differs from PFC3D in the addition of the moisture force F_m. For a moisture model in PFC3D, we adapt the details of the established liquid bridge

theory, specifically, that the moisture force is at a maximum when particles are in contact, and decreases as the particles are separated. Eventually when the particles are separated over a critical distance, the moisture (liquid bridge) connecting them together 'ruptures' and the particles no longer feel any attraction due to moisture. Here we assume that the moisture force decreases with particle separation 2*s* exponentially with a decay length R_m as in Equation 20:

$$F_m = \begin{cases} F_{m;max} e^{-s/R_m}; s < S_{cr} \\ 0 \qquad\qquad ; s \geq S_{cr} \end{cases} \tag{36}$$

For the moisture force, the peak value $F_{m,max}$, decay length R_m and critical half-separation S_{cr} have to be specified by the user. Values for these can be determined theoretically using suitable models like the liquid bridge theory or parameters developed for models 2 and 3 described earlier in this report.

Finally, in addition to the details for the contact model, the boundary conditions which define the LWD and DCP tests needed to be written into driver files appropriate for PFC3D. As for the simulations run in PFC-3D, for both the LWD and DCP model tests, a mixture with a specified size distribution of spheres representing the coarse granular mixture is contained with a circular cylinder. The mixture is compacted, and then the LWD or DCP test is carried out. Appropriate boundary conditions for each of these tests are described in the following subsections.

9.3 PFC3D LWD Test Simulation Procedure

In the DEM simulation of the LWD field tests, we model the load falling onto our plate with a linearly increasing and decreasing stress, with a peak applied stress of 0.2 MPa. It is not possible to model an entire half-space of granular material, so instead we use a cylindrical container (260 mm diameter) filled with spherical particles.

The specific steps taken in the PFC3D simulations (to be detailed in the following subsections) are, wherever possible, identical to those performed for the DEMP-3D simulations, namely:

1. Sample is prepared to specified solid fraction or maximum possible solid fraction, whichever is lower.
   (a) Dry particles are dropped into the cylindrical container.
   (b) Moisture is introduced.
   (c) A disc is dropped repeatedly to compact the system.
2. LWD test is run on prepared sample.
   (a) The LWD plate is placed on top of the particles.
   (b) LWD loading is applied multiple times, until the peak deflection is relatively unchanging from one application to the next.

Sample plots of variables used to monitor the status of the system, e.g. average bulk particles' vertical position and solid fraction, for each step in the PFC3D simulations are included in the

subsections below. Comparable plots, from the DEMP-3D LWD simulations, are included in Task Reports 2 and 4.

9.3.1 PFC3D LWD Particle Initiation

The first step in the simulations is to create a random array of particles for our simulated LWD experiment. For this, particles are first randomly suspended within a cylinder and released under gravity with small random velocities, shown in Figure 70.

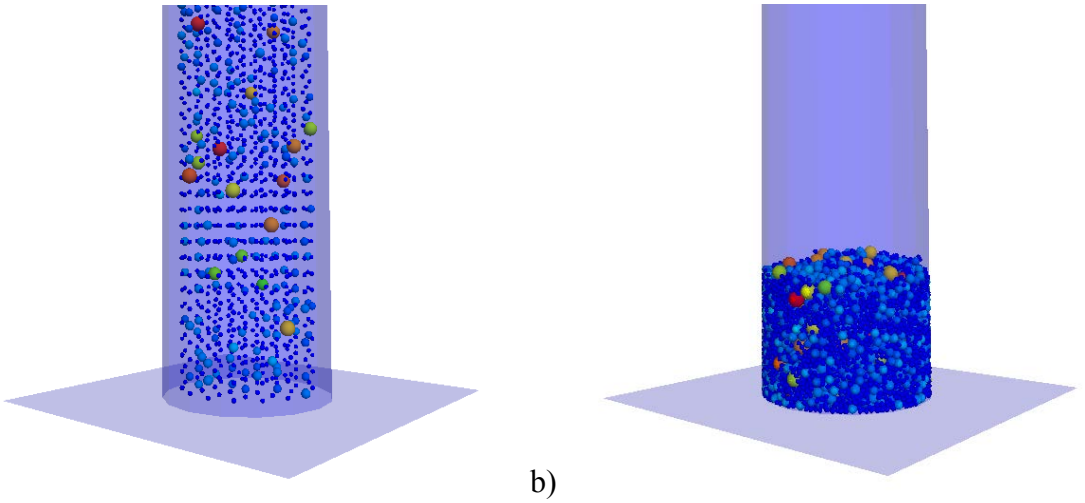

a) b)

Figure 70: Screenshots of the initialization stage of the LWD test in PFC3D: (a) A suspended arrangement of spheres is dropped into a cylinder. (b) This method of initialization method results in an non-segregated mixture.

To reduce computational time, no moisture forces are included in this stage. To determine the approach of the system to a steady settled state, the average vertical position and velocity of the bulk particles can be tracked over time. Due to limits in the numerical precision of the simulations, the change in average vertical position and velocity will never be zero, so we consider the system to be sufficiently settled when both variables reach an approximately steady state, as in Figure 71.

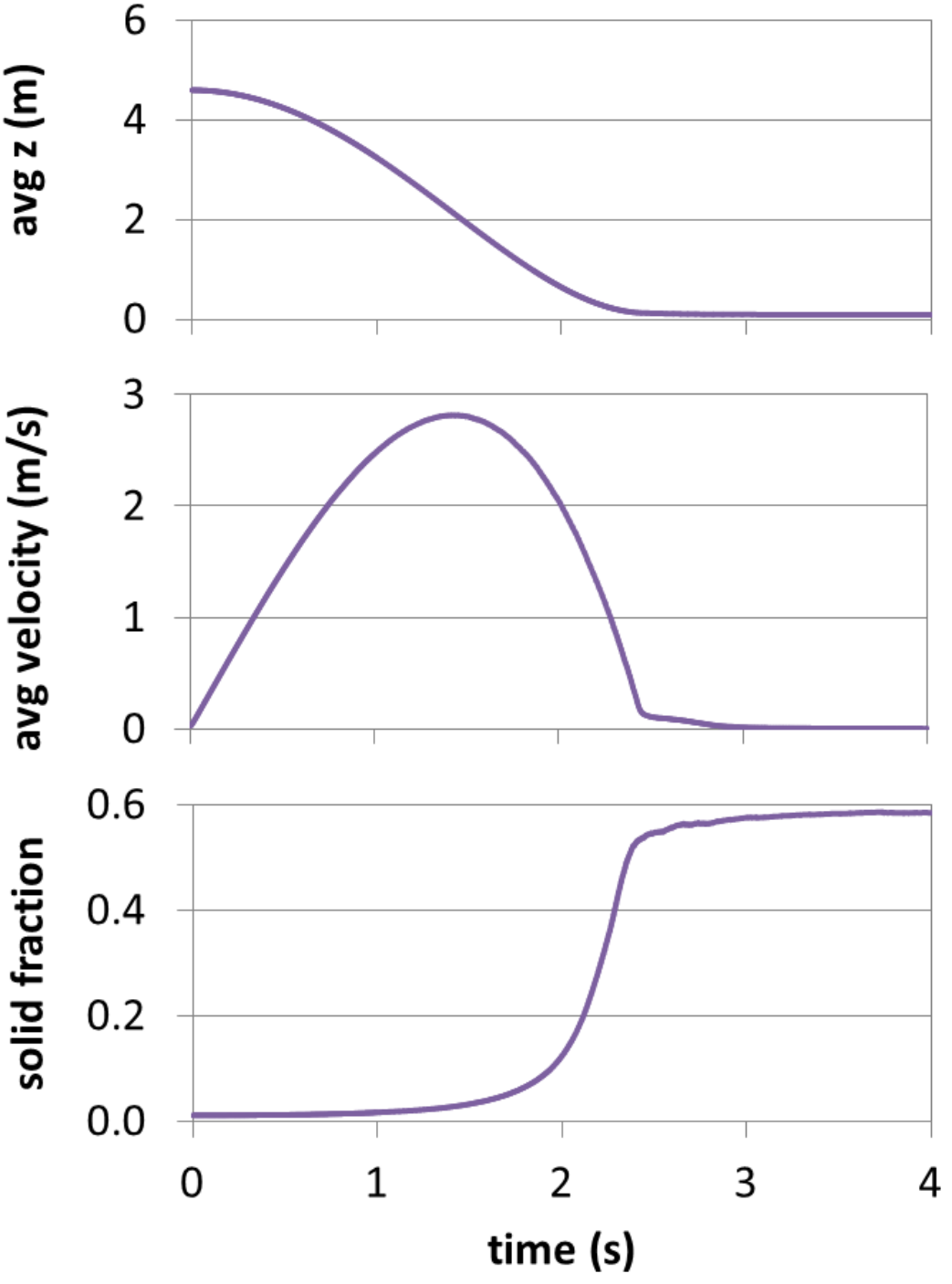

Figure 71: Average particle position and velocity, and solid fraction of the system during the particle-dropping initialization stage of the LWD test simulation.

9.3.2 PFC3D LWD Compaction

After the particles have settled, moisture is added. Then, a 'lid' with the same diameter as the cylinder (see Figure 72) is dropped onto the particles from a small height a few times to compact the system.

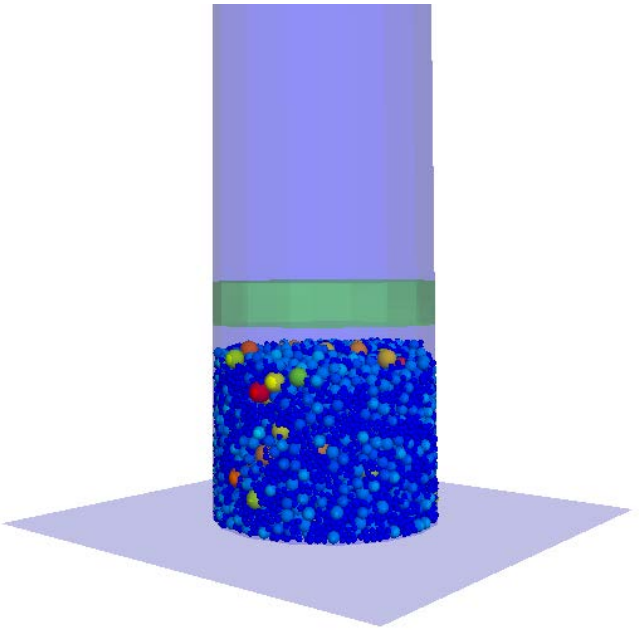

Figure 72: Screenshot of the compaction stage of the LWD test in PFC3D: The cylinder filled with spheres representing the macroscopic particles, and the 'lid' used for compaction. The 'lid' is dropped from a short height repeatedly to compact the mixture.

To determine the manner in which the compaction evolves (and when the system reaches a steady state), the average vertical position of the bulk particles can be tracked, as well as the position of the 'lid' and the system's solid fraction (see Figure 73). The solid fraction is calculated by summing up the volumes of particles below the disc, and dividing by the volume of the cylinder below the disc.

For our numerical simulations, we found that four impacts were generally sufficient to reach near steady state - for the third and forth impacts the increase in solid fraction was less than 0.001 - so we stopped compacting after four cycles. However, the user can specify the number of impacts or another criteria for stopping the compression process.

After this active compaction process, the 'lid' is lifted up and away from the particles, and the system allowed to settle once again. There is relatively little change in the system during this time.

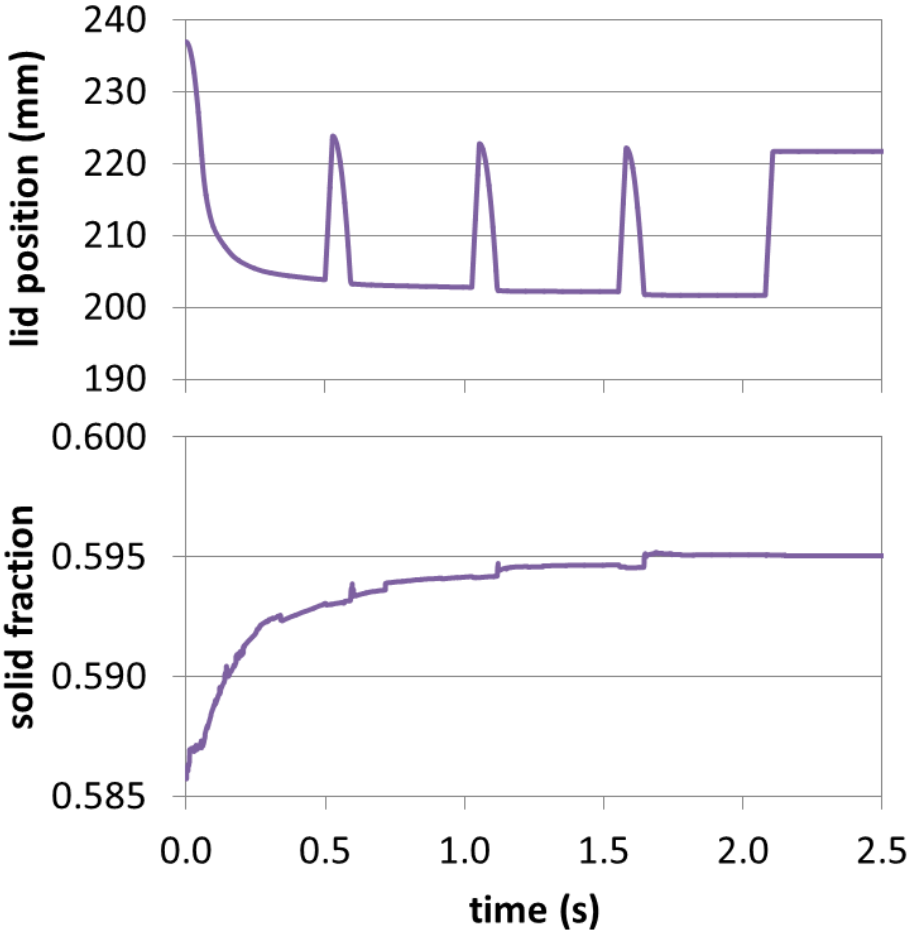

Figure 73: 'Lid' position and solid fraction of the system during the compaction stage of the LWD test simulation.

9.3.3 PFC3D LWD Plate Placement

Before the LWD test is applied, the LWD plate (essentially a solid disc of user-specified diameter and mass) is released from rest onto the top of the particles (Figure 74). Due to the weight of the LWD plate, the system generally compacts a bit more during this stage. It is important to allow the system to settle before applying the LWD load to avoid instabilities that otherwise may arise.

Figure 75 shows the evolution of the vertical position of the plate and the system solid fraction over time, both of which can be used to determine whether the system has reached a steady state.

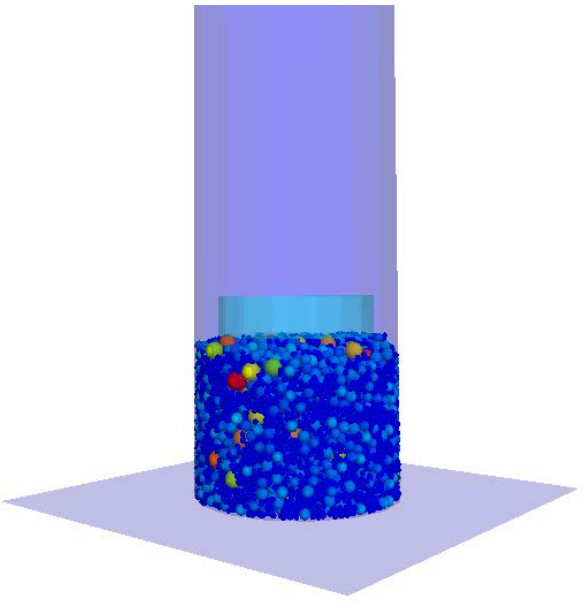

Figure 74: Screenshot of the plate-placement stage of the LWD test in PFC: The cylinder filled with spheres representing the macroscopic particles, and the disc representing the LWD plate resting on the surface of the particles. The 'plate' is allowed to settle for a short time before applying the load.

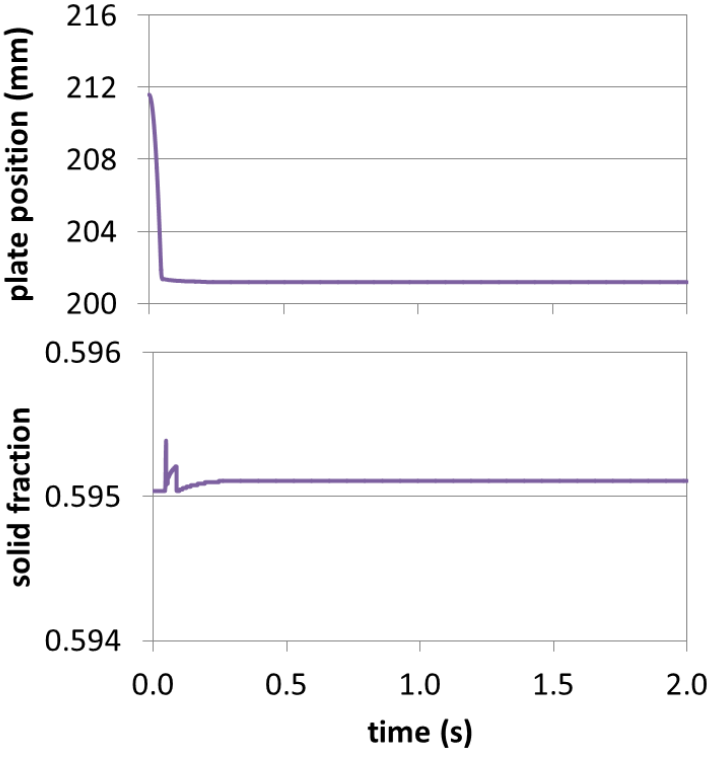

Figure 75: LWD plate position and solid fraction of the system after the plate is released from rest a short distance above the surface of the particles.

9.3.4 PFC3D LWD Loading

In the physical implementation of the LWD test, the LWD load is applied by dropping a known load from a fixed height. In the DEM model of the LWD test, we replace the falling load with an equivalent time-varying load $F_{load}(t)$ applied to the plate (as described for DEMP-3D).

During this process the vertical position of the plate is used to track the amount of deflection obtained during impacts, as shown in Figure 76. Generally the first three impacts are treated as seating drops and ignored; the subsequent impacts are continued until the deflection obtained is relatively unchanging between impacts. This deflection is then used to calculate a bulk modulus for the granular material.

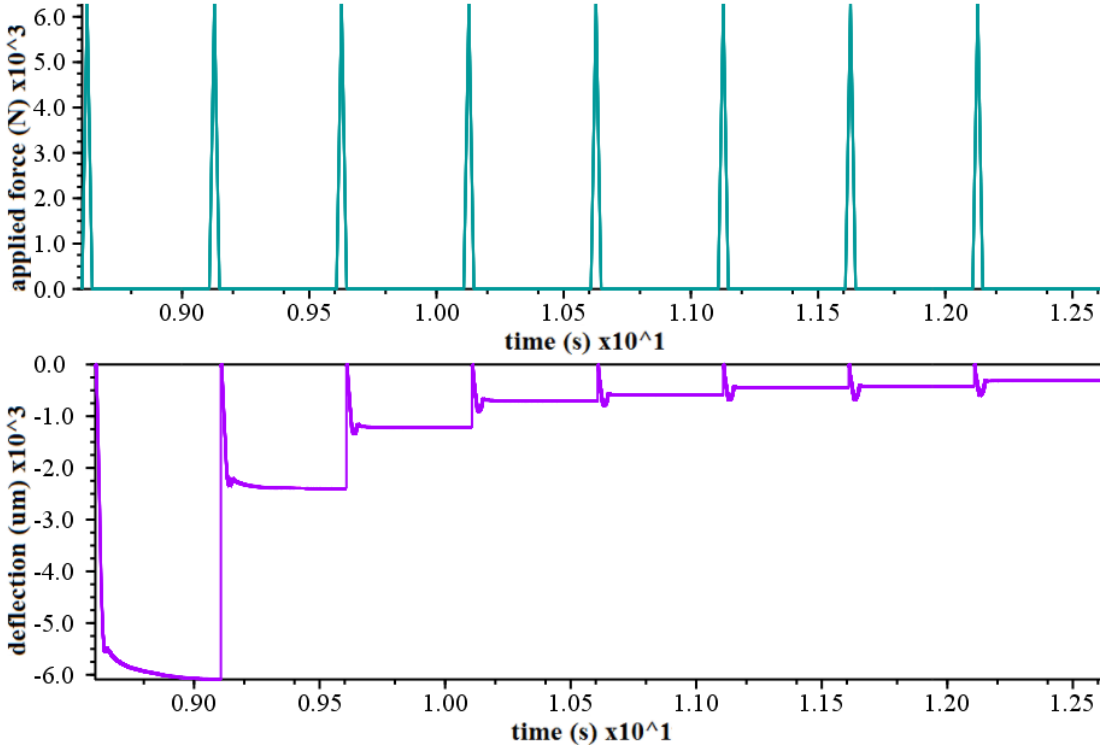

Figure 76: Screenshot of plotted histories in PFC3D of applied external load and deflection of the LWD plate during 8 consecutive loading impacts.

9.4 PFC3D DCP Test Simulation Procedure

In our DEM simulation of the DCP field tests, we model an 8 kg load falling onto a cone-rod assembly of 20 mm diameter submerged in a cylindrical container (150 mm diameter) filled with spherical particles.

The specific steps taken in the DEM simulations are, as much as possible, identical to those performed for DEMP-3D:

1. Sample is prepared to specified solid fraction or maximum possible solid fraction, whichever is lower.

   (a) Dry particles are dropped into the cylindrical container.

(b)Moisture is introduced.

(c)A surcharge load is dropped repeatedly to compact the system.

2. DCP test is run on prepared sample.

(a)The DCP cone-rod assembly is placed on top of the particles.

(b) DCP loading is applied five times.

Sample plots of variables used to monitor the status of the system, e.g. average bulk particles' vertical position and solid fraction, for each step in the PFC3D simulations are included in the subsections below. Comparable plots, from the DEMP-3D DCP simulations, are included in early sections in this report.

9.4.1 PFC3D DCP Particle Initiation

The first step in the simulations is to create a random array of particles for our simulated DCP experiment. For this, particles are first randomly suspended within a cylinder and released under gravity with small random velocities, shown in Figure 77.

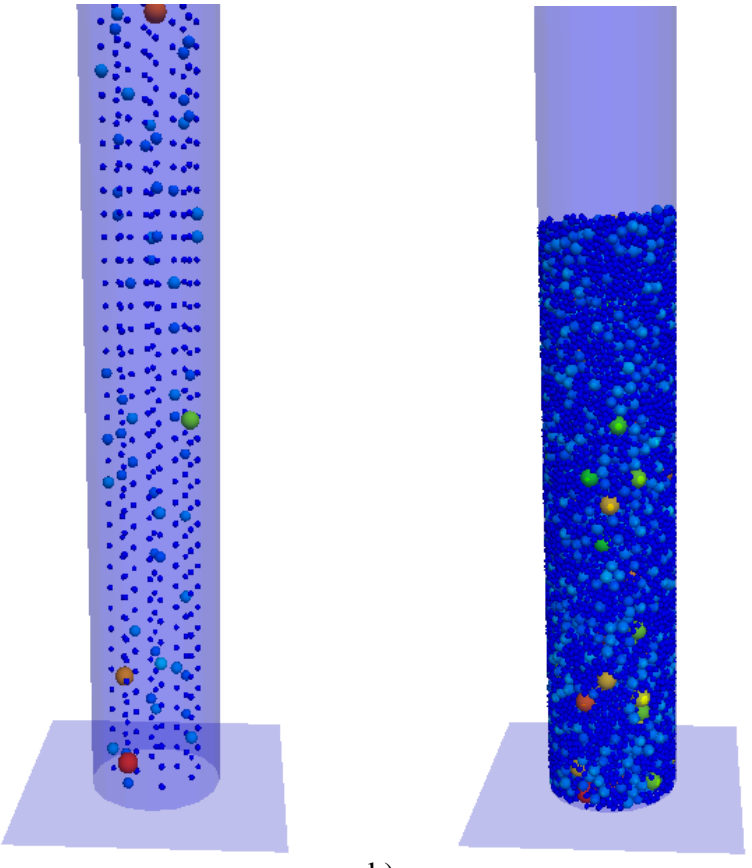

a) b)

Figure 77: Screenshots of the initialization stage of the DCP test in PFC: (a) A suspended arrangement of spheres is dropped into a cylinder. This initialization method results in an non-segregated mixture (b).

To reduce computational time, no moisture forces are included in this stage. To determine the approach of the system to a steady settled state, the average vertical position and velocity of the bulk particles can be tracked over time. Due to limits in the numerical precision of the simulations, the change in average vertical position and velocity will never be zero, so we consider the system to be sufficiently settled when both variables reach an approximately steady state, as in Figure 78.

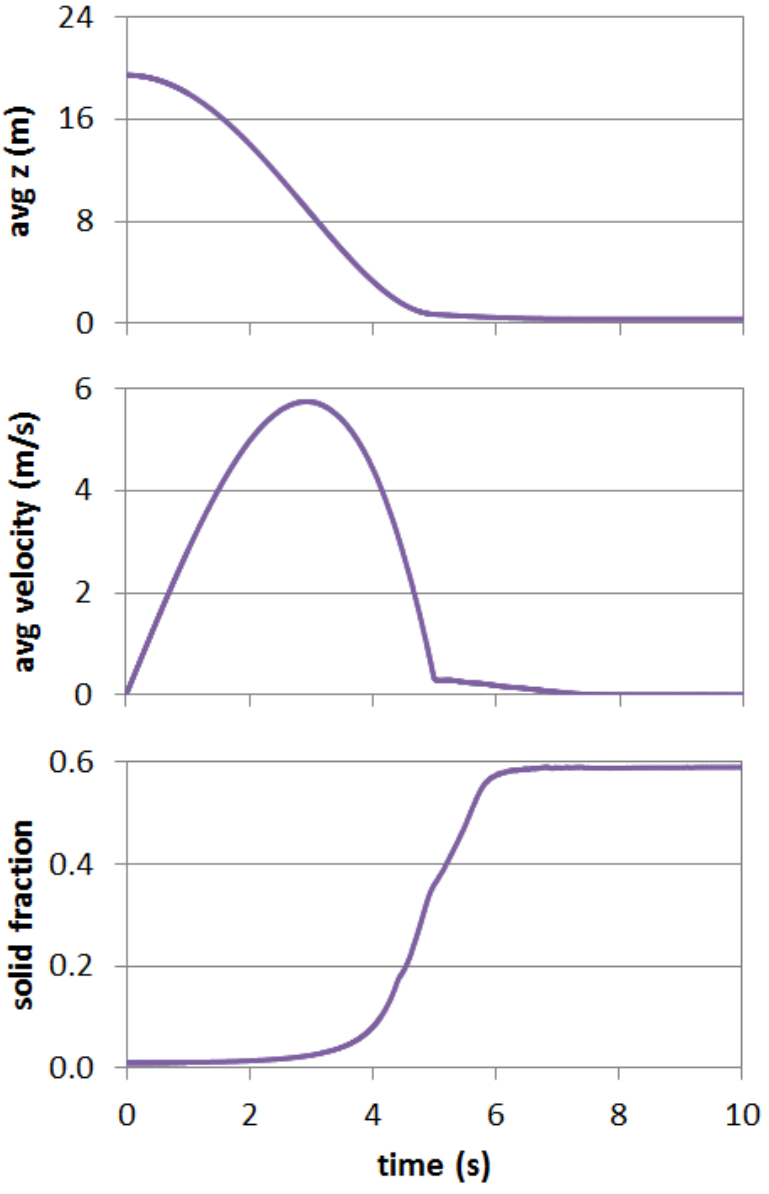

Figure 78: Average particle position and velocity, and solid fraction of the system during the particle-dropping initialization stage of the DCP test simulation.

9.4.2 PFC3D DCP Compaction

After the particles have settled, moisture is added. Then, a disc of thickness t_s and with the same diameter as the cylinder (see screenshot in Figure 79) is dropped onto the particles from a small height a few times to compact the system.

One suggestion for the surcharge is to have it represent a 600 mm layer of granular material with bulk density 2650 kg/m^3 and solid fraction 0.6, and with an equivalent mass of 16.9 kg. We leave this surcharge on top of the particles after compaction as this saves the computational expense of modeling the loose top layer of granular material, and also eliminates the need to perform seating drops as is usually done in the field.

To determine the manner in which the compaction evolves (and when the system reaches a steady state), the average vertical position of the bulk particles can be tracked, as well as the position of the surcharge and the solid fraction. The solid fraction is calculated by summing up the volumes of particles below the surcharge, and dividing by the volume of the cylinder below the disc. Figure 80 shows the evolution of surcharge position and solid fraction of the system over time during compaction of a mixture with 12% gravimetric moisture content.

In our simulations we found that six to eight impacts were generally sufficient to reach near steady state. However, the user can specify the number of impacts or another criteria for stopping the compression process.

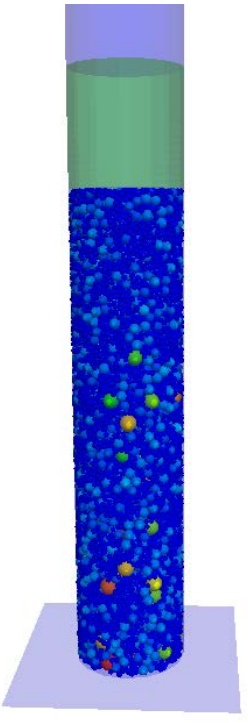

Figure 79: Screenshot of the compaction stage of the DCP test in PFC: a cylinder representing a surcharge load is dropped repeatedly onto the particles to compact the system. After compaction the surcharge is retained.

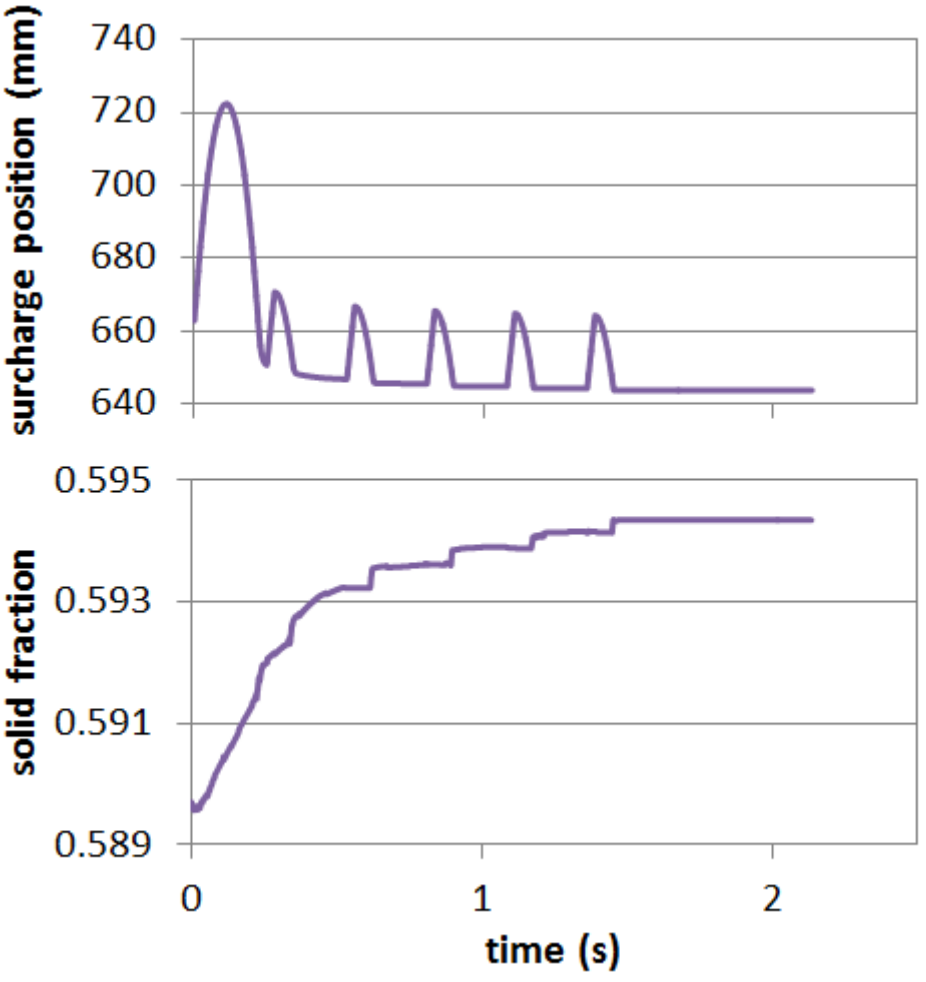

Figure 80: Surcharge vertical position and solid fraction of the system during the compaction stage of the DCP test simulation for a mixture with 12% gravimetric moisture content.

9.4.3 PFC3D DCP Cone Placement

Before the DCP test is applied, the cone-rod assembly is released from rest at the interface between the surcharge load and the particles (see screenshot in Figure 81). There is no interaction between the cone-rod assembly and the surcharge, as the DCP is assumed to have already penetrated through that layer during the seating drops and thus will only interact with the particles below the surcharge.

Due to its weight, the cone-rod assembly penetrates the system of particles a short distance. It is important to allow the system to settle before applying the DCP load to avoid instabilities that may otherwise arise. Figure 82 shows the typical evolution of the cone-tip's vertical position and velocity during this stage.

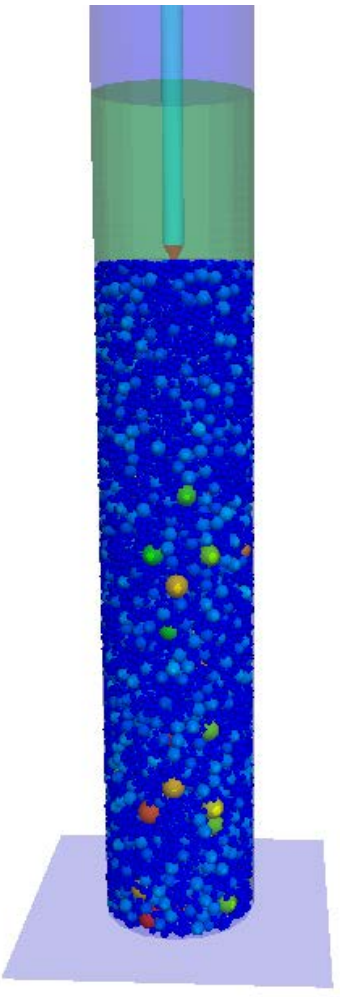

Figure 81: Screenshot of the cone-placement stage of the DCP test in PFC: a cone-rod assembly representing the DCP is placed at the surface of the particles, with the tip just below the base of the surcharge. The cone-rod assembly is allowed to penetrate the mixture under its own weight before beginning loading.

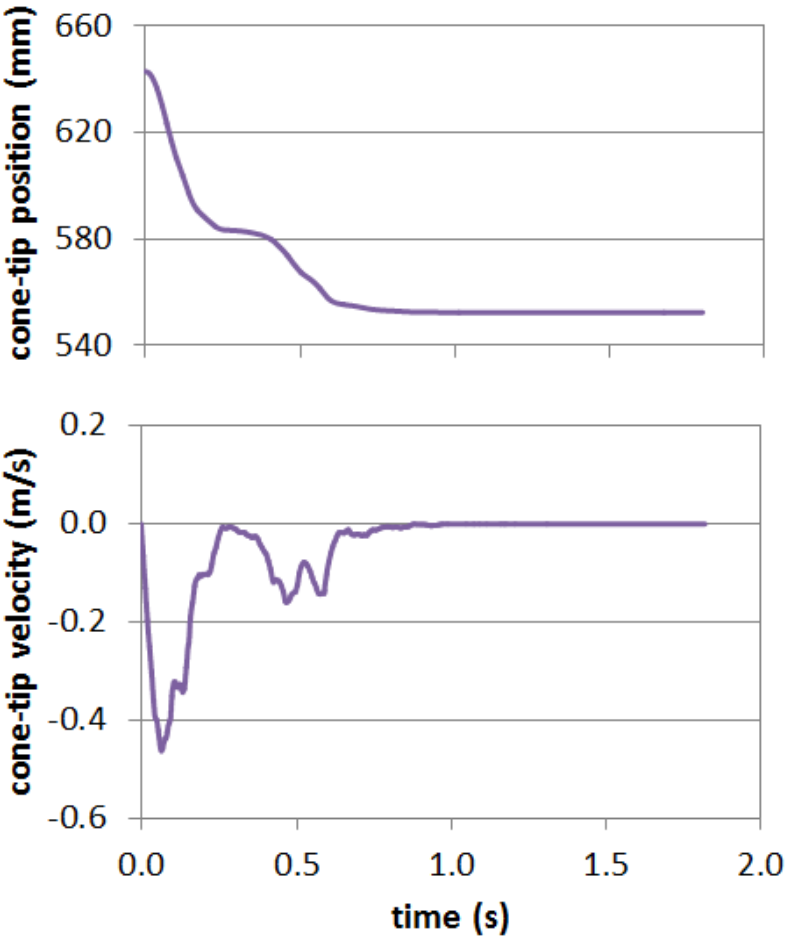

Figure 82: Vertical position and velocity of the cone-tip during the placement stage of the DCP test simulation for a mixture with 12% gravimetric moisture content.

9.4.4 PFC3D DCP Loading

In the physical implementation of the DCP test, an 8 kg hammer is dropped from a height of 575 mm onto the anvil connected to the top of the rod. In the DEM simulations, to save computation time, we replace the load applied by the falling hammer with an equivalent time-varying load $F_{load}(t)$ applied to the cone-rod assembly. $F_{load}(t)$ increases linearly from zero to a peak force of 105 kN over 0.05 ms, decreases linearly back to zero over the next 0.05 ms, and then remains zero (see Figure 83).

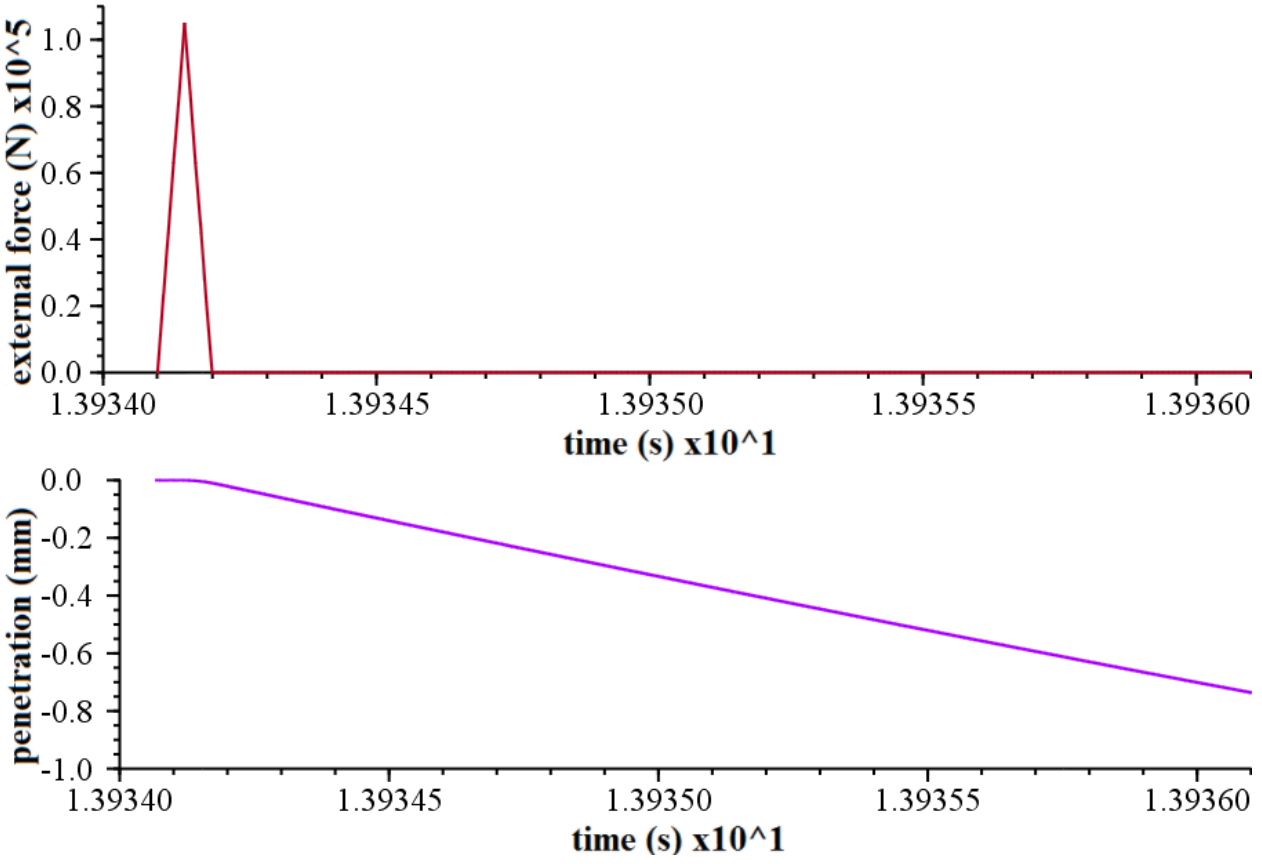

Figure 83: Screenshot of plotted histories in PFC3D of applied external load and penetration of the DCP (after initial placement) during a single loading impact beginning at t=13.934s, for a mixture with 12% gravimetric moisture content.

During the loading process the vertical position of the cone-tip is tracked over time, which can be used then to calculate the penetration of the cone-rod system during a series of impacts (representing the hammer blows), as shown in Figure 83. The penetration is calculated for each impact, and hence is always re-zeroed at the beginning as shown in Figure 84 for a series of impacts.

The total penetration during all five consecutive impacts, corresponding to the data in Figure 84, is shown in Figure 85.

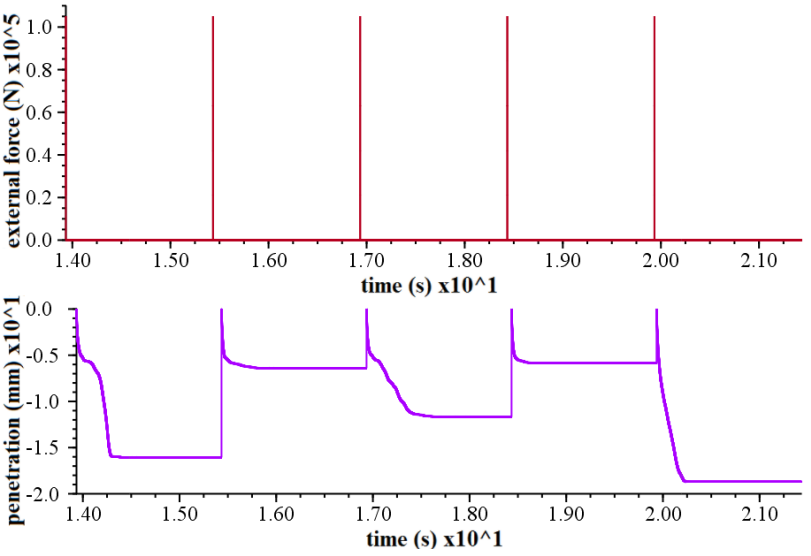

Figure 84: Screenshot of plotted histories in PFC3D of applied external load and penetration of the DCP (after initial placement) during 5 consecutive loading impacts, for a mixture with 12% gravimetric moisture content.

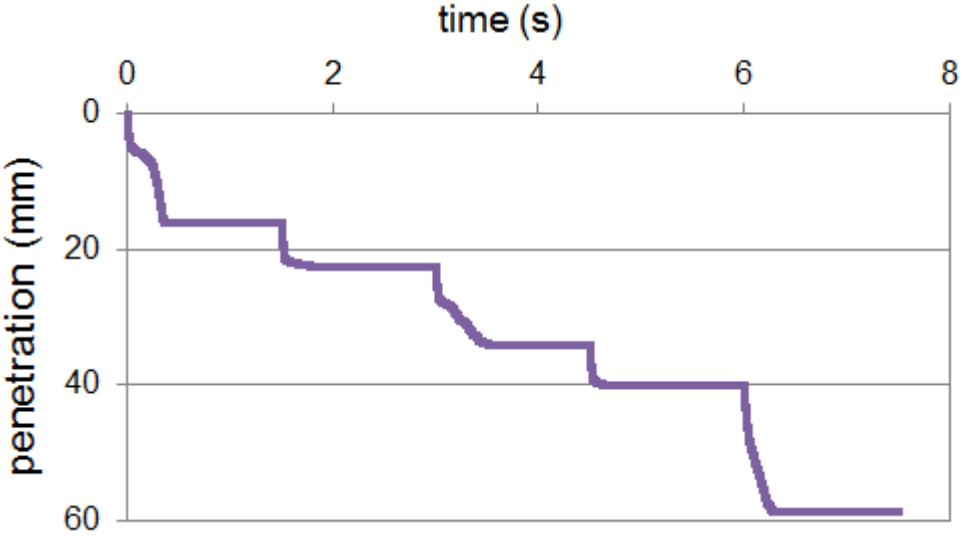

Figure 85: Total penetration of the DCP (excluding initial placement) during 5 consecutive loading impacts, for a mixture with 12% gravimetric moisture content.

9.5 Comparison between DEMP-3D and PFC3D

The majority of the results for this project were obtained using the research group's DEMP-3D code, and only a few simulations were performed using PFC3D for comparison purposes. As will be seen later, the results from both codes are similar but not identical; the minor discrepancies due to some differences between the two codes. Some of these differences are intrinsic, subtle ways where PFC3D differs from DEMP-3D, and others are modifications necessary to implement DEMP-3D as closely as possible into PFC3D.

In this section we first highlight these differences and their significance; then we present numerical comparisons of identical granular mixtures undergoing both the LWD and DCP tests in both DEMP-3D and PFC3D.

9.5.1 Intrinsic Differences between DEMP-3D and PFC3D

As a commerical software, PFC3D is largely written to reduce computation time and also includes several in-built functions that users do not have access to. DEMP-3D on the other hand, was developed specifically for the research group's purposes, with a higher emphasis on more accurate reproduction of the underlying mechanics in particle-particle interactions rather than computation speed. This arises in a number of intrinsic differences between the codes written in the two, that the user has little to no control over:

- timestep size
- integration method
- contact (between neighbouring particles) detection
- calculation of tangential vector

It must be noted that as both PFC3D and DEMP-3D are made up of several complex functions, there may be more intrinsic differences between them than those listed that we are aware of.

DEMP-3D uses a fixed timestep size of $\sim 1\mu s$, whereas in PFC3D this timestep size varies as the simulation progresses. This enables the PFC3D simulation to potentially progress faster than DEMP-3D, but the non-constant timestep makes an estimation of the number of steps required for an expected time difficult. However it is possible to specify a maximum value for the timestep, which minimises this issue and also helps prevent accidentally having timesteps that are too large.

Newton's Laws of Motions relate interparticle forces to the accelerations experienced by the particles in a contacting pair. This acceleration is then integrated to obtain velocities and displacements. PFC3D utilises a central difference scheme to perform integrations, as opposed to the 4th order Runge-Kutta numerical integration used in DEMP-3D. The second order central difference scheme thus requires half as many steps for an integration as DEMP-3D; however it would also have lower accuracy.

DEMP-3D includes a routine that calculates the proximity between particles. Any particles that are within in a set distance of each other are considered neighbours, and are thus always checked to see if the particles are in contact. It is unknown how this neighbour/contact-detection is performed in PFC3D, but the user generally has no control over it. In a dry granular system this would be inconsequential, however for the unsaturated systems in this project, moisture forces are present in between particles even before they come into contact, so this is an important aspect that must be considered. Our Itasca liaison, David Potyondy, has ensured that for our moisture contact model, PFC3D will not 'erase' the contact until the particles' separation far exceeds the user-specified critical distance. However there is still no control over when the contacts turn 'on', i.e. when a pair of particles are considered to be a potential contacting pair.

Lastly, there is a subtle difference in the way both codes calculate the direction of the tangential force between a pair of contacting particles. DEMP-3D sums the incremental tangential displacement vector after integrating the non-constant tangential velocity vector. PFC3D however, first rotates the previous tangential displacement vector to remain in the plane of contact between

the particles before adding the incremental vector. For contacts between a particle and a wall, there is little difference between these two methods. However for contacts between two particles, the plane of contact does not remain constant and hence the resulting tangential vector could be different. This vector concerns the frictional sliding/rolling movement between particles, so a granular mixture under loading will respond with slightly different particle arrangements for these two methods. There is no accepted 'correct' method of obtaining this vector, and we believe that while the end results may be quantitatively different, the qualitative behaviour will be similar.

9.5.2 Implementation Differences between DEMP-3D and PFC3D

There are two minor differences in implementation that the user should be aware of, which we do not believe will have significant effect on the simulation results.

Firstly, PFC3D is capable of handling sharp edges like the corners of walls. As such, there is no need to replace the sharp edges formed by the intersections of surfaces (the 'walls' comprising the cylinders used for compaction and to represent the LWD and DCP) present in the simulations with tiny spheres as is done in DEMP-3D. The only exception is the tip of the cone-rod assembly representing the DCP - the cone is composed of a slanted cylinder and a tiny sphere as the tip, in both the DEMP-3D and PFC3D codes.

The second difference concerns controlling the motion of the non-spherical bodies in the simulation - the 'lid'/cylinder for compaction, the LWD plate and the DCP cone-rod assembly. In DEMP-3D, these are treated as rigid bodies with mass and hence their accelerations (and from that, velocities and displacements) are calculated in a similar manner to the spherical particles. However in PFC3D, the 'walls' forming these have no mass and are velocity-controlled; additional FISH functions had to be written to perform a similar procedure as in DEMP-3D and produce a velocity to be applied to the 'walls' at each timestep.

9.5.3 Simulation Duration

In order to obtain a comparison of the computation speed of both codes, an LWD test simulation, performed on a single dry granular mixture, was run using both DEMP-3D and PFC3D. Both were started from the same initial configuration (arrangement and initial velocity of particles), and the maximum timestep size in PFC3D was set to be the value used in DEMP-3D. The output frequency was also fixed to be identical in both simulations.

We found the computation duration to be comparable: the DEMP-3D simulation took approximately 13 days in total on a Linux system (Dual Intel X5675 3.0 GHz CPU, 48 GB RAM, 6 processors per core), while the PFC3D simulation took 11 days on a Windows system (Intel Core i5-3550, 3.30 GHz CPU, 4 GB RAM).

9.5.4 DEMP-3D vs PFC3D: Simulation Results

Here we compare the results of both LWD and DCP simulations performed on identical granular mixtures, using the DEMP-3D and PFC3D codes. As expected the results are qualitatively similar, and generally comparable.

9.5.4.1 DEMP-3D vs PFC3D: LWD Simulation Results

Table 13 compares the results of an LWD simulation performed on three unsaturated granular mixtures by both codes. The fill height and solid fraction after compaction, and the average peak deflection Δ and resulting bulk modulus E_{LWD} are included.

Dry	5% gmc	8% gmc
Fill height 176 mm	Fill height 192 mm	Fill height 176 mm
Solid fraction 65.4%	Solid fraction 60.3%	Solid fraction 65.4%
Δ = 137 μm	Δ = 165 μm	Δ = 250 μm
E_{LWD} = 203 MPa	E_{LWD} = 168 MPa	E_{LWD} = 111 MPa
Fill height 190 mm	Fill height 202 mm	Fill height 201 mm
Solid fraction 60.1%	Solid fraction 59.4%	Solid fraction 59.5%
Δ = 590 μm	Δ = 667 μm	Δ = 650 μm
E_{LWD} = 47 MPa	E_{LWD} = 42 MPa	E_{LWD} = 43 MPa

Comparing the fill height and solid fractions for similar mixtures, we observe that the DEMP-3D system is generally more compacted, which explains why there is less plate deflection obtained. This is reflected partially in Figure 86, where the less compacted system in PFC3D exhibits a larger deflection during loading and becomes more compacted; whereas the already more highly-compacted system in PFC3D experiences greater resistance during loading - leading to less deflection - and exhibits significantly greater restoration back to its original state.

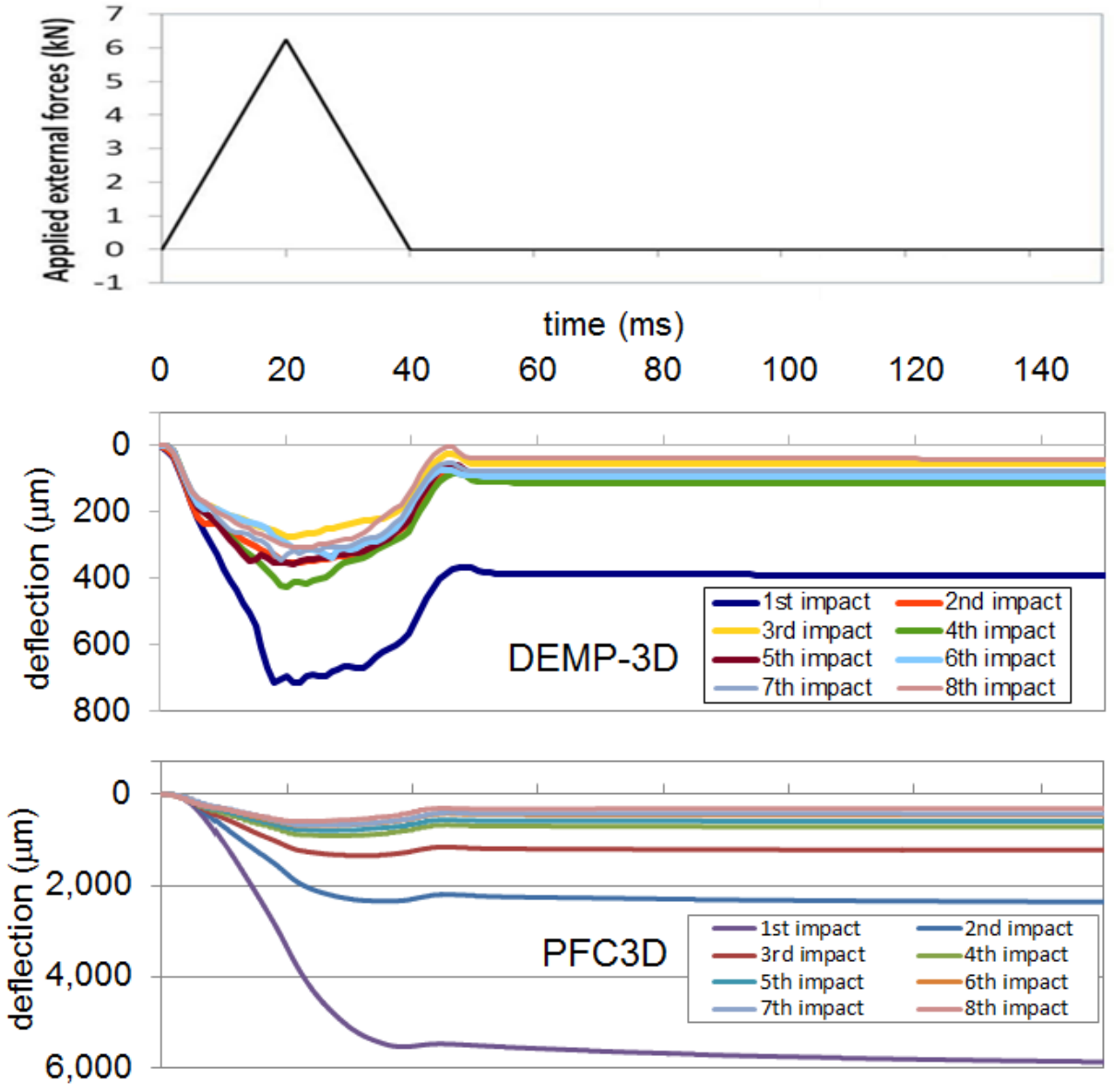

Figure 86: LWD plate deflection during successive impacts for a granular mixture with 8% gravimetric moisture content, for both the DEMP-3D and PFC3D codes.

Another reason for the larger plate deflections observed in the PFC3D system is demonstrated in Figure 87, which shows screenshots of the system after consecutive impacts. In the PFC3D system, some particles are displaced up and around the LWD plate after loading. However this does not occur in the DEMP-3D system.

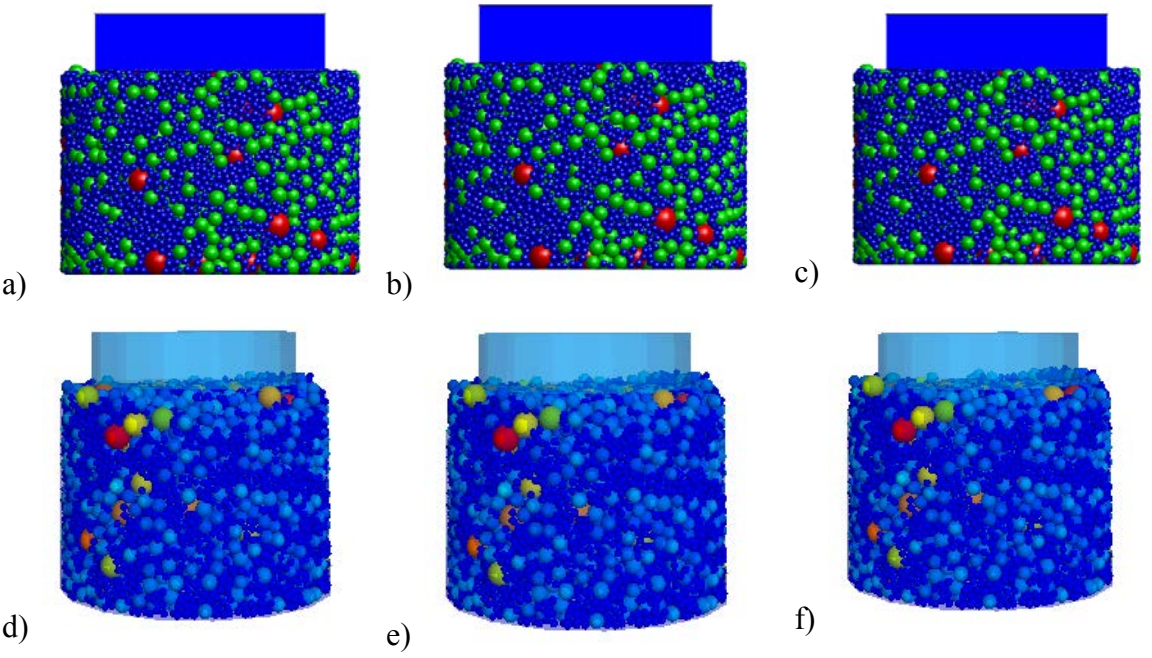

Figure 87: Screenshots of a granular mixture with 8% gravimetric moisture content during the LWD test using the DEMP-3D (a-c) and PFC3D (d-f) codes: after the 1st impact (a,d), after the 3rd impact (b,e), and after the 5th impact (c,f).

A possible reason for this difference in behaviour is the different tangential vector calculation used by both codes. As previously mentioned, this is strongly connected to the frictional sliding/rolling behaviour between particles, and would manifest as different particle rearrangements in response to applied loading.

However apart from this difference in behaviour around the edges of the LWD plate, we find that qualitatively the LWD test simulations in both codes are comparable.

9.5.4.2 DEMP-3D vs PFC3D: DCP Simulation Results

A granular mixture with three levels of moisture content (dry, 6% and 12% gravimetric moisture content) are used for comparing the DCP test simulations in DEMP-3D and PFC3D. Table 14 lists the cylinder fill height and solid fraction after compaction, as well as the penetration obtained during initial placement of the cone-rod assembly and five consecutive hammer blows, and lastly the average penetration.

Table 14: Fill height and solid fraction after compaction, penetration during intial placement $\delta_{initial}$ and 5 consecutive hammer blows (δ_1 to δ_5), and average penetration per blow $\bar{\delta}$. Values given are for three unsaturated granular mixtures (dry, 6% and 12% gravimetric moisture content), obtained from the DCP test simulations in both DEMP-3D and PFC3D.

	Dry	6% gmc	12% gmc
DEMP3D	Fill height 603 mm	Fill height 637 mm	Fill height 637 mm
	Solid fraction 63.1%	Solid fraction 61.3%	Solid fraction 61.4%
	$\delta_{initial}$ = 45.4mm	$\delta_{initial}$ = 47.0 mm	$\delta_{initial}$ = 40.2 mm
	δ_1 = 69.9 mm	δ_1 = 45.9 mm	δ_1 = 29.4 mm
	δ_2 = 21.9 mm	δ_2 = 28.0 mm	δ_2 = 24.9 mm
	δ_3 = 9.1 mm	δ_3 = 25.0 mm	δ_3 = 29.9 mm
	δ_4 = 9.0 mm	δ_4 = 24.5 mm	δ_4 = 17.5 mm
	δ_5 = 3.3 mm	δ_5 = 23.0 mm	δ_5 = 9.3 mm
	$\bar{\delta}$ = 22.6 mm	$\bar{\delta}$ = 29.3 mm	$\bar{\delta}$ = 26.2 mm
PFC3D	Fill height 643 mm	Fill height 645 mm	Fill height 642 mm
	Solid fraction 59.5%	Solid fraction 59.4%	Solid fraction 59.4%
	$\delta_{initial}$ = 118.9 mm	$\delta_{initial}$ = 87.5 mm	$\delta_{initial}$ = 90.5 mm
	δ_1 = 26.8 mm	δ_1 = 2.9 mm	δ_1 = 16.1 mm
	δ_2 = 66.6 mm	δ_2 = 24.1 mm	δ_2 = 6.4 mm
	δ_3 = 44.6 mm	δ_3 = 4.3 mm	δ_3 = 11.7 mm
	δ_4 = 13.6 mm	δ_4 = 6.0 mm	δ_4 = 5.8 mm
	δ_5 = 3.8 mm	δ_5 = 5.7 mm	δ_5 = 18.7 mm
	$\bar{\delta}$ = 31.1 mm	$\bar{\delta}$ = 8.6 mm	$\bar{\delta}$ = 11.7 mm

In general, the PFC3D systems are only slightly less compacted than the DEMP-3D systems prior to loading (reflected in the similar post-compaction fill height), except for the dry case which has nearly 4% less solid fraction than the DEMP-3D dry case. However the PFC3D systems exhibit much larger penetrations during the initial cone-placement, which could be due to the different tangential vector calculation in the contact model, as mentioned before, resulting in 'easier'

particle rearrangement. The larger initial penetrations lead to the cone-rod assemblies being buried deeper in the cylinder for the PFC3D systems, which may be the reason why the penetrations obtained for the five consecutive hammer blows are generally smaller than those obtained in the corresponding DEMP-3D systems. The dry PFC3D case still has larger penetrations though, likely due to the lower solid fraction than in the dry DEMP-3D system.

Figure 88 shows the penetration over time starting from the initial placement for the mixture with 12% moisture content, in both the DEMP-3D and PFC3D systems. We note that in the DEMP-3D systems, the penetrations during the hammer blows generally decrease in magnitude; however this is not the case with the PFC3D systems. This is, again, probably due to the particles having a different tangential response under loading which may cause the particles to rearrange more easily, dissipating the force of the hammer blows more rapidly so that the cone-rod assembly penetrates less.

Overall, despite the difference in magnitude of the penetrations, we believe the DCP test simulations in both PFC3D and DEMP-3D to be qualitatively comparable.

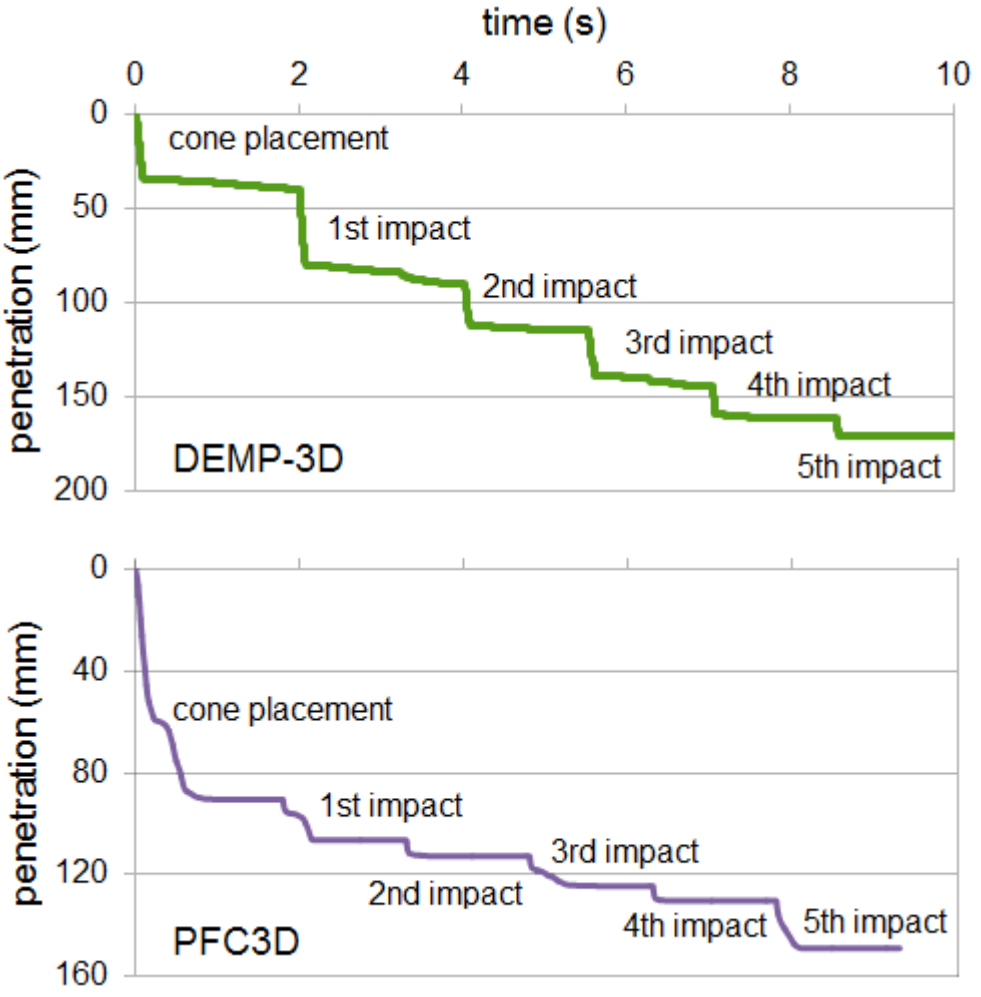

Figure 88: Penetration of cone-rod assembly from initial placement through 5 successive hammer blows for a granular mixture with 12% gravimetric moisture content, for both the DEMP-3D and PFC3D codes.

Chapter 10 Conclusions

In this report we presented DEM numerical modeling results which simulate the effects of moisture and fine particles on LWD and DCP tests of a granular mixture and compared the results from the simulations with existing experimentally-based target values. In the simulations, the coarse particle size distribution is represented explicitly through the DEM particles. The fine particle size distribution and moisture are represented implicitly via the force model between the coarser DEM particles. Three such implicit models were investigated. A 'first generation' of tests were performed on a unimodal mixture for the first moisture model, while the later 'second generation' tests were performed on a trimodal mixture, with a size distribution chosen to be similar to that found in MnDOT's Class 5 aggregate materials.

The first model is based on the liquid bridge theory, where moisture in an unsaturated granular mixture forms liquid bridges between pairs of particles. This results in an attractive force between them that is maximum when the particles are touching and decreases as the particles are separated. This maximum value of the moisture force depends on the amount of moisture and the value of surface tension. Using a dynamic similarity argument, we scale the surface tension value used in the DEM simulations relative to that of the prototype system that generally has smaller coarse particles. This scaling idea is further expanded to model an increasing amount of fine particles – the model surface tension is scaled larger to represent more fines (and thus a lower average particle size) in the prototype system. Using this model we obtained slight increases in peak deflection under LWD loading with increasing moisture content, which agreed qualitatively with physical trends. However, we were unable to obtain similar agreement with increasing fines content, in both the LWD and DCP tests. This implies that modeling the effects of fine particles using the surface tension value was inappropriate.

The second model is based on experimental work that explicitly considers the mixture composition, and provides an empirical relationship between volumetric moisture content and the suction (negative pore pressure) in the mixture. Given a mixture composition it is possible to determine the suction corresponding to a given moisture content. This can then be related to the attractive moisture force between particle pairs. Unfortunately an appropriate translation between this empirical suction and the equivalent model suction is not immediately obvious, and could be rather complex (for instance it may depend on local particle arrangement). Also, the work focused largely on fine particles as opposed to the coarse particles used in the DEM simulations. This, in addition to the form of the empirical relation being such that the same suction value is possible for different mixture compositions, meant that considering the simulation results explicitly as functions of moisture content and fines content may not be appropriate. As such we considered the results in terms of the equivalent model suction instead, and found a monotonic increase in peak deflection with decreasing suction values. Generally, suction decreases with increasing moisture content or decreasing fines content. This translates to having a qualitative agreement with variation in moisture content but an opposite trend with fines content.

Because neither of the first two models produced satisfactory results with respect to fines content, we believe that modeling the effects of moisture by modifying only the normal force between particles is insufficient. We considered that the fines content might also mediate the tangential force via the effective friction between coarse particles.

For the third moisture model, we investigated the effect of varying the friction coefficient as a way of representing the change in 'lubrication' between coarse particles due to the presence of fine particles. For this model, we found that with decreasing friction coefficient (representing increasing fine material), the peak deflection from LWD tests and average penetration from DCP tests increased, which is in agreement with estimated target value trends. This leads us to conclude that this third model is the closest to a qualitative representation of how moisture and fines affect the bulk characteristics of an unsaturated granular mixture.

The third model was satisfying qualitatively but the representation of fines and moisture content was not quantitatively mechanistic. Therefore, this model necessitated the development of a relationship between model parameters and physical measures. There are a number of ways this might be done; we describe one that led to a qualitative and mostly quantitative agreement between our model results and estimated target values. For a relatively simple set of relationships, we calibrated the effect of moisture with the suction coefficient alone and the effect of fine particles via the friction coefficient between coarse particles. While, admittedly, this method is relatively simplistic – there is likely interdependence among the two force model parameters – the results capture the behavior exhibited by a set of estimated target values from experimental LWD and DCP tests

We expect that in its current form, the model can be used to predict behavior for a relatively narrow range of base materials as encompassed by MnDOT's Class 5 specifications. We expect that with some modest improvements, specifically the manner in which the fine particles and moisture parameters are represented by the friction and suction coefficients within the force model, this framework can be extended to a wide range of granular bases. Then, provided separate coarse grading numbers (CGN's) for the DEM particles and fine grading numbers (FGN's) and moisture content for the interparticle force model parameters (e.g., Ref. 41) DEM simulations could aid in developing more rigorous guidelines for granular bases and may even be able replace experimental tests in developing target values for new and recycled materials. As computers increase in speed, we expect this this framework will even be able to represent field conditions where conditions are not completely uniform and even layered granular bases are used.

Despite the model limitations, this DEM approach with calibration for the effects of fines and moisture offers a viable alternative to continuum models where the form of the bulk moduli must be empirically determined. In contrast, the calibrated DEM model represents coarse particle movement distinctly and captures, even prior to calibration, complex trends associated with particle size distribution and moisture content measured in experiments.

While in this project we focused on one specific class of aggregate bases, this framework offers the potential to reduce otherwise required extensive experimental tests that would be required for innovative and recycled pavement materials. Further, when adapted to other tests of unbound materials this model framework provides the potential of increased confidence in calibration parameters developed between results of different tests for more reliable and consistent quality control.

References

[1] F. Lekarp, U. Isacsson, and A. Dawson, "State of the Art. i: Resilient Response of Unbound Aggregates," *J. Transp. Engrg.*, vol. 126, no. 1, pp. 66–75, 2000.

[2] F. Lekarp, U. Isacsson, and A. Dawson, "State of the Art. ii: Permanent Strain Response of Unbound Aggregates," *J. Transp. Engrg.*, vol. 126, no. 1, pp. 76–83, 2000.

[3] P. Davich, F. Camargo, B. Larsen, R. Roberson, and J. Siekmeier, *Validation of DCP and LWD Moisture Specifications for Granular Materials*, Tech. Rep. MN/RC-2006-20, Minnesota Department of Transportation, St. Paul, July 2006.

[4] J. Siekmeier, C. Pinta, S. Merth, J. Jensen, P. Davich, F. Camargo, and M. Beyer, *Using the Dynamic Cone Penetrometer and Light Weight Deflectometer for Construction Quality Assurance*, Tech. Rep. MN/RC-2009-12, Minnesota Department of Transportation, St. Paul, February 2009.

[5] Y. Xiao and E. Tutumluer, *Best Value Granular Material for Road Foundations*, Tech. Rep. MN/RC-2012-01, Minnesota Department of Transportation, St. Paul, 2012.

[6] T. Eaves and T. M. Jones, "Effect of Moisture on Tensile Strength of Bulk Solids I: Sodium Chloride and Effect of Particle Size," *J. Pharmaceutical Sciences*, vol. 61, February 1972.

[7] P. A. Cundall and R. D. Hart, "Numerical Modelling of Discontinua," *Engineering Computations*, vol. 9, no. 2, pp. 101–113, 1992.

[8] J. Bardet and J. Proubet, "A numerical investigation of the structure of persistent shear bands in granular media," *Geotechnique*, vol. 41, no. 4, p. 599-613, 1991.

[9] T. Ke and J. Bray, "Modeling of particulate media using discontinuous deformation analysis," *Journal of Engineering Mechanics*, vol. 121, no. 11, p. 1234-1243, 1995.

[10] M. Kuhn, "A flexible boundary for the three-dimensional dem particle assemblies," *Engineering Computations*, vol. 12, no. 2, p. 175-183, 1995.

[11] J. Ting, L. Meachum, and J. Rowell, "Effect of particle shape on the strength and deformation of mechanism of ellipse-shaped granular assemblages," *Engineering Computations*, p. 99-108, 1995.

[12] J. Williams and R. Nabha, "Granular vortices and shear band formation," *Mechanics of Deformation and Flow of Particulate Materials (ASCE)*, p. 62-71, 1997.

[13] P. Thomas and J. Bray, "Capturing nonspherical shape of granular media with disk clusters," *Journal of Geotechnical and Geoenvironmental Engineering*, vol. 125, no. 3, p. 169-178, 1999.

[14] H. Tanaka, M. Momozu, A. Oida, and M. Yamazaki, "Simulation of soil deformation and resistance at the bar penetration by the distinct element method," *The Journal of Terramechanics*, vol. 37, 2000.

[15] W. G. Buttlar and Z. You, "Discrete element modeling of asphalt concrete," *Journal of Transportation Research Board*, vol. 1757, p. 111-118, 2001.

[16] T. Ng and C. Wang, "Comparison of 3d DEM simulation with MRI data," *International Journal for Numerical and Analytic Methods in Geomechanics*, vol. 25, p. 497-507, 2001.

[17] P. Ullidtz, "Distinct element method for study of failure in cohesive particulate media," *Journal of the Transportation Research Board*, vol. 1757, p. 127-133, 2001.

[18] W. Khogali and M. Zeghal, "A comprehensive system for characterizing granular materials: providing material input for pavement design," in *Annual conference of the Transportation Association of Canada*, (St. Johnâ€™s, Newfoundland and Labrador), 2003.

[19] T. Ng, "Triaxial test simulation with discrete element method and hydrostatic boundaries," *Journal of Engineering Mechanics*, vol. 130, no. 10, p. 1188-1194, 2004.

[20] M. Zeghal, "Discrete-Element Method Investigation of the Resilient Behavior of Granular Materials," *J. Trans. Eng.*, pp. 503–509, July/August 2004.

[21] M. Jiang and H.-S. Yu, "Application of Discrete Element Method to Geomechanics," *in Modern Trends in Geomechanics, Springer Proceedings in Physics*, vol. 106, p. 241-269 2006.

[22] M. Lu and G. R. McDowell, "Discrete element modeling of ballast abrasion," *Geotechnique*, vol. 56, no. 9, p. 651-655, 2006.

[23] L. Uthus, M. A. Hopkins, and I. Horvli, "Discrete element modeling of the resilient behaviour of unbound granular aggregates," *International Journal of Pavement Engineering*, vol. 9, no. 6, p. 387-395, 2008.

[24] B. Yohannes, K. Hill, and L. Khazanovich, *Mechanistic Modeling of Unbound Granular Materials*, Tech. Rep. MN/RC-2009-21, Department of Civil Engineering, University of Minnesota, Minneapolis, June 2009.

[25] K. M. Hill, B. Yohannes, and L. Khazanovich, "A Unified Mechanistic Approach for Modeling Tests of Unbound Pavement Materials," *Journal of Transportation Engineering*, vol. 138, no. 9, pp. 1091–1098, 2012.

[26] B. Yohannes, D. Tan, L. Khazanovich, and K. Hill, "Mechanistic modelling of tests of unbound granular materials," *International Journal of Pavement Engineering*, DOI: 10.1080/10298436.2013.775442, 2013.

[27] R. Hicks and C. Monismith, "Factors influencing the resilient response of granular material," *Highway Research Record*, vol. 345, p. 15-31, 1971.

[28] F. N. Hveem and R. M. Carmany, "The Factors Underlying the Rational Design of Pavements," *Highway Research Board*, 1948.

[29] V. Ganesan, K. A. Rosentrater, and K. Muthukumarappan, "Flowability and handling characteristics of bulk solids and powders - a review with implications for DDGS," *Biosystems Engineering*, vol. 101, pp. 425–435, 2008.

[30] P. Pierrat, D. K. Agrawal, and H. S. Caram, "Effect of moisture on the yield locus of granular materials: theory of shift," *Powder Technology*, vol. 99, pp. 220–227, 1998.

[31] S.-R. Yang, W.-H. Huang, and Y.-T. Tai, "Variation of Resilient Modulus with Soil Suction for Compacted Subgrade Soils," *Transportation Research Record*, no. 1913, pp. 99–106, 2005.

[32] S. Gupta, A. Singh, and A. Ranaivoson, "Moisture Retention Characteristics of Base and Sub-base Materials," Tech. Rep. MN/RC-2005-06, Department of Soil, Water and Climate,

University of Minnesota, December 2004.

[33] S. C. Gupta and W. E. Larson, "Estimating Soil Water Retention Characteristics From Particle Size Distribution, Organic Matter Percent, and Bulk Density," *Water Resources Research*, vol. 15, pp. 1633–1635, December 1979.

[34] G. Mason and W. C. Clark, "Liquid bridges between spheres," *Chem. Engrg. Sci.*, vol. 20, pp. 859–866, 1965.

[35] Y. Shimada, Y. Yonezawa, and H. Sunada, "Measurement and Evaluation of the Adhesive Force between Particles by the Direct Separation Method," *Journal of Pharmaceutical Sciences*, vol. 92, pp. 560–568, March 2003.

[36] T. Gillespie and W. J. Settineri, "The Effect of Capillary Liquid on the Force of Adhesion between Spherical Solid Particles," *J. Colloid Interface Sci.*, vol. 24, pp. 199–202, 1967.

[37] K. Hotta, K. Takeda, and K. Iinoya, "The Capillary Binding Force of a Liquid Bridge," *Powder Technology*, vol. 10, pp. 231–242, 1974.

[38] G. Lian, C. Thornton, and M. J. Adams, "A Theoretical Study of the Liquid Bridge Forces between Two Rigid Spherical Bodies," *J. Colloid Interface Sci.*, vol. 161, pp. 138–147, 1993.

[39] Y. Muguruma, T. Tanaka, and Y. Tsuji, "Numerical simulation of particulate flow with liquid bridge between particles (simulation of centrifugal tumbling granulator)," *Powder Technology*, vol. 109, pp. 49–57, 2000.

[40] S. H. Liu and D. A. Sun, "Simulating the collapse of unsaturated soil by DEM," *Int. J. Numer. Anal. Meth. Geomech.*, vol. 26, pp. 633–646, 2002.

[41] M. Oman, *Advancement of Grading and Base Material Testing*, Tech. Rep., Office of Materials, Minnesota Department of Transportation, St. Paul, 2004.

[42] Y. Tsuji, T. Tanaka, and T. Ishida, "Lagrangian numerical simulation of plug flow of cohesionless particles in a horizontal pipe," *Powder Technology*, vol. 71, pp. 239–250, 1992.

[43] P. Fleming, M. Frost, and J. Lambert, "Review of Lightweight Deflectometer for Routine In Situ Assessment of Pavement Material Stiffness," *Transportation Research Record*, no. 2004, pp. 80–87, 2007.

[44] S. Nazarian, V. Tandon, K. Crain, and D. Yuan, "Use of Instrumented Dynamic Cone Penetrometer in Pavement Characterization," in *Nondestructive Testing of Pavements and Backcalculation of Moduli: Third Volume* (S. D. Tayabji and E. O. Lukanen, eds.), pp. 214–228, American Society for Testing and Materials, West Conshohocken, PA: ASTM STP 1375, 2000.

Appendix A: Discrete Element Method Details

The discrete element method (DEM) treats individual components in a system - in this case, the individual particles in a granular mixture - as separate bodies, each with their own masses and forces acting upon them. For this project, we want to investigate how particle-level changes such as moisture and fines content as well as changes in local grain size distribution (e.g., due to segregation) affect the bulk properties of a granular material. To that end, a DEM approach is more appropriate than a continuum approach for studying these effects.

In a discrete element model, the rotational and translational positions (and velocities and accelerations) are tracked throughout the simulation. The net forces and moments associated with the particle masses and all contacting particles are calculated at each time step. Next, the equations of motion for all particles in the whole system for each time step is calculated. Then, numerical integration is performed to calculate subsequent particle velocities and displacements. This gives a new set of particle positions and velocities, and the process is repeated.

The properties of the particles are inputs into the DEM contact model - how the effective particle deformations relate to interparticle forces. The model we used for Phase 1 [24] uses Hertz-Mindlin contact theory with a damping component specified by Tsuji et al. [42] and Coulomb sliding friction:

$$F_n = \begin{cases} -k_n \delta_n^{3/2} - \eta_n \delta_n^{1/4} \delta_n ; \delta_n > 0 \\ 0 \qquad\qquad\qquad\quad ; \delta_n \leq 0 \end{cases} \tag{A.1}$$

$$F_t = \begin{cases} min\left\{ -k_t \delta_n^{1/2} \delta_t - \eta_t \delta_n^{1/4} \delta_t ; : \mu F_n \right\} ; \delta_n > 0 \\ 0 \qquad\qquad\qquad\qquad\qquad\quad ; \delta_n \leq 0 \end{cases} \tag{A.2}$$

where F_n and F_t are the contact forces in the directions normal and tangential directions to the contact plane between two contacting particles and δ_n and δ_t are the corresponding deformations. Figure 89 shows a sketch of a pair of particles in contact.

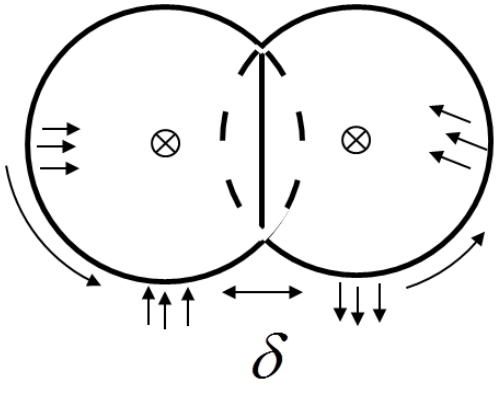

Figure 89: Sketch of a pair of overlapping particles, with the deformation δ labelled.

The stiffness and damping coefficients used to calculate the contact forces depend on the material properties of the contacting particles:

$$k_n = \frac{4}{3}\sqrt{R_{eff}}E_{eff}, \tag{A.3}$$

$$k_t = 8\sqrt{R_{eff}}G_{eff}, \tag{A.4}$$

$$\eta_n = \alpha\sqrt{m_{eff}k_n}, \tag{A.5}$$

$$\eta_t = \alpha\sqrt{m_{eff}k_t}. \tag{A.6}$$

R_{eff}, E_{eff}, G_{eff} and m_{eff} are the effective radius, Young's modulus, shear modulus and mass of the contact:

$$\frac{1}{R_{eff}} = \frac{1}{R_1} + \frac{1}{R_2}, \tag{A.7}$$

$$\frac{1}{E_{eff}} = \frac{1-\nu_1^2}{E_1} + \frac{1-\nu_2^2}{E_2}, \tag{A.8}$$

$$\frac{1}{G_{eff}} = \frac{2\left(1+\nu_1\right)\left(2-\nu_1\right)}{E_1} + \frac{2\left(1+\nu_2\right)\left(2-\nu_2\right)}{E_2}, \tag{A.9}$$

$$\frac{1}{m_{eff}} = \frac{1}{m_1} + \frac{1}{m_2}, \tag{A.10}$$

where R_1, R_2, E_1, E_2, ν_1, ν_2, m_1 and m_2 are the radius, Young's modulus, Poisson's ratio and mass of the two particles in contact, and α is a parameter that depends solely on the coefficient of restitution [42]. In this paper we use $\alpha=0.07$, which corresponds to a typical restitution coefficient of 0.9.

For the moisture models, we introduce an attractive moisture force, $F_{m\,(f)}$, which acts in the normal direction. The magnitude of this moisture force is determined depending on the moisture model used (detailed in Chapter 5, Chapter 6, and Chapter 7). Also, the presence of moisture and fine materials may affect the rolling/sliding behavior between contacting particles, and we model that effect by replacing the material friction coefficient μ with a variable $\mu_{m\,(f)}$. The general contact model which incorporates the effects of moisture and fines is then:

$$F_n = \begin{cases} -k_n\delta_n^{3/2} - \eta_n\delta_n^{1/4}\dot{\delta}_n + F_{m\,(f)}; & \delta_n > 0 \\ F_{m\,(f)} & ; -2s_{cr} < \delta_n \le 0 \\ 0 & ; \delta_n \le -2s_{cr} \end{cases} \tag{1.11}$$

$$F_t = \begin{cases} min\ \left\{ -k_t \delta_n^{1/2} \delta_t - \eta_t \delta_n^{1/4} \delta_t ,: \mu_{m(f)} F_n \right\} ; \delta_n > 0 \\ 0 \qquad\qquad\qquad\qquad\qquad\qquad\qquad\qquad\qquad\qquad ; \delta_n \leq 0 \end{cases} \tag{1.12}$$

where $2s_{cr}$ is some critical separation distance between a pair of particles, beyond which it is assumed the moisture force no longer has any effect.

Appendix B: Three Issues of Boundary Condition

In this Appendix, we investigate three explicit questions regarding boundary conditions of these simulations: (1) The effect of the coarse particle size distribution; (2) Physical boundaries specific to the LWD simulations, and (3) The choice of the implicit model of the hammer drop in the DCP test.

Varying the Coarse Particle Size Distribution (LWD Test)

In this section, we use some relatively simple mixtures to understand qualitatively the effect of a variation in macroscopic particle size distribution. We consulted the 2009 report of Siekmeier et al. [4] for some reasonable macroscopic combinations of grain sizes. Table 15 shows the percentage by volume of different macroscopic particle sizes in three mixed-size systems we used. As for our mono-sized 10 mm particle system, there is 10% variation in diameter for each mean particle diameter in the table.

Table 15: Percentage by volume size distribution of bulk particles in dry mixed-size systems. 10% polydispersity is added to each mean macroscopic particle size.

Mixture	Size 1		Size 2		Size 3	
	mm	%	mm	%	mm	%
Mono	10	100	-	-	-	-
Bi1	22	15	13	0	7	85
Bi2	22	0	13	7.5	7	92.5
Tri1	22	15	13	46	7	39

The size distributions were chosen to have some spread in the coarse grading number (CGN), as defined by Siekmeier et al. [4]:

$$CGN = \frac{(\%\leq 25mm) + (\%\leq 19mm) + (\%\leq 9.5mm) + (\%\leq 4.75mm)}{100\%} \qquad \text{(B.1)}$$

The *CGN* is a non-unique description of a granular mixture, but, as true of the *GN*, in general a high grading number corresponds to a mixture with a large amount of smaller and finer particles. Table 16 shows two representative values for the calculated grading number for each mixture in Table 15. The first number represents the macroscopic system only, and the second is the *CGN* calculated based on the assumption that the void space (~35%) is filled with material with diameters smaller than 4.75mm, which is not explicitly modeled in the DEM. Due to computational constraints, the number of bulk particles used in the DEM simulations was capped at 20,000.

Table 16: Coarse Grading Number for mixtures of different macroscopic size.

2*Mixture	CGN	
	0 % < 4.75mm	35% < 4.75mm
Mono	2.00	2.70
Bi1	2.70	3.15
Bi2	2.93	3.30
Tri	2.24	2.85

Figure 90 shows the peak deflection and effective modulus plotted as a function of *CGN* for the mixtures of different size distributions outlined in Tables 15 and 16. From these results we can see that size distribution has a significant effect on the LWD test results. However, in contrast with the estimated target values from Siekmeier et al. [4], the maximum deflection decreases with *CGN* and the effective modulus E_{LWD} increases with *CGN*. We note that this is not necessarily physically significant, as all of the results shown in Figure 90 are representative of results at the far left hand side of the plots in Figure 6. In other words, the estimated target value trends indicating an decrease of *E* with *CGN*, such as those reported by Siekmeier et al. [4] shown in Figure 6, could be due to chemical and other electromagnetic forces important for fine particles present in non-negligible quantities in the estimated target value data in Ref. [4]. These cannot be captured by simply changing the size distribution of the coarse particles. The latter results in macroscopic geometric packing effects, but does not give rise to the extreme surface forces present in fine particles such as clays and silts.

For this project, we use the tertiary mixture as a better representation of the actual distribution of the *coarse* particle size distribution more typical of granular mixtures used in pavement foundations. Yet we acknowledge that this does not capture the complex effects associated with the presence of fines.

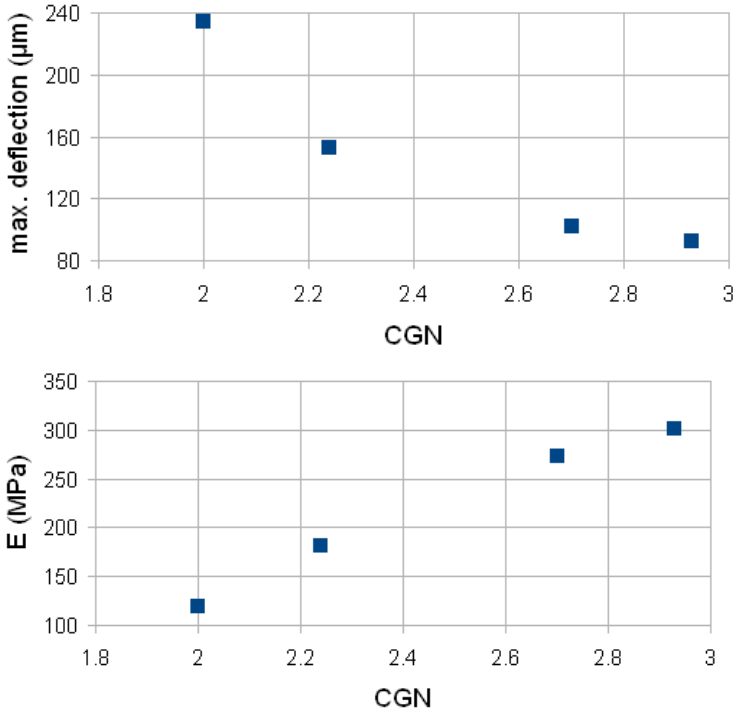

Figure 90: Peak deflection and effective modulus for mixed-size systems, plotted as a function of grading number (assuming no material smaller than 4.75mm in diameter.)

Boundary Effects in the LWD Test Simulation

Here we an exploration of the effect of boundary conditions on the results for our tertiary mixtures. Figure 91 is a sketch of the model cylinder with pertinent parameters in considering various boundary effects:

(1) those related to the finite cylinder size D_c;

(2) those related to the finite plate size D_p and

(3) those related to the finite size of the gap between the LWD plate and the cylinder walls δ (Figure 91).

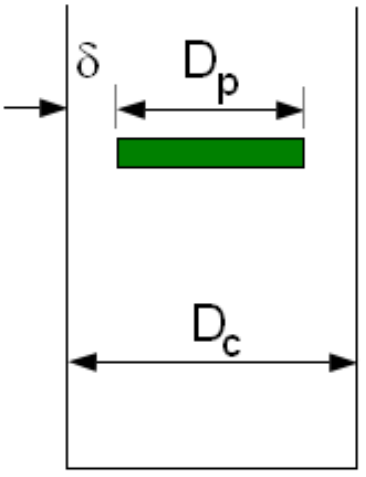

Figure 91: Sketch of cylinder, LWD plate and gap δ.

We investigated the boundary effects using five different combinations of plate diameter and cylinder diameter. These combinations are given in Table 17. In all cases, the cylinder is filled to the same height (170 mm) with the dry tertiary mixture *Tri* whose details are given in Table 15.

Table 17: Combinations of LWD plate diameter and cylinder diameter

Setup	Cylinder Diameter D_c (mm)	Plate Diameter D_p (mm)	Gap δ (mm)
1	260	200	30
2	260	100	80
3	130	100	15
4	130	70	30
5	160	100	30

Figure 92 shows the peak deflection Δ plotted as a function of δ. This is perhaps the boundary condition of greatest concern because the δ arising from our combination of cylinder diameter and plate diameter is of the same order of the largest particles in the mixture *Tri* (22 mm). However, there appears to be no systematic variation between Δ and δ within this range of parameters.

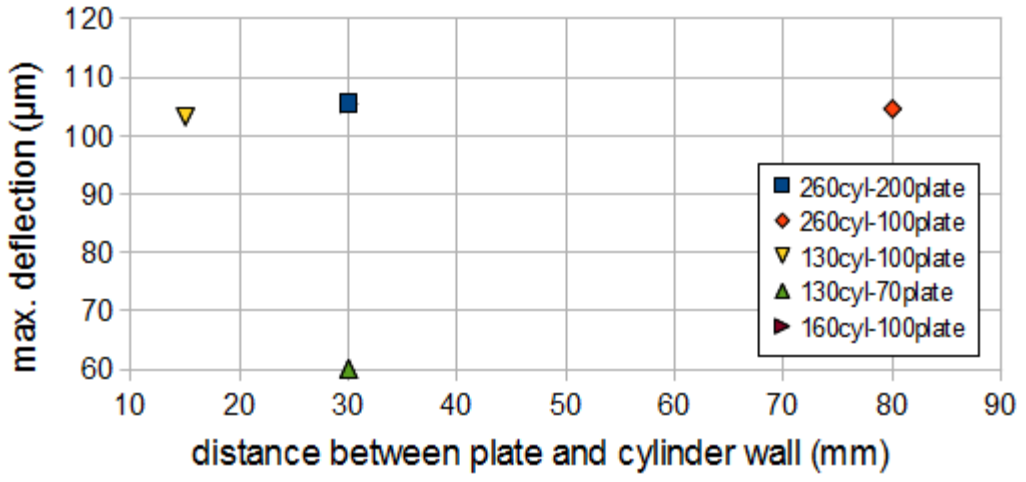

Figure 92: Peak deflection plotted as a function of gap δ.

Figure 93 shows the peak deflection Δ plotted as a function of cylinder diameter D_c. Again, while this would cause reasonable concern based on the artificial limitation of the system, there appears to be no systematic variation with D_c.

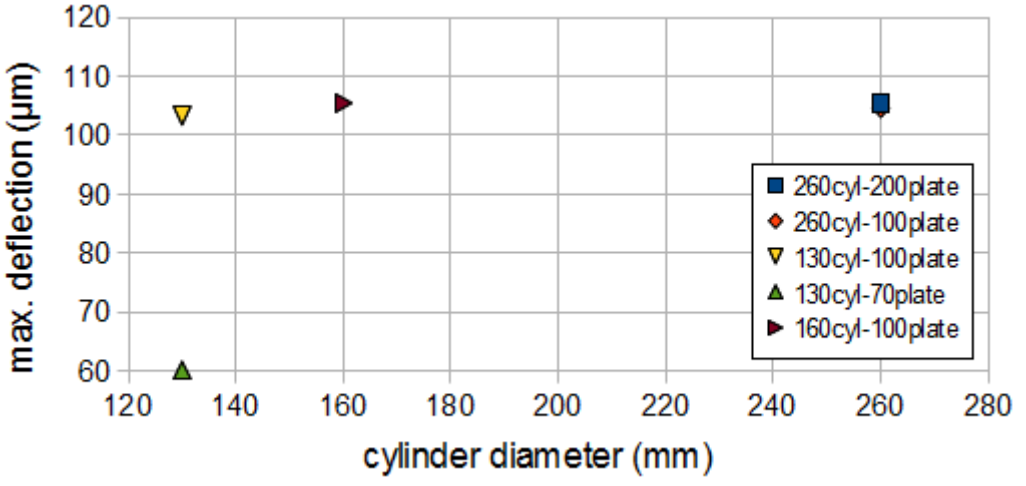

Figure 93: Peak deflection plotted as a function of cylinder diameter D_c.

Figure 94 shows the peak deflection Δ plotted as a function of plate diameter D_p. Here, there appears to be the clearest trend. For small values of D_p, Δ increases quickly and then plateaus. For all systems of the same value of D_p but different values of D_c and of δ, the resulting deflection Δ is essentially the same. Finally, the value of Δ plateaus well below the plate size we use. obtained for dry system with different size combinations, plotted against the distance between the plate edge and cylinder walls (δ), the cylinder diameter and the plate diameter respectively. Therefore, for the

parameters we use for this project, we feel that boundary effects associated with finite values of D_c and therefore δ are negligible.

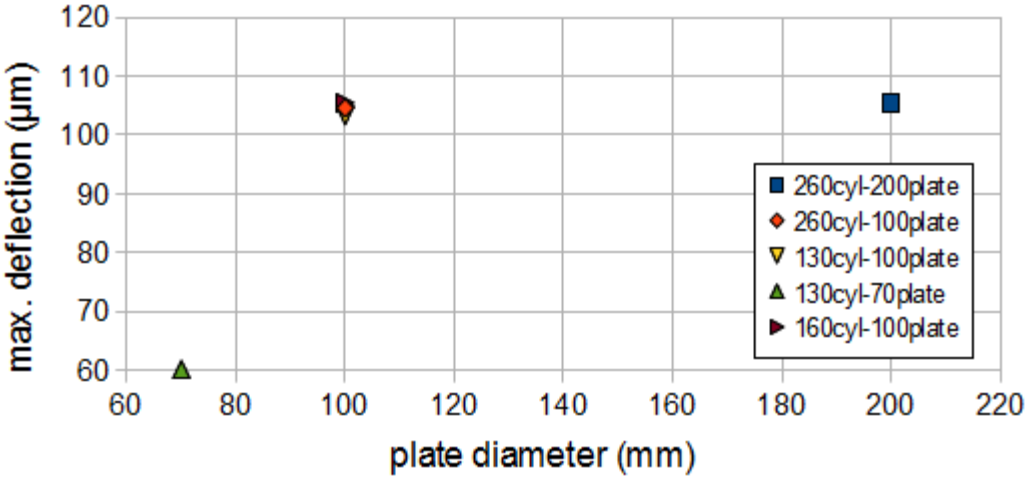

Figure 94: Peak deflection plotted as a function of plate diameter D_p.

Implicit Model of Hammer Drop (DCP Test)

As mentioned previously, the penetrations obtained with the original model described in Section 2.2 and the monosized 10 mm granular system have been significantly larger than that measured in the field. This is problematic in three ways. First, this may be an indication that our model for the DCP loading is unrealistic for the real physical properties of the DCP cone-rod assembly. Second, due to the limited height of the DEM cylinder, we are unable to perform consecutive impacts for the same system. Third, the proximity to the cylinder base brings up the question of whether the cylinder base is affecting the results.

In order to provide a solution to these problems, we derived an explicit time-varying load which is applied directly to the cone and used this instead of the modeled hammer drop. This provided the added benefits of reducing some computational time and allowing control of the load.

To determine an appropriate form for the load as a function of time, we considered measurements reported by Nazarian et al. [44]. Nazarian et al. [44] experimentally determined the load history during a DCP test by mounting a load cell on the anvil. They measured an approximately triangular force history over 0.1 ms duration with a peak force of ~80 kN. Similarly, we approximate the impact forces with a triangular force function over the same impact duration of 0.1 ms and vary the peak force. Figs. 95 and 96 show the load force histories for the original falling-hammer simulation, and the approximated loading with different peak forces.

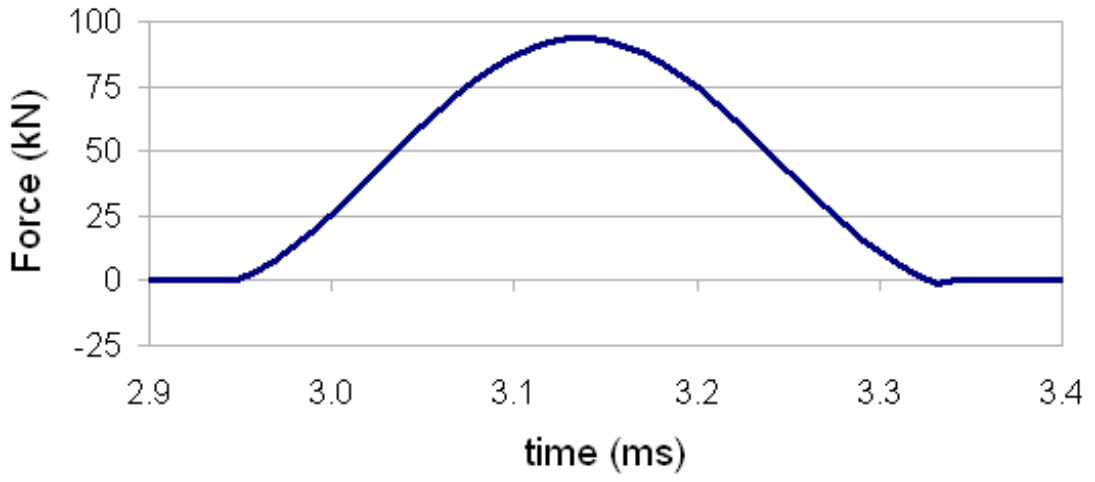

Figure 95: Force imparted by modeled falling hammer DCP cone-rod assembly.

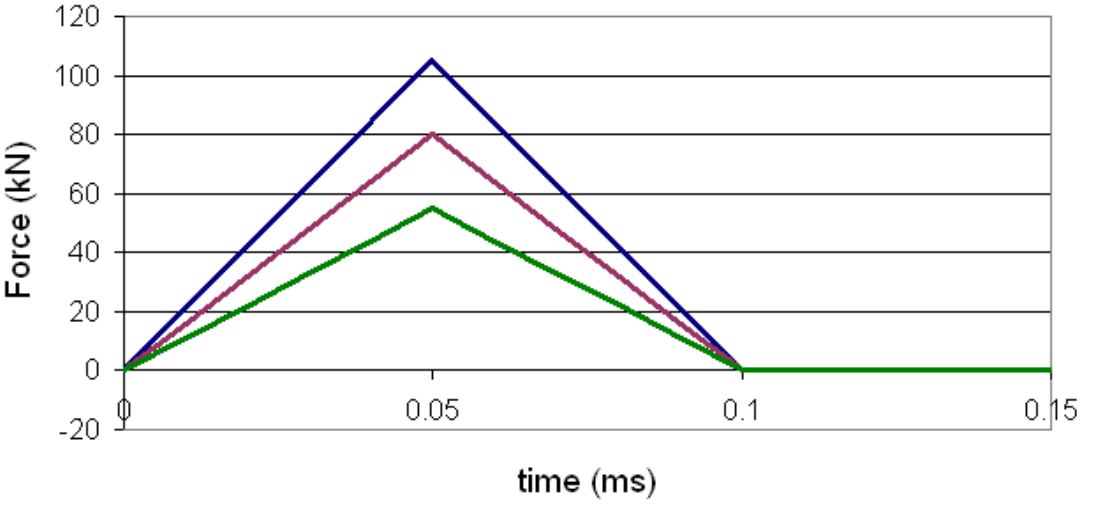

Figure 96: Trial force functions applied directly to DCP cone-rod assembly, as approximation of falling hammer.

The original falling-hammer simulation force function is slightly bell-shaped, but for the new model and the results reported here, we approximated the load vs. time function as a triangular function. The impact duration is ~0.4 ms, with a peak force of 93 kN. This resulting impulse is more than four times larger than that of Nazarian et al., which would explain the large penetrations we obtained in our 'first generation' results. We hypothesize that with a smaller impulse, which is true of the triangular force functions we applied, the penetration should be smaller.

Figure 97 shows the penetration obtained during the first impact for a mono-sized system with the different triangular force functions applied directly to the DCP cone-rod assembly.

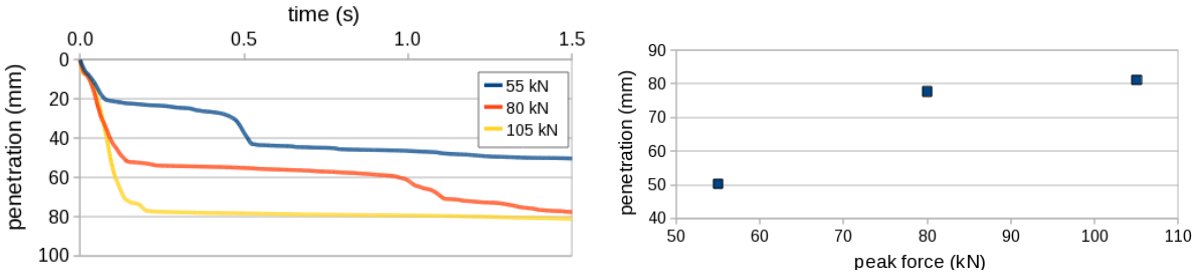

Figure 97: Penetration during single hammer impact given three different peak applied forces, for a mono-sized system with 5.1% gravimetric moisture content and surface tension γ*, plotted as a function of time (left) and as a function of peak force (right).

From Figure 97, for 0.1 ms impact duration, the penetration appears to reach a plateau of approximately 80 mm for large peak forces. This value is acceptable, as it allows us to perform multiple consecutive impacts while ensuring that the DCP remains far enough from the cylinder base to not need to consider boundary effects. For the simulation test results described in Section 5.4, we use a triangular force function as in Figure 98, with a peak force of 105 kN and a total impact duration of 0.1 ms.

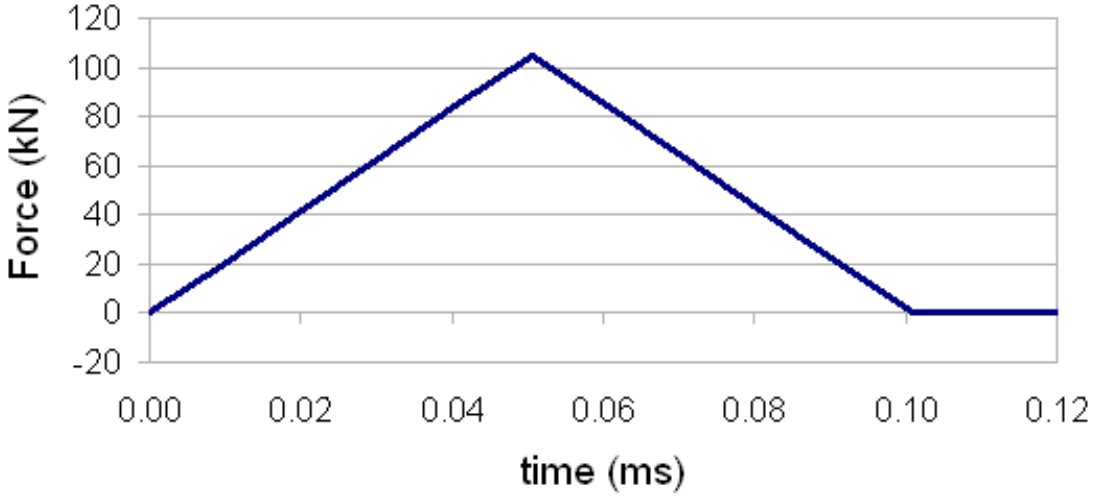

Figure 98: Force function applied directly to DCP cone-rod assembly for the model test results described in this report.

Appendix C: User’s Manual for DEMP-3D PFC3D Macro Use

Introduction

In this Appendix, we provide a user's manual for the DEMP-3D routines in PFC3D. In addition to the instructions in this Appendix, to run the code the user will need the appropriate macros for each of the tests (we provide these to MnDOT and LRRB in folders entitled 'Template_LWD' and 'Template_DCP' for each of the tests). The user will also need a license for the required version of PFC3D: PFC3D_EV 4.0 with the C++/UDM option.

We have provided the template files to MnDOT and LRRB in an electronic folder entitled 'MoistureModel_PFC3D'. This folder contains three sets of files: (1) the relevant version of the PFC3D installation (folder 'PFC4.0_1-8') (2) the corresponding technical memo from Itasca describing the details of the translation of the DEMP-3D contact model into a format appropriate for PFC3D (included in this task report as Appendix), and (3) template folders with files for each of the tests ('Template_LWD' and 'Template_DCP').

We begin this Appendix with a brief set of instructions on how to install the files we provide and how we recommend the user maintain them in the context of running PFC3D. The majority of the Appendix is intended to orient the user to the use of the routines themselves. This includes details as to which files correspond to specific stages of the LWD and DCP model tests and instructions for the user on how to adapt the files to the user's specifications.

Instructions for Initial One-Time Set-up Procedures

When the user first installs the DEMP-3D files to use on his / her computer (s)he must perform two one-time procedures as outlined below. The first is to make sure the paths are set up correctly, and the second is so that the computer type is correctly identified for the program. These steps only have to be performed once, unless the provided folders are shifted and/or renamed.

- Path set-up
  1. Open the file 'fistp_load.dat' in the folder 'PFC4.0_1-8' in a suitable text editor.
  2. Check that the two lines with the paths of the folders 'fist' and 'fistp' are accurate. In the files provided to MnDOT and LRRB, these files are in the same directory as 'fistp_load.dat', but the whole path depends on where the user copies the files.
  3. Update the directory path(s) if either are incorrect.
  4. Save and close the file 'fistp_load.dat'.
- Computer model set-up
  1. Determine if the computer's operating system is 32-bit or 64-bit.
  2. Open the folder 'fistp' in 'PFC4.0_1-8'.
  3. Open the file 'fistp_new.dvr' in a suitable text editor.
  4. Go to line 23, which reads 'model load....dll'.
  5. Change the two digits immediately before the '.dll' to '32' if the computer uses 32-bit, or '64' if the computer uses 64-bit.
  6. Save and close the file.

We emphasize here that, aside from the changes to the files 'fistp_load.dat' and 'fistp_new.dvr' mentioned above, the contents of 'MoistureModel_PFC3D' should *never* be modified; it is only to be used to start the program.

Before beginning to run any simulations, we recommend that the user makes a copy of the template folders for their active use (we will refer to this copy as the 'project folder') and that they save the original template folders in a location where they will not accidentally alter the files to serve as backup.

Basic Start-up Procedures

Once PFC3D is installed, we recommend the following procedure for starting up PFC3D for use with the DEMP-3D files we provide:

1. Check that the license key (if needed) is inserted.
2. Navigate to the location of 'MoistureModel_PFC3D'.
3. Open the folder 'PFC4.0_1-8'.
4. Open the folder 'pfc3d400_64' if the operating system is 64-bit (or 'pfc3d400_32' if the operating system is 32-bit).
5. Double-click on the PFC3D-EV executable '**evpfc3d_64**' (or '**evpfc3d_32**' if the operating system is 32-bit).
6. Select 'Open Existing Project...' when the window pops up.
7. Navigate to and open the project folder of choice, 'Template_LWD' or 'Template_DCP' (The user should navigate to a copy of the original template folder, not the original template folder itself which is serving as back-up)
8. Double-click on the file with extension '.p3prj'.

Basic Running Procedures

For details on how to run PFC3D, we refer the reader to the PFC3D user manual. Here, we provide a short set of instructions on how to use and run the files central to the DEMP-3D files for PFC3D.

Once the file with the extension '.p3prj' has been opened, a set of files and plot windows opens within PFC3D. As detailed in the next sections, each step in a particular DEMP-3D model test (e.g., particle initialization, compaction, and loading in the DCP or LWD test) has two files associated with it. Most, if not all, of the modifications will be performed by the user on the file with the extension '.p3dvr'.

1. Choose the model test step of choice (e.g., initializing, compaction, etc.)
2. Navigate to the window associated with that test step with extension '.p3dvr'.
3. Assign desired values to all parameters (initial values are included based on tests performed for this project, but they may be considered arbitrary).
4. If relevant, choose any additional variables to track throughout the simulation governed by this step. We anticipate that most users will find the default tracked variables sufficient (as detailed in the sections that follow). However, the advanced user may choose to modify which variables are plotted.

5. Save the '.p3dvr' file, particularly if there are not plans to run the simulation immediately.
6. If desired, open additional plot windows for new tracked variables.
7. Run the program. The most straightforward way to do this is to make sure the driver file window (i.e., associated with '.p3dvr' file) is open and then click on the 'run' button on the top menu bar.
8. Follow any special procedural steps required by the model test step. This may include, for example, 'continuing' the code after a programmed pause allows the user to check a crucial detail (we include detailed instructions in the sections that follow).
9. Allow the program to run to completion. We not that if the user stops the code before this point, the system state will not be saved, so this should only be done if there seems to be an error in the process.

As suggested in the procedure outlined above, throughout the test simulations we recommend that the user tracks variables that provide him/her an idea of how the system is evolving to help in their evaluation of the final results. We have included specific commands in the driver (.p3dvr) files that track certain variables. Examples for all tests include the average bulk particle vertical position and velocity, and the solid fraction of the system. Additionally, during each LWD model test, we have specified the tracking of the vertical position and velocity of the LWD plate, and during each DCP model test we track the cone-tip position of the DCP cone-rod assembly. PFC records these variables throughout time to a file specified in the driver file (detailed for some variables in the sections that follow). These variables may also be plotted, 'real-time', in the optional series of plot windows as the simulation progresses. The definitions (how they are calculated, etc.) of these tracked variables are written in FISH (PFC-specific programming language) and included in the .p3fis files for each test.

As we have noted, the tracking of each of these variables is optional. The user has the option of modifying the form of the variables that are tracked or even defining new variables to track. To do this, they must edit their respective FISH functions within the '.p3fis' file and then include appropriate tracking command within the corresponding '.p3dvr' file. In this way, whichever tracked variables the user chooses can be written to an output file and the plotted graphs exported. We describe briefly how to do so in the following sections, but for detailed instructions, we recommend the user refer to the appropriate sections in the PFC3D user manual involving the FISH language. Details regarding the variables that we used are given in the following sections for each test, as each variable first appears.

For any of the chosen tracked variables, the user can modify the associated plot windows following basic procedures within PFC3D (again, we refer the reader to the PFC3D user manual to do so). The experienced PFC3D user will note that those we include with the files we provide to MnDOT and LRRB were written for the PFC3D-EV version, and hence there are no separate plot formatting commands available within the code.

The next sub-section contains a bit more detail on the types of files written to adapt the DEMP-3D framework to PFC3D. It is included to orient the user to the types of files written for the model DCP and LWD tests to run in PFC3D with the particle contact model described for this project. However, it is not necessary for running the code unless the user intends to modify the contact model itself. If the user plans to adapt the code essentially as is, (s)he may choose to skip the next subsection and proceed to the details of each test beginning in Section 2.

Introduction to required FISH and C++ routines

To use the DEMP-3D LWD and DCP routines in the framework of PFC3D, two sets of details of the tests were translated into language usable by the routines in PFC3D: (1) the boundary conditions defining the LWD and DCP test simulations, and (2) the contact model including moisture and in which the coefficients depend on material parameters. As we detail shortly, the user need only to specify required test parameters within the driver (.p3dvr) files (the PFC-3D macros)) corresponding to each stage of the model LWD and DCP tests. We used C++ to translate the DEMP-3D contact model into the appropriate format for PFC3D. The details of the adaptation of the DEMP-3D contact model into the C++ code usable by PFC3D is provided in Appendix D. However, the user should never have to work with C++ unless a different contact model is desired. Instead, the parameters for the contact model and the boundary conditions of the test are all contained within the FISH language.

FISH is, as mentioned, the programming language specific to PFC that may be used to define additional functions or subroutines, sets of PFC commands that are rolled into a single command line. These new functions are saved in a file with a '.p3fis' extension for PFC3D. They are called at the beginning of the executable driver file (with an extension '.p3dvr') corresponding to each stage of the test simulations. In this project, for the LWD and DCP tests, some of the FISH functions we wrote set up the initial random configuration of particles, including the initial arrangement and random initial velocities of particles prior to their release. Other functions concern the details of the motion of objects with external applied forces, e.g., the LWD plate and the DCP cone-rod assembly. These are all detailed in the following sections.

PFC3D requires the use of C++ for a user-defined contact model, that is, a model which relates relative position and velocities of two objects with the force between them. This is compiled into a .dll which the program uses at each timestep to obtain the normal and tangential forces on a pair of objects (particle-particle or particle-wall). Instructions on creating a user-defined model are included in the user manual for PFC and so will not be detailed here. It is more important to note that because the DEMP-3D implementation requires the use of a specific non-standard model,

1. the PFC3D installation must come with the C++/UDM option and
2. the user must start PFC3D from the folder we provide and *not* from the Windows start menu which runs the regular installation of PFC3D.

As mentioned briefly we have already written and compiled a general form of the moisture contact model, and thus no further compilation on the user's end is necessary. However if the user intends to make modifications to the form of the contact model, the two files (source and header files) to modify are in 'PFC4.0_1-8/udmp/src'. The necessary compiler is Microsoft Visual C++ 2005, and the instructions to compile the .dll and after are included in the PFC instruction manual.

The rest of this Appendix is intended to orient the user to the FISH routines themselves. This includes details as to which files correspond to specific stages of the LWD and DCP model tests and instructions for the user on how to adapt the files to the user's specifications.

LWD Test Simulation

This section presents a brief guide to performing the LWD test using the DEMP-3D codes written for PFC3D. The required steps and corresponding files, in order of use, are:

1. Initializing
   - DropParticles.p3dvr
   - DropParticles.p3fis
2. Compaction
   - CompactParticles.p3dvr
   - CompactParticles.p3fis
   - AddMoisture.p3fis (optional)
3. Placement of LWD plate
   - AddPlate.p3dvr
   - AddPlate.p3fis
4. Loading
   - LWDLoading.p3dvr
   - LWDLoading.p3fis

The template project folder contains the project file LWD.p3prj which includes the driver and function files listed above, as well as several files to generate plot windows for visualization of the simulation progress. Changeable variables and tracked 'histories' used to produce these plots are detailed in the following subsections, with illustrations including the specific lines of code.

We note that all parameters in the code use SI units (m, kg, s etc). Additionally, we note that the .p3fis files contain internal FISH functions which are generally not meant to be modified by the user unless significant modification to details such as the test procedure, output variables, or contact model is required. Otherwise, all user-input should be performed within the .p3dvr files.

C.3.1 Initializing

DropParticles.p3dvr contains parameters required to initialize the system: spherical particles of a specified size distribution are suspended in a circular cylinder and then dropped under gravity. DropParticles.p3dvr also calls the accompanying file DropParticles.p3fis (Figure 99) which contains the required FISH functions to run this procedure with input values from the corresponding .p3dvr file.

```
new
call %fistp%\3d\new-Hill.dvr
call DropParticles.p3fis
```

Figure 99: PFC commands in file DropParticles.p3dvr starting a new simulation, and calling the relevant contact model and necessary function file.

Figure 99 shows the first few lines in DropParticles.p3dvr. Since this file is the very first file used in the simulation, the '**new**' command serves to begin a new simulation. The second line tells PFC to use the contact model from our DEMP-3D code instead of the default linear contact model. DropParticles.p3fis, called in the third line, contains the FISH functions relevant to the initializing and dropping process. These functions/subroutines contained within DropParticles.p3fis include details like how the particles' initial velocities are assigned and their initial suspended radial arrangement. They do not need to be modified, but if the user chooses to do so, we refer them to the PFC3D manual for detailed instructions.

```
; generate cylinder & base
set dp_cylrad = 0.13     ; cylinder radius
set dp_cylht = 10.0      ; cylinder height
dp_cylinder

; generate particles (note: 10% polydispersity for each size)
set dp_natm = 14662                          ; total number of particles
set dp_vol1frac = 0.15   dp_rad1 = 0.011  ; volume fraction with radius #1
set dp_vol2frac = 0.46   dp_rad2 = 0.0065 ; volume fraction with radius #2
set dp_vol3frac = 0.39   dp_rad3 = 0.0035 ; volume fraction with radius #3
dp_generateparticles
```

Figure 100: PFC commands in file DropParticles.p3dvr in which variables for setting up the LWD system are defined. (Values are given in SI units)

Some basic input parameters (Figure 100) are the cylinder radius **dp_cylrad**, the cylinder height **dp_cylht**, the total number of particles **dp_natm**, the mean diameters of each particle size, and the fraction of each particle size. The last two sets of variables define the size distribution are as follows: **dp_vol1frac**, **dp_vol2frac** and **dp_vol3frac** are the respective volume fractions of the total number of particles with corresponding mean diameters **dp_rad1**, **dp_rad2** and **dp_rad3**. There is a 10% polydispersity for each mean size to prevent local ordering or so-called 'crystallization'. Although Figure 100 shows only 3 mean sizes, the code currently allows for up to five different mean sizes.

Material properties (Figure 101) also have to be specified for both the particles and cylinder. For the particles these are: density, elastic modulus **hlg_E_b** and Poisson's ratio **hlg_nu_b**. For the walls, elastic modulus **hlg_E_w** and Poisson's ratio **hlg_nu_w**. Values for the friction coefficient between a pair of particles (**hlg_fric_bb**) and between a particle and a wall (**hlg_fric_bw**) also have to be given. These properties are required specifically for the Hertz-Mindlin contact model used in DEMP-3D, and are allocated to the relevant memory spaces in PFC using the command '**hl_setENu**'.

```
; assign material properties
prop density 2650.0      ; all existing particles
set hlg_E_b=29e9 hlg_nu_b=0.15 hlg_fric_bb=0.4
set hlg_E_w=210e9 hlg_nu_w=0.3 hlg_fric_bw=0.3
set hlg_dcon=0.07 hlg_Scr=0.0 hlg_Fmmax=0.0

hl_setENu
```

Figure 101: PFC commands in file DropParticles.p3dvr in which material properties are defined. (Values are given in SI units)

In Figure 101, the parameter **hlg_dcon** refers to a coefficient in the Hertz-Mindlin contact model which takes into account the coefficient of restitution. It is set to 0.07, which corresponds to a coefficient of restitution of 0.9. The user is encouraged to refer to Ref. [42] if he/she wishes to modify this value to reflect a different coefficient of restitution.

The next two parameters **hlg_Scr** and **hlg_Fmmax** are related to the moisture force contribution (more detail in next subsection). At this initialization stage to save computational time, we generally do not recommend moisture is included. In otherwords, for this step we recommend there is no 'moisture' and so both parameters are set initially to 0.

In PFC the timestep size is calculated internally and generally is not constant. It is possible to set a maximum stepsize - in Figure 102 it is set to be no larger than 1 μs.

```
set dt max 0.000001
save BeforeDropping.sav
pause
```

Figure 102: PFC commands in file DropParticles.p3dvr setting the maximum timestep size, and saving the system state prior to dropping the particles from their suspended arrangement. (Values are given in SI units)

At this point, before any calculations are made or terms defined for tracking, the system state is saved (BeforeDropping.sav). This is optional and included to provide the opportunity for reusing the initial arrangement of particles, as rerunning this file from the beginning results in a new initial random configuration. There is a built-in '**pause**' in the code, at which point the user should check that all the particles are within the cylinder and not touching the walls (the optional plot window 'LWD-system' shows the cylinder and particles in 3D). If all is fine then the user should type '**continue**' in the console which will allow the simulation to proceed.

```
; track average position, velocity and solid fraction over time
set fishcall 0 dp_trackproperties    ; set function to be called
history id=1 dp_time
history id=2 dp_avgz
history id=3 dp_avgv
history id=4 dp_maxz
history id=5 dp_volfrac
```

Figure 103: PFC commands in file DropParticles.p3dvr defining variables to be tracked throughout simulation.

Next, calculated variables (see Figure 103) include the maximum vertical position of the particles, their average vertical position and velocity, and the solid fraction. These terms are calculated using the FISH function **dp_trackproperties**. Their evolution with time is recorded (histories 1-5) and plotted in the optional plot windows 'VerticalPositions', 'VerticalVelocities' and 'SolidFraction'. There is another '**pause**' included at this point as a last minute check before beginning calculations. It is advised not to have any of the plot windows highlighted as the main view while calculations are ongoing as this forces PFC3D to update these plots continuously, and slows the progression of the model tests significantly.

```
cycle 1250000
history write 2 3 4 5 vs 1 file DropParticles.out
save AfterDropping.sav
```

Figure 104: PFC commands in file DropParticles.p3dvr concerning the calculations, final output and final saved state during the particle-dropping initialization stage.

After the assigned number of calculation cycles, the histories are written to a text file, and the system state saved to AfterDropping.sav (see Figure 104). If more calculation cycles are required, then repeat the '**cycle**' and '**save AfterDropping.sav**' commands as needed. It is also possible to terminate the calculations early (refer to the PFC user manual), if the user feels that a suitable state has already been reached. If this is the case, we note that the system state (needed to begin the next step) is not saved automatically. The user will have to enter a command manually in the console window, e.g., '**save AfterDropping.sav**' (see the PFC3D user manual for details).

C.3.2 Compaction

The compaction procedure follows immediately after the dropping procedure, and the relevant commands are in the driver file named CompactParticles.p3dvr. CompactParticles.p3fis contains the FISH functions relevant to the compaction process, while AddMoisture.p3fis contains a subroutine to calculate the volume-averaged radius of the current system. It is not pertinent to the compaction itself, but the calculated value is a possible length-scale used for the moisture force contribution.

```
;restore AfterDropping.sav
call CompactParticles.p3fis
call AddMoisture.p3fis     ; only if using volume-averaged radius as an input
```

Figure 105: PFC commands in file CompactParticles.p3dvr regarding the starting state for compaction, and calling necessary function files.

Figure 105 shows the first few lines in CompactParticles.p3dvr. The first line (commented out in the figure) concerns the starting system state (particle positions, velocities etc). If the user keeps the format of the files we originally provide to MnDOT and LRRB, the file will be entitled AfterDropping.sav as indicated in Figure 105. (If the user has chosen to save the completed dropping system state as something different, that filename, instead of 'AfterDropping.sav' should be included here). Typically, the user will be starting the compaction immediately after the dropping has completed. If this is the case, and PFC3D has not been turned off since the dropping routine has been run, then PFC3D will already be in the required state (AfterDropping.sav). The user can verify this by checking the list of saved states in PFC3D (we recommend the user consults the PFC3D manual for instructions on how to do this)– the current system state will be highlighted. On the other hand, if, before running the current (compaction) subroutine, the user had to shut down PFC3D, the 'system state' may not be the desired one as PFC3D automatically returns to its last active saved state prior to shut-down. In that case, the user must restore the system to the final saved state from when the initialization stage was completed (e.g., AfterDropping.sav). This is done by uncommenting the first line in the code (delete the ';' in front of the '**restore**' command). Otherwise if the user has just completed the initialization stage and is now commencing the

compaction stage, this first line is extraneous and can remain as a commented line. The next two lines call the necessary function files: CompactParticles.p3fis contains the FISH functions relevant to the compaction process, while AddMoisture.p3fis contains a subroutine to calculate the volume-averaged radius of the current system. It is not pertinent to the compaction itself, but the calculated value is a possible length-scale used for the moisture force contribution.

Moisture is 'added' at this point in the LWD test simulation procedure. Details regarding the moisture force model are included in the body of this report and so we include only the details of the model here necessary to follow and modify the code. The moisture force contribution to the normal force between a pair of particles has the form

$$F_m = \begin{cases} F_{m;max} e^{-s_{ij}/R_m}; s_{ij} < S_{cr} \\ 0 \qquad\qquad\quad ; s_{ij} \geq S_{cr} \end{cases} \tag{C.1}$$

where s_{ij} is half of the distance between a pair of particles *i* and *j*, and R_m is a 'decay' lengthscale which controls the decrease in moisture force with increasing particle separation. When s_{ij} exceeds a critical value S_{cr} the moisture force drops to zero.

In CompactParticles.p3dvr, the input parameters for the moisture force contribution are the critical half-separation distance **am_Scr**, the decay lengthscale **am_Rm** and the peak moisture force **am_maxFm**. Figure 106 shows a set of these values, with the critical half-separation and peak moisture force calculated using the liquid bridge model for a system with 8% gravimetric moisture content, and the volume-averaged bulk particle radius as the decay lengthscale. The advanced user may choose a different form for the decay length. If that is the case, they would not need the volume-averaged bulk particle radius and the line involving 'AddMoisture.p3fis' in the beginning of the file (see Figure 105) is unnecessary (as is the file AddMoisture.p3fis itself).

```
; input terms for moisture (Values must be calculated using appropriate model)
set am_Scr=0.001064675       ; approximate rupture distance of liquid bridge
set am_maxFm=0.225111633     ; maximum attractive force (N) due to moisture
set am_Rm=am_volrad          ; decay length scale  = volume-averaged radius

; assign moisture parameters for moisture force calculation
PROP hl_Rm=am_Rm  hl_Scr=am_Scr  hl_Fmmax=am_maxFm  ; for existing contacts
SET hlg_Rm=am_Rm hlg_Scr=am_Scr hlg_Fmmax=am_maxFm  ; for would-be contacts
```

Figure 106: PFC commands in file CompactParticles.p3dvr concerning the moisture. (Values are given in SI units)

Figure 107 shows the code associated with the creation of a 'lid' for the compaction process. The lid is assigned the same material properties as the cylinder (in the 'initiation' – particle dropping – routine) automatically, but other parameters like mass (**cp_lidm**) and its initial velocity (**cp_lidv_initial**) and height above the particles (**cp_lidz_lift**) for each impact are independently defined, as indicated in Figure 107. New variables that are tracked in this routine are the position

and velocity of the lid, which are also visualized in the plot windows 'VerticalPositions' and 'VerticalVelocities'. Due to settling time, we suggest that the minimal total time between impacts, **cp_impacttime**, is 0.5s.

```
; generate lid
cp_lid

; set material properties
hl_setENu

; impact-related settings
set cp_lidm = 15.0                ; lid mass 15kg
set cp_lidz_lift = 0.02          ; distance to lift lid for impact
set cp_lidv_initial = 0.0        ; initial velocity of lid at start
set cp_impacttime = 0.5       ; duration of single lid-drop

; track lid position and velocity over time
history id=6 cp_lidz
history id=7 cp_lidv

set dt max 0.000001       ; max timestep 1 microsecond
pause
```

Figure 107: PFC commands in file CompactParticles.p3dvr creating the 'lid' used for compaction. (Values are given in SI units) We note that the lid is assigned the same material properties as the cylinder automatically.

As with the dropping procedure, there is a 'pause' in the compaction procedure, during which the following items should be checked for before proceeding:

- Click the plot window 'LWD-system' in which the visualization of the system should appear. In this window, a short cylinder spanning the entire cross-section of the original tall cylinder should be present a small distance above the surface of the particles.
- Upon typing '**print fishcall**' in the console window, '**0 : dp_trackproperties**' and '**8 : _hl_NewContact**' should be among the output (see Figure 108).

The second check-item is especially important, as it indicates that the DEMP3D Hertz-Mindlin model is active, and that the bulk properties of the system (average vertical position and velocity, solid fraction etc) will be calculated. If the expected output is not present, in the console window type '**set fishcall 0 dp_trackproperties**'; press 'enter'; and then proceed with the rest of CompactParticles.p3dvr by typing '**continue**' in the console window.

```
Pfc3D>print fishcall
  Fishcall number     function name
  ---------------     -------------
   0                  dp_trackproperties
   8                  _hl_NewContact
```

Figure 108: Expected output in PFC console window after typing 'print fishcall', before commencing with compaction process.

The compaction process is a series of impacts, performed by cycling the commands '**cp_drop**' and '**cp_raise**' (see Figure 109). We suggest that the user saves the system state after each impact, and we have included the appropriate commands to do so in the code (see Figure 109). After the last impact (generally four are sufficient), the system is allowed to settle with the lid removed by having a relatively small number of calculation cycles following the last '**cp_raise**' command. The tracked histories are then written to an output file for postprocessing entitled "CompactParticles.out".

```
; drop lid, then lift after a while
; repeat 'cp_drop' and 'cp_raise' as needed (recommend 4 impacts).
cp_drop
cp_raise
save AfterCompaction1.sav
cp_drop
cp_raise
save AfterCompaction2.sav
cp_drop
cp_raise
save AfterCompaction3.sav
cp_drop
cp_raise
save AfterCompaction4.sav

cycle 500000     ; let system settle after last impact
save AfterCompaction.sav

history write 2 3 6 7 5 vs 1 file CompactParticles.out
```

Figure 109: PFC commands in file CompactParticles.p3dvr performing the compaction process.

C.3.3 Placement of LWD plate

The compaction procedure is followed immediately by the placement of the LWD plate on top of the system; the relevant commands are in the driver file named AddPlate.p3dvr. The necessary FISH functions are in AddPlate.p3fis.

Following compaction, the system is prepared for loading by placing the LWD plate on the surface. This routine requires the state of the system obtained from the compaction process. As such, as in the compaction routine, the user needs to make sure this state is loaded. If PFC3D has been restarted since the compaction has been run, or the user has any reason to believe the system is not in this state, the user should uncomment the line with 'AfterCompaction.sav' (or any other user-created name for the relevant system state) to which the system should be restored (see Figure 110).

```
;restore AfterCompaction.sav
call AddPlate.p3fis
```

Figure 110: PFC commands in file AddPlate.p3dvr regarding the starting state for placement of the LWD plate, and calling the necessary function file.

In this routine, the 'lid' used for compaction is replaced by a plate with specified radius **ap_platerad** and mass **ap_platem** representative of the LWD loading plate. The relevant commands are shown in the code in Figure 111.

```
; delete compaction lid
ap_removelid

; generate plate
set ap_platerad=0.1
ap_plate

; set material properties
hl_setENu

; plate settings
set ap_platem = 15.0          ; lid mass 15kg
```

Figure 111: PFC commands in file AddPlate.p3dvr deleting the compaction 'lid' and creating the plate representing the LWD. (Values are given in SI units)

The line '**set fishcall 3 ap_dropplate**' in the routine provided to MnDOT and LRRB 'turns on' the calculation of the vertical position and velocity of the LWD plate (see Figure 112). Walls in PFC do not have mass and so this function is necessary to ensure that the walls that are identified as the plate move as if the LWD plate is a rigid body with mass.

```
; track plate position and velocity over time
set fishcall 3 ap_dropplate          ; call ap_dropplate
history id=8 ap_platez
history id=9 ap_platev

set dt max 0.000001        ; max timestep 1 microsecond
save BeforePlate.sav
pause
```

Figure 112: PFC commands in file AddPlate.p3dvr defining the histories relevant for tracking the LWD plate and saving the system state prior to beginning calculations.

As with the compaction process, the following items should be checked for at the built-in pause, before proceeding:

- In the 'LWD-system' plot window, the compaction 'lid' should be replaced by a smaller disc representing the LWD plate.
- After typing '**print fishcall**' in the console window, the user should see '**0 : dp_trackproperties**', '**3 : ap_dropplate**' and '**8 : _hl_NewContact**' among the output (see Figure 113).

```
Pfc3D>print fishcall
  Fishcall number     function name
  ---------------     -------------
   0                  dp_trackproperties
   3                  ap_dropplate
   8                  _hl_NewContact
```

Figure 113: Expected output in PFC console window after typing 'print fishcall', before commencing with LWD plate placement.

The second check-item is especially important, as it indicates that the DEMP3D Hertz-Mindlin model is active, the bulk properties of the system (average vertical position and velocity, solid fraction etc) will be calculated, and the plate calculation function is in place. If the expected output is not present, type '**set fishcall 0 dp_trackproperties**' or '**set fishcall 3 ap_dropplate**' as needed and then proceed with the rest of AddPlate.p3dvr.

Figure 114 shows the PFC code concerning the final details of the placement of the plate. Essentially, the system is allowed to cycle through a number of timesteps (2000000, two seconds if the timestep size is approximately 1 μs as in the original version of the files, e.g., Figure 112). After this, the system state is saved to AfterPlate.sav and the tracked histories are written to an output file. The plate-specific calculation function **ap_dropplate** is stopped at the end with the line '**set fishcall 3 remove ap_dropplate**'.

We recommend that the user considers the the time dependence of the plate and particle displacements at this point. If the user determines that the system is not sufficiently steady, we recommend that the user allows the plate to continue settling before proceeding to the next step. This is done by restoring the system to the last saved state (AfterPlate.sav), allowing the system to cycle through an appropriate number of additional steps, and saving the system state again. For instance to extend the simulation by an additional 50000 steps, enter the following commands in the console window:

1. restore AfterPlate.sav
2. cycle 50000
3. save AfterPlate.sav

This causes PFC to calculate a further 50000 steps, and resave the system state under AfterPlate.sav. The user can, of course, choose to save this new state as something else to avoid overwriting the previous file.

```
cycle 2000000
save AfterPlate.sav
history write 2 3 8 9 5 vs 1 file AddPlate.out
set fishcall 3 remove ap dropplate
```

Figure 114: PFC commands in file AddPlate.p3dvr performing the plate placement process and writing output.

On the other hand, the user may find that the LWD plate has already reached a satisfactory 'settled' state and wishes to terminate the calculations early (see PFC manual to do so). In that case the

system state is *not* automatically saved, and the user must enter '**save AfterPlate.sav**' into the console window.

C.3.4 Loading

The next procedure is the actual model LWD test. LWDLoading.p3dvr and LWDLoading.p3fis contain the commands and FISH functions, respectively, for the loading stage of the LWD test simulation. This process requires the system in the state produced from the LWD plate-placement, so the system should be restored to this state (e.g., AfterPlate.sav as in Figure 115) if not already in that state.

```
;restore AfterPlate.sav
call LWDLoading.p3fis
```

Figure 115: PFC commands in LWDLoading.p3dvr starting the loading stage.

In the files we present to MnDOT and LRRB, we have set up the code to track the 'external' force applied to the LWD plate, representing the falling load, as well as the plate deflection (in μm). The relevant commands are shown in Figure 116.

We have set up the external force applied to the LWD plate as described in the task report. Specifically, it increases linearly to a peak of 6.25 kN (corresponding to 0.2 MPa normal stress on the LWD plate) over a period of 20 ms, then decreases linearly over the next 20 ms back to zero. This force function is written as a FISH function within LWDLoading.p3fis, and it is possible for an advanced user to modify it (please refer to the PFC user manual for help with FISH if necessary).

```
; track applied loading force and plate deflection over time
history id=11 lwd_extforce
history id=12 lwd_deflection
```

Figure 116: PFC commands in LWDLoading.p3dvr specifying the applied force and plate deflection as tracked variables.

Before running the loading function, the user should make use of the built-in 'pause' to check that the output in the console window after typing '**print fishcall**' is exactly as shown in Figure 108. This is to ensure that the previous calculation function regarding the LWD plate (**ap_dropplate**) is no longer 'turned on'. If it is still 'turned on', then the user will see an output similar to Figure 113, and the user should remove this calculation function by entering '**set fishcall 3 remove ap_dropplate**'. Otherwise, if the output is correct (i.e. similar to Figure 108) then the user can proceed by entering '**continue**' into the console window.

As with the field procedure, the LWD test comprises a series of loading impacts, each followed by a pause allowing for the system to settle. Here, a single impact is performed by specifying the total duration of an impact with pause time **lwd_impacttime**, and running the function '**lwd_load_start**' (see Figure 117).

```
set lwd_impacttime = 0.5
set dt max 0.000001
pause

lwd_load_start
save AfterImpact1.sav
```

Figure 117: PFC commands in file LWDLoading.p3dvr for a single impact. (Values are given in SI units)

We recommend the user check the progression of the plate and particles before proceeding with each additional impact. For example, if the plate has not finished 'settling' before the second impact starts, in other words, the specified impact duration of the first impact is found to be insufficient, and the user wants to extend the impact by 0.2 seconds then (s)he would enter the following commands in the console window:

1. restore AfterImpact1.sav
2. set lwd_impacttime = 0.2
3. lwd_load_continue
4. save AfterImpact1.sav

If, on the other hand, the user finds that the time initially specified for the impacts were too long, they can adjust the subsequent impacts' time using commands shown in Figure 118.

```
set lwd_impacttime = 0.55
lwd_load_start
save AfterImpact1.sav
lwd_load_start
save AfterImpact2.sav
lwd_load_start
save AfterImpact3.sav

set lwd_impacttime = 0.5
lwd_load_start
save AfterImpact4.sav
lwd_load_start
save AfterImpact5.sav
lwd_load_start
save AfterImpact6.sav
```

Figure 118: PFC commands in file LWDLoading.p3dvr for a series of impacts. (Values are given in SI units)

The impact duration **lwd_impacttime** can be adjusted in-between impacts if needed; otherwise the last specified value is used. The successive impacts are performed by repeating the '**lwd_load_start**' function. Saving the system state after each impact is highly recommended. Once the loading sequence is complete, an output file containing the evolving values of the tracked variables is set up to be written as shown in Figure 119.

```
save AfterLoading.sav
history write 2 3 8 9 5 vs 1 file LWDLoading.out
history write 11 12 vs 1 file LWDForceDeflection.out
```

Figure 119: PFC commands in file LWDLoading.p3dvr saving the final system state and writing the tracked variables to output files.

DCP Test Simulation

This section presents a brief guide to performing the DCP test using the codes written for PFC3D. The general procedure and corresponding required files, in order of use, are:

1. Initializing
    - DropParticles.p3dvr
    - DropParticles.p3fis
2. Compaction
    - CompactParticles.p3dvr
    - CompactParticles.p3fis
    - AddMoisture.p3fis (optional)
3. Placement of DCP cone-rod assembly
    - AddCone.p3dvr
    - AddCone.p3fis
4. Loading
    - DCPLoading.p3dvr
    - DCPLoading.p3fis

The template project folder contains the project file DCP.p3prj which includes the driver and function files listed above, as well as several plot windows for visualisation of the simulation progress. Changeable variables and tracked 'histories' used to produce these plots are detailed in the following subsections, with illustrations including the specific lines of code.

We note that all parameters in the code use SI units (m, kg, s etc). Additionally, we note that the .p3fis files contain internal FISH functions which are generally not meant to be modified by the user unless significant modification to details such as the test procedure, output variables, or contact model is required. Otherwise, all user-input should be performed within the .p3dvr files.

C.4.1 Initializing

DropParticles.p3dvr contains commands to initialize the system: spherical particles of a specified size distribution are suspended in a circular cylinder and then dropped under gravity. The accompanying file DropParticles.p3fis contains the required FISH functions, and reads input values from the corresponding .p3dvr file.

```
new
call %fistp%\3d\new-Hill.dvr
call DropParticles.p3fis
```

Figure 120: PFC commands in file DropParticles.p3dvr starting a new simulation, and calling the relevant contact model and necessary function file.

Figure 120 shows the first few lines in DropParticles.p3dvr. This file is the very first file used in the simulation, hence the '**new**' command to begin a new simulation. The second line tells PFC to use the contact model from our DEMP-3D code instead of the default linear contact model. DropParticles.p3fis, called in the third line, contains the FISH functions relevant to the initializing and dropping process. These functions/subroutines include details like how the particles' initial velocities are assigned and their initial suspended radial arrangement.

```
; generate cylinder & base
set dp_cylrad = 0.075        ; cylinder rad
set dp_cylht = 10.0          ; cylinder height
dp_cylinder

; generate particles (note: 10% polydispersity for each size)
set dp_natm = 17476                          ; total number of particles
set dp_vol1frac = 0.15   dp_rad1 = 0.011  ; volume fraction with radius #1
set dp_vol2frac = 0.46   dp_rad2 = 0.0065 ; volume fraction with radius #2
set dp_vol3frac = 0.39   dp_rad3 = 0.0035 ; volume fraction with radius #3
dp_generateparticles
```

Figure 121: PFC commands in file DropParticles.p3dvr in which variables for setting up the DCP system are defined. (Values are given in SI units)

Input variable parameters (Figure 121) are the cylinder radius **dp_cylrad**, the cylinder height **dp_cylht**, and the total number of particles **dp_natm**, as well those defining the size distribution: **dp_vol1frac**, **dp_vol2frac** and **dp_vol3frac** are the respective volume fractions of the total number of particles with corresponding mean diameters **dp_rad1**, **dp_rad2** and **dp_rad3**. There is a 10% polydispersity for each mean size to prevent crystallization. Although Figure 121 shows only 3 mean sizes, the code currently allows for up to five different mean sizes.

Material properties (Figure 122) have to be specified for both the particles and cylinder. For the particles these are: density, elastic modulus **hlg_E_b** and Poisson's ratio **hlg_nu_b**. For the walls, elastic modulus **hlg_E_w** and Poisson's ratio **hlg_nu_w**. Values for the friction coefficient between a pair of particles (**hlg_fric_bb**) and between a particle and a wall (**hlg_fric_bw**) also have to be given. These properties are required specifically for the Hertz-Mindlin contact model used in DEMP-3D, and are allocated to the relevant memory spaces in PFC using the command '**hl_setENu**'.

```
; assign material properties
prop density 2650.0      ; all existing particles
set hlg_E_b=29e9 hlg_nu_b=0.15 hlg_fric_bb=0.4
set hlg_E_w=210e9 hlg_nu_w=0.3 hlg_fric_bw=0.3
set hlg_dcon=0.07 hlg_Scr=0.0 hlg_Fmmax=0.0

hl_setENu
```

Figure 122: PFC commands in file DropParticles.p3dvr in which material properties are defined. (Values are given in SI units)

In Figure 122, the parameter **hlg_dcon** refers to a coefficient in the Hertz-Mindlin contact model which takes into account the coefficient of restitution. It is set to 0.07, which corresponds to a coefficient of restitution of 0.9. The user is encouraged to refer to Ref. [42] if he/she wishes to modify this value to reflect a different coefficient of restitution.

The next two parameters **hlg_Scr** and **hlg_Fmmax** are related to the moisture force contribution (more detail in next subsection). At this initialization stage there is no 'moisture' and so both parameters are set to 0.

In PFC the timestep size is calculated internally and generally is not constant. It is possible to set a maximum stepsize - in Figure 123 it is set to be no larger than 1 μs.

```
set dt max 0.000001
save BeforeDropping.sav
pause
```

Figure 123: PFC commands in file DropParticles.p3dvr setting the maximum timestep size, and saving the system state prior to dropping the particles from their suspended arrangement. (Values are given in SI units)

At this point, before any calculations are made or terms defined for tracking, the system state is saved (BeforeDropping.sav). This is optional and included to provide the opportunity for reusing the initial arrangement of particles, as rerunning this file from the beginning results in a new initial random configuration. There is a built-in '**pause**' in the code, at which point the user should check that all the particles are within the cylinder and not touching the walls (the optional plot window 'DCP-system' shows the cylinder and particles in 3D). If all is fine then typing '**continue**' in the console window will proceed with the simulation.

```
; track average position, velocity and solid fraction over time
set fishcall 0 dp_trackproperties    ; set function to be called
history id=1 dp_time
history id=2 dp_avgz
history id=3 dp_avgv
history id=4 dp_maxz
history id=5 dp_volfrac
```

Figure 124: PFC commands in file DropParticles.p3dvr defining variables to be tracked throughout simulation.

Next, calculated variables (see Figure 124) include the maximum vertical position of the particles, their average vertical position and velocity, and the solid fraction. These terms are calculated using the FISH function **dp_trackproperties**. Their evolution with time is recorded (histories 1-5) and plotted in the optional plot windows 'VerticalPositions', 'VerticalVelocities' and 'SolidFraction'. There is another '**pause**' included at this point as a last minute check before beginning calculations. It is advised not to have any of the plot windows as the main view while calculations are ongoing as this forces PFC3D to update these plots continuously, and slows the progression of the model tests significantly.

```
cycle 2500000
history write 2 3 4 5 vs 1 file DropParticles.out
save AfterDropping.sav
```

Figure 125: PFC commands in file DropParticles.p3dvr concerning the calculations, final output and final saved state during the particle-dropping initialization stage.

After the assigned number of calculation cycles, the histories are written to a text file, and the system state saved to AfterDropping.sav (see Figure 125). If more calculation cycles are required, then repeat the '**cycle**' and '**save AfterDropping.sav**' commands as needed. It is also possible to terminate the calculations early (refer to the PFC user manual), if the user feels that a suitable state has already been reached. If this is the case, we note that the system state (needed to begin the next step) is not saved automatically. The user will have to enter a command manually in the console window, e.g., '**save AfterDropping.sav**' (see the PFC3D user manual for details).

C.4.2 Compaction

The compaction procedure follows immediately after the dropping procedure, and the relevant commands are in the driver file named CompactParticles.p3dvr. CompactParticles.p3fis contains the FISH functions relevant to the compaction process, while AddMoisture.p3fis contains a subroutine to calculate the volume-averaged radius of the current system. It is not pertinent to the compaction itself, but the calculated value is a possible length-scale used for the moisture force contribution.

```
;restore AfterDropping.sav
call CompactParticles.p3fis
call AddMoisture.p3fis     ; only if using volume-averaged radius as an input
```

Figure 126: PFC commands in file CompactParticles.p3dvr regarding the starting state for compaction, and calling necessary function files.

Figure 126 shows the first few lines in CompactParticles.p3dvr. The first line (commented out in the figure) concerns the starting system state (particle positions, velocities etc). If the user keeps the format of the files we originally provide to MnDOT and LRRB, the file will be entitled AfterDropping.sav as indicated in Figure 126. (If the user has chosen to save the completed

dropping system state as something different, that filename, instead of 'AfterDropping.sav' should be included here). Typically, the user will be starting the compaction immediately after the dropping has completed. If this is the case, and PFC3D has not been turned off since the dropping routine has been run, then PFC3D will already be in the required state (AfterDropping.sav). The user can verify this by checking the list of saved states in PFC3D (we recommend the user consults the PFC3D manual for instructions on how to do this)– the current system state will be highlighted. On the other hand, if, before running the current (compaction) subroutine, the user had to shut down PFC3D, the 'system state' may not be the desired one as PFC3D automatically returns to its last active saved state prior to shut-down. In that case, the user must restore the system to the final saved state from when the initialization stage was completed (e.g., AfterDropping.sav). This is done by uncommenting the first line in the code (delete the ';' in front of the '**restore**' command). Otherwise if the user has just completed the initialization stage and is now commencing the compaction stage, this first line is extraneous and can remain as a commented line. The next two lines call the necessary function files: CompactParticles.p3fis contains the FISH functions relevant to the compaction process, while AddMoisture.p3fis contains a subroutine to calculate the volume-averaged radius of the current system. It is not pertinent to the compaction itself, but the calculated value is a possible length-scale used for the moisture force contribution.

Moisture is 'added' at this point in the DCP test simulation procedure. Details regarding the moisture force model are included earlier in this report and so the model will not be elaborated in great detail here. The moisture force contribution to the normal force between a pair of particles has the form

$$F_m = \begin{cases} F_{m;max} e^{-s_{ij}/R_m}; s_{ij} < S_{cr} \\ 0 \qquad\qquad\quad ; s_{ij} \geq S_{cr} \end{cases} \tag{C.2}$$

where s_{ij} is half of the distance between a pair of particles *i* and *j*, and R_m is a 'decay' lengthscale which controls how rapidly the moisture force decreases with increasing particle separation. When s_{ij} exceeds a critical value S_{cr} the moisture force drops to zero.

In CompactParticles.p3dvr, the input parameters for the moisture force contribution are the critical half-separation distance **am_Scr**, the decay lengthscale **am_Rm** and the peak moisture force **am_maxFm**. Figure 127 shows a set of these values, with the critical half-separation and peak moisture force calculated using the liquid bridge model for a system with 12% gravimetric moisture content, and the volume-averaged bulk particle radius as the decay lengthscale. The advanced user may choose a different form for the decay length. If that is the case, they would not need the volume-averaged bulk particle radius and the line involving 'AddMoisture.p3fis' in the beginning of the file (see Figure 126) is unnecessary (as is the file AddMoisture.p3fis itself).

```
; input terms for moisture (Values must be calculated using appropriate model)
set am_Scr=0.001064675       ; approximate rupture distance of liquid bridge
set am_maxFm=0.225111633     ; maximum attractive force (N) due to moisture
set am_Rm=am_volrad          ; decay length scale  = volume-averaged radius

; assign moisture parameters for moisture force calculation
PROP hl_Rm=am_Rm  hl_Scr=am_Scr  hl_Fmmax=am_maxFm  ; for existing contacts
SET hlg_Rm=am_Rm hlg_Scr=am_Scr hlg_Fmmax=am_maxFm  ; for would-be contacts
```

Figure 127: PFC commands in file CompactParticles.p3dvr concerning the 'addition' of moisture. (Values are given in SI units)

Figure 128 shows the code overseeing the creation of a closed cylinder for the compaction process. In subsequent stages of the code – the DCP model test itself – this cylinder is used as a surcharge load of granular material, and is thus assigned the same material properties as the particles (in the 'initiation' – particle dropping – routine) automatically. Its mass (**cp_surchargem**) and its initial velocity (**cp_surchargev_initial**) and height above the particles (**cp_surchargez_lift**) for each impact are user-defined (the mass given in Figure 128 is the equivalent mass for a 600mm-thick layer of granular material with 2650 kg/m^3 density and 0.6 solid fraction). Additional terms to be tracked are the position and velocity of the base of the cylinder (surcharge layer), which are also visualized in the plot windows 'VerticalPositions' and 'VerticalVelocities'. Based on our experience with the parameters we tested, we suggest that the time from the beginning of one impact to the next, **cp_impacttime**, is at least 0.25 seconds to allow for the system to settle after each impact.

```
; generate surcharge layer
cp_surcharge

; assign material properties
hl_setENu

; impact-related settings
set cp_surchargem = 16.86       ; surcharge mass (= 0.6m layer
set cp_surchargez lift = 0.02   ; distance to lift lid for impact
set cp_surchargev_initial = 0.0; initial velocity of surcharge
set cp_impacttime = 0.25        ; duration of single lid-drop

; track surcharge position and velocity over time
history id=6 cp_surchargez
history id=7 cp_surchargev

set dt max 0.000001        ; max timestep 1 microsecond
pause
```

Figure 128: PFC commands in file CompactParticles.p3dvr creating the 'lid' used for compaction. (Values are given in SI units)

As with the dropping procedure, there is a 'pause' in the compaction procedure, during which the following items should be checked for before proceeding:

- Click the plot window 'LWD-system' in which the visualization of the system should appear. In this window, a short cylinder spanning the entire cross-section of the original tall cylinder should be present a small distance above the surface of the particles.
- Upon typing '**print fishcall**' in the console window, '**0 : dp_trackproperties**' and '**8 : _hl_NewContact**' should be among the output (see Figure 129).

The second check-item is especially important, as it indicates that the DEMP3D Hertz-Mindlin model is active, and that the bulk properties of the system (average vertical position and velocity, solid fraction etc) will be calculated. If the expected output is not present, in the console window type '**set fishcall 0 dp_trackproperties**'; press 'enter'; and then proceed with the rest of CompactParticles.p3dvr by typing '**continue**' in the console window.

```
Pfc3D>print fishcall
  Fishcall number     function name
  ---------------     -------------
   0                  dp_trackproperties
   8                  _hl_NewContact
```

Figure 129: Expected output in PFC console window after typing 'print fishcall', before commencing with compaction process.

The compaction process is a series of impacts, performed by cycling the commands '**cp_drop**' and '**cp_raise**' (see Figure 130). We suggest that the user saves the system state after each impact, and we have included the appropriate commands to do so in the code (see Figure 130). After the last impact (generally six provide sufficient compaction), the system is allowed to settle with the cylinder (surcharge) *remaining on the surface* by ending with a number of calculation cycles following the last '**cp_drop**' command instead of another '**cp_raise**'. The tracked histories are then written to an output file named 'CompactParticles.out' for postprocessing, if needed.

```
; drop surcharge, then lift after a while
; repeat 'cp_drop' and 'cp_raise' as needed (recommend 6 impacts).
cp_drop
cp_raise
save AfterCompaction1.sav
cp_drop
cp_raise
save AfterCompaction2.sav
cp_drop
cp_raise
save AfterCompaction3.sav
cp_drop
cp_raise
save AfterCompaction4.sav
cp_drop
cp_raise
save AfterCompaction5.sav
cp_drop
save AfterCompaction6.sav

cycle 500000     ; let system settle after last impact without removing surcharge
save AfterCompaction.sav

history write 2 3 6 7 5 vs 1 file CompactParticles.out
```

Figure 130: PFC commands in file CompactParticles.p3dvr performing the compaction process.

C.4.3 Placement of DCP cone-rod assembly

Following compaction, the system is prepared for loading by placing the cone-rod assembly representing the DCP on the surface. The relevant commands are in the driver file named AddCone.p3dvr. The necessary FISH functions are in AddCone.p3fis. This routine requires the state of the system obtained from the compaction process. As such, as in the compaction routine, the user needs to make sure this state is loaded. If PFC3D has been restarted since the compaction has been run, or the user has any reason to believe the system is not in this state, the user should uncomment the line with 'AfterCompaction.sav' (or any other user-created name for the relevant system state) to which the system should be restored (see Figure 131).

```
;restore AfterCompaction.sav
call AddCone.p3fis
```

Figure 131: PFC commands in file AddCone.p3dvr regarding the starting state for placement of the cone-rod assembly, and calling the necessary function file.

For this test, a cone-rod assembly is used to represent the DCP. It is made up of a thin cylinder with a specified radius **ac_conerad**, a 60° cone with the same base radius, and a sphere of 1mm radius at the tip of the cone. The entire assembly is assigned a mass **ac_conem**, and automatically given the same material properties as the cylinder (defined during the initializing - dropping - subroutine) containing the particles. Here the only user input required is for **ac_conerad** and **ac_conem**, as shown in the code in Figure 132.

```
; generate cone-rod assembly
set ac_conerad=0.01
ac_cone

; assign material properties
hl_setENu

; cone-rod assembly settings
set ac_conem = 13.0          ; DCP mass 13kg
```

Figure 132: PFC commands in file AddCone.p3dvr creating the cone-rod assembly representing the DCP. (Values are given in SI units)

Even though the surcharge layer is still present, it does not interact with the cone-rod assembly. As it is meant to be a loose layer of material that the DCP has already penetrated, the initial position of the tip of the cone-rod assembly is just below the base of the surcharge cylinder.

The line '**set fishcall 3 ac_dropcone**' in the routine provided to MnDOT and LRRB 'turns on' the calculation of the vertical position and velocity of the cone-tip (see Figure 133). Walls in PFC do not have mass and so this function is necessary to ensure that the walls that are identified as the cone-rod assembly move as if the DCP is a rigid body with mass.

```
; track position and velocity of cone-tip over time
set fishcall 3 ac_dropcone           ; cone motion
history id=8 ac_conez
history id=9 ac_conev
pause
```

Figure 133: PFC commands in file AddCone.p3dvr defining the histories relevant for tracking the cone-tip and activating the calculation function for the DCP.

As with the compaction process, the following items should be checked for at the built-in pause before proceeding:

- In the 'DCP-system' plot window, the surcharge layer should still be resting on top of the particles.
- The cone-rod assembly representing the DCP should be penetrating the surcharge layer, with the tip just penetrating the base. This may not be obvious unless the user 'zooms' in.
- After typing '**print fishcall**' in the console window, the user should see '**0 : dp_trackproperties**', '**3 : _cp_dropsurcharge**', '**3 : ac_dropcone** and '**8 : _hl_NewContact**' among the output (see Figure 134).

```
Pfc3D>print fishcall
  Fishcall number      function name
  ---------------      -------------
   0                   dp_trackproperties
   3                   ac_dropcone
   3                   _cp_dropsurcharge
   8                   _hl_NewContact
```

Figure 134: Expected output in PFC console window after typing 'print fishcall', before commencing with DCP placement penetration.

The third check-item is especially important, as it indicates that the DEMP3D Hertz-Mindlin model is active, the bulk properties of the system (average vertical position and velocity, solid fraction etc) will be calculated, and both the surcharge and cone-rod assembly calculation functions are in place. If any of the expected output is not present, type '**set fishcall 0 dp_trackproperties**', '**set fishcall 3 _cp_dropsurcharge**' or '**set fishcall 3 ac_dropcone**' as needed and then proceed with the rest of AddCone.p3dvr.

Figure 135 shows the PFC code concerning the final details of the placement of the cone-rod assembly. Essentially, the system is allowed to cycle through a number of timesteps (1800000, 1.8 seconds if the timestep size is approximately 1 μs as in the original version of the files, e.g., Figure 128). After this, the system state is saved to AfterCone.sav and the tracked histories are written to an output file.

We recommend that the user considers the the time dependence of the cone-tip and particle displacements at this point. If the user determines that the system is not sufficiently steady, we recommend that the user allows the cone-rod assembly to continue settling before proceeding to the next step. This is done by restoring the system to the last saved state (AfterCone.sav), allowing the system to cycle through an appropriate number of additional steps, and saving the system state again. For instance to extend the simulation by an additional 50000 steps, enter the following commands in the console window:

1. restore AfterCone.sav
2. cycle 50000
3. save AfterCone.sav

This causes PFC to calculate a further 50000 steps, and resave the system state under AfterCone.sav. The user can, of course, choose to save this new state as something else to avoid overwriting the previous file.

```
cycle 1800000
save AfterCone.sav
history write 2 3 8 9 vs 1 file AddCone.out
```

Figure 135: PFC commands in file AddCone.p3dvr performing the cone-rod placement process and writing output.

On the other hand, the user may find that the cone-rod assembly has already reached a satisfactory 'settled' state and wishes to terminate the calculations early (see PFC manual to do so). In that case the system state is *not* automatically saved, and the user must enter '**save AfterCone.sav**' into the console window.

C.4.4 Loading

The next procedure is the actual model DCP test. DCPLoading.p3dvr and DCPLoading.p3fis contain the commands and FISH functions, respectively, for the loading stage of the DCP test simulation. This process requires the system in the state produced from the DCP cone-rod assembly placement, so the system should be restored to this state (e.g., AfterCone.sav as in Figure 136) if not already in that state.

```
;restore AfterCone.sav
call DCPLoading.p3fis
```

Figure 136: PFC commands in DCPLoading.p3dvr starting the loading stage.

In the previous subroutine (initial placement of the cone-rod assembly), no 'external' force was applied to the cone-rod assembly so that calculation function ('**ac_dropcone**') has to be removed, as shown in the first line of Figure 137. In the files we present to MnDOT and LRRB, we have set up the code to track the 'external' force applied to the DCP cone-rod assembly, representing the falling load, as well as the cone-tip penetration (in mm). The relevant commands are shown in Figure 137.

We have set up the external force applied to the DCP as described in the task report. Specifically, it increases linearly to a peak of 105 kN over a period of 0.05 ms, then decreases linearly over the next 0.05 ms back to zero. This force function is written as a FISH function within LWDLoading.p3fis, and it is possible for an advanced user to modify it (please refer to the PFC user manual for help with FISH if necessary).

```
; track applied external force and cone-tip penetration over time
set fishcall 3 remove ac_dropcone    ; remove old calculation for cone
history id=11 dcp_extforce
history id=12 dcp_penetration
```

Figure 137: PFC commands in DCPLoading.p3dvr removing the previous cone-specific calculation function and specifying the applied force and cone-tip penetration as tracked variables.

Before running the loading function, the user should make use of the built-in 'pause' to check that the output in the console window after entering '**print fishcall**' is exactly as shown in Figure138. This is to ensure that the previous calculation function regarding the cone-rod assembly (**ac_dropcone**) is no longer 'turned on'. If it is still 'turned on', then the user will see an output similar to Figure 135, and the user should remove this calculation function by entering '**set fishcall 3 remove ac_dropcone**'. Otherwise, if the output is correct (i.e. similar to Figure 138) then the user can proceed by entering '**continue**' into the console window.

```
Pfc3D>print fishcall
  Fishcall number     function name
  ---------------     -------------
   0                  dp_trackproperties
   3                  _cp_dropsurcharge
   8                  _hl_NewContact
```

Figure 138: Expected output in PFC console window after typing 'print fishcall', before commencing with DCP loading.

As with the field procedure, the DCP test is made up of a series of penetrations due to succesive hammer blows, each followed by a pause allowing for the system to settle. Here, a single blow is performed by specifying the total duration of an impact with pause time **dcp_impacttime**, and running the function '**dcp_load_start**' (see Figure 139).

```
set dcp_impacttime = 1.5
pause

dcp_load_start
save AfterImpact1.sav
```

Figure 139: PFC commands in file DCPLoading.p3dvr for a single hammer blow. (Values are given in SI units)

We recommend the user check the progression of the cone-tip and particles before proceeding with each additional hammer blow. For example, if the cone-rod assembly has not finished 'settling' before the second hammer blow starts, in other words, the specified impact duration of the first hammer blow is found to be insufficient, and the user wants to extend the impact by 0.2 seconds then (s)he would enter the following commands in the console window:

1. restore AfterImpact1.sav
2. set dcp_impacttime = 0.2
3. dcp_load_continue
4. save AfterImpact1.sav

If, on the other hand, the user finds that the time initially specified for the hammer blows were too long, they can adjust the subsequent hammer blows' time using commands shown in Figure 140.

```
set dcp_impacttime = 1.5
dcp_load_start
save AfterImpact1.sav
dcp_load_start
save AfterImpact2.sav

set dcp_impacttime = 1.55
dcp_load_start
save AfterImpact3.sav
dcp_load_start
save AfterImpact4.sav
dcp_load_start
save AfterImpact5.sav
```

Figure 140: PFC commands in file DCPLoading.p3dvr for a series of impacts. (Values are given in SI units)

The impact duration **dcp_impacttime** can be adjusted in-between hammer blows if needed; otherwise the last specified value is used. The successive hammer blows are performed by repeating the '**dcp_load_start**' function. Saving the system state after each impact is highly

recommended. Once the loading sequence is complete, an output file containing the evolving values of the tracked variables is set up to be written as shown in Figure 141.

```
save AfterLoading.sav
history write 2 3 8 9 vs 1 file DCPLoad.out
history write 11 12 vs 1 file DCP_PenetrationHistory.out
```

Figure 141: PFC commands in file DCPLoading.p3dvr saving the final system state and writing the tracked variables to output files.

Appendix D: PFC3D Technical Memorandum

Technical Memorandum

ITASCA
Consulting Group, Inc.

Date: February 8, 2013

To: Kimberly Hill and Danielle Tan

From: David Potyondy

Re: Hill Contact Model in *PFC3D_EV*

Ref: ICG12-2721-08TM

The Hill contact model, as implemented in *PFC3D_EV*,[1] is described in this memo. The implementation is embodied in a parameterized set of FISH functions, which we refer to as a FISH environment. The FISH environment is contained in PFC private Fishtank 1-8 (which uses *PFC3D_EV* 4.0-196 and PFC Fishtank 1-117).[2] The Hill contact model is implemented within *PFC3D_EV* 4.0 as the user-defined contact model **udm_Hill** version 8. Both dry and wet DEM materials are supported.

[1] *PFC3D_EV* is the Enhanced-Visualization option for *PFC3D*. Both *PFC3D* and *PFC3D_EV* are built on the same computational kernel, but *PFC3D_EV* replaces the graphical interface of *PFC3D* with a state of the art graphical user interface that includes advanced visualization techniques. Both programs will produce the same results when executing the same set of commands, and the save files are interchangeable between the two programs.

[2] The term PFC is used to refer to *PFC2D*, *PFC3D* and *PFC3D_EV*. FISH is a programming language embedded within PFC. The PFC Fishtank is a consistent set of FISH functions that extends the range of modeling that can be done with the PFC codes. It is a standard component of the PFC codes. The PFC private Fishtank is a PFC Fishtank that encapsulates particular model developments.

111 Third Avenue South • Suite 450 • Minneapolis, Minnesota 55401
Tel: (612) 371-4711 • icg@itascacg.com • www.itascacg.com • Fax: (612) 371-4717

1.0 HILL CONTACT MODEL

The Hill contact model is described in Sections 2.1 and 2.2 of Yohannes et al. (2009). Before describing the Hill contact model, we summarize the PFC distinct-element framework. We denote vectors by boldface type, such as $\mathbf{A}$; the length or magnitude of $\mathbf{A}$ is denoted $\|\mathbf{A}\|$ or simply A, and the addition of a circumflex denotes a unit vector, such as $\hat{\mathbf{A}} = \mathbf{A}/\|\mathbf{A}\| = \mathbf{A}/A$.

1.1 PFC Distinct-Element Framework

The PFC codes provide a distinct-element model that is wrapped by a graphical user interface. A particular instance of the distinct-element model is referred to as a *PFC model* (see Figure 1a). The PFC model consists of *bodies* and *contacts*. There are three types of bodies: balls, clumps and walls. A ball is a rigid sphere[3], a clump is a rigid collection of spherical pebbles[4] and a wall is a rigid manifold surface. Each body has a surface that is defined by a collection of *pieces*: a ball has one piece, which is the ball itself; the pieces of a clump and faceted wall are called *pebbles* and *facets*, respectively. The mechanical interaction between the surfaces of two bodies occurs at a contact (see Figure 1b) between two pieces. The contact is an interface that defines a middle surface between two locally flat notional surfaces. The contact location, $\mathbf{x}_\mathbf{c}$, is centered within the interpenetration volume of the two bodies, and the contact normal direction, $\hat{\mathbf{n}}_\mathbf{c}$, is directed from body 1 to body 2. The contact location and normal direction are given by (see Figure 2):

$$\mathbf{x}_\mathbf{c} = \mathbf{x}^{(1)} + \left(R^{(1)} + \frac{u_n}{2} \right) \hat{\mathbf{n}}_\mathbf{c}, \quad \hat{\mathbf{n}}_\mathbf{c} = \begin{cases} \dfrac{\mathbf{x}^{(2)} - \mathbf{x}^{(1)}}{d}, & \text{sphere-sphere} \\ \dfrac{\left\| \mathbf{x}_\mathbf{w} - \mathbf{x}^{(1)} \right\|}{d}, & \text{sphere-wall} \end{cases}$$

$$\text{with} \quad d = \begin{cases} \left\| \mathbf{x}^{(2)} - \mathbf{x}^{(1)} \right\|, & \text{sphere-sphere} \\ \left\| \mathbf{x}_\mathbf{w} - \mathbf{x}^{(1)} \right\|, & \text{sphere-wall} \end{cases} \tag{1}$$

$$u_n = \begin{cases} d - \left(R^{(1)} + R^{(2)} \right), & \text{sphere-sphere} \\ d - R^{(1)}, & \text{sphere-wall} \end{cases}$$

where $\mathbf{x}^{(s)}$ and $R^{(s)}$ are the center and radius, respectively, of sphere (s); $\mathbf{x}_\mathbf{w}$ is the point on the wall that is closest to $\mathbf{x}^{(1)}$; and u_n is the gap ($u_n > 0$ denotes a gap, while $u_n < 0$ denotes an overlap).

[3] The sphere is rigid as opposed to deformable. In an assembly of balls, all deformation occurs at the contacts. This is referred to as a soft-contact model.

[4] Each pebble does not deform, and the collection of pebbles behaves as a rigid body — i.e., the position of each pebble relative to the position of every other pebble does not change. All deformation occurs at the contacts, and contacts do not exist between pebbles that are part of the same clump.

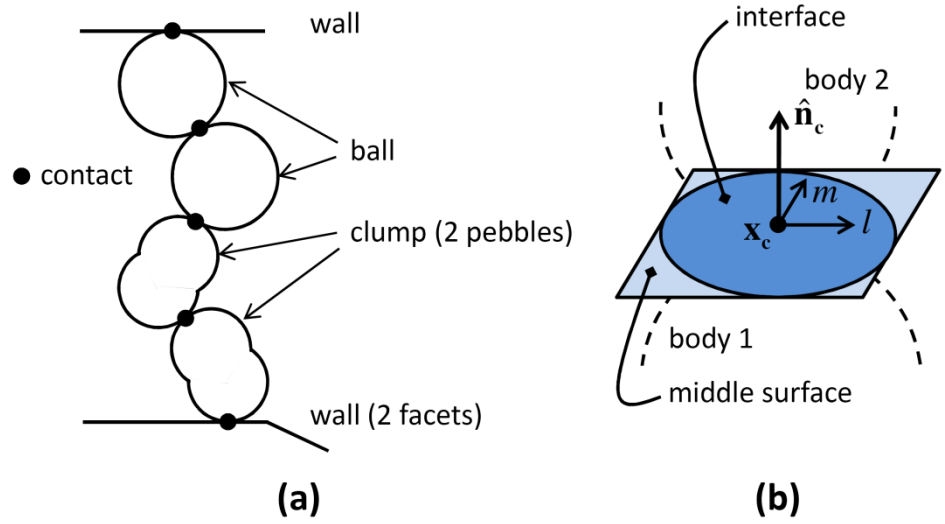

Figure 1 ***Definition of a PFC model: (a) bodies (ball, clump and wall), pieces (pebble and facet) and contacts and (b) effective interface geometry at a contact.***

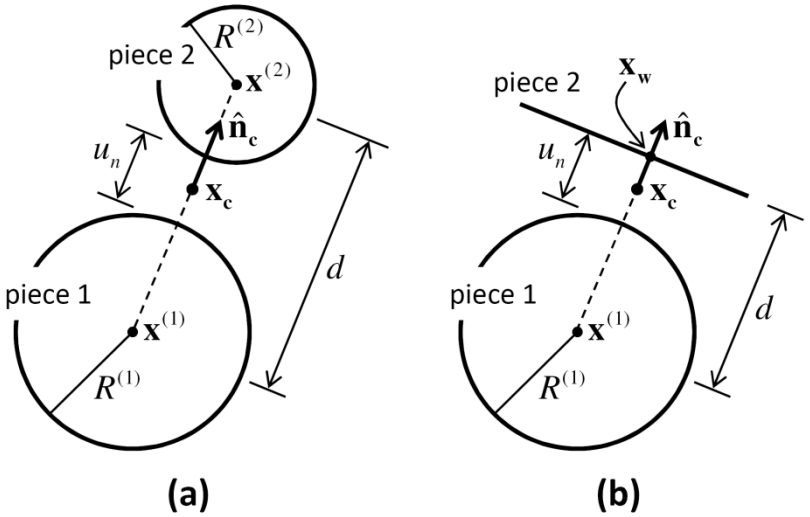

Figure 2 ***Contact location and normal direction: (a) sphere-sphere contact and (b) sphere-wall contact.***

The middle surface coordinate system, lmn, establishes l and m as orthogonal coordinates on the middle surface and n as normal to the middle surface such that $\hat{\mathbf{n}} = \hat{\mathbf{l}} \times \hat{\mathbf{m}}$. n coincides with the contact normal direction $\left(\hat{\mathbf{n}} = \hat{\mathbf{n}}_c\right)$, l is aligned initially with the projection of the global x or y direction, respectively, onto the middle surface (whichever is not parallel with $\hat{\mathbf{n}}$) and thereafter rotated to ensure that it remains fixed w.r.t. the middle surface during rigid-body motion ($\dot{\mathbf{u}} = \dot{\boldsymbol{\theta}} = \mathbf{0}$, defined in section 1.2.1) of the notional surfaces. The new orientation of $\hat{\mathbf{l}}$ is given by

$$\hat{\mathbf{l}} = \left(\frac{l^*}{l_2}\right)\mathbf{l}_2$$

$$\text{with} \quad \mathbf{l}_2 = \mathbf{l}_1 - \mathbf{l}_1 \times \tilde{\boldsymbol{\omega}}\Delta t, \quad \tilde{\boldsymbol{\omega}} = \left(\tfrac{1}{2}\left(\boldsymbol{\omega}^{(1)} + \boldsymbol{\omega}^{(2)}\right)\cdot \hat{\mathbf{n}}_\mathbf{c}\right)\hat{\mathbf{n}} \tag{2}$$

$$\mathbf{l}_1 = \hat{\mathbf{l}}^* - \hat{\mathbf{l}}^* \times \left(\hat{\mathbf{n}}_\mathbf{c}^* \times \hat{\mathbf{n}}_\mathbf{c}\right)$$

where the first rotation (to give $\mathbf{l}_1$) is about the line common to the old and new contact planes and the second rotation (to give $\mathbf{l}_2$) is about the new normal direction; the star ($*$) denotes the value at the end of the previous time step; $\boldsymbol{\omega}^{(b)}$ is the rotational velocity of body (b); and $\tilde{\boldsymbol{\omega}}$ is the average rotational velocity of the two bodies about the new normal direction.

Each contact stores a force ($\mathbf{F}_\mathbf{c}$) and moment ($\mathbf{M}_\mathbf{c}$) that are updated (to satisfy the generalized force-displacement law provided by the contact model) based on the relative motion of the notational surfaces associated with the interface. The generalized forces act in an equal and opposite sense on the associated surface pair (see Figure 3). A cell-space reduces the computational effort of determining pair interactions by localizing the search for candidate body pairs, and guaranteeing that a contact will be created before any two pieces overlap.

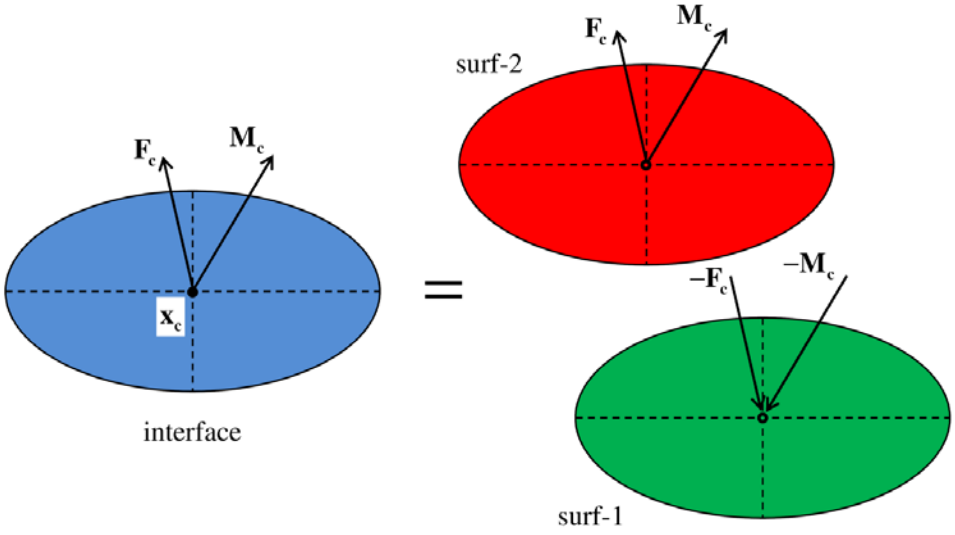

Figure 3 Generalized forces acting on surface pair associated with the interface.

1.2 Formulation

A Hill contact simulates the behavior of an interface between two rigid spherical particles with locally flat and disk-shaped (of negligible radius) notional surfaces. The interface mechanical behavior is elastic, frictional and dissipative. The elastic response arises from normal and tangential springs, the frictional response arises from a tangential slider and the dissipative response arises from

normal and tangential dashpots. The properties of these mechanical entities (with the exception of the damping-factor constant) are derived from properties of the two contacting bodies.

1.2.1 Kinematics

The relative motion of the notional surfaces at the contact is described by the relative translational $(\dot{\mathbf{u}})$ and rotational $(\dot{\boldsymbol{\theta}})$ velocities:

$$\begin{aligned}\dot{\mathbf{u}} &= \dot{\mathbf{x}}_c^{(2)} - \dot{\mathbf{x}}_c^{(1)} \\ \dot{\boldsymbol{\theta}} &= \boldsymbol{\omega}^{(2)} - \boldsymbol{\omega}^{(1)}.\end{aligned} \tag{3}$$

In this expression, $\dot{\mathbf{x}}_c^{(b)}$ is the translational velocity of body (b) at the contact location:

$$\dot{\mathbf{x}}_c^{(b)} = \dot{\mathbf{x}}^{(b)} + \boldsymbol{\omega}^{(b)} \times \left(\mathbf{x}_c - \mathbf{x}^{(b)} \right) \tag{4}$$

where $\mathbf{x}$ is either the centroid (if the body is a ball or clump) or the center of rotation (if the body is a wall); $\mathbf{x}_c$ is the contact location; $\boldsymbol{\omega}$ is the rotational velocity w.r.t. $\mathbf{x}$; and $\dot{\mathbf{x}}$ is the translational velocity (see Figure 4). If we consider each body as a rigid disk with a pin hole at the shared contact location, then $\dot{\mathbf{x}}_c^{(b)}$ is the translational velocity of the pin hole in disk (b).

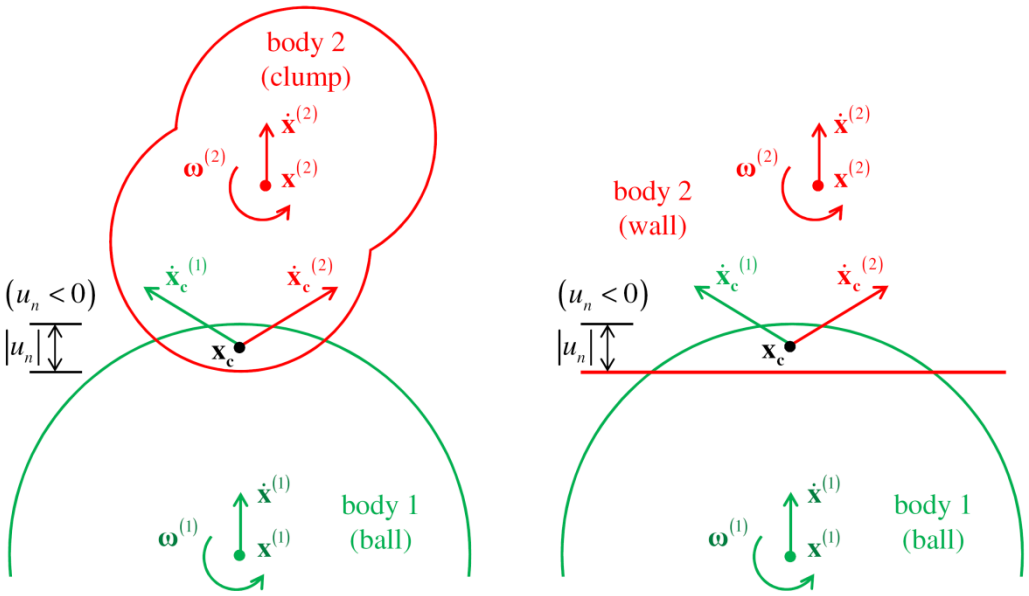

Figure 4 Motion of the bodies at a ball-clump (left) and ball-wall (right) contact.

The relative translational velocity can be expressed as

$$\begin{aligned} &\dot{\mathbf{u}} = \dot{\mathbf{u}}_\mathbf{n} + \dot{\mathbf{u}}_\mathbf{s} \\ &\text{with} \quad \dot{\mathbf{u}}_\mathbf{n} = \left(\dot{\mathbf{u}} \cdot \hat{\mathbf{n}}_\mathbf{c}\right)\hat{\mathbf{n}}_\mathbf{c} = \dot{u}_n \hat{\mathbf{n}}_\mathbf{c}, \quad \dot{\mathbf{u}}_\mathbf{s} = \dot{\mathbf{u}} - \dot{\mathbf{u}}_\mathbf{n} \end{aligned} \tag{5}$$

where $\dot{\mathbf{u}}_\mathbf{n}$ ($\dot{u}_n > 0$ is moving apart) and $\dot{\mathbf{u}}_\mathbf{s}$ are the relative translational velocities normal and tangential, respectively, to the middle surface, and the subscripts n and s correspond with normal and shear action, respectively (see Figure 5 — the centering of the contact location within the interpenetration volume ensures that the relative displacement is symmetric w.r.t. the interface). The relative velocities are tracked.[5]

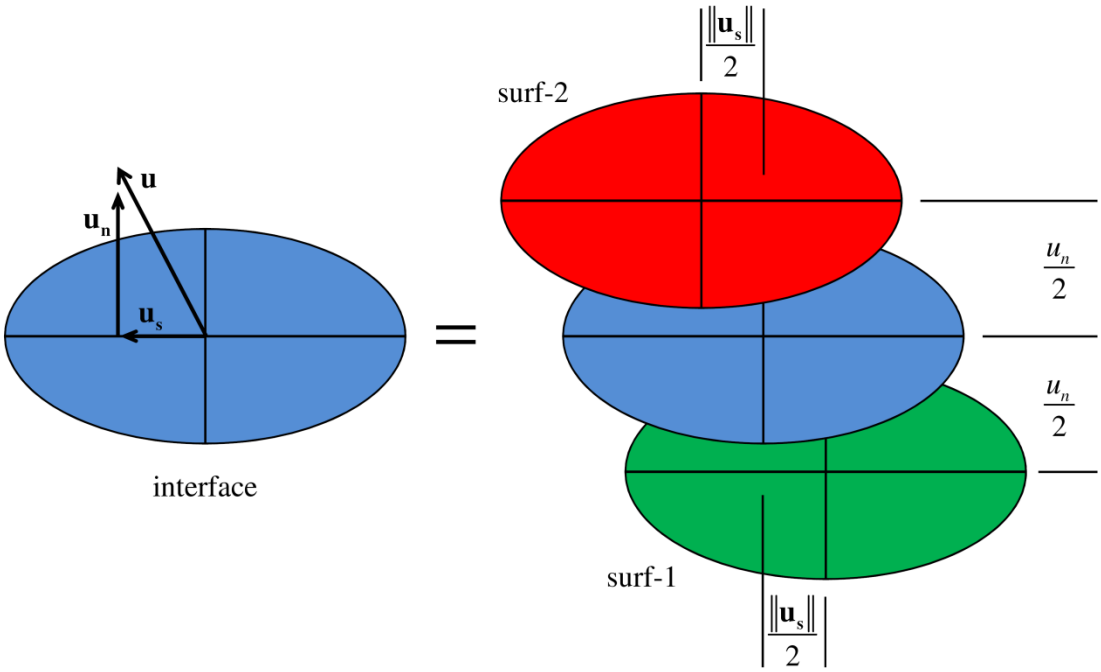

Figure 5 Kinematics of a contact showing interface (blue) with relative displacement and motion of notional surfaces (red and green).

The relative displacement increment during the time step Δt is

$$\Delta\mathbf{u} = \left(\dot{u}_n \Delta t\right)\hat{\mathbf{n}}_\mathbf{c} + \dot{\mathbf{u}}_\mathbf{s}\Delta t = \Delta u_n \hat{\mathbf{n}}_\mathbf{c} + \Delta\mathbf{u}_\mathbf{s} \tag{6}$$

so that the gap and the relative shear displacement (u_n and $\mathbf{u}_\mathbf{s}$, respectively) at the center of the interface are tracked via

[5] The values $\dot{u}_n$, $\dot{\mathbf{u}}_\mathbf{s}$ and $\dot{\boldsymbol{\theta}}$ are input to the UDM as **`FdBlock:{u_dot_n, ptu_dot_s, ptt_dot_rel}`**, respectively.

$$u_n := u_n + \Delta u_n, \quad \mathbf{u_s} := \mathbf{u_s} + \Delta \mathbf{u_s}. \tag{7}$$

1.2.2 Kinetics (or Force-Displacement Law)

The mechanical components of the Hill model include a normal spring and dashpot as well as a tangential spring, dashpot and slider (see Figure 6) to provide mechanical behavior that is elastic, frictional and dissipative. The elastic response arises from the normal and tangential springs, the frictional response arises from the tangential slider and the dissipative response arises from the normal and tangential dashpots.

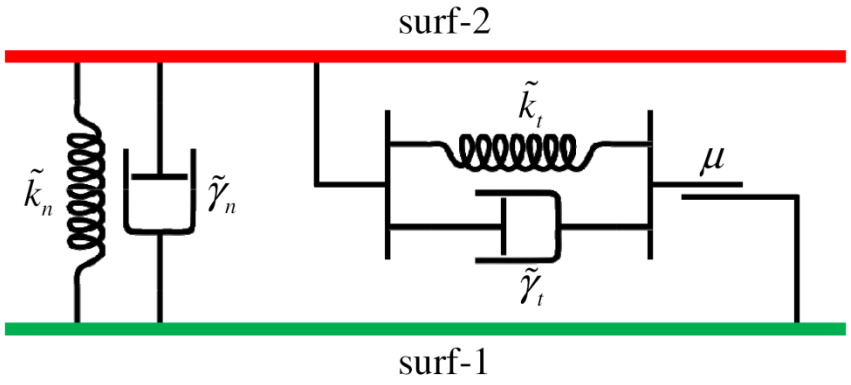

Figure 6 Mechanical components of the Hill model.

The force-displacement law of the Hill model (see Figure 7) is described in terms of the normal overlap (δ_n), the effective tangential overlap ($\boldsymbol{\delta}_\mathbf{t}^\mathbf{e}$) and the relative normal and tangential translational velocities ($\dot{\delta}_n$ and $\dot{\boldsymbol{\delta}}_\mathbf{t}$, respectively), which are expressed in terms of the preceding notation as

$$\begin{aligned} \delta_n &= -u_n, \quad & \boldsymbol{\delta}_\mathbf{t}^\mathbf{e} &= f\left(\dot{\mathbf{u}}_\mathbf{s}\right) \\ \dot{\delta}_n &= -\dot{u}_n, \quad & \dot{\boldsymbol{\delta}}_\mathbf{t} &= \dot{\mathbf{u}}_\mathbf{s} \end{aligned} \tag{8}$$

with the function f given by Eqn. (11). Normal overlap and relative normal translational velocity are signed scalars ($\delta_n > 0$ is overlap, and $\dot{\delta}_n > 0$ is increasing overlap). Effective tangential overlap and relative tangential velocity are vectors that lie on the interface, and as such, remain fixed w.r.t. the middle surface during rigid-body motion of the notional surfaces. The contact moment is zero.

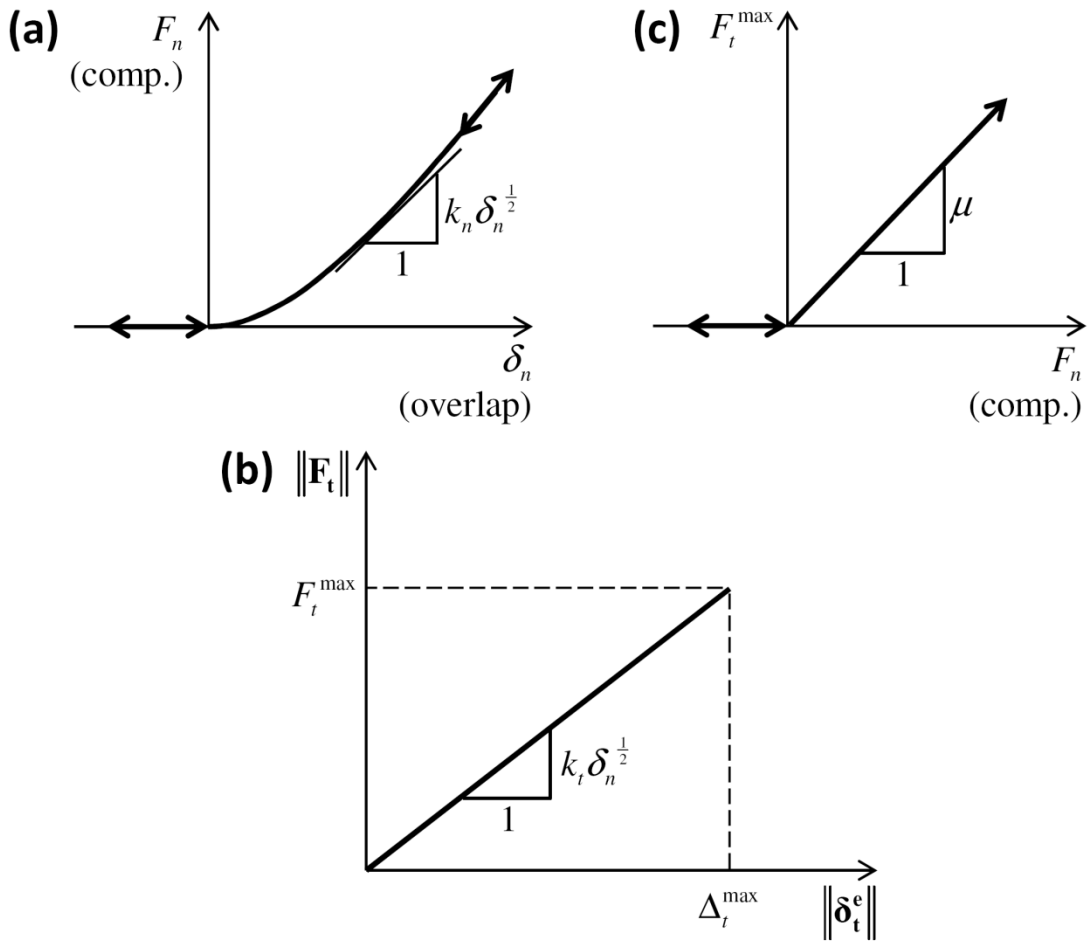

Figure 7 Force-displacement law for a Hill contact: (a) normal force versus normal overlap, (b) tangential force versus effective tangential overlap and (c) strength envelope.

The contact force ($\mathbf{F_c} = F_n\hat{\mathbf{n}}_\mathbf{c} + \mathbf{F_t}$, $F_n > 0$ is compression) is updated using the following three-step process.

1. Compute F_n based on the normal overlap (δ_n) at the end of the cycle and the relative normal translational velocity ($\dot{\delta}_n$) during the cycle via

$$F_n = \begin{cases} k_n\delta_n^{\frac{3}{2}} + \gamma_n\delta_n^{\frac{1}{4}}\dot{\delta}_n, & \delta_n > 0 \\ 0, & \text{otherwise} \end{cases} \tag{9}$$

   where k_n and γ_n are the normal stiffness and damping factors, respectively.

2. Update F_n to account for moisture by adding a moisture force (F_m , $F_m \geq 0$) via

$$F_n := F_n - F_m$$
$$F_m = \begin{cases} 0, & \delta_n < -2S_{cr} \\ F_{m\max} \exp\left(\frac{\delta_n}{2R_m}\right), & -2S_{cr} \leq \delta_n \leq 0 \\ F_{m\max}, & \delta_n > 0 \end{cases} \tag{10}$$

where $F_{m\max}$ is the maximum moisture force, S_{cr} is the critical half-separation at which the liquid bridge ruptures making the moisture force zero (see Figure 8) and R_m is the average bulk radius. If S_{cr} is greater than zero and the distance between the two contacting bodies becomes greater than $4S_{cr}$, then the contact between the two bodies may be deleted.

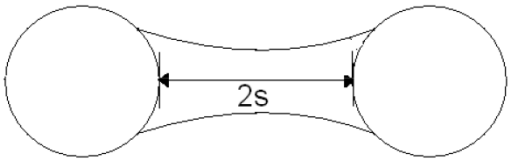

Figure 8 Definition of a liquid bridge in terms of the half-separation (S) between the two contacting bodies.

3. Compute $\mathbf{F_t}$ based on the effective tangential overlap ($\boldsymbol{\delta}_\mathbf{t}^\mathbf{e}$) at the end of the cycle and the relative tangential translational velocity ($\dot{\boldsymbol{\delta}}_\mathbf{t}$) during the cycle. Update $\boldsymbol{\delta}_\mathbf{t}^\mathbf{e}$ via

$$\boldsymbol{\delta}_\mathbf{t}^\mathbf{e} = \begin{cases} 0, & \delta_n \leq 0 \\ \left\{\boldsymbol{\delta}_\mathbf{t}^\mathbf{e}\right\}_{\text{rot}} + \dot{\boldsymbol{\delta}}_\mathbf{t}\Delta t, & \delta_n > 0 \text{ and } \left\|\mathbf{F}_t^*\right\| \leq F_t^{\max} \\ \Delta_t^{\max}\left(-\mathbf{F}_t^* / \left\|\mathbf{F}_t^*\right\|\right), & \delta_n > 0 \text{ and } \left\|\mathbf{F}_t^*\right\| > F_t^{\max} \end{cases}$$

$$\text{with} \quad \mathbf{F}_t^* = -k_t \delta_n^{\frac{1}{2}} \left\{\boldsymbol{\delta}_\mathbf{t}^\mathbf{e}\right\}_{\text{rot}} - \gamma_t \delta_n^{\frac{1}{4}} \dot{\boldsymbol{\delta}}_\mathbf{t} \tag{11}$$

$$F_t^{\max} = \begin{cases} \mu F_n, & F_n > 0 \text{ (compression)} \\ 0, & F_n \leq 0 \text{ (tension)} \end{cases}$$

$$\Delta_t^{\max} = \frac{F_t^{\max}}{k_t \delta_n^{\frac{1}{2}}}$$

where k_t and γ_t are the tangential stiffness and damping factors, respectively; μ is the friction coefficient; and $\left\{\boldsymbol{\delta}_{\mathbf{t}}^{\mathbf{e}}\right\}_{\text{rot}}$ is $\boldsymbol{\delta}_{\mathbf{t}}^{\mathbf{e}}$ from the end of the previous cycle that has been rotated via Eqn. (2) to ensure that it remains fixed w.r.t. the middle surface during the rigid-body motion of the notional surfaces that has occurred during the current cycle. $\boldsymbol{\delta}_{\mathbf{t}}^{\mathbf{e}}$ is zeroed whenever a gap forms and does not increase during sliding. Update $\mathbf{F}_{\mathbf{t}}$ via

$$\mathbf{F}_{\mathbf{t}} = \begin{cases} 0, & \delta_n \le 0 \\ \mathbf{F}_{\mathbf{t}}', & \delta_n > 0 \text{ and } \left\|\mathbf{F}_t'\right\| \le F_t^{\max} \\ F_t^{\max}\left(\mathbf{F}_{\mathbf{t}}' \Big/ \left\|\mathbf{F}_{\mathbf{t}}'\right\|\right), & \delta_n > 0 \text{ and } \left\|\mathbf{F}_t'\right\| > F_t^{\max} \end{cases} \tag{12}$$

$$\text{with} \qquad \mathbf{F}_{\mathbf{t}}' = \mathbf{F}_{\mathbf{t}}^{\text{sp}} + \mathbf{F}_{\mathbf{t}}^{\text{d}} = -k_t \delta_n^{\frac{1}{2}} \boldsymbol{\delta}_{\mathbf{t}}^{\mathbf{e}} - \gamma_t \delta_n^{\frac{1}{4}} \dot{\boldsymbol{\delta}}_{\mathbf{t}}$$

where $\mathbf{F}_{\mathbf{t}}^{\text{sp}}$ and $\mathbf{F}_{\mathbf{t}}^{\text{d}}$ are the tangential forces in the spring and dashpot, respectively (see Figure 9).

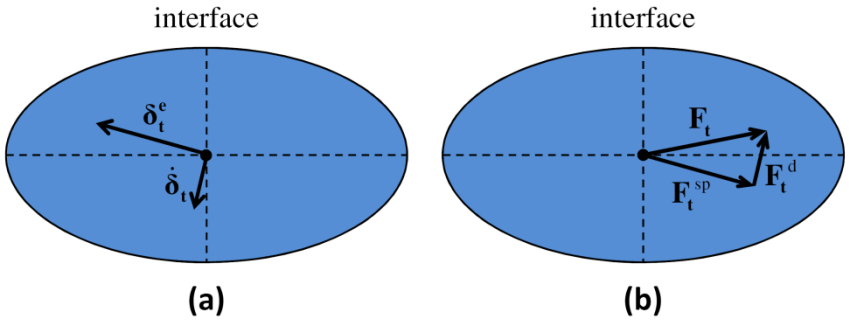

Figure 9 Tangential behavior of the Hill model: (a) effective tangential overlap and relative tangential velocity and (b) tangential force.

The internal Hill-model parameters are $\{k_n, k_t, \mu, \gamma_n, \gamma_t\}$ with SI units:

$$[k_n] = [k_t] = \text{kg} \cdot \text{m}^{-\frac{1}{2}} \cdot \text{s}^{-2}, \quad [\mu] = \text{dimensionless}, \quad [\gamma_n] = [\gamma_t] = \text{kg} \cdot \text{m}^{-\frac{1}{4}} \cdot \text{s}^{-1}. \tag{13}$$

The stiffness and damping factors are derived from properties of the two contacting bodies. The stiffness factors satisfy:

$$k_n = \tfrac{4}{3}\sqrt{R_{\text{eff}}}E_{\text{eff}}, \quad k_t = 8\sqrt{R_{\text{eff}}}G_{\text{eff}} \tag{14}$$

where R_{eff} , E_{eff} and G_{eff} are the effective radius, Young's modulus and shear modulus, respectively, of the contact; and

$$\begin{aligned} R_{\text{eff}} &= \left(\frac{1}{R_1} + \frac{1}{R_2} \right)^{-1} \\ E_{\text{eff}} &= \left(\frac{1-\nu_1^{\,2}}{E_1} + \frac{1-\nu_2^{\,2}}{E_2} \right)^{-1}, \quad G_{\text{eff}} = \left(\frac{2(1+\nu_1)(2-\nu_1)}{E_1} + \frac{2(1+\nu_2)(2-\nu_2)}{E_2} \right)^{-1} \end{aligned} \tag{15}$$

where R_b, E_b and ν_b are the radius, Young's modulus and Poisson's ratio, respectively, of body (b).

The damping factors satisfy:

$$\gamma_n = \alpha\sqrt{m_{\text{eff}} k_n}, \quad \gamma_t = \alpha\sqrt{m_{\text{eff}} k_t}; \quad m_{\text{eff}} = \left(\frac{1}{m_1} + \frac{1}{m_2} \right)^{-1} \tag{16}$$

where α is the dimensionless damping constant, m_{eff} is the effective mass of the contact and m_b is the mass of body (b). If body 2 is a wall, then

$$R_2 = m_2 = \infty. \tag{17}$$

The external Hill-model parameters (see Table 1) are $\{\mu, \alpha, R_b, m_b, E_b, \nu_b\}$ with SI units:

$$[\mu] = [\alpha] = [\nu_b] = \text{dimensionless}, \quad [R_b] = \text{m}, \quad [m_b] = \text{kg}, \quad [E_b] = \text{kg} \cdot \text{m}^{-1} \cdot \text{s}^{-2} \tag{18}$$

where the subscript (b) refers to a body (which can be a ball, clump or wall — see Figure 10).

Table 1 Hill model external parameters

Parameter	Description
Associated with bodies (ball, clump or wall):	
E_b	Young's modulus $[\mathrm{kg}\cdot\mathrm{m}^{-1}\cdot\mathrm{s}^{-2}]$
ν_b	Poisson's ratio [-]
R_b	radius [m], $R_b = \begin{cases} R_{bl}, & \text{ball radius} \\ R_{pb}, & \text{clump contacting-pebble radius} \\ \infty, & \text{wall} \end{cases}$
m_b	mass [kg], $m_b = \begin{cases} \rho_{bl}\frac{4}{3}\pi R_{bl}^3, & \text{ball } (\rho_{bl} \text{ is ball density}) \\ m_{cl}, & \text{clump mass} \\ \infty, & \text{wall} \end{cases}$
Associated with macroscopic material (contacts):	
μ	friction coefficient [-]
α	damping constant [-]
S_{cr}	critical half-separation [m], moist material
$F_{m\max}$	maximum moisture force $[\mathrm{kg}\cdot\mathrm{m}\cdot\mathrm{s}^{-2}]$, moist material
R_m	average bulk radius [m], moist material

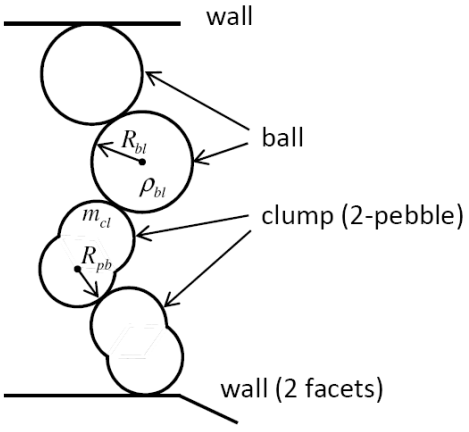

Figure 10 Definition of body as a ball, clump or wall for specification of Hill model external parameters.

1.2.3 Determining a Stable Time Step

The procedure to compute a stable time step in *PFC3D* 4.0 (see Section 1.6 in the Theory & Background volume of Itasca (2008)) requires that the UDM return the contact translational and rotational stiffnesses. If the contact model includes dashpots, then the translational stiffnesses must be increased via

$$\begin{aligned} \tilde{k}_n &:= \tilde{k}_n / F(\beta_n)^2, \quad \tilde{k}_t := \tilde{k}_t / F(\beta_t)^2 \\ F(\xi) &= \sqrt{1+\xi^2} - \xi, \quad 0 \le \xi \le 1 \end{aligned} \tag{19}$$

where β_n and β_t are the critical damping ratios in the normal and tangential directions, respectively. The translational stiffnesses can be expressed in terms of the mechanical components of the Hill model (shown in Figure 6) via

$$\tilde{k}_n = k_n \delta_n^{\frac{1}{2}}, \quad \tilde{\gamma}_n = \gamma_n \delta_n^{\frac{1}{4}}, \quad \tilde{k}_t = k_t \delta_n^{\frac{1}{2}}, \quad \tilde{\gamma}_t = \gamma_t \delta_n^{\frac{1}{4}}. \tag{20}$$

For the Hill model, the contact rotational stiffnesses are zero and it can be shown that the critical damping ratios are related to the damping constant via

$$\beta_n = \beta_t = \frac{\alpha}{2}. \tag{21}$$

1.3 Implementation

The Hill model is implemented as a user-defined contact model with C++ source files of **`Hill.cpp`** and **`Hill.h`**, which are compiled into **`udm_hl_{32,64}.dll`**. The 32 and 64 suffixes indicate compatibility with the 32- or 64-bit executable, respectively. The model name is **udm_Hill**, and the property names are prefixed by **hl_**.

The Hill model has the following properties:

hl_fric	friction coefficient (μ , $\mu \ge 0$).
hl_dcon	damping constant (α , $\alpha \ge 0$)
hl_Scr	critical half-separation (S_{cr} , $S_{cr} \ge 0$, moist material)
hl_Fmmax	maximum moisture force ($F_{m\max}$, $F_{m\max} \ge 0$, moist material)
hl_Rm	average bulk radius (R_m , $R_m > 0$, moist material)

The above properties are specified at the start of a simulation before any contacts exist, and used to assign the corresponding values to all contacts created subsequently. The properties are defined via the variables **hlg_fric_bb** (ball-ball contacts), **hlg_fric_bw** (ball-wall contacts), **hlg_dcon**, **hlg_Scr**,

hlg_Fmmax and **hlg_Rm**. If the moisture state is changed during a simulation, the following commands should be given (with **v1**, **v2** and **v3** denoting new values):

```
PROP  hl_Scr=v1  hl_Fmmax=v2  hl_Rm=v3 ; existing contacts
SET  hlg_Scr=v1 hlg_Fmmax=v2 hlg_Rm=v3 ; would-be contacts
```

The following internal state variables of the Hill model can also be accessed:

hl_snfac	normal stiffness factor (k_n) (read-only)
hl_stfac	tangential stiffness factor (k_t) (read-only)
hl_dnfac	normal damping factor (γ_n) (read-only)
hl_dtfac	tangential damping factor (γ_t) (read-only)
hl_nol	normal overlap (δ_n) (read-only)
hl_etolm	effective tangential overlap magnitude ($\left\|\boldsymbol{\delta}_{\mathbf{t}}^{\mathbf{e}}\right\|$) (read-only)
hl_Fm	moisture force (F_m) (read-only)

The following properties are assigned to all bodies (and are not part of the Hill UDM):

hlg_E_{b,w} Young's modulus of all balls and walls (E_b), stored in extra slot 1

hlg_nu_{b,w} Poisson's ratio of all balls and walls (ν_b), stored in extra slot 2

Density and radius are assigned to all balls (ρ_{bl} and R_{bl}) and used to obtain body mass $\left(m_b\right)$; if the body is a clump, then body mass is the clump mass (m_{cl}) and body radius is the radius of the contacting pebble (R_{pb}).

1.4 Examples

1.4.1 Two Granite Spheres

We compute the force-displacement response of two 10-mm diameter granite spheres (see data file **GraniteSpheres.dvr**). The properties of this system are listed in Table 2. We first compute the normal stiffness factor using Eq. (14):

$$k_n = \tfrac{4}{3}\sqrt{R_{\text{eff}}}E_{\text{eff}}, \qquad R_{\text{eff}} = \frac{R_{bl}}{2} = 2.5\times10^{-3}\ \text{m}$$
$$E_{\text{eff}} = \frac{E_b}{2\left(1-\nu_b{}^2\right)} = 14.834\ \text{GPa} \tag{22}$$
$$k_n = 9.89\times10^{8}\ \text{N}\cdot\text{m}^{-\frac{3}{2}} = 9.89\times10^{8}\ \text{kg}\cdot\text{m}^{-\frac{1}{2}}\cdot\text{s}^{-2}.$$

We next compute the tangential stiffness factor using Eq. (14):

$$k_t = 8\sqrt{R_{\text{eff}}}G_{\text{eff}}, \qquad R_{\text{eff}} = \frac{R_{bl}}{2} = 2.5\times10^{-3}\ \text{m}$$
$$G_{\text{eff}} = \frac{E_b}{4\left(1+\nu_b\right)\left(2-\nu_b\right)} = 3.408\ \text{GPa} \tag{23}$$
$$k_t = 1.36\times10^{9}\ \text{N}\cdot\text{m}^{-\frac{3}{2}} = 1.36\times10^{9}\ \text{kg}\cdot\text{m}^{-\frac{1}{2}}\cdot\text{s}^{-2}.$$

The damping factors are obtained using Eq. (16):

$$\gamma_n = \alpha\sqrt{m_{\text{eff}}k_n}, \quad \gamma_t = \alpha\sqrt{m_{\text{eff}}k_t}; \quad m_{\text{eff}} = \left(\frac{1}{m_1}+\frac{1}{m_2}\right)^{-1}$$
$$m_1 = m_2 = m_b = \rho_{bl}\tfrac{4}{3}\pi R_{bl}{}^3 = 1.388\times10^{-3}\ \text{kg}, \quad m_{\text{eff}} = \frac{m_b}{2} = 6.938\times10^{-4}\ \text{kg} \tag{24}$$
$$\gamma_n = 0.07\sqrt{\left(6.938\times10^{-4}\ \text{kg}\right)\left(9.89\times10^{8}\ \text{kg}\cdot\text{m}^{-\frac{1}{2}}\cdot\text{s}^{-2}\right)} = 57.98\ \text{kg}\cdot\text{m}^{-\frac{1}{4}}\cdot\text{s}^{-1}$$
$$\gamma_t = 0.07\sqrt{\left(6.938\times10^{-4}\ \text{kg}\right)\left(1.36\times10^{9}\ \text{kg}\cdot\text{m}^{-\frac{1}{2}}\cdot\text{s}^{-2}\right)} = 68.00\ \text{kg}\cdot\text{m}^{-\frac{1}{4}}\cdot\text{s}^{-1}.$$

Table 2 Properties of the two granite spheres

Property	Value
Hill model material:	
E_b [GPa], ν_b, R_{bl} [mm], ρ_{bl} [kg/m^3]	29, 0.15, 5, 2650
μ, α	0.5, 0.07

The normal force-displacement response is given by Eq. (9); for quasi-static loading ($\dot{\delta}_n \cong 0$):

$$F_n = k_n\delta_n^{\frac{3}{2}} = \left(9.89\times10^{8}\ \text{N}\cdot\text{m}^{-\frac{3}{2}}\right)\delta_n^{\frac{3}{2}} \tag{25}$$

which is plotted in Figure 11. The tangential force-displacement response is given by Eq. (12); for quasi-static loading ($\dot{\delta}_t \cong 0$) and no sliding:

$$F_t = k_t \delta_n^{\frac{1}{2}} \delta_t = \left(1.36 \times 10^9 \ \mathrm{N \cdot m^{-\frac{3}{2}}}\right) \delta_n^{\frac{1}{2}} \delta_t \tag{26}$$

which is plotted for two values of overlap in Figure 12.

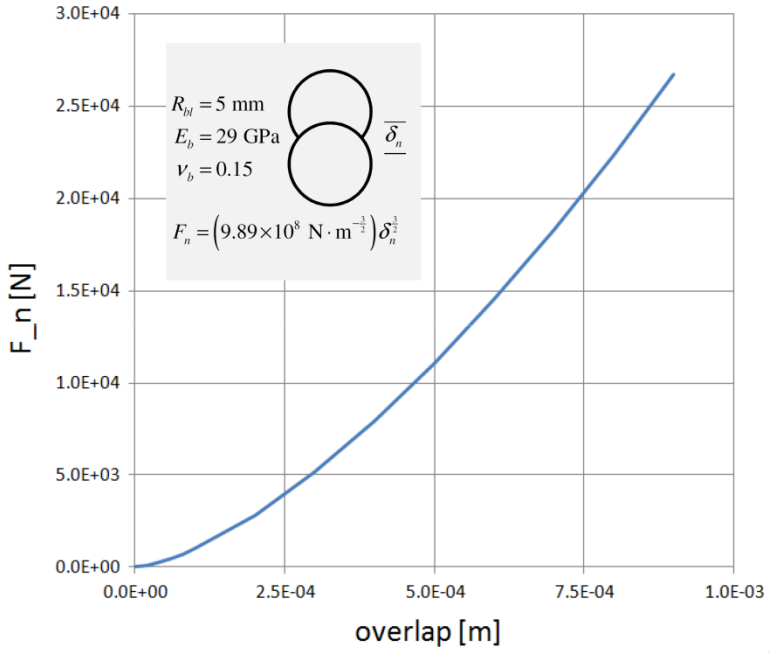

Figure 11 Normal force versus overlap for the two granite spheres.

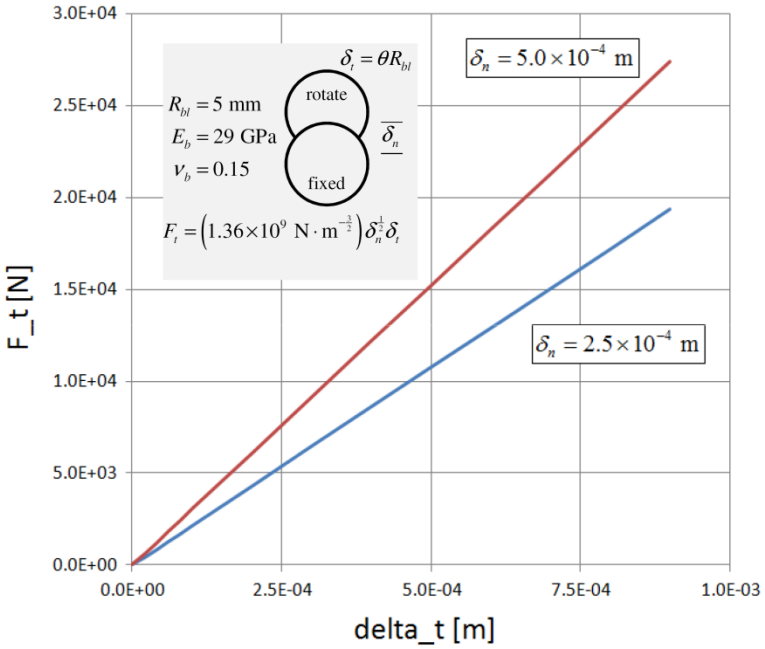

Figure 12 Tangential force versus tangential displacement (with no sliding) for the two granite spheres.

1.4.2 Granite Spheres and Wall

We compute the behavior of two 10-mm diameter granite spheres and a flat wall (see data file **`BallWall.dvr`**). This example demonstrates the initial existence of a ball-ball contact, which is then destroyed as a result of subsequent motion which induces the formation of a new ball-wall contact.

1.4.3 Cylinder Filled with Granite Spheres

We fill a cylindrical container with 10-mm diameter granite spheres and allow them to settle under gravity loading (see data file **`FillCylinder.dvr`**).

1.4.4 Relative Rigid Body Motion of Two Granite Spheres

We confirm that the tangential force remains fixed w.r.t. the middle surface during large rigid-body motion of the notional surfaces (see **`UDM-relativeRBM.pptx`** and data files **`SpinMe1.dvr`** and **`SpinMe2.dvr`**).

1.4.5 Behavior of Tangential Force for Large Sliding Motion

The behavior of the tangential force when subjected to large sliding motion is illustrated by data file **`BallWall-LargeSlide.dvr`** in which we create a ball and wall, with initial 1-mm normal overlap. We then move the ball horizontally and watch the tangential force develop and reach the frictional limit. We now reverse the ball direction. We observe that the tangential force

immediately begins to reduce to zero, and then increases back to the frictional limit while acting in the opposite direction. This is the expected behavior — i.e., reversing the relative shear velocity for a contact at the frictional limit causes the tangential force to immediately begin to reduce in magnitude.[6]

2.0 REFERENCES

Itasca Consulting Group, Inc. (2008) ***PFC3D (Particle Flow Code in 3 Dimensions)***, Version 4.0. Minneapolis: ICG.

Yohannes, B., K. Hill and L. Khazanovich. (2009) "Mechanistic Modeling of Unbound Granular Materials," Dept. of Civil Engr., University of Minnesota, Report to Minnesota Dept. of Transportation, Saint Paul, Minnesota, MN/RC 2009-21, June.

[6] This expected behavior did not occur for the **udm_Hill** version 3 contact model, because that model used total tangential overlap instead of effective tangential overlap to obtain the force in the tangential spring.